

Improved thermo-mechanical reliability of anode-supported solid oxide fuel cells

THÈSE N° 8470 (2018)

PRÉSENTÉE LE 25 MAI 2018

À LA FACULTÉ DES SCIENCES ET TECHNIQUES DE L'INGÉNIEUR

GROUPE SCI STI JVH

PROGRAMME DOCTORAL EN SCIENCE ET GÉNIE DES MATÉRIAUX

ÉCOLE POLYTECHNIQUE FÉDÉRALE DE LAUSANNE

POUR L'OBTENTION DU GRADE DE DOCTEUR ÈS SCIENCES

PAR

Fabio GRECO

acceptée sur proposition du jury:

Prof. P. Murali, président du jury
Dr J. Van Herle, Dr A. Nakajo, directeurs de thèse
Dr J. Laurencin, rapporteur
Prof. T. Kawada, rapporteur
Prof. S. Haussener, rapporteuse



ÉCOLE POLYTECHNIQUE
FÉDÉRALE DE LAUSANNE

Suisse
2018

*A Gloria,
a mio padre,
e a tutti coloro che stanno combattendo,
con la speranza che la ricerca possa trovare quanto prima delle soluzioni.*

Acknowledgements

My first, main acknowledgement goes to Jan Van herle, director of this thesis, because he has always trusted me, and put at my disposal often large budgets, especially for the fabrication of the setups of this thesis. He has always given relevant importance to my work and achievements. This has really helped to keep my motivation high.

An enormous contribution to this work has come from Dr. Arata Nakajo, co-director of this thesis. From the first until the last day of my doctorate, he has always been available for clarifications and help, with outstanding patience and completeness. Particularly during the thesis writing, he contributed largely to bring the document to an adequate level.

I would like to thank Dr. Stefan Diethelm, firstly because he helped me during the installation of my lab setups and answered to all my practical questions, and secondly for having shared many lunches while discussing on Swiss news. Besides this, he helped me a lot to improve my French skills.

This thesis has been reviewed by Prof. Tatsuya Kawada, Prof. Sophia Haussener and Dr. Jérôme Laurencin. I thank you all for your time and efforts, and for the useful and motivating discussions.

This thesis has received funding from the Swiss Confederation through the project SOF-CH-ASE (SwissElectric Research and Ofen), and from several EU projects: Endurance, Prosofc and CH2P. From SOLIDpower, I would like to thank Dr. Zacharie Wullemin and Dr. Dario Montinaro, for all their inputs and explanations. From Dynardo Austria GmbH, I really appreciated all the time that Dr. Christopher Zechmeister has spent for explaining me meticulously several theoretical and software-related questions, as well as the assistance that Prof. Christian Bucher and Dr. Sebastian Wolff have given me during these years. Discussions with Dr. Henrik Lund Frandsen were also of great help for the analysis of the sealing failure. The two mechanical testing setups of this work have been fabricated by the precious contribution of the workshop ATMX. In this work, numerical simulations have been carried out on EPFL cluster "Fidis".

I would like to thank Priscilla for the several chats we have had together, especially during the thesis writing. Your moral support has always been valuable and contributed many times to resume working with more motivation. I would like to thank also Giorgio, with whom I could share many conversations, especially during the train travels. Also, he took care of the workstations and let me use them, sometimes intensively. Many thanks to Thierry, for all the exchanges we have had together, from strictly scientific to more general topics. I have received many encouragements from Manuel, always accompanied by a good coffee, thanks to the coffee machine he bought and that I have used frequently. My acknowledgements go also to my (first and second year) office-mate Hossein and his wife Morgane, and Bardia, who will surely become a very good scientist like his father. On the experimental side, I would like to thank Steve for his availability to perform the mechanical tests and his exceptional patience for the samples polishing. Still within GEM team, I thank Guillaume, Mar, David, Nicola, Dirk, Samuel, Martin, Michel, Ligang, Quentin, Stéphane. Our secretaries, Alex and Chantal, have taken care with patience of all the administrative jobs.

A man without a woman is like a train without rails. In my case, these rails have been my girlfriend Raffaella, without whom I could not withstand the psychological stress of these years. Her support has been priceless, from simple logistic stuffs (preparing dinner and lunches, providing vitamin B, etc.) up to more “challenging” tasks like encouraging me to hang on in there. A sincere thank goes to my parents, to my brother Ilario, my sister-in-law Jenni and my niece Mira, for being an omnipresent family, even though distance and job make meeting each other not easy. A warm thank goes to Gianna, Davide, Laura and Enrico, for organising and spending the weekends in Torino in the best way possible and making me start a new week with more energies and happiness, and also to Piera and Mimino. I would like to thank “Maestro” Francesco, for all the conversations we have had, especially on the Swiss bureaucracy (looking forward to set-up a new concert). I thank Alberto (and Olga), to make the train travels from/to Sion funnier and make them pass quicker (when I meet him on the train, I keep my laptop in the backpack with pleasure), as well as Stefano (I here reaffirm that good people eat late) for the several conversations we have had during lunch, especially on the Italian politics (by the way, not the most proper topic for digestion). Lastly, I ought to thank “il vecchio della betoniera”, reference person during the toughest moments of this thesis.

*“guarda me, prendo tutta la vita com'è
non la faccio finita, ma incrocio le dita e mi bevo un caffè”*

[M. Gazzè]

Lausanne, May 3rd, 2018

Fabio Greco

Abstract

Solid oxide fuel cell (SOFC) based systems are co-generators of electricity and heat that excel for their high efficiency, low pollutant emissions and fuel flexibility. Their reliability is close to meet the requirements for market deployment. Recent research improved the reliability during both thermal cycling and polarisation, mostly by series of incremental modifications. However, the transition from small- to large-scale production imposes ever more severe costs requirements, which from the perspective of manufacturing and operation, largely depend on thermo-mechanical aspects. The end of life of SOFC stacks still often occurs because of mechanical failure, which therefore remains a major hurdle for commercialization.

The purpose of this study is to advance the understanding of the mechanical failures in SOFC stacks. It has two principal scopes: (a) the characterisation of the mechanical properties of SOFC materials and (b) investigations by thermo-mechanical modelling of the failure modes. The two activities are interrelated, because the prediction of failure mode by modelling relies on the knowledge of the mechanical properties.

Two setups for mechanical testing were designed and fabricated. Both are capable of testing multiple samples in one experimental stage, under the adequate temperature and atmosphere. A model-based parameters estimation approach was developed to measure the elastic and both primary and secondary creep properties and overcome the limitations of analytical solutions. The experimental and numerical developments were applied to the characterization of the NiO/Ni-YSZ electrode material and complemented with analyses using 3-D imaging and computational homogenization. The strength was further analysed by the Weibull statistics approach. An extension of thermo-elastic computational homogenisation was finally implemented to estimate the anisotropic visco-elastic properties of the gas-diffusion layers. A detailed continuum thermo-mechanical model for SOFC stack analysis was developed. Differences in modelling assumptions, selected design modifications and operation conditions were examined. Further, the effects on the stack reliability of component geometrical imperfections caused by manufacturing were for the first time modelled.

Parameters for the modelling of both primary and secondary creep in Ni-YSZ were identified, which is needed for advancing stack modelling capabilities. The thermo-elastic properties were not found to vary significantly during operation. The analysis of the strength measurements highlighted the combined beneficial effects of residual stress and plasticity of the Ni phase in the heterogeneous Ni-YSZ structure. The stack simulations allowed the analysis of cell and sealing failures and distribution of

contact pressure at electrically conducting interfaces. The effects of operation conditions were found to overall dominate, and worst for counter-flow with high internal reforming. Component imperfections altered the distribution of the contact pressure in the short-term, which was alleviated by creep relaxation during operation, without leading to strong history-dependence. The effect of the geometrical imperfections considered in this work remained mild, compared to that of the mechanical properties. The risk of cell failure is strongly affected by the operation conditions, whereas that of the sealants by the design and position in the stack.

Keywords: Solid oxide fuel cells, mechanical testing, computational homogenisation, primary creep, thermo-mechanical modelling, contact, mechanical failures, reliability

Sommario

I sistemi a celle a combustibile ad ossidi solidi (SOFCs) sono co-generatori di elettricità e calore che eccellono per la loro elevata efficienza, le basse emissioni e la flessibilità nel combustibile adoperato. La loro affidabilità è prossima a soddisfare i requisiti di mercato. Negli ultimi anni, la ricerca ha migliorato la loro affidabilità durante il funzionamento. Tuttavia, il passaggio alla produzione su larga scala impone requisiti di costo rilevanti, che dipendono in gran parte dagli aspetti termo-meccanici durante la produzione e il funzionamento. Negli stacks SOFC si verificano spesso rotture meccaniche, barriera importante per la loro commercializzazione.

Lo scopo di questo studio è di far progredire la conoscenza sulle rotture meccaniche degli stacks SOFC attraverso (a) la caratterizzazione delle proprietà meccaniche dei materiali delle SOFCs e (b) l'analisi sulle modalità di guasto, mediante modellazione termo-meccanica.

Due setups per prove meccaniche sono stati progettati e costruiti: entrambi sono in grado di testare più campioni in una fase sperimentale, a determinate temperature e atmosfere. È stato sviluppato un approccio alla stima dei parametri basato su modelli per misurare le proprietà elastiche e di creep primario e secondario, per superare i limiti delle soluzioni analitiche. I risultati sperimentali e numerici sono stati applicati alla caratterizzazione del cermet NiO/Ni-YSZ e integrati con analisi effettuate mediante l'uso di imaging 3D ed omogeneizzazione computazionale. La resistenza meccanica è stata analizzata utilizzando l'approccio statistico di Weibull. È stata infine implementata un'estensione dell'omogeneizzazione computazionale per stimare le proprietà visco-elastiche anisotropiche dei gas distribution layers. È stato sviluppato un modello termo-meccanico dettagliato per l'analisi dello stack SOFCs. Sono state esaminate le differenze nei criteri di modellizzazione, le modifiche di design e le condizioni di funzionamento. Inoltre, per la prima volta sono stati ricreati gli effetti delle deformazioni dei componenti dello stack causate dalle lavorazioni.

Sono stati identificati i parametri del creep primario e secondario del Ni-YSZ, necessari per lo sviluppo nella modellizzazione degli stacks. Le proprietà termo-elastiche non sono risultate variare in modo significativo durante il funzionamento. L'analisi di resistenza meccanica ha evidenziato gli effetti benefici dello stress residuo combinato alla plasticità della fase Ni nel cermet Ni-YSZ. Le simulazioni dello stack hanno consentito l'analisi di rottura delle celle e dei sigillanti, nonché della distribuzione della pressione di contatto nelle interfacce a conduzione elettrica.

Gli effetti delle condizioni di funzionamento sono in generale preponderanti. Le imperfezioni dei componenti hanno dapprima alterato la distribuzione della pressione di contatto nel breve periodo, per

poi divenire ininfluenti grazie al creep durante il funzionamento, senza portare ad un grande impatto nel lungo termine. L'effetto delle deformazioni considerate in questo lavoro è modesto, rispetto a quello delle proprietà meccaniche. Il rischio di rottura della cella è fortemente influenzato dalle condizioni operative, mentre quello dei sigillanti, dal design e dalla posizione nello stack.

Parole chiave: Pile a combustibile a ossido solido, Test meccanici, Omogenizzazione computazionale, Creep primario, Modellazione termo-meccanica, Contatto, Rotture meccaniche, Affidabilità

Table of Contents

Acknowledgements	iii
Abstract	v
Sommario	vii
List of Figures.....	xi
List of Tables.....	xxi
List of Acronyms	xxiii
List of Symbols.....	xxv
1 Introduction	1
1.1 Context	2
1.2 Objectives	6
1.3 Thesis outline	7
1.4 Fundamentals of SOFC technology	9
1.4.1 Operation of an SOFC.....	9
1.4.2 Stack and cell designs.....	11
1.4.3 Materials.....	13
1.5 Thermo-mechanical modelling of SOFCs: State-of-the-art	19
2 Mechanical properties of SOFC materials.....	31
2.1 Four-point bending testing.....	32
2.1.1 Modelling of 4-point bending.....	34
2.1.2 Design of 4-point bending setups.....	37
2.1.3 Experimental validation of the SEP and CRP setups.....	49
2.2 Estimation of the mechanical properties of Ni-YSZ anode	53
2.2.1 Samples for 4-point bending tests	53
2.2.2 Parameter estimation.....	54
2.2.3 Estimation of the elastic modulus and coefficient of friction	59
2.2.4 Primary and secondary creep.....	67
2.3 Strength of NiO/Ni-YSZ anode cermet	79
2.3.1 Experimental data processing	80
2.3.2 Experimental	81
2.3.3 Results and discussion.....	83
2.4 Computational homogenisation.....	88
2.4.1 Thermo-elastic properties of NiO/Ni-YSZ.....	89
2.4.2 Homogenised elasto-viscoplastic behaviour	96
3 Thermo-mechanical modelling of SOFC stacks.....	105

3.1	Model description	106
3.1.1	Geometry and mesh.....	106
3.1.2	Mechanical properties of the materials	111
3.1.3	Boundary conditions	115
3.1.4	Modelling of the mechanical interactions between the SRU components	117
3.1.5	Implementation of component geometrical imperfections	120
3.1.6	Simulation procedure.....	123
3.1.7	Post-processing of simulation results.....	128
3.2	Temperature profiles in operation.....	136
3.3	Overview of the thermo-mechanical results.....	139
3.3.1	Stress in the cell.....	139
3.3.2	Deformation profiles and stress in the MIC	141
3.3.3	Contact pressure at the interfaces between the cell and GDLs	144
3.3.4	Sealing	147
3.4	Analysis of the effects of pre-deformation, operation conditions and model formulation ...	151
3.4.1	Contact pressure	151
3.4.2	Failure of the cell.....	163
3.4.3	Sealing Failure	170
3.5	Modelling the impact of creep on the probability of failure of a solid oxide fuel cell stack...	177
3.5.1	Description of the modelling approach.....	177
3.5.2	Simulation results.....	183
4	Summary and conclusions	185
4.1	Mechanical properties of SOFC materials.....	186
4.2	Thermo-mechanical modelling of SOFC stacks	187
4.2.1	Overview of the thermo-mechanical results.....	187
4.2.2	Analysis of the effects of pre-deformation, operation conditions and model formulation	188
4.2.3	Modelling the impact of creep on the probability of failure of a solid oxide fuel cell stack	191
4.3	Recommendations for further work	192
	Bibliography.....	193
	Curriculum Vitae.....	207

List of Figures

Figure 1: Comparison of the most common types of fuel cells [4].	3
Figure 2: On the left-hand side, representation of the operating principle of an SOFC. On the right-hand side, the electrochemical and transport processes in the electrodes and electrolyte are illustrated [8].	9
Figure 3: Representation of the most common configurations for bending test of planar samples: a) four-point bending, b) three-point bending, c) ring-on-ring (ROR), d) ball-on-ring (BOR) and e) ball-on-three balls. Figure reproduced from Wei et al. [99].	32
Figure 4: Geometry of the four-point bending test configuration.	33
Figure 5: View of the full geometry of the 4-point bending test (left) and computational domain for the simulations (right).	35
Figure 6: Mesh dependence study of the FEM model of four-point bending setup. The y-axis is the ratio between the computed reaction force at the outer rollers for each mesh and for that for the finest mesh.	36
Figure 7: Comparison of the computed reaction force at the outer rollers over displacement at the inner rollers, from different simulation cases of the FEM model (curves from #1 to #4) and from analytical solution (curve #5). On the right-hand side, schematic representations of the potential analysed source of errors are shown.	36
Figure 8: 3-D sketch of upper side of the SEP setup. Components in transparency are shown for reference.	42
Figure 9: Representation of the load cell model (K11-500N005, Transmetra GmbH) used in the SEP setup.	43
Figure 10: Tracking of the contact points (depicted by magenta points) between samples and rollers upon downwards displacement of the samples dispenser. The frontal steel strip of the samples dispenser is shown in transparency.	44
Figure 11: Overview of the SEP setup in the laboratory of GEM group (EPFL Valais-Wallis).	46
Figure 12: 3-D sketch of CRP setup and detailed views of the testing fixture.	47
Figure 13: Overview of the CRP setup in the laboratory of GEM group (EPFL Valais-Wallis).	49
Figure 14: Reaction force versus displacement at the inner rollers measured experimentally (red circles) and simulated by the FEM model of the sample (continuous lines).	50
Figure 15: View of the simulated model with the left inner roller initially not in contact, and stress component along the x-direction upon bending.	51
Figure 16: Displacement at the inner rollers over time during creep deformation measured experimentally (red, magenta, blue and green points) and simulated by the FEM model of the sample (black lines). The dashed lines correspond to the direct results of the simulation. The continuous lines	

depict the simulation data result but shifted onto the experimental curves for direct visual comparison.	51
Figure 17: Representation of the perturbed geometry as a combination of shapes and amplitudes.....	58
Figure 18: Reaction force measured on the outer rollers versus position of the inner rollers during bending test of NiO-YSZ and Ni-YSZ samples at RT and high temperature conditions. Downwards and upwards triangle symbols depict respectively loading (i.e. downwards displacement of the inner rollers) and unloading (i.e. upwards displacement of the inner rollers) curve.	60
Figure 19: Simulated elastic bending (loading, from point 0 to 1a, followed by unloading, from 1b to 0) of the 3D FEM model of Paragraph 2.1.1 , with friction between the sample and the rollers. The deformation-reaction force plot (on the right hand side) depicts the three signals extracted from the output of the models.	61
Figure 20: Extended correlation matrix of the sensitivity analysis for the ELF mode.....	62
Figure 21: COP matrices of the three F-MOPs of the workflow for parameters estimation in ELF mode.	63
Figure 22: MOPs of the amplitude z_1 (i.e. corresponding to shape function ϕ_1) constituting the F-MOP _{Loading} , as a function of the three design variables E_m , μ and h_s	64
Figure 23: Estimated elastic modulus (filled circle) and coefficient of friction between the sample and the rollers (empty triangle). Green and grey refers to NiO-YSZ and Ni-YSZ, respectively. Interpolating straight lines between data points are provided as guide.	65
Figure 24: Plot of the responses simulated by the FEM model (black lines) of the tested sample using the parameters estimated by each data-set of mechanical tests. The experimental reaction force versus displacement at the inner rollers, already plotted in Figure 18, are here reported for comparison with the results of the simulations.....	66
Figure 25: Displacement at the inner rollers over time for the four mechanical loads, caused by creep at the three testing temperatures (the initial elastic deformation caused by the application of the load on the sample is here not plotted). Upwards and downwards triangle symbols depict respectively experimental data at 800 and 700 °C, whereas circle symbols are for the test at 750 °C.....	69
Figure 26: 4-point bending creep experiment with the 3-D FEM model.	70
Figure 27: Extended correlation matrix of the sensitivity analysis of the workflow for parameters estimation in CRP mode.	71
Figure 28: COP matrices of the four F-MOPs of the workflow for parameters estimation in CRP mode.	73
Figure 29: Plot of the experimental (green, blue, orange and red markers) and simulated (black lines) displacement at the inner rollers (black lines) over time for the four mechanical loads. Simulated curves are computed using the parameters estimated by the workflow. Top, middle and bottom plot are referred respectively to testing at 800, 750 and 700 °C.	74

Figure 30: Arrhenius plot of the natural logarithm of the estimated creep rate constant A from the experiments at 700, 750 and 800 °C. The values of B and Q reported on the plot are obtained from the linear fitting.	76
Figure 31: Plot of the error on the characteristic strength (red, green and blue lines, for different Weibull moduli) and on the Weibull modulus (black line) as a function of the number of tested samples. The curves are generated using the 90% confidence interval.	82
Figure 32: Measured strength of NiO-YSZ (green), Ni-YSZ (grey) and (Ni)-YSZ (orange) at RT (circles) and 800 °C (triangles). The Weibull failure probabilities calculated with the estimated parameters are plotted for reference in continuous lines.	84
Figure 33: Grid independence of (a) the Young modulus and (b) CTE on a 2.25 μm^3 sample; (c) Young modulus and (d) CTE on a 6.375 μm^3 sample.	93
Figure 34: Volume independence study based on growing cubic samples for: (a) the Young modulus and (b) the CTE.	93
Figure 35: (a) Phase and (b) neck size distribution of the solid phase (Ni and YSZ together) before and after aging.	95
Figure 36: Ageing study of: (a) Young modulus at room temperature, (b) Young modulus at 800°C and (c) CTE.	95
Figure 37: Periodic structure considered in this study and analysed RVE.	100
Figure 38: Von Mises stress in the analysed RVE for the six cases of loading. Meshes correspond to the undeformed configuration.	100
Figure 39: Values of diagonal terms of M matrix over applied macro-strain computed from this study.	101
Figure 40: Macro-stress versus Macro-strain computed from micro- and macro- model simulations (in dashed and continuous line, respectively). Data points, reproduced from Tsuda et al. [138], and the simulated mechanical behaviour of the base material (in black continuous lines) are plotted for comparison.	102
Figure 41: Exploded view of the geometry of the SRU.	107
Figure 42: Overview of the mesh.	109
Figure 43: Close-up view of a sealing region, where the mesh is automatically adjusted to modify the component thickness.	110
Figure 44: Temperature dependence of the anisotropic elastic properties of the GDLs materials obtained from computational homogenisation and implemented in the stack model.	114
Figure 45: Schematic of the modified periodic boundary conditions applied on the lower and upper node sets of the repeating unit, and linear multi-point node equations involving nodal displacements (u) implemented in the model. The temperature increase along the flow path (positive x direction) is depicted qualitatively by a colour scale from blue to red.	116

Figure 46: Schematic of the limitations using simple in-plane periodicity on the modelled SRU (on the left-hand side), and simplified configuration using modified PBC (on the right-hand side)..... 116

Figure 47: Representation of the simulated displacement of the upper and lower MICs of one SRU using enforced MIC flatness (FBC, on the top) and modified periodic boundary conditions (PBC, at the bottom). 117

Figure 48: Schematic view of the mechanical interactions (shown in dashed lines) between the components for “Model v1” (upper) and “Model v2” (lower). Black solid lines ($\partial\Omega_r$): tie contact. Black dashed lines ($\partial\Omega_{ct}$): default non-linear pressure-overclosure relationship. Red dashed lines ($\partial\Omega_{mct}$): modified non-linear pressure-overclosure relationship. Green dashed lines (depicted by $\partial\Omega$): frictionless contact with detachment throughout the whole simulation. 118

Figure 49: Non-linear pressure-overclosure relationships for “Model v1” (black line) and “Model v2” (red line). 119

Figure 50: Schematic view of the steps in the approach for modelling the pre-deformation of the components in the stack simulations..... 121

Figure 51: View of the initial deformation profile of the two MICs used in the stack model comprising 1 SRUs. For illustration purpose, the deformation is magnified. GDLs, cells and sealants are not represented..... 122

Figure 52: Plot of the initial deformation profile of the three MICs used in the stack model of two SRUs. For illustration purpose, the deformation is magnified. GDLs, cells and sealants are not represented. 122

Figure 53: Overview of the simulation sequence. Points from “A1” to “RT 0 h” comprise the phases of the stack production and qualification, including the first thermal cycle (“A3” to “RT 0h”). Points “HT 0 h” to “HT 150 h” (“Model v1”) and to “HT 10 k h” (“Model v2”) correspond to operation under constant thermo-electrochemical operation, which is followed by a second thermal cycle (“HT 150 h” to “RT 150 h” in “Model v1”, “HT 10 kh” to “RT 10 kh” in the “Model v2”)...... 123

Figure 54: Schematic view of the information flow in the thermo-electrochemical model. (a) 3-D imaging for the computation of the effective transport and electrochemical properties of the heterogeneous electrode materials using methods equivalent to the computational homogenization presented in Chapter 2.4. (b) Micrograph showing the layers discretized in 1-D in the local gPROMS electrochemical model. (c) 1-D discretization in the finite difference gPROMS stack model. (d) Importation of the species source and sink terms in the Fluent CFD model (only the subset of the computational domain that comprises the SRU solid parts is shown). 127

Figure 55: Contact resistance as a function of the contact pressure for the anode (left-hand side) and cathode (right-hand side) interfaces. Plots reproduced from Ref. [17]..... 129

Figure 56: Schematic of the multi-layer stripe used for the description of the energy-based analysis of the failure of the manifold sealants. 133

Figure 57: Comparison between VCCT computation and the analytical solution for the energy release rate as a function of crack length for a single material double cantilever beam (DCB). 134

Figure 58: Schematic of the stripe (a) and axisymmetric (b) simplification of the manifold sealing region (not to scale). The crack propagation directions and interfaces are indicated by a1 (upper) and a2 (lower). 135

Figure 59: Simulated temperature profiles for the conditions listed in Table 26: co-flow and fraction of pre-reforming (PR) of 0.5 (a), counter-flow and fraction of pre-reforming of 0.5 (b), 0.1 (c) and 0.99 (d). Only the lower MIC and cell are shown for illustration purpose. 136

Figure 60: Current density in operation computed along the symmetry lines corresponding to the temperature profiles shown in Figure 59..... 137

Figure 61: Evolution of the first principal stress (σ_1) in the anode (GDL-fuel side) and the manifold sealing during stack assembly (A1-A3), thermal cycling (RT 0 h, RT 10 kh) and operation in co-flow with a fraction of pre-reforming of 0.5 (HT 0 h, HT 10 h, HT 10 kh). 139

Figure 62: Evolution of the third principal stress (σ_3) in the YSZ electrolyte and GDC compatibility layer during stack production (A1-A3), thermal cycling (RT 0 h, RT 10 kh) and operation in co-flow with a fraction of pre-reforming of 0.5 (0 h, 10 h, 10 kh). 140

Figure 63: Evolution of the displacement in the y-direction along the x-axis (symmetry line) on the lower MIC during stack assembly (a) and operation (b). (c) Schematics showing highly magnified view of the y-deformation at the start and after 10 kh of operation, with color-coded temperature. 142

Figure 64: Evolution of the von Mises stress (σ_{Mises}) in the lower MIC during thermal cycling (RT 0 h-RT 10 kh) and operation in co-flow with a fraction of pre-reforming of 0.5 (HT 0 h, HT 10 h, HT 10 kh). .. 143

Figure 65: Evolution of the contact pressure (σ_{press}) on the anode (left) and cathode (right) sides during stack assembly (A1-A3), thermal cycling (RT 0 h, RT 10 kh) and operation in co-flow with a fraction of pre-reforming of 0.5 (HT 0 h, HT 10 h, HT 10 kh). The temperature profile is shown at the top right. . 145

Figure 66: Schematic of the thickness variation of the manifold sealant, GDLs and cell because of thermal shrinkage upon cool down. Dashed and continuous line depicts the components at HT and RT conditions, respectively..... 146

Figure 67: Cumulative density functions of the opening (a) and norm of the shear components (b) of the stress at the interface between the manifold sealing and the MICs during thermal cycling. Dots: RT 0 h, inlet and outlet, red: RT 10 kh air inlet, blue: RT 10 kh air outlet. Co-flow, fraction of pre-reforming of 0.5..... 148

Figure 68: Cumulative density functions of the uniaxial components of the stress in the manifold sealing during thermal cycling. Dots: 0 h, inlet and outlet, red: 10 kh air inlet, blue: 10 kh air outlet. Co-flow, fraction of pre-reforming of 0.5. 149

Figure 69: Cumulative density functions of the opening (a) and norm of the shear components (b) of the stress at the interface between the manifold sealing and the MICs during long-term polarisation in co-

flow. Dots: HT 0 h, red: air inlet, blue: air outlet. Continuous lines: HT 10 kh. Co-flow, fraction of pre-reforming of 0.5..... 149

Figure 70: Cumulative density functions of the opening (a) and norm of the shear components (b) of the stress at the interface between the cell sealing, the MICs and the cell during thermal cycling. Black: RT 0h, grey: RT 10 kh air. Co-flow, fraction of pre-reforming of 0.5..... 150

Figure 71: Cumulative density functions of the contact pressure at the interface between the anode and fuel GDL for the points RT 0 h (end of first thermal cycle), HT 0 h (start of polarisation), HT 10 kh (end of long-term polarisation) and RT 10 kh (end of second thermal cycle after long-term polarisation in co-flow with a fraction of pre-reforming of 0.5). The model version is “v2” if not indicated. Case of ideal MICs..... 151

Figure 72: Cumulative density functions of the contact pressure at the interface between (a) the anode and the fuel GDL and (b) the cathode and the air GDL for the four considered operation conditions, at the operating points at RT (end of both first and second thermal cycles), HT 0 h (start of polarisation), HT 10 kh (end of long-term polarisation). Case of ideal MICs, modified periodic boundary conditions, “Model v2” with 0.7 mm sealants..... 154

Figure 73: Evolution over the operation points of the mean (a) and standard deviation (b) of the contact pressure at the interface between the cathode and air GDL during assembly (A1-A3), operation (HT 0 h – HT 10 kh) and thermal cycling (RT 0h, RT 10 kh) for the four considered operating conditions cases (co-flow with PR=0.5, counter-flow with PR=0.1, 0.5 and 1.0). Case of ideal MIC, modified boundary conditions, “Model v2”..... 155

Figure 74: Relationship between the mean of the contact pressure on the cathode gas diffusion layer and the difference between the mean temperature in the active area and manifold sealant for varying operating conditions during thermal cycling (RT) and operation (HT 0 h and HT 10 kh). The dashed lines are not computed but provided as visual guides. Modified periodic boundary conditions, case of ideal MICs. The temperature profiles on the right are repeated from Figure 59..... 156

Figure 75: Contact pressure on the air inlet (left) and outlet (right) manifold sealants at the start of operation in co-flow with a methane pre-reforming fraction of 0.5 (upper) and counter-flow with a pre-reforming fraction of 0.1 (lower). Modified periodic boundary conditions without MIC pre-deformation..... 157

Figure 76: Highly magnified view of the simulated deformation with different MIC pre-deformation profiles. Two units computational domain, co-flow operation with a methane pre-reforming fraction (PR) of 0.5 and modified periodic boundary conditions. Pre-deformation profiles (a) 2Def00 after 150 h of operation (“Model v1”), (b) profile 2DefA, (c) profile 2DefB, both 10 kh of operation in “Model v2”..... 158

Figure 77: Evolution of the displacement in the y-direction along the symmetry line, before (A3) and after (RT 0 h) the first thermal cycle and at the start of operation in co-flow with a methane pre-

reforming fraction of 0.5 (HT 0 h) for varying MIC pre-deformations (shown in inserts), PBC. The first plot refers to the ideal (flat) MIC case.	158
Figure 78: Cumulative density functions of the contact pressure at the interface between anode and GDL-fuel before the first thermal cycling (point: A3) for (left) a computational domain comprising on unit, pre-deformed MICs and modified PBC and (right) two units computational domain, pre-deformed MICs, modified PBC and enforced flatness (FBC).....	159
Figure 79: Cumulative density function of the contact pressure at the interface between anode and GDL-fuel before the first thermal cycle (point: A3) for (left column). one unit computational domain, pre-deformed MICs and modified PBC and (right column) two units computational domain, pre-deformed MICs, modified PBC and enforced flatness (FBC).....	160
Figure 80: Evolution over the operation points of the standard deviation of the contact pressure at the interface between cathode and GDL-air for the four polarisation cases (co-flow with PRF=0.5, counter-flow with PRF=0.1, 0.5 and 1.0). Modified periodic boundary conditions without MIC pre-deformation.	161
Figure 81: Evolution of the contact pressure on the cathode gas diffusion layer and discrepancy between the first and second unit, during thermal cycling (RT 0 h and RT 10 kh) and operation in co-flow with a methane pre-reforming fraction of 0.5. Modified periodic boundary conditions, MIC pre-deformation profile 2DefB. For comparison, the corresponding reference case with ideal MIC is shown in Figure 65.....	162
Figure 82: (a) Evolution of the contact pressure on the cathode gas diffusion layer and discrepancy between the first and second unit. During thermal cycling (RT 0 h and RT 900 h) and operation in co-flow with a methane pre-reforming fraction of 0.5 (HT 0 h and HT 900 h). Modified periodic boundary conditions, MIC pre-deformation profile 2Def00 insert in (b), the corresponding reference case without MIC pre-deformation is shown in (c).	163
Figure 83: Effect of boundary conditions (FBC, PBC) on the probability of failure of the anode computed for a 70-cell stack (P_f) during the assembly steps (A1-A3), operation in co-flow with a methane pre-reforming fraction of 0.5 (HT 0 h – HT 10 kh) and thermal cycling (RT 0 h and RT 10 kh). Case of ideal MIC, “Model v2”	164
Figure 84: View of the stress σ_{11} in the anode at the end of the assembly process (A3) for modified periodic (PBC, left) and enforced flatness (FBC, right) boundary conditions, with ideal MICs.....	165
Figure 85: Evolution of the 1 st principal stress σ_1 in the anode from the end of the assembly process (A3, upper left) and after up to 10 kh of operation (HT 0 h to HT 10 kh, lower serie of figures) for modified periodic (PBC, left) and enforced flatness (FBC, right) boundary conditions. Operation in co-flow with a fraction of pre-reformed of 0.5 (upper right: temperature profile repeated from Figure 59) and case of ideal MICs.....	166

Figure 86: Effect of the operation conditions (co- and counter-flow and varying methane pre-reforming fractions) on the probability of failure computed for a 70-cell stack (P_f). Case of ideal MIC with modified periodic boundary conditions (PBC)..... 167

Figure 87: Evolution of the 1st principal stress σ_1 in the anode during operation from 0 h (a) up to 10 kh (b), in counter-flow with a fraction of pre-reformed methane of 0.1 (left side) and 1.0 (right side). (c) Corresponding temperature profiles repeated from Figure 59. Case of ideal MICs with modified periodic boundary conditions (PBC)..... 168

Figure 88: Effect of MIC pre-deformation on the 1st principal stress σ_1 in the anode at the start of operation (HT 0h). (a,b) Simulation with one unit, comparison between the ideal case (left) and pre-deformation profiles (right) 1DefA and 1DefB. (c,d) Comparison of the stress in the first (left) and second cell (right) simulated with the 2 unit models with pre-deformation profiles 2DefA (c) and 2DefB (d). Modified periodic boundary conditions (PBC) and co-flow with a fraction of pre-reformed methane of 0.5..... 169

Figure 89: Cumulative probability density function of the opening and shear stress at the sealing interfaces in the air outlet manifold at room temperature, after 10 kh of operation in co-flow with a fraction of pre-reformed methane of 0.5 (CO 0.5) simulated by the “Model v1” and “Model v2” models with modified periodic (PBC) or enforced flatness (FBC) boundary conditions. 171

Figure 90: Effect of the operation conditions on the cumulative probability density function of the opening and shear stress at the sealing interfaces in the air outlet manifold at room temperature, after 10 kh of operation. Case of ideal MICs with modified periodic boundary conditions and “Model v2”. 171

Figure 91: Effect of MIC pre-deformation and boundary conditions on the cumulative probability density function of the opening and shear stress at the sealing interfaces in the air outlet manifold at room temperature, after 10 kh of operation in co-flow with a fraction of pre-reformed methane of 0.5 (CO 0.5)..... 172

Figure 92: Energy release rate computed for the stripe (a) and axisymmetric (b) simplification of the manifold sealing region shown in Figure 58 a and b, respectively. Dashed lines correspond to computations based on total energy variation, similar to that applied at the stack scale..... 173

Figure 93: Elastic energy release rate at the manifold sealants computed by releasing the interfaces without (a) or with frictionless contact (b). Detachment simulations were performed after the first (RT 0 h, black and grey) and after the second thermal cycle (blue: air inlet, red: air outlet) after 10 kh of operation in co- (light blue and red) or counter-flow with varying fraction of methane pre-reforming. Square and circles refer to FBC and PBC, respectively. Filled and empty markers refer to the interface a1 (upper) and a2 (lower), respectively. Thickness of the sealing is 0.7 mm. 174

Figure 94: Elastic energy release rate at the manifold sealants computed by releasing the interfaces without (planes with continuous contour) or with frictionless contact (planes with dashed contour). Detachment simulations were performed after the first and second thermal cycle after 10 kh of

operation in co-flow and for two sealing thickness (0.2 and 0.7 mm), and varying boundary conditions (EFLT and MPBC). For each condition, only the worst case is shown (corners of the planes, which are provided as a guide). 175

Figure 95: Representation of the three dimensional model of the SRU and denomination of the components..... 177

Figure 96: temperature-dependent Young's modulus from data in Ref. [4–6]. The Young's modulus of 20YDC was assumed to be equal to that of 8YSZ..... 178

Figure 97: On top: spatial-dependent temperature fields (in °C) on the SRU for different current intensities. At the bottom: thermal load profile over the SOFC stack lifetime implemented into the SRU model..... 182

Figure 98: Probability of failure of the anode, electrolyte and compatibility layer for the case of the cell B. The thermal load profile over the SOFC stack lifetime is plotted for reference..... 183

List of Tables

Table 1: Sensitivity of the error caused by friction to the inner and outer span.....	38
Table 2: Sensitivity of the error caused by wedging stresses to the inner and outer span.	38
Table 3: Sensitivity of the error caused by load mislocation to the inner and outer span.	39
Table 4: Sensitivity of the error caused by anticlastic curvature to the sample width and outer span. ..	40
Table 5: Elastic and creep properties of Crofer 22 APU from the literature (Ref. [103,104], tensile testing).....	49
Table 6: Computed creep bending rates (in mm/h) from experimental and simulation data.	52
Table 7: Overview of the estimated parameters, materials and reference conditions for the elastic and creep properties studies.	54
Table 8: Design variables, models and computed signals in the sensitivity analysis of the ELF and CRP parameter estimations.....	55
Table 9: F-MOPs and components of the random field simulations for the parameters estimation mode ELF.	62
Table 10: Validation tests on the parameters estimation workflow, ELF case.	64
Table 11: Comparison of the elastic modulus computed from estimation procedure and analytical solution.....	67
Table 12: Overview of the creep test conditions at the three testing temperatures.	68
Table 13: F-MOPs and components of the random field simulations for the parameters estimation mode CRP.	72
Table 14: Overview of the tests for the numerical validation of the parameters estimation, CRP case. .	73
Table 15: Creep parameters A, n and m of Ni-YSZ at 700, 750 and 800 °C obtained from estimation procedure.	75
Table 16: Displacement rates at the inner rollers obtained from linear fitting of the experimental data (see Figure 25).	78
Table 17: Creep parameters A and n obtained from the estimation procedure and from the analytical solution.....	78
Table 18: Weibull statistics parameters estimated from the RT and 800 °C testing.	84
Table 19: Thermo-elastic and strength properties of NiO and YSZ.....	85
Table 20: Thermo-elastic properties of Ni and YSZ at room temperature and 800°C.	92
Table 21: Young modulus and CTE obtained by experimental methods and 3-D imaging.	94
Table 22: Metric and topological properties of the pristine and aged Ni-YSZ volume samples.	94
Table 23: Kinematic equations of the boundary conditions at the RVE for the six loading modes.....	99

Table 24: Thermo-mechanical properties of the materials of the SRU for “Model v1”. Data from Ref. [15,68,103,104,110,112,121,128,146–155].	112
Table 25: Thermo-mechanical properties of the materials of the SRU for “Model v2”. Data from Ref. [15,68,103,104,110,112,121,128,146–155].	113
Table 26: List of selected thermo-electrochemical conditions	128
Table 27: Maximum thermal gradients in the cells along the x and z directions for the four temperature profiles.	137
Table 28: Weibull parameters and strength of the SOFC materials [15].	179
Table 29: Thermo-mechanical properties and creep parameters of the SRU materials.	180

List of Acronyms

ALHS	Advanced Latin Hypercube Sampling
BC	Boundary conditions
BCAS	Barium-calcium-aluminosilicate glass-ceramic
BCS	Bonded compliant sealing
BoP	Balance of Plant
BOR	Ball-on-ring
CAD	Computer aided design
CTE	Coefficient of thermal expansion
CO	Co-flow
CR	Counter-flow
CRP	Creep
DCB	Double cantilever beam
DoE	Design of experiment
ESB	Energy selective backscatter
ELF	Elastic properties
ERR	Energy release rate
FEM	Finite-element method
FBC	Enforced flatness boundary conditions
FIB-SEM	Focused ion beam-scanning electron microscopy
FF	Full Factorial
FU	Fuel utilisation
GDC	Gadolinia-doped ceria
GDL	Gas distribution layer
HT	High temperature
LEFM	Linear elastic fracture mechanics
MIC	Metallic interconnect
LSCF	Lanthanum strontium cobalt ferrite
LSM	Lanthanum strontium manganite
LVDT	Linear variable displacement transducer
PBC	Modified periodic boundary conditions
PR	Partial reforming fraction
ROR	Ring-on-ring
RT	Room temperature
RVE	Representative volume element
SEP	Setup for the measurement of the elastic and strength properties
SOEC	Solid oxide electrolysis cell
SOFC	Solid oxide fuel cell
SRU	Single repeating unit
TPB	Triple-phase boundary
VCCT	Virtual crack closure technique
YSZ	Yttria-stabilised zirconia

List of Symbols

Letters

a	Inner rollers span, [mm]
a_c	Crack length, [mm]
A	Creep rate constant, [$\text{h}^{-1} \text{MPa}^{-n}$]
B	Creep pre-exponential factor, [$\text{h}^{-1} \text{MPa}^{-n}$]
C_0	Clearance at zero contact pressure, [mm]
CoP	Coefficient of prognosis, [%]
d	Grain size, [mm]
D_{ij}	Stiffness tensor, [MPa]
D_{tr}	Diameter of the tie rods, [mm]
E	Potential difference, [V]
Em	Elastic modulus, [GPa]
F	Faraday's constant, [C mol^{-1}]
g	Grain size parameter
G	Energy release rate, [J mm^{-2}]
H^0	Molar Gibbs free energy, [J mol^{-1}]
h, h_s	Sample thickness, [mm]
I	Second moment of area, [mm^4]
I_d	Deviatoric operator
j	Current density, [A cm^{-2}]
K	Stiffness parameter, [N mm^{-1}]
K_{ic}	Fracture toughness, [$\text{MPa m}^{0.5}$]
L	Length, outer rollers span [mm]
m	Primary creep exponent, [-]. Weibull modulus, [-]
M	Anisotropy matrix, [-]
Mf	Bending moment, [N mm]
n	Stress exponent, [-]
N	Total set of measurements, [-]
p	Pressure, [Pa]
P	Mechanical load, [N]
Pf	Probability of failure, [-]
Q	Activation energy for creep, [kJ mol^{-1}]
R	Gas constant, [$\text{kJ mol}^{-1} \text{K}^{-1}$]
RF	Reaction force, [N]
s_{ij}	Deviatoric stress tensor, [MPa]
S	Surface, [mm^2]
tSRU	SRU thickness, [mm]
T	Temperature, [K, °C]
u_i	Displacement at mesh node i^{th} , [mm]

U	Voltage, [V]
U_{el}	Stored elastic energy of a system, [J]
w	Sample width, [mm]
W	External work, [J]
V	Volume, [mm ³]
x, y, z	Spatial coordinates
z^i	Amplitude correspondent to i^{th} shape function
α	Porosity, [-]
γ	Specific surface energy, [J mm ⁻²]
Γ	Free surface energy, [J]
δ	Deformation at the application point of the force, [mm]
Δs	Deviation from design of the positions of the inner rollers, [mm]
ε_{ij}	Strain tensor, [-]
$\dot{\varepsilon}_{ij}$	Strain rate tensor, [-]
E_{ij}	Macro-strain tensor, [-]
\dot{E}_{ij}	Macro-strain rate tensor, [-]
μ	Coefficient of static friction, [-]
ν	Poisson's ratio, [-]
Π	Potential energy, [J]
σ_{eq}	Equivalent stress, [MPa]
σ_{ij}	Stress tensor, [MPa]
σ_0	Characteristic strength, [MPa]
$\sigma_{1,2,3}$	First, second, third principal stress, [MPa]
σ_{max}	Maximum stress at failure, [MPa]
σ_Y	Yield strength, [MPa]
Σ_{eq}	Equivalent macro-stress, [MPa]
Σ_{ij}	Macro-stress tensor, [MPa]
φ	Elastic strain energy density, [J m ⁻³]
\emptyset	Shape function

Subscript

0	Reference
a	Anode
act	Activation losses
c	Cathode
conc	Concentration and diffusion
d	Dense material
e	Electrolyte
eq	Equivalent
exp	Experimental
f	Final

fail	Sample failure
fri	Friction (four-point bending)
g	Gas
i	Initial
IR	Inner rollers
mis	Load mislocation (four-point bending)
ohm	Ohmic
OR	Outer rollers
pre	Anticlastic curvature (four-point bending)
red	Reduced state
rev	Reversible
ss	Steady state
tr	Tie rods
wdg	Wedging stress (four-point bending)

Superscript

crp	Creep
el	Elastic
LBT	Linear beam theory
LD	Loading configuration of the RVE
tot	Total
T	Transposed

1 Introduction

1.1 Context

The requirement of both higher efficiency and lower environmental impact in electrical energy production is continuously gaining in importance. Electricity generation is worldwide still dominated by thermal cycles, which mainly operate on fossil fuels [1]. At the Swiss level, the current energy policies aim by 2050 at a reduction of both electricity consumption and CO₂ emissions, respectively by 50% and 70-80%. In parallel, a progressive phase-out of the Swiss nuclear power plants is scheduled. Such ambitious objectives require an increase of the energy efficiency and an extensive integration of renewable energy sources into the electrical grid [2].

In conventional thermal systems, the thermal energy of the gases generated by the reaction of combustion is converted into first mechanical work and then electricity in most cases by turbomachines or internal combustion engines. However, only part (typically from 30 up to 50%) of the available thermal power can be effectively converted into mechanical power, the main limiting factor being the Carnot cycle efficiency, which applies to all systems converting thermal energy to mechanical work [3]. Relevant technical improvements were achieved over the last decades, but increases in efficiency and reduction of pollutant emissions become ever more difficult to obtain as the thermodynamic limitations of the technology is approached. On the contrary, electrochemical energy conversion systems are not affected by the Carnot cycle efficiency, because they convert the chemical energy of a fuel directly into electricity by electrochemical reactions. Neither combustion nor moving parts are involved in the energy conversion process. As a result, the achievable efficiency of this second category of energy systems can be significantly higher. Electrochemical energy conversion devices include fuel cells and batteries, among others. Conversely to batteries, fuel cells can generate electricity ceaselessly, as long as fuel is supplied. The electrochemical reactions can be reverted, which permits the inversion of the operating mode from fuel to electrolysis mode, and vice-versa, using the same device. In electrolysis, electricity is supplied to the system to produce fuel from excesses of electricity. In the realm of electrochemical energy conversion and storage, this feature is of interest to meet the end user's demand, despite an uneven electrical energy supply.

Several types of fuel/electrolyser cells are developed. An overview is provided in Figure 1. Structurally, they all share the same arrangement: two electrodes, anode and cathode, separated by an impervious electrolyte. They mainly differ in the type of ions transported by the electrolyte, electrochemical reactions at the electrodes and therefore in the cell materials and temperature levels.

The performance, power, size and thus practical application of each type of fuel/electrolyser cell, is related to the electrochemical reactions and ion transport mechanism in the cell, as outlined in Figure 1. Among the types of fuel/electrolyser cells developed to date, solid oxide cells (SOCs), which include SOFCs (solid oxide fuel cells) and SOECs (solid oxide electrolyser cells) are the most promising in the case high electrical efficiency is needed together with high fuel flexibility, low vulnerability to contaminants in the gas streams and large variations in power output. This thesis is dedicated to SOFCs.

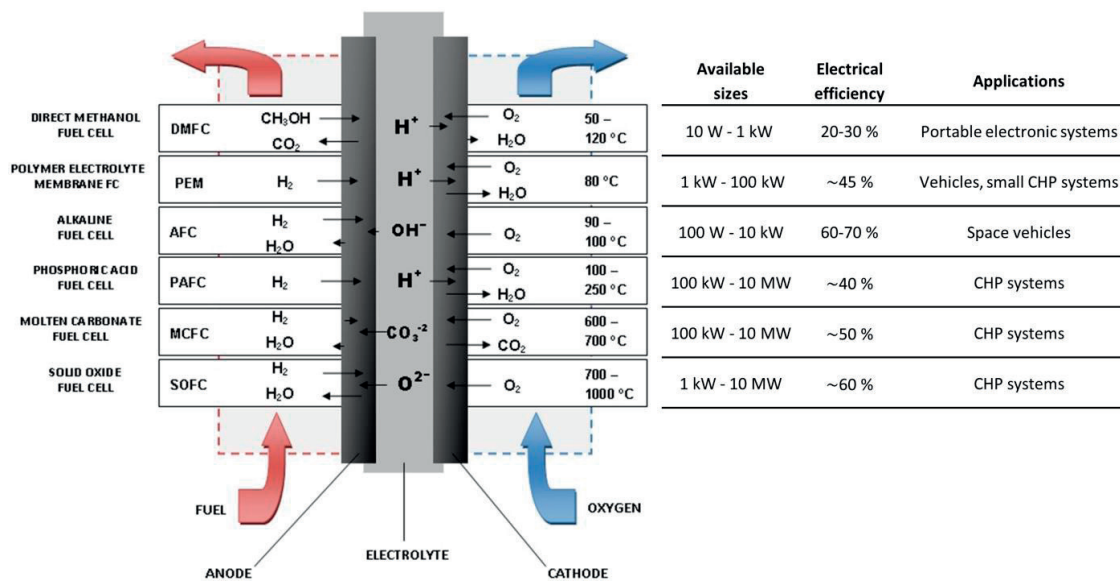


Figure 1: Comparison of the most common types of fuel cells [4].^a

The foreseen transition from small- to mass-market production of SOFC-based systems imposes ever stricter requirements in terms of costs, which encompasses production, performance, durability, availability and maintenance. Production cost reductions can be obtained for instance by increased volume production, manufacturing technology improvement, material selection or stacks scale-up, among others. Performance requirements are ascribed to the capability of the SOFC-based system to convert the chemical energy of the fuel into electricity with maximised efficiency. Mostly because of the degradation of the material effective properties, the nominal performance of SOFC-based systems progressively decreases during long-term operation. The length of time during which the system is expected to operate before the degradation rate of the performance exceeds a defined threshold is a measure of durability. Availability^b is the ratio between the time during which the system is operative and the lifetime. Strict quantitative targets for durability and availability requirements of SOFC-based systems are not explicitly specified yet, since they are market-dependent. As an indication, the operation lifetime targets for fuel cells based combined heat and power (CHP) systems operated on natural gas specified by the United States of America Department of Energy for 2020 are 60'000 and 80'000 h, respectively for small (< 10 kWe) and large (> 100 kWe) systems, and an availability of 99% [5].

^a Reprinted with permission from Novocell Energy Systems SA

^b Measure of the percentage of time during which the system is operative over a specific range of time (typically the predicted lifetime of the system), i.e. independently of the frequency of interruptions (because of failures, predictive maintenance, etc.). Over the same period, a system having highly frequent interruptions but fast maintenance has the same availability of a system with lower frequent interruptions but longer maintenance.

Additional requirements in terms of low degradation during thermal cycling, short start-up time and quick transient response are demanded from small CHP systems.

SOFCs belong to the category of high temperature cells, since they are polarized at temperatures ranging from 600 to 1000 °C. The advantage is that the high enthalpy of the exhausts allows i) the possibility to integrate the SOFC system with a gas turbine for higher system efficiency; ii) the heat recovery for hot water supply, making thus SOFC devices co-generator systems; iii) for internal reforming of the fuel. On the other hand, the relatively high temperature i) is not beneficial for material degradation, ii) complicates the start-up and shutdown procedure of the SOFC stack, limiting SOFC-based systems to stationary rather than mobile applications and iii) increases the risks of stack mechanical failures.

An SOFC system comprises the SOFC stack, the core device, and balance of plant (BoP) components, which includes ancillaries as well as fuel and power management. With the advances of the technology, the mechanical reliability of the technology is gaining increasing relevance. The failures in a single component may affect the performance, availability and durability of the whole system. At the system level, failures in the stack affect in the best case only the performance, in the worst case the system availability and durability. At the stack level, possible mechanical reparations or replacement of damaged components is not feasible, because of the stack elements being joined together and the brittleness of the ceramic parts. This means that the mechanical failure of even a single component in the SOFC stack will likely require its replacement as a whole. Nowadays, the occurrence and severity of mechanical failures in SOFC stacks remain main limitations for the commercialisation of SOFC-based systems, and pose restrictions on the practical operation of such systems. A single mechanical failure may induce a sequence of deleterious effects acting in a coupled manner [6], and several failure modes may contemporaneously appear in an SOFC stack [7]. To the best of our knowledge, the capability to monitor experimentally the structural integrity of the SOFC stack during its fabrication and operation is not demonstrated yet. Therefore, numerical thermo-mechanical investigations are of high interest during the development phase of new designs and validation of existing systems. They help in understanding and predicting the potential failure modes in SOFC stacks.

The knowledge of the mechanical properties of the materials in the stack and their evolution during the lifetime of the system is of crucial importance for stack thermo-mechanical modelling. The wide range of material compositions in SOFC stack, the aggressive conditions to which the materials are exposed and the modification of the material microstructure upon ageing complicates mechanical testing, whereas the knowledge reported to date in the literature is not yet sufficient to characterise distinctively the mechanical behaviour of such materials. Furthermore, due to either simplifications in the post-processing of mechanical testing data or intrinsic capabilities of the setups, the estimated properties are often not fully representative of the behaviour of the real material, or the measurement uncertainty is too high for clearly understanding the degradation.

Models based on finite elements method (FEM) are commonly developed for numerical thermo-mechanical investigations of SOFC stacks, which consider idealised components, i.e. computational domains imported from computer-aided design. In reality, the dimensions and geometry of the produced stack components have statistical variations, because of imperfect manufacturing processes and of the costs associated with component quality. As an example, production data show that the metallic interconnect (MIC) is a component displaying such manufacturing variability. The understanding of the trade-offs between quality and costs, because of tight manufacturing tolerances, which are believed to largely depend on thermo-mechanical aspects, is currently at best qualitative. As an example, a variety of detrimental effects can be anticipated because of variability in the shape of the SRU parts, e.g. flatness and/or thickness. All warrant detailed analyses. The effect on the uniformity of the contact pressure on the active area of the cell is an example among several others. The integrity of the cells, as well as of the sealants that provide gas-tight separation of the fuel and air compartments over the whole stack lifetime, i.e. including polarisation and thermal cycling, are required for reliable SOFC stacks. Because a stack is a multilayer of materials with different thermo-mechanical properties subjected to high temperature, and foremost of brittle components, the effects of history, because of irreversible deformation, must be integrated in the analysis of the failure mode. A minor failure may not instantaneously lead to the end of life of the stack, and classified as non-critical at a first appraisal. They may however trigger a sequence of deleterious mechanical failures.

1.2 Objectives

The objective of this thesis is the understanding and prediction of thermo-mechanical failures in SOFC stacks. The most relevant analyses are for stack designs for commercial use, to directly identify the potential for improvements in design, manufacturing and operation from a thermo-mechanical perspective. The first part of this thesis presents the development dedicated to the measurement of the mechanical properties of SOFC materials, which consisted in the achievements listed hereafter:

- 1) Two setup-ups were designed and fabricated for the mechanical testing of SOFC ceramics at room and high temperatures in controlled atmospheres. A main requirement is the high throughput of measurements, to reduce the testing time needed for characterization.
- 2) A parameters estimation workflow was developed for improving the accuracy and flexibility in terms of constitutive laws compared to standard methods. The workflow uses the experimental data measured by the two set-ups. The elastic properties of NiO/Ni-YSZ were estimated first, followed by the creep properties of Ni-YSZ both in the primary and secondary regime.
- 3) The strength of the NiO/Ni-YSZ cermet material was measured by the Weibull statistics approach.
- 4) Computational homogenisation methods were implemented to overcome the limitations in terms of sample size imposed by mechanical testing to measure the elastic properties of NiO/Ni-YSZ anodes as well as the anisotropic elastic and creep properties of the GDLs.

The mechanical properties are then used in the investigations of the second part of this thesis, which consisted in developing a SOFC stack thermo-mechanical model. The topics on which the focus was placed are listed hereafter:

- 5) The effects on the stack reliability of design variations, stacking conditions, type of mechanical interface and mechanical properties were investigated.
- 6) The possibility for including in the analysis the component geometrical imperfections because of the manufacturing tolerances was implemented in the model, to identify the main effects on the thermo-mechanical behaviour of the stack.
- 7) The analysis of the results was focused on understanding the mechanical failures in the stack in terms of loss of contact pressure on the active area of the cell, failure of the cell and that of the sealants.

1.3 Thesis outline

This thesis comprises a first part, dealing with the estimation of the mechanical properties of SOFC materials, and a second part where a SOFC stack thermo-mechanical model is developed and simulated to predict the mechanical failures for selected scenarios.

Part I - Mechanical properties of SOFC materials

- In Chapter 2.1, the development of the two setups for mechanical testing of SOFC materials is described, from the choice of the samples dimensions and type of testing, up to the setup fabrication and validation. The aim is the accurate measurement of the mechanical properties of foremost the NiO/Ni-YSZ anode support under different testing conditions.
- In Chapter 2.2, a model-based parameter estimation workflow is developed to overcome the limitations of standard post-processing of the experimental data based on analytical solutions for the measurement of the mechanical properties. It post-processes experimental data obtained from the two developed setups. The elastic properties of NiO/Ni-YSZ and then the creep properties of Ni-YSZ in the primary and secondary regime were investigated.
- In Chapter 2.3, strength tests were performed on NiO/Ni-YSZ samples with one of the two setups fabricated and reported in Chapter 2.1. In addition, the tests are performed on samples made by the residual YSZ skeleton (after removal of Ni). The Weibull statistics parameters are determined from the experimental strength dataset and used for the cell failure analysis in Chapter 3.4.2.
- In Chapter 2.4, computational homogenisation methods were applied to estimate the elastic properties and the coefficient of thermal expansion of the Ni-YSZ anode material, in order to compare the results with those of the parameters estimation and analysed aged samples. The effective anisotropic elastic properties of the GDLs used in the stack design of Part II were further estimated using the same methodology. An extension from the literature was then implemented and applied to compute the effective anisotropic creep properties.

Part II - Thermo-mechanical modelling of the SOFC stack

- In Chapter 3.1, the implementation in a thermo-mechanical FEM model of the stack design currently produced by SOLIDpower S.p.A. (Mezzolombardo - TN, Italy) is presented and the modelling assumptions discussed. A numerical framework to implement components with geometrical imperfections in the stack model simulations is here developed for the first time. The analysed component pre-deformation is in this work that of the interconnect. The simulation sequence comprises a preliminary initialisation, where the steps of the stack assembly are simulated, and a combination of stack polarisation and thermal cycling. The temperature field under polarisation is simulated by a thermo-electrochemical, described in

this chapter. The stresses computed from the series of simulations are then used to assess the reliability of the stack, as discussed in Chapter 3.3 and Chapter 3.4.

- In Chapter 3.3, an overview of the results from the thermo-mechanical simulation is presented. They are referred to a base case. The aim of this chapter is to provide first insight on the causes of the stack mechanical failures predicted by numerical simulations and prepare the discussions in Chapter 3.4.
- In Chapter 3.4, the effects on the stack reliability of i) modelling assumptions, ii) pre-deformed MICs and iii) operation conditions with respect to the base case analysed in Chapter 3.3 are investigated. The contributions of each of these factors on the predicted stack mechanical failures are investigated in terms of a) evolution of the contact pressure at the cell interfaces, b) cell failure and c) sealing failure.

The thesis ends with the conclusion including recommendations for future work.

1.4 Fundamentals of SOFC technology

1.4.1 Operation of an SOFC

Solid oxide fuel cell (SOFC) based systems are co-generators that generate electricity and heat, with low pollutant emissions, high efficiency and fuel flexibility. The core component is the SOFC, which comprises two porous electrodes, the anode (negative electrode) and the cathode (positive electrode), separated by a dense electrolyte. A schematic view is provided in Figure 2.

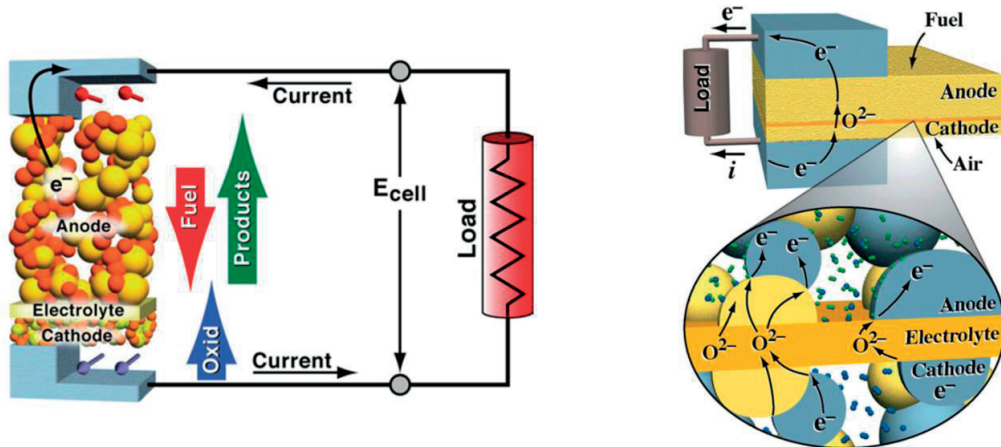


Figure 2: On the left-hand side, representation of the operating principle of an SOFC. On the right-hand side, the electrochemical and transport processes in the electrodes and electrolyte are illustrated [8]^f.

The operation principle of SOFCs requires oxygen reduction on the cathode side and concomitant oxidation of fuel on the anode. The half reaction is the electrochemical reduction of oxygen, taking place close to the interface between the cathode (i.e. cathode (c) - gas (g) - electrolyte (e)), is [8]:



Because electrons, ions and gas species are involved, the reaction occurs at triple-phase boundary (TPB) points. The oxygen ions are transported through the electrolyte to the TPBs on the anode side (i.e. anode (a) - gas (g) - electrolyte (e)), where oxidation of the fuel occurs:



Combination of the two half reactions yields the global exothermic reaction



Since the electrolyte has a negligible electronic conduction, the electric circuit is closed by a load between the cathode and the anode. In this configuration, the voltage of a single cell is however too

^c Reprinted from Proceedings of the Combustion Institute, 30, Robert J. Kee, Huayang Zhu, David G. Goodwin, Solid-oxide fuel cells with hydrocarbon fuels, 2379-2404, 2005, with permission from Elsevier.

low for practical applications, typically less than 1 V at nominal power density [8]. Therefore, cells are assembled in series to form a stack. The cells are maintained separated from each other by an interconnect, which provides electrical contact on one side with the anode of a cell, and on the other side with the cathode of another cell. Since the interconnect provides electron conduction, transport of electrons from the anode to the cathode of two distinct cells occurs and the voltage of the stack can be adjusted by the number of elements.

The potential difference across the electrolyte of a reversible fuel cell is expressed by the Nernst equation [9]:

$$U_{rev} = -\frac{\Delta H^0}{2F} - \frac{RT}{2F} \ln \left[\frac{p_{H_2O,a}}{p_{H_2,a} \cdot p_{O_2,c}^{1/2}} \right] \quad (4)$$

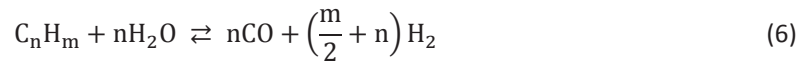
For practical applications, which require the polarisation of the cell, the potential is lower because of irreversibility. The main losses in lowering the thermodynamic voltage are i) ohmic losses, because of resistance to both electron (electrodes) and ion transport (electrolyte and composite electrodes), ii) charge transfer at material interfaces, referred to as activation losses, which correspond to the overpotential required for driving the electrochemical reactions at the electrodes and iii) concentration and diffusion losses, caused by the depletion of reactants along the flow path and gas-phase transport of the species through the heterogeneous electrodes up to the TPBs. These voltage drops are respectively denoted by ΔU_{ohm} , ΔU_{act} and by ΔU_{conc} and lower the cell potential in operation:

$$U = U_{rev} - \Delta U_{ohm} - \Delta U_{act} - \Delta U_{conc} \quad (5)$$

Voltage losses and the global exothermic reaction of the SOFC generate heat. The temperature in operation is high to ensure sufficient ion conductivity and electrocatalytic activity.

1.4.1.1 Fuel for SOFC operation

The high operating temperatures along with the good tolerance of Ni-YSZ anodes to carbon monoxide allow feeding SOFCs with hydrocarbon fuels, instead of pure hydrogen. The established operation strategy is based on the steam reforming reaction, which, combined with the water-gas shift reaction, converts a hydrocarbon fuel to hydrogen. The steam reforming reaction of hydrocarbons can be expressed in the following generic form [10]:



This reaction is endothermic. Natural gas or biogas is of interest for SOFC operation. If the hydrocarbon is methane, reaction (6) becomes:



In this case, the enthalpy of the reaction is 206 kJ/mol. At temperatures above approximately 500 °C, the equilibrium of the reaction is significantly shifted towards the products. In this case, the heat generated by the polarisation of the SOFCs is therefore advantageous and internal reforming can be

beneficial for stack thermal management. The steam not consumed by reaction (7) can further convert the carbon monoxide into hydrogen through the water-gas shift reaction:



This reaction is exothermic, with a variation of enthalpy of -41 kJ/mol. Steam-hydrocarbon reforming can be achieved either directly in the anode compartment (internal reforming) or externally (external reforming). Internal steam-hydrocarbon reforming is possible because of both the sufficient catalytic properties of Ni (i.e. of the Ni-YSZ anode) at SOFC operation temperature and the heat and steam generated by the electrochemical oxidation reactions. A smaller, or ideally the absence of an external reformer device provides several advantages [11], which are: i) faster start-up and dynamics during load following, ii) reduced system costs and iii) especially in the case of counter-flow configuration, higher system efficiency [12]. Internal steam-hydrocarbon reforming however requires mitigating the i) risks of carbon deposition at the TPBs of the anode, ii) potential acceleration of coarsening of the Ni phase in the electrodes, because of the higher steam partial pressure, and iii) higher local thermal gradients in the cell, because the endothermic steam-hydrocarbon reforming reaction is relatively fast under SOFC conditions and typically cools down the fuel inlet region [13]. Performances in the long-term and mechanical reliability of the stack may therefore be affected. In practice, systems are typically still designed with an external reformer and the fraction of pre-reformed fuel (PR, between 0 and 1) is controlled for the thermal management of the stack.

1.4.2 Stack and cell designs

Research in the SOFC field has resulted over time to a number of design solutions, each of them characterised by advantages and disadvantages in terms of electrochemical performance, mechanical reliability and costs.

At the cell level, a first distinction is made between planar and tubular SOFCs. The multilayer structure, i.e. comprising electrodes and electrolyte, is shared by all designs to maintain the functionality of the device. Planar SOFCs are typically flat rectangular plates or disks, whereas a tubular SOFC is a tube-like assembly with the layers arranged concentrically to each other. The description of the existing design alternatives is hereafter dedicated to planar SOFCs, which is the focus of the present thesis.

The reduction of the thickness of the electrodes and electrolyte layers is a way to increase the electrochemical performance and lower costs. However, thickness reduction can affect the mechanical robustness of SOFCs, i.e. if all the layers are made very thin, manufacturing with adequate tolerances and production yield as well as handling of the cell for assembly can become practically very difficult. For these reasons, a thick layer is maintained as a physical support of the multilayer assembly, which then allows focusing on reducing the thickness of the remaining layers. As a result, a main distinction between planar SOFCs is the type of supporting layer, i.e. commonly anode-, electrolyte-, cathode- or metal- supported SOFCs. Electrolyte and anode-supported cells are the most mature versions in terms

of research and development, and thus most widely adopted in stack production. The anode-supported cell typically provides higher power density because the thinner electrolyte (5 to 20 μm) results in lower ohmic loss, which further allows reducing the operation temperatures (about 750 $^{\circ}\text{C}$ or lower). The thickness of the anode support ranges between 250 and 1000 μm . There are however drawbacks. An increase of the thickness of the anode does not enhance properties relevant for electrochemical performance. The porosity of the support must be adjusted to limit diffusion overpotentials, while ensuring mechanical integrity. In the case a same layer provides the supporting and electrochemically activity functions, the TPB density must be sufficient. Reduction of the stack performance due to low in-plane effective conductivity is usually larger on the cathode side, because of the lower effective electronic conductivity of the materials.

The electrolyte-supported configuration was dominant in the first generation of SOFCs is still used today, despite a shift towards anode- and metal-supported cells. The dense and thick electrolyte (typically around 150 μm) provides to the cell a high mechanical robustness and good tolerance to anode re-oxidation. The shortcoming is the need for higher operation temperatures of the cell (i.e. 850-900 $^{\circ}\text{C}$), for sufficient ionic conductance and thus adequate performance. Therefore, the choice of stack materials and also the range of operation conditions become limited to guarantee low degradation. The need for expensive alloys for the MICs is one of the most stringent consequences.

Cathode-supported SOFCs were developed as well and, similarly to the anode-supported ones, they enable the use of thin electrolytes to achieve high electrochemical performances. In practice, large-scale production proved challenging, mainly because the optimal sintering temperatures of cathode materials is low compared to that needed to easily fabricate sufficiently dense electrolytes.

Metal-supported SOFCs are relatively recent and still under development. Here, a porous layer with a foam structure (between 400 and 1000 μm) made of ferritic alloy provides the structural support to the cell, whereas the anode, electrolyte and cathode are deposited on one side. Both electrodes and electrolyte can thus be very thin. Hence, this type of SOFCs permits i) higher electrochemical performance, because of the shorter electrons/ions current paths, ii) cost reduction, because a lower amount of expensive, electroactive ceramic raw materials is needed and the reduced operating temperature (550-650 $^{\circ}\text{C}$) enables the use of less expensive alloys for stack and BoP components, and iii) theoretically less critical and sudden mechanical failures, because of the plasticity of the support. However, the corrosion and interfacial reactions of the metal support upon manufacturing and operation as well as the mismatch of the thermo-elastic properties between ceramics and metals are remaining challenges in the development of reliable metal-supported SOFCs.

A distinction between high and intermediate temperature SOFCs is commonly made among anode-supported SOFCs. In the high temperature version, the cathode usually comprises LSM, and can be directly interfaced with the electrolyte. Such cells operate at temperatures of about 800 $^{\circ}\text{C}$. Conversely, in intermediate temperature SOFCs, operated at lower temperatures (i.e. about 700 $^{\circ}\text{C}$), the cathode is

based on mixed ionic and electronic conducting materials such as LSCF, which requires a thin compatibility layer between electrolyte and cathode to limit the formation of secondary electrically insulating phases.

In SOFC stacks, fuel and air can be fed following a co-, counter- or cross-flow configuration. Complex combined flow patterns, such as Z-flow, serpentine, radial, among others, are reported [13]. Each flow configuration results in different spatial distribution of temperature, gas composition and therefore overpotential and current in the stack. Stack designs are also characterised by the position of the gas manifolds for the incoming and exhaust air and fuel streams. Internal manifolds cross both the MICs and the cells, integrated manifolds cross the MIC but do not penetrate the cells, whereas in the external manifolds version, the gas manifolds run externally from the stack, along its height. These three gas manifolds arrangements affect the flow field, the sealing compartment and the thermal management of the stack.

1.4.3 Materials

Stack component materials are metal and ceramic based. Materials were first tailored for electrolyte-supported SOFCs operating at relatively high temperatures. Chemical, crystallographic and morphological adaptations or complete change of the material type were performed over the years before the transition to the relatively recent intermediate-temperature anode-supported SOFCs. Research continues to obtain improved properties. Manufacturing methods need adaptations for the scale-up of the production for mass-market implementation. In this context, the cost of the raw materials, i.e. ceramic powders and alloys, can contribute massively, depending on the cell and stack design. Therefore, at the current technology readiness level, the identification of the trade-off between cost and electrochemical and mechanical properties is of interest, since the performance, durability and thermo-mechanical reliability of SOFC stacks are highly affected by the proper choice of materials. The following list is focused on the materials for anode-supported SOFC stacks that is the focus of this thesis and is therefore not exhaustive.

1.4.3.1 Anodes

The most common SOFC anode material is the ceramic and metal (cermet) Ni-YSZ, which has a heterogeneous structure. The porosity enables gas-phase transport to the electroactive sites, whereas the metallic and the ceramic phases must provide adequate effective electronic and ionic conductivity, respectively. Furthermore, electronic conduction from the interconnect to the TPBs can occur only if the metallic phase is percolated. The boundaries where the ceramic, metallic and pore phases co-exist represent the site of the fuel oxidation, and is referred to as triple phase boundary (TPB). The targets for microstructural design aimed at improved electrochemical performances comprise the maximisation of the TPB density, and of the effective ionic conductivity, close to the electrochemically active region [14]. Nickel is typically used as metallic phase for SOFC anodes since it is an excellent H₂

electro-catalyst and possesses high electrical conductivity [3], whereas 3YSZ or 8YSZ is used as ceramic phase. 3YSZ provides higher mechanical strength to the cermet, whereas improved ionic conductivity is achieved with 8YSZ [15]. In anode-supported SOFCs, the anode is often composed by a thick substrate and a thin functional layer. The substrate provides the mechanical support, and has a higher porosity to facilitate gas-phase transport, whereas the functional layer, deposited between the anode support and the electrolyte, is characterised by a microstructure optimised for high TPB density. Adequate mechanical strength together with maximised TPB density requires sintering of the cermet at a certain temperature, which is around 1300-1400 °C.

1.4.3.2 Electrolytes

The functions of the electrolyte are the solid-state transport of oxygen ions and separation of the fuel and air compartments. Hence, to maximise the electrochemical performances of the cell, the electrolyte must have high ionic as well as low electric conductivity. The highest ionic conductivity is achieved by stabilisation of the ZrO_2 with 8% mol Y_2O_3 . This composition is extensively used for SOFC electrolytes. The electrolyte must be gas-tight, to avoid reactant cross-over [14] and potential parasitic combustions. High density is achieved by sintering at relatively elevated temperatures. For 8YSZ electrolytes, sintering is usually performed at 1400 °C. Co-firing with the anode is therefore possible.

1.4.3.3 Cathodes

The cathode must achieve similar functions as the anode, i.e. possess adequate effective electronic and ionic conductivities, and electrocatalytic properties for the oxygen reduction reaction. Materials based on lanthanum manganite often remain the preferred choice for high temperature SOFCs. However, reaction with the YSZ electrolyte occurs during fabrication or potentially under high overvoltage conditions leading to the formation of $La_2Zr_2O_7$ at the interface. This secondary phase has low conductivity, which degrades the performance. Doping with strontium, i.e. LSM, mitigates the formation of these insulating phases, allowing improved cathode performance. At high temperatures, i.e. 900 °C or higher, LSM cathodes are characterised by a good electric conductivity, whereas the ionic conductivity can be sufficient. The ionic conductivity of LSM is however too low for operation at lower temperatures, i.e. 700-800°C. For this reason, LSM-8YSZ composites were first developed for intermediate-temperature SOFC and are being further replaced with lanthanum strontium cobaltite ferrite (LSCF) single solid phase or composites.

The stability of LSCF is lower. At the interface with the electrolyte, LSCF reacts with the YSZ at temperatures lower than that of the cell sintering. This reaction results in either strontium or lanthanum zirconate formation at the interface. Both are insulating phases and thus strongly degrade the SOFC performances [16]. Therefore, a compatibility layer as thin as possible is commonly deposited between the electrolyte and the LSCF cathode. Typical materials for such compatibility layers are GDC and YDC.

TPB length of SOFC cathodes is highly influenced by the temperature at which the material is sintered. Co-firing with the electrolyte would lead to excessive densification, resulting in low TPB density, hence decreased electrochemical performance. For this reason, the deposition of the cathode layers is often made separately by screen printing and at sintering temperatures around 1050-1100 °C. The emphasis is therefore not on mechanical strength. In the case of anode-supported-cell and LSCF oxygen electrode, the most likely failure is channel cracking of the cathode, which has a lower detrimental effect.

1.4.3.4 Contact layers

When the parts of the SOFC stack are in contact, the statistical variability in shape and dimensions caused by the manufacturing tolerances affects the uniformity of the contact pressure at the interface. In turn, the contact pressure uniformity may affect the electrical resistance of the interface [17]. Therefore, contact pastes are deposited during the assembly onto the interface between the cell and GDLs, either as a continuous layer or as discrete contact pads. They help providing a continuous electrical path between the cell and GDLs and can also contribute to an improvement of the in-plane conductivity near the interface [18].

Contact paste materials must fulfil a number of requirements: they must be chemically compatible with the neighbour materials, provide high electronic conductivity and good adhesion to both metallic and ceramic stack components. To maintain these properties over the long term and during thermal cycling, their coefficient of thermal expansion should therefore be close to those of the joined materials and their sinterability should be sufficient at relatively low temperatures (800-900 °C). Once sintered, the porosity of the contact layer can be a paramount parameter depending upon the interconnection design, since it can affect the resistance to gas-phase transport from/to the cell electrodes, the apparent strength of the contact material and its electrical resistance. Sintering of the contact pastes occurs when the stack is heated up for the first time. The temperature of this process step must not be too high, typically below 900 °C to avoid excessive oxidation of the metallic interconnect and to not alter the properties of the sealant material. All these requirements are challenging to meet all together. Therefore, an external compression load is applied on the stack to help the adequate formation of the interface and improve the electric conduction across the contact interfaces [18].

Contact issues differ whether the anode/GDL-fuel or the cathode/GDL-air interface is considered: the cathode has a lower electric conductivity and thickness than the anode, therefore the effects of current constrictions at the scale of the interconnection system are more severe on the cathode/GDL-air interface [19]. In addition, gold or platinum are discarded for stack applications for cost reasons. Common materials are therefore ceramic-based. Obtaining an adequate mechanical strength of this interface and capability to accommodate component geometrical imperfections and the relatively low strength of the cathode is complicated [20].

A wide range of candidates for contact pastes for the cathode/GDL-air interface were tested [18,21,22]. The choice of the most suitable contact paste composition is often a trade-off between mechanical integrity of the interface, contact electrical resistance and chemical compatibility of the materials [23]. As an example, Tucker et al. [18] report that the most promising cathode contact paste materials are LSCF, LSCuF, SSC and LSC. Alternative materials are LNF, LNC and LSFMC. The first two possess high electric conductivity, whereas the last one is preferred from a mechanical integrity perspective [23]. At the anode/GDL-fuel interface, noble metals like gold, platinum and to a lesser extent silver can be used as contact layer materials [20]. However, they present a cost disadvantage and are thus adopted as contact layer materials only for laboratory testing. Alternatively, good stack performances are reported using NiO-based pastes [22].

1.4.3.5 Gas distribution layers

Gas distribution layers (GDLs) ensure the supply of the reactants (i.e. fuel and air) and the removal of the exhaust gases over the cell active area, as well as electrical conduction. The GDL design comes usually from a trade-off between fluid dynamics considerations, proper mechanical stability at high temperatures, enhancement of the current path and minimisation of the material/manufacturing costs. The GDL on the air side is either made by milling the gas channels on the metallic interconnect [24–29] or by inserting corrugated metallic sheets between cell and interconnect [30,31]. On the fuel side, the use of nickel meshes is often reported [27,28]. The gas channel section of the GDL is typically larger on the air-side than on the fuel side, because of the relative higher air flow needed for stack thermal management during polarisation and the need to minimise the pressure drop across the stack to lower the power consumed by the air blower.

1.4.3.6 Interconnects

The requirements for a SOFC interconnect material are i) high electrical conductivity, ii) low chemical reactivity with the other stack components, iii) gas tightness, to maintain the air and fuel compartments separated and iv) in most cases an ability for forming into shapes with some level of complexity. In the first generations of SOFCs, ceramics were often used to fabricate the interconnects. For this purpose, the most common ceramics were doped lanthanum and yttrium chromites. One of the reasons for the development over the last decades of the intermediate-temperature SOFCs was the use of metallic interconnects. Metallic interconnects have lower thermal inertia compared to ceramic ones, but higher thermal conductivity, which guarantees faster stack start-ups. Alloys with low growth rate of the oxide scale and reduced costs are preferred. Furthermore, if the MIC is obtained by extensive metalworking and/or milling (e.g. to make the GDL), a good workability of the alloy is needed. Ferritic steels fulfil these requirements, and thus are largely used to fabricate the MICs of intermediate-temperature SOFC stacks. Especially at the interface with the cathode, coatings of manganese cobalt spinel are deposited onto the MIC, to minimise both the chromium evaporation and the electrical contact resistance.

1.4.3.7 Sealants

The main requirement for SOFC sealants is, in the same way as the electrolyte, the gas-tight separation of the fuel and air compartments. Besides, for the sealants joining adjacent interconnects, electrical insulation must be guaranteed. Two main categories of SOFC sealing solutions exist, compressive gaskets and rigid sealants. A compressive gasket consists in a foil with through the thickness compliance, which is shaped and inserted between the surfaces to be sealed, for example between the edge of the cell and the interconnect. The foils of all SRUs in the stack are maintained compressed by applying a relatively high assembly load on the stack end plate. Materials typically used for such gaskets are made by compacted sheet of silicates. Since the gaskets are not rigidly bonded to the interfaced parts, a relative sliding is allowed, especially during thermal cycling, which mitigates potential deleterious stresses in the cell. The drawback is that fully gas tight assembly is never achieved using compressive gasket sealants. The main reason is the porous nature of the gasket material and the limitations in terms of mechanical load that can be applied, because in a stack the interfaces to seal are multiple (in-series for identical regions, but also different in terms of materials and geometry, depending on the region). In operation, the risk of relaxation of the contact pressure by creep of the mechanical loading system must be overcome. These shortcomings promote the degradation rate of the stack performance. Besides, the need of a mechanical system to maintain the assembly load on the stack adds undesirable complexities and weight.

The class of rigid sealants includes numerous solutions: glass-ceramic sealants, hybrid sealants, bonded compliant sealants (BCS) and metal brazes. With rigidly bonded sealants, the systems to maintain the assembly load on the stack are simpler, cheaper and lighter than those required to compressive gaskets. Furthermore, the low porosity of the materials used for rigid sealants drastically reduces the gas leakages between air and fuel compartments. However, due to the rigid bonding, the thermal expansions mismatch between the sealant and the components must be minimised to reduce the stresses, especially during thermal cycling of the stack.

In the case of glass-ceramic sealants, the material is deposited between the interfaces to be bonded in the form of a paste during the assembly of the stack. After the first heat-up, the stack is exposed to high temperature for a determined period, to initiate and control the crystallisation. Concomitantly, its stiffness increases. The viscosity of the glass-ceramic paste at high temperature is a central parameter, among many others, because upon the first stack heat-up the paste must wet properly the interfaced components without overflowing, to maintain the design shape of the sealant. As material, barium-alumino-silicate glass-ceramics are commonly used [32]. Rheological, mechanical and adhesion properties of the glass-ceramic materials can be tailored to the specific needs to some extent by adjustment of the composition.

Hybrid sealants are composed of a shaped foil of sheet silicates (like in the compressive gasket solution) and a thin layer of glass on both faces. During the first stack heat-up, i.e. upon stack manufacturing, the

glass infiltrates the sheet silicate foil and wets the cell or the interconnect at the interface region. As a result, excessive viscous flows of the glass are prevented and the leak rate through the sheet silicate foil is reduced, mostly by decreasing interface leaks. Upon glass crystallisation, the sealant becomes stiffer, and the interface with cell and interconnect rigidly bonded. Improved mechanical reliability of hybrid sealants upon thermal cycling is reported [33].

The bonded compliant sealant (BCS) solution was proposed as a trade-off between glass-ceramic seals and compressive gaskets [35,37]. A BCS is made by a S-shaped thin metallic strip bonded on the two lateral sides respectively to the cell and to the metallic frame, whereas the central band is left free to deform, accommodating thus the thermal expansion mismatches between cell and metallic support as well as the bending of the cell. Filler metals joints are used for the bonding of the strip with the cell and the interconnect.

Metal brazing is an attractive sealant solution because the melted pool of metal enables proper adhesion with the joined components, the cell and the interconnect. In contrast to glass-ceramic sealants, risk of mechanical failures in the bulk of the metal braze sealants are low, because they can withstand plastic deformations and thus accommodate thermal and mechanical strains. However, a limited range of alloys are compatible, typically expensive noble metals, and the electrical conductivity of such sealants restricts their applicability.

1.5 Thermo-mechanical modelling of SOFCs: State-of-the-art

SOFC stack numerical thermo-mechanical simulations require as inputs the i) modelled geometries, ii) meshing of the computational domain, iii) constitutive laws describing the mechanical behaviour of the materials, iv) mechanical boundary conditions, i.e. modelling of the external constraints acting on the computational domain, v) mechanical interactions between the components, in the case of multi-parts models and vi) the conditions (e.g. temperature fields) to be simulated. The sensitivity of the computed stress fields to these inputs is known to be significant in most cases, even though typically not quantified by in-depth sensitivity analysis. Therefore the accurate knowledge of material and interface properties is needed for reliable insights on the failure modes of the modelled system. As an example, thermomechanical issues between tubular and planar SOFCs designs are different, although they share the same or similar materials. In planar SOFCs, a further distinction of the failure modes should be made between the cell support type (i.e. anode, electrolyte, metallic or cathode support), because both the dimensions of the cell (i.e. the layers thickness) and the operation characteristics of the stack (temperature range, flow configuration, etc.) change for the different cell types. For these reasons, the emphasis in this literature survey is placed on planar, anode-supported SOFCs.

Research and developments at different research institutions have resulted in a fairly broad number of cells and stacks designs. Hence, considering the single variability in modelled geometries, different outcomes of the thermomechanical investigations may be expected. Considering the variability of all model input parameters, the formulation of fully generalised guidelines in terms of designs, manufacturing and operation of SOFC stacks is challenging. From a practical standpoint, thermo-mechanical modelling and simulations are needed, because of the difficulty to probe mechanical failures in operation, among others. This literature survey aims at providing and discussing general solutions to develop such thermomechanical models of SOFC stacks.

1.5.1.1 Domains of investigation

The size of the computational domain of SOFCs thermo-mechanical investigations reported in the literature spans from single GDL channels up to short stacks. The choice of the domain depends upon the available computation resources and the objective of the study. Because of the relatively simple geometry, a domain corresponding to a volume element comprising a single gas channel, a rib of the GDL milled in the MIC as well as the adjacent regions of cell and MIC is often considered for SOFC stack analysis to yield low computation requirements [35–38]. This approach assumes the geometrical periodicity along the direction perpendicular to the gas flow and that the channel is representative. A first limitation is that most of the effects of thermal gradients in the y direction are not captured. A second limitation is that generally the contour of the cell bonded to the sealant as well as in most cases all manifold sealants are neglected, despite their potential critical contribution to mechanical failures.

Several studies consider only the cell as domain for the thermo-mechanical investigations. Within the anode-supported cell, the anode and the electrolyte are the layers where the consequences of mechanical failures are expected to be the most detrimental. Given the relatively regular geometry of the cell, in several studies [39–42] the stresses in the layers are estimated analytically using the Euler-Bernoulli beam theory for multilayer structures [43,44]. The runtime and computational resources are much lower for analytical solutions than numerical calculations. Thus, they can be efficiently used for preliminary studies and sensitivity analyses of the thermo-elastic properties and thickness on the stresses in the cell [39–41]. The Euler-Bernoulli beam theory can also include the effect of rigid glass-ceramic sealants on the stress in the cell [40].

Two studies [45,46] model and simulate the stress in cell-BCS-metallic frame assemblies over thermal cycles with homogenous temperature fields. They show that compared to the case with rigidly bonded glass-ceramic seals and similar geometry, the stresses computed in both the BCS configuration and in the cell are computed. The results therefore suggest that the BCS solution can help improving the reliability of SOFC stacks. Implementation in the simulations of both non-uniform temperature fields [47] and residual stresses in the BCS (generated by the brazing process) [48,49] shows the critical influence on the mechanical integrity of the sealant. Damage of the BCS (i.e. crack growth) caused by tertiary creep is investigated numerically upon long-term operation and thermal cycling [50]. The simulation results show that upon long-term operation the risk of cracking of the BCS starts after the targeted stack lifetime (40000 h), whereas thermal cycles may lead to crack growth. In the same study, a sensitivity analysis on the component dimensions indicate that thinner strip and filler metal joints contribute to reduce the risk of damage. The simulated stresses are confirmed by neutron diffraction measurements [51].

The studies by Yakabe et al. [52] and by Selimovic et al. [53] focused on SOFC stacks including ceramic interconnects. In the first work, the computational domain is the interconnect alone. The stresses simulated during stack operation are shown to be sensitive to the composition of the ceramic material. Further, chemical expansion (because of the uneven oxygen vacancy concentration in operation) significantly contributes to the stress build-up. In the second work, the effects of selecting a ceramic or metallic interconnect are investigated. Because of the higher thermal conductivity of the metallic interconnect, the thermal stresses in the SRU are decreased, allowing thus more flexibility in terms of system operation and design. These advantages, together with the lower cost and better manufacturability of alloys compared to ceramics, significantly favoured the development of SOFC stacks based on metallic rather than ceramic interconnects.

The nominal power of an SOFC stack is proportional to the number of in-series single repeating units (SRUs). An SRU is the elementary unit of a stack. The idealised geometry of the components and the materials are consequently identical for all the SRUs in a stack. Therefore, an intuitive approach to reduce the model run-time is to consider as computational domain one SRU instead of the whole stack.

In this type of modelling approach, the domain comprises all the components of the SRU and to some extent also their mechanical interactions, sometimes modelled by e.g. contact. Hence, the focus is on investigating not only the individual mechanical failures at the component level but also their reciprocal influences. A limited number of studies are carried out at the level of SRU domain. Several contributions come from the GEM-EPFL group [19,54–56], that analyse the rigid glass-ceramic and compressive gaskets sealant solutions, this work, and [57–59]. Compared to the cases of single components and representative channels, the computational requirements for numerical simulation of the whole SRU domains is considerably higher, because i) of the higher number of elements and ii) modelling of mechanical interactions between the SRU components require additional iterative solution procedures. The main limitation of modelling a single SRU domain is that the temperature field during polarisation is assumed the same over the stack height. In reality, the SRUs adjacent to the end plates of the stack are colder than those in the centre.

1.5.1.2 Meshing approaches

The details of the meshing procedure are reported for part of the studies published in the literature. A first distinction is the shape of the mesh elements: given the relatively regular geometry of the SOFC stack components, meshing by hexahedral (in 3-D models) or quadrilaterals (in 2-D models) is preferred, because of the better numerical accuracy at lower computational cost [60]. Tetrahedral/triangular mesh elements are dedicated to more complex SRU geometries [57] and for stress analysis at components singularities [61–64]. A second main distinction concerns the order of the shape functions, i.e. either first or second order for standard mesh elements. Second order elements provide better accuracy in the case of non-negligible bending [60] with the drawback of higher computational cost, due to the higher number of integration points and thus of degrees of freedom per element. For this reason, in relatively simple models, i.e. where the cell with or without the sealants is implemented as computation domain, second order elements are usually preferred [42,65]. On local models of the SOFC active area, i.e. using as computation domain the representative channel, the bending of the portion of modelled cell is negligible. In this case, the accuracy provided by first order elements can be considered sufficient [35,36]. For models at the stack level, simulation of mechanical contact between the components places requirements on the meshing of the SRU assembly. A mechanical contact interface is modelled by assigning a “master” and a “slave” property to each of the two surfaces involved in the interfacing. The master surface is modelled by an analytical function interpolating the mesh nodes of the surface. Proper contact simulation implies that the nodes belonging to the slave surface no dot penetrate the master surface. This requires careful meshing, i.e. the mesh on the slave should be finer than on the master surface, which can result in the relatively rapid growth of the required number of mesh elements in the whole model and thus increased computational needs and model runtime. Furthermore, by discretization by second order elements of one or both of the parts in contact (e.g. the cell, because foreseen to bend), the computational demand

increases further, because of the higher number of integration points and thus of equations solved by the contact algorithm. Besides the requirements for simulating mechanical contact, an important bottleneck in structural analysis of SOFC stacks is the high ratio between the in-plane dimensions and thickness of several domains (i.e. the cell, GDLs and MIC), which typically leads to either excessively fine meshes or with elements of high aspect ratio. Attention to this limitation is becoming more relevant with the recent interest in producing stacks with larger active area and thinner cells, respectively to increase the electrical power and reduce the operating temperatures of the SOFC systems. Mesh elements with high aspect ratio are undesirable, since they lead to poorly conditioned matrices and therefore affect both speed of the numerical solver and accuracy of the solution [66]. An alternative is therefore to use shell elements for components with thickness considerably smaller than the in-plane dimensions (i.e. in the SOFC stack, the electrolyte, compatibility layer and cathode). Conventional shell elements discretise a domain by defining the geometry at a reference surface. Hence, in the meshing of the electrolyte, compatibility layer and cathode domains by conventional shell elements, the reference surface is the top/bottom face of the anode.

The cells, which can bend because of the mismatch between the thermal expansion coefficients of the materials of the layers, are meshed by second order elements. The anode, being the thickest layer of the cell, is meshed by solid continuum elements, whereas conventional shell elements are used for meshing the electrolyte, compatibility layer and cathode. For the meshing of the MIC and glass-ceramic sealants, first order continuum elements can be sufficient for most cases. Further reduction of the computational requirements can be achieved by meshing the GDLs by special-purpose elements, i.e. like the so-called “gasket” elements. In gasket elements, the in-plane and through the thickness mechanical behaviour of the element are uncoupled. Gasket elements simulating only the thickness behaviour are also commonly available. Compared to regular gasket elements, they require lower computational requirements, but shear stresses caused by friction between GDL and interfacing parts and membrane behaviour are not computed. To minimise the computational requirements of the simulations while keeping adequate accuracy, a combination of these mesh element types is used in several stack thermo-mechanical studies [19,54–56,59]. An alternative meshing approach is proposed by Lin et al. [67–72]. They used continuum shell elements to discretize all the components of a 3 SRUs stack model. Continuum shell elements correspond to the shape of the three-dimensional solid domains, whereas the kinematic and constitutive behaviour is similar to that of conventional shell elements [60].

1.5.1.3 Material constitutive laws

Several SOFC thermo-mechanical investigations by numerical methods, in particular the earlier ones, neglect the dependence of the mechanical properties on temperature. Given the large range of temperatures to which SOFC stacks are exposed during their lifetime, a comprehensive thermo-mechanical model should include these dependencies. Instead, on a large number of published models, the values of the thermo-elastic properties (i.e. elastic modulus, Poisson’s ratio and coefficient of

thermal expansion) are implemented only for a specific temperature. Thermo-mechanical models comprising the temperature dependence of the thermo-elastic properties are reported in Refs. [19,36,42,54–59,65,67–74].

Several of the materials used in SOFC stacks are known to have non-linear mechanical behaviour. The implementation of non-linear constitutive laws adds significant complexity to the model. The accurate characterization, i.e. testing for the identification of the deformation mechanisms and calibration of the model parameters, is also much more difficult and can rapidly become far-reaching in case the knowledge of multiple materials is needed. Reported non-linear mechanical behaviours of SOFC stack materials are plasticity in the metallic components (MIC, GDLs, etc.) [68], creep in all materials because of the high temperature [15,19,56], inelastic strain in the anode because of the Ni reduction [15], and ferroelasticity of LSCF cathodes [75]. The combined resolution of multiple non-linear mechanical constitutive laws usually further slows down the solution time. The implementation of the non-linear constitutive laws in stack thermo-mechanical models is discussed hereafter. Rate-independent plastic behaviour of the metallic components of the stack is often not considered in numerical thermo-mechanical models. Where included, the formulation is usually based on the Von Mises yield criterion and isotropic hardening [19,36,50,51,54–56,76–78] or to a lesser extent kinematic [45,46,48,49,73,79] strain hardening. In these studies, the choice of either the first or the last strain hardening model remains at present presumably arbitrary. In reality, a combination of isotropic and kinematic strain hardening was reported for several alloys [80].

To our knowledge, the number of studies that include creep behaviour of the stack materials in numerical thermomechanical simulations is growing but remains limited. It likely stems from the limited information on the creep properties of SOFC stack materials available in the literature. Further, the implementation of creep constitutive laws requires time-dependent simulations, which are demanding on computational time and the effect of history complicates the analysis. The constitutive law for the creep behaviour normally used for SOFC stack simulations is the Norton power law model [81], limited to the steady-state creep regime. The primary creep regime is usually neglected, mainly because the effort to establish an understanding has just started. Creep deformations in the context of SOFC stacks are expected to remain low, i.e. not beyond the secondary creep regime, because of the relatively strong mechanical interactions between the components. Hence, tertiary creep can be neglected in stack thermo-mechanical models, and used for specific studies such as damage modelling of bonded compliant seals [50].

Creep is recognised to affect the stack failure modes, e.g. [82]. In the thermo-mechanical analysis carried out at GEM-EPFL [57], simulations show that creep in the materials affects differently the mechanical reliability of the stack upon variations of the electrical load, leading to higher (lower) probability of failure of the cell during load decrease (increase). Because of creep in the metallic GDLs, modification of the gas channel sections upon operation cannot be excluded for all designs [83]. These

variations from the design configuration change the overall stack performance and may have an impact on the mechanical failure modes. These are only a few examples of the relevance of including creep behaviour in thermo-mechanical models of stacks.

Stack thermo-mechanical numerical simulations including the GDL geometry in full detail remains at present challenging, because computational needs induced by the large amount of mesh elements require to discretize with adequate accuracy relatively complex shapes and more complex verification of the solution accuracy. Computational homogenisation can help to estimate the effective mechanical properties of heterogeneous materials, i.e. for a fully periodic GDL, the representative volume would contain metal and gas phases. Besides the rigorous measurement of the thermo-elastic parameters, approaches to extend computational homogenisation to the creep behaviour of single solid phase metallic unit cells were also proposed [31]. The developments so far are applicable only for the secondary creep regime. Using this computational homogenisation approach, it is worth mentioning that in the case anisotropy is included in both creep and plasticity constitutive laws, FEM software (e.g. ABAQUS) computes only the creep strains, neglecting potential plasticity and leading thus to potential misleading interpretations of the failure modes [60].

Simulations where both creep and plasticity material constitutive laws are implemented require an implicit integration scheme (backward Euler), which is more computationally demanding than explicit methods because of the iterative process. If creep is included but not plasticity, more efficient computation may be carefully achieved by forcing the solver to use an explicit integration method [60]. At least in metallic GDLs and within the stress state range in SOFC stacks, plastic deformations remain likely limited [31] and irreversible deformation is dominated by creep. This statement cannot be considered fully general, because i) the equivalent stress and thus potential plastic yielding is dependent upon the local geometry of the component, and ii) at higher temperatures, i.e. above 600 °C, even though creep strain and thus stress relaxation are relevantly higher, the yield of metals occurs at much lower values of equivalent stress than at lower temperatures. Plasticity as well as creep constitutive laws must be implemented in SOFC stack models, at least in first tentative studies. Afterwards, if the simulated stress state in all components and at all times is well below the plastic yield point of the correspondent materials, the computational requirements for simulating the model can be lowered by neglecting the plasticity constitutive law.

Measurements suggest that the NiO-YSZ anode cermet shrinks upon reduction of the nickel phase. The reduction step occurs by injecting H₂ in the stack after the first heat-up, to make the anode electrochemically active. The shrinking of the anode is constrained by both the other cell layers (i.e. electrolyte, compatibility layer and cathode) and by the mechanical interactions with the sealant and the GDLs. As a consequence, the stress state can change in all the components upon anode reduction. Stack thermo-mechanical investigations with a simplified attempt to include such effect were

performed at GEM-EPFL [19,54–56] [58,59] and by Wang et al. [77] by applying isotropic artificial strain in the anode domain. Reduction strain of the anode can also be included in analytical models [41].

1.5.1.4 Mechanical boundary conditions

Central questions remain on the appropriate boundary conditions for SOFC stack thermo-mechanical simulations, which are yet to be answered in a rigorous way. They clearly differ depending upon the types of modelled domain, e.g. if only the cell or the whole stack is considered in the numerical simulation, because in a simplified view the potential deformation modes of the domain change. In the studies by Clague et al. [42,65], where only the cell domain is modelled, three types of boundary conditions are simulated: i) enforced flatness over the whole face of the cell, ii) cell free to bend and iii) enforced flatness limited to the sealing region of the cell. The last boundary condition, which is expected the closest to that of a cell in a stack with fairly thick MICs (because after the stack qualification, the sealant is stiffer whereas the GDLs are relatively compliant), yields the highest stresses in the anode. In other studies dedicated to the cell domain only, either enforced flatness on the face of the cell [76] or periodic boundary conditions [84] are implemented. In FEM models at the stack level, the mechanical boundary conditions aim at simulating the deformation modes of SRUs either near or far from the end plates of the stack. In the 3 SRUs model by Lin et al. [68] three configurations of boundary conditions are compared: the displacement along the direction normal to the bottom face of the SRUs is constrained at the bottom side of the assembly at the i) vertex, ii) edges and iii) face. On the top side of the assembly, the clamping load is applied as a uniformly distributed pressure. The stress states between the three configurations are similar. A different approach has been tested at GEM-EPFL to simulate stack designs such as commercialized by SOLIDpower [19,54–56]. The flatness of both the lower and bottom faces are constrained to remain flat, but they are allowed to rotate along the direction perpendicular to the gas flow. As a result, the deformation of the SRU along its thickness is allowed to vary linearly as function of the gas flow direction. This configuration of boundary conditions aims at considering in the simulation both the SRUs adjacent to the end plates of the stack and the higher thermal expansion towards the air flow outlet. For simulating SRUs far from the end plates, modified periodic boundary conditions (PBC) are used [19,54–56]. The simulation results suggest that the contact pressure on the active area is more uniform and the cell bending is lower in the case of enforced flatness [19].

Considerable reduction of the computational requirements for simulating 3-D stack thermo-mechanical models is achieved by taking advantage of symmetry in the stack in terms of i) geometry of the components and ii) temperature field in stacks with co- and counter-flow configuration. For example, symmetric boundary conditions along both in-plane directions of the SRU may be used for e.g. preliminary studies of thermal cycling assuming uniform temperature, which reduces the domain to one quarter of the real 3-D domain [73]. For simulations under polarization characterized by heterogeneous temperature fields, only symmetry boundary conditions along the in-plane direction

perpendicular to the gas flow direction can be applied, which allows the modelling of half a SRU geometry. Instead, if cross-flow configuration temperature field is simulated, the symmetry boundary condition cannot be applied and the whole SRU geometry needs to be implemented.

1.5.1.5 Mechanical interactions between the components

The understanding of the mechanical interactions between the stack component is believed critical to identify the failure modes in most stack designs [56]. In most multi-part SOFC models, mechanical interactions between the components is simulated either by constraining the displacement at nodes of the two surfaces to be identical, i.e. the components are considered as tightly joined together, or by contact. The number of studies with modelling approaches for a better description of the mechanical interfaces is at present very low. Mechanical contact is a source of non-linearity in the FEM simulations, because the stiffness matrix changes upon calculation of the contact stresses. In the studies where the implementation of mechanical contact is reported, the numerical algorithms for mechanical contact simulation are often not explicitly reported. In the studies performed at GEM-EPFL [19,54–56][58,59], the contact over the active area is approximated by the non-linear penalty method, which allows a smoothed variation of the contact pressure as the parts reach contact [60]. Frictionless tangential behaviour between the stack components is commonly implemented [59,67–72,85], supposedly because less computationally expensive. The presence of friction constraints in the model generates unsymmetric terms in the stiffness matrix storage. If the relative tangential displacement between the parts in contact is highly governed by the friction forces, i.e. when the coefficient of friction is high, these terms complicate the convergence of the numerical computation [60]. In most stack designs sealants made by glass-ceramic pastes and contact pastes deposited as contacting layers between the cell and GDLs can be considered highly plastic prior to the stack sintering, because of the presence of binders. Therefore, until the first stack heat-up, the constraint to the relative sliding between the parts is negligible, and the contact tangential behaviour may approximatively be modelled as frictionless. In the studies where friction between the components is considered, the values of the coefficient of friction are arbitrarily chosen. Values reported in the literature are equal to 0.1 [19,56,58], 0.16 [86], 0.2 [54,55] and 0.3 [70]. Caution is needed when relatively high values of friction coefficients are imposed between cell and GDLs and/or between MIC and GDLs, because i) FEM software like ABAQUS switch automatically to unsymmetric matrix storage, which is computationally more demanding, and ii) incompressibility in computing creep and plastic strain by FEM is imposed, and thus the high friction forces would induce high shear stresses in the GDLs, which in turn may lead to unrealistic loss of contact pressure upon creep/plastic deformations.

In SOFC stack models where gasket sealants are used, contact interface is implemented [24,25,50]. GEM-EPFL studies [19] compared the implementation of sealing gasket with contact and tied interfaces. For the considered stack design, the probability of failure of the cell was reduced in the former case, but the risk of contact pressure on the active area is higher. The beneficial or detrimental effects of the

mechanical behaviour of interface remains currently difficult to quantify and identify upfront, because of the dependence on the design and material mechanical properties. For glass-ceramic sealants, tie constraints are commonly implemented both between sealant and MIC and between sealant and cell [19,56,67–72,83].

1.5.1.6 Simulated operation scenarios

The initial stress state in each component of the modelled assembly is needed for comprehensive thermo-mechanical analyses. Neglecting initial stress state affects the accurate quantification of the stresses over the simulated load cases, and thus the correct prediction of the mechanical failure modes. For example, stress relaxation caused by creep strain may change conspicuously if the computational domain is considered pre-stressed or not. Possibility of mechanical failures is reported to occur already in the early stages of stack manufacturing [63]. Other studies report that the residual stresses in the cell do not cause directly its failure, but must be included in thermo-mechanical simulations [70,87–89].

A number of manufacturing steps have to be simulated to capture the initial stress state prior to the simulation of the stack operation (i.e. thermal cycling, polarisation, heat-up, cool-down, etc.). Several studies assume the whole computational domain stress-free before the simulation of the operation. This condition corresponds often to that when the stack is at the temperature at which crystallisation of the glass-ceramic sealants occurs, i.e. typically around 800 °C [28,68–70,74,90–93]. Other studies consider stress-free conditions at higher temperatures [67,77]. A lowering of the initial stress-free temperature intuitively yields less critical thermal stresses [67]. A presumably less realistic assumption is setting the stress-free condition at RT [53], which indeed neglects the presence of relatively high residual stresses at this temperature in the layers of anode-supported cells [41].

In the studies performed at GEM-EPFL [19,54–56] the steps in the SOFC stack manufacturing are approximated individually by simulating an “initialisation” sequence. The numerical output, i.e. the stress state in the computational domain, corresponding to the end of the initialisation sequence is then used as initial condition for the subsequent simulation of the stack operation (e.g. long-term polarisation, transients, thermal cycling etc.). The initialisation sequence includes sintering of the cell, application of the clamping load, first heat-up and reduction of the NiO-YSZ anode.

Variations in the operation conditions under polarization, such as flow configuration, maximum SRU temperature, air inlet temperature, system specific power and fraction of internal/external fuel reforming, can reduce the probability of failure of anode and cathode by an order of magnitude of 2 and 1, respectively [19]. In most studies in the literature, the temperature fields imposed on the computational domain are simulated by thermo-electrochemical models. The thermo-electrochemical output therefore affects the thermo-mechanics, but the feedback is typically neglected [91], except in the case of isothermal stress in ceramic MIC or cells with GDC electrolyte. Experience based on stack testing however suggests that the two aspects are coupled and contribute together to degradation. Several types for interaction can be imagined and likely occur in a SOFC stack, ranging from an increase

of the ohmic losses because of contact alteration or changes in the uniformity of the gas-flow distribution because of deformations of the GDL channels, leading to modifications of the temperature and overpotential distributions [83]. Therefore, the meaningful coupling of the physics should be an objective of future stack modelling developments.

Investigations typically compare i) flow configurations, ii) types of fuel and iii) transient/steady-state operation. Simulation results reported in the literature indicate that co-flow is beneficial compared to counter-flow in terms of mechanical reliability, mainly because of the smaller in-plane thermal gradient [19,35–37,54,94,95], but the electrochemical performance is typically also lower.

Further, from a thermo-mechanical viewpoint, internal reforming affects the in-plane spatial thermal gradient of the temperature profile, because the endothermic fast reactions tend to locally cool the fuel inlet region. Several thermo-mechanical studies on full internal reforming were carried out [35,36,94,95]. They all concluded that severe stresses arise in the electrolyte, especially if internal reforming is combined with counter-flow configuration. Instead, partial or even full reforming alleviates the risk of mechanical failures [52,54] to the detriment of system performances. Partial oxidation of the fuel is also investigated [54], and from a thermo-mechanical viewpoint is found less critical than internal reforming. Most stack thermo-mechanical studies consider steady-state thermo-electrochemical conditions, or a succession of them. At GEM-EPFL [54], transients including variations of the electrical load were simulated with a dynamic stack thermo-electrochemical model and the temperature profiles imported in a steady-state thermo-mechanical model. The results highlighted that a control strategy is of relevance for the mitigation of failure during load following. At least on the probability of failure of cell, thermo-electrochemical degradation simulations revealed that the contribution of the alteration of the temperature field is limited [56].

1.5.1.7 Failure criterions

Commonly, thermo-mechanical investigations of cells and stacks aim at identifying the conditions, during e.g. polarization, thermal cycling, and locations (i.e. in which component of the assembly and/or the region) the stresses are the highest. The occurrence of mechanical failures is then estimated by comparing the values of stress with the strength of the material based on the maximum stress criterion. The knowledge on technological ceramics however indicate that such approach is practically inadequate to assess the mechanical failure of such materials, because they do not fail at a certain value of stress, rather the values of stress at which cracking occurs follow a Weibull distribution. The straightforward approach to apply simplified Weibull statistics under the principle of independent assumption requires post-processing of the results of SOFC thermo-mechanical simulations. The three principal stresses simulated in the components of interest are extracted together with the corresponding element volume integration to compute analytically a probability of failure, with as input Weibull statistics parameters obtained from mechanical tests on the same material considered in the numerical model. Using the Weibull statistics parameters available in the literature, the probability of

failure of the anode considering variations of the Weibull parameters within the 95% confidence interval may lead to significant changes in the insights of the mechanical reliability [19,54,56].

The standard Weibull approach assumes that only mode I crack opening tensile stresses contribute to the failure of the component. This approach further postulates the principle of independent actions, which entails that the principal stresses act independently in each principal direction. Therefore, when the investigated stress state is multiaxial, this approach may not estimate accurately the probability of failure. The reason is that shear and compressive stresses can also contribute to the crack propagation, and should not be neglected. This shortcoming is documented and supported by experimental observations [62,96]. Batdorf proposed an extension of the standard Weibull approach, which is not yet commonly applied for thermo-mechanical investigations of SOFC stacks [62]. The Weibull statistical approach and its extension can treat only part of the failure modes that can affect a SOFC cell. Fracture mechanics approaches are needed to analyse the failure of e.g. thin layers on substrate and at singularities but are not covered in the present overview.

The cracking of the metallic interconnects is typically not observed, because metallic alloys developed for SOFC can accommodate deformations by plastic strain. However, inelastic deformations in the MIC and potentially buckling may cause mechanical failure of the interfaces or of the adjacent components. The risks of buckling of the MIC are expected to scale with the reduction of MIC thickness and may be promoted by compressive stresses, mostly caused by thermal gradients of the temperature field during polarisation. First analyses were performed at GEM-EPFL [55], based on the analysis of the MIC alone, with geometrical non-linearity but without creep. The results suggested that the risk should increase with the reduction of the thickness, whereas the effects of operating conditions were less clear. In reality, stress relaxation occurs at operating temperature because of creep, which is expected to lower the risk of buckling.

In the case of stack thermo-mechanical analysis where the mechanical interaction between the components is modelled by contact, the mechanical reliability can be assessed by verifying that the simulated mechanical contact over the active area of the cell remains sufficient over the whole life-time of the SOFC stack. This potential failure mode is so far not intensively characterised, despite its importance for stack thermo-mechanical reliability and performances, because the loss of contact pressure on the active area is expected to increase the electrical contact resistance of the interface [17]. Studies performed at GEM-EPFL [55] showed that the contact pressure can be guaranteed over different cases of electrical load variation, but lost on large regions of the gaskets. In contrast, analyses including creep behaviour in the material constitutive laws [19] predicted that the simulated contact pressure is lost on large regions of the active area, particularly if the gasket is rigidly bonded to the MIC and the cell. In a different study using the same thermo-mechanical model [56], the loss of contact pressure on the active area can be promoted by the deflection of the SRU, caused by the cell bending. Furthermore, thermal cycling of the stack can affect the contact pressure over the active area [58].

When post-mortem images of the simulated stack design are available, results of the numerical simulations can be interpreted and validated based upon visual inspection tracking e.g. interface detachments or large cracks. Comparison with the results of stack simulation provide first elements for qualitative validation [90].

1.5.1.8 Concluding remarks

Further research is necessary to understand and quantify thoroughly the trade-offs between mechanical reliability, performance and costs of SOFC stacks [19]. Within similar stack designs and thermo-electrochemical conditions, the use of simple indicators (e.g. thermal gradient over the active area, maximum temperature on the cell and temperature difference outlet-inlet region) to assess qualitatively the risk of mechanical failures in the cells without dedicated thermo-mechanical simulation may still be acceptable for comparison purposes. Instead, if new stack geometries and operating conditions are explored, the reliability of such indicators can become questionable, and may potentially lead to misleading insights [54]. In these circumstances, thermo-mechanical modelling and simulation cannot be neglected.

Often, the cell is considered the core component of the SRU. However, mechanical reliability of the cell is not only governed by the strength of its materials, but also by its mechanical interaction with the other SRU components. Thermo-mechanical investigations should therefore take into account the whole SRU domain, including adequate modelling of the mechanical interactions between the components.

From this literature survey, it is acknowledged that the gas tightness between the air and fuel compartments is a vital requirement for SOFC stack reliability. If this condition is not fulfilled, parasitic combustion unavoidably occurs in the location where fuel and gas meet. This combustion is exothermic, i.e. the surrounding materials would be exposed to relatively high temperatures. Losses of gas tightness are caused by materials becoming either excessively porous or by cracking, or both. Possible causes of unwanted porosities in electrolytes and sealants are improper manufacturing processes and/or faulty materials and degradation.

2 Mechanical properties of SOFC materials

2.1 Four-point bending testing

The research on the thermo-mechanical properties of SOFC materials and adequate measurement methods is growing but remains limited and therefore of high interest for the development of the technology. The brittle failure of ceramics poses several practical issues for the handling and mechanical testing of samples. Furthermore, differences in the metric and topological microstructural parameters of the tested sample and of the real component materials must be such that the effect on the effective thermo-mechanical properties is minimal. This practically requires production using the same manufacturing route, because guaranteeing that slight modifications of the process parameters to e.g. increase the thickness of the deposited layer do not change the material microstructure and thermo-mechanical properties can rapidly become a far-reaching task by itself. A requirement for a conventional mechanical testing method is therefore the capability to accommodate samples that have a thickness similar to that of the components (Chapter 3.1).

Tensile testing is the preferred method for the mechanical testing of metals, but is not appropriate for ceramic samples, because the machining of thin sheets made of brittle materials into the relatively complex adequate sample geometry (e.g. the typical dog-bone shape) can be difficult. Unwanted fractures can occur during the mounting of the sample in the setup or because of compression caused by the grips on the sample shoulders. This explains the limited number of tensile tests on SOFC ceramic materials reported in the literature [97–99]. The compressive testing of ceramics is reported in e.g. [99]. However, the deformation of the sample upon the application of considerably high mechanical loads is small and comparable with the roughness of the sample surfaces in contact with the setup. This effect is more pronounced for thin materials and thus the measurement accuracy may be insufficient.

Bending is currently the most common method for the mechanical testing of SOFC ceramics, because the handling of the samples is relatively easy and the deformation that can be applied on thin samples by bending is usually large compared to the sample imperfections. However, the stress state in the sample induced by bending is not uniform: i) it changes across the thickness, from compressive to tensile, and ii) between the outer and inner testing fixture.



Figure 3: Representation of the most common configurations for bending test of planar samples: a) four-point bending, b) three-point bending, c) ring-on-ring (ROR), d) ball-on-ring (BOR) and e) ball-on-three balls. Figure reproduced from Wei et al. [99]^d.

^d Reprinted from Ceramics International, 40, J. Wei, G. Pećanac, J. Malzbender, Review of mechanical characterization methods for ceramics used in energy technologies, 15371-15380, 2014, with permission from Elsevier.

Post-processing of the experimental data to estimate the effective mechanical properties is therefore required and typically based on analytical methods. The common configurations for bending tests of planar samples comprise three-point, four-point, ring-on-ring (ROR), ball-on-ring (BOR) and ball-on-three-balls setups [99], see Figure 3. An additional requirement for setups for fracture testing of large batches of samples in a sequential manner [100] is the reliable automatic removal of the broken sample from the testing fixture prior to the testing of the next sample. This feature is simpler to implement in either a three- or four-point bending configuration. Compared to three-point bending, the four-point bending configuration yields a larger volume of material subjected to a uniform stress state, i.e. between the two inner rollers, and it is unaffected by the contact pressure of the rollers. This increases the accuracy of the material strength measurements following statistical methods (Chapter 2.3): larger volumes of tested material are more statistically representative, because they include a larger population of flaws [101]. Therefore, the four-point bending configuration was selected for the design of the two mechanical testing setups. A representation is shown in Figure 4.

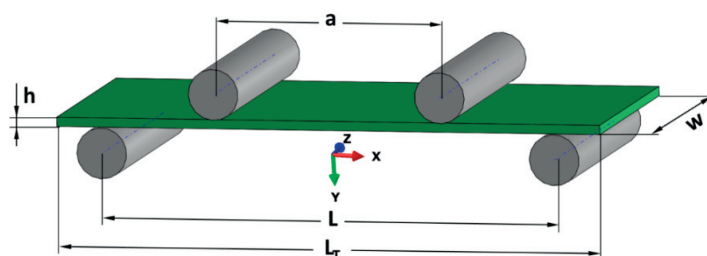


Figure 4: Geometry of the four-point bending test configuration.

To our knowledge, the characterization of the mechanical properties of SOFC materials remains incomplete, even for the Ni-YSZ electrode. The experimental part of the present study comprises the development of setups for mechanical testing, model-based parameter estimation and measurement campaign. The focus is on:

- The primary and secondary creep of the Ni-YSZ anode at the temperatures of relevance for anode-supported SOFCs (i.e. 700-800 °C). Since creep testing is relatively long, the possibility for the simultaneous measurement of multiple samples is a requirement for the design of the setup.
- The strength of the anode cermet both in oxidised (NiO-YSZ) and reduced state (Ni-YSZ), at room and high temperatures. This study is based on statistical approaches. Hence, relatively large batches of samples need to be tested under the same experimental conditions.

Two in-house setups were designed and fabricated. Both are capable of measuring the creep behaviour and strength of materials up to 900°C in either oxidizing or reducing atmospheres. The setup for the measurement of creep behaviour is referred to as “CRP”, whereas that for the measurement of the strength as “SEP”.

2.1.1 Modelling of 4-point bending

The calculation of the stress state during four-point bending by closed-form analytical solutions is fast and simple. The standard approach is based on the linear beam theory. The two main assumptions are that an arbitrary section along the beam length and orthogonal to the neutral axis i) remain planar and ii) its slope variation is negligible upon the deflection of the beam. These two assumptions imply that i) the thickness and the width of the sample must be small compared to its length and ii) the maximum sample deflection during bending is small compared to the sample thickness. The analytical solution of the stress in the beam between the two inner rollers is:

$$\sigma_{xx}(y) = \frac{\left(\frac{y}{2}\right) M_f}{I} \quad \text{with } M_f = \frac{P(L-a)}{4} \quad \text{and } I = \frac{wh^3}{12} \quad (9)$$

The reaction force on the outer rollers RF as a function of the sample deformation at the inner rollers y_{IR} is [100]:

$$RF = \frac{4wh^3 y_{IR} Em}{(L-a)(L^2 + aL - 2a^2)} \quad (10)$$

In practice, sliding of the sample with respect to the rollers occurs during testing, which results in additional inaccuracies in the estimation of the stress by the linear beam theory solutions. Indeed, higher bending deformations entail not only a deviation from the linear beam theory, but also a translation of the sample/roller contact lines upon bending, i.e. the position on the sample at which the force is applied, because the geometry of the testing fixture remains unmodified. In reality, the tangential contact behaviour between the sample and the rollers is not frictionless. In the case the Poisson's ratio of the material is not zero, the sample does not bend only longitudinally but also transversally, resulting in a biaxial stress state. These effects eventually yield together to a deviation from the theoretical stress state estimate. The use of analytical solutions in post-processing of experimental data may result in significant inaccuracies in the estimation of the mechanical properties, which must therefore be quantified (see Paragraph 2.1.2).

In the present study, 3-D modelling using the finite-element method (FEM) is used to first quantify the effects of such phenomena on the accuracy of the post-processing for measurements. The FEM model is implemented in the commercial software ABAQUS and its main purpose is model-based estimation of the mechanical properties of the Ni-YSZ anode (Chapter 2.2).

The FEM model assumes symmetry along the X and Y axis and therefore comprises one fourth of the real geometry (see Figure 5). The sample domain is meshed with reduced-integration, second order elements (C3D20R), whereas cylindrical analytical surfaces are used to model the rollers. Since testing occurs under the regime of large deformations, non-geometrical non-linearity is included in the FEM kinematic equations. The sample material constitutive law is linear elasticity. The mechanical boundary conditions of the model are encastre at the outer roller, whereas at the inner roller all degrees of freedom are constrained except for the displacement along y-axis, which is varied linearly during the

bending simulation from 0 (undeformed sample) to the desired value. The mechanical interaction between the sample domain and the rollers is simulated by contact. The normal behaviour at the contact interface is computed by a “softened” non-linear pressure-overclosure relationship, which facilitates the numerical convergence and can include in the simulation if information is available the effect on the contact pressure of potential dusts, small sample waviness and grease (used in the tests to minimise the friction between sample and rollers). A large-sliding contact tracking algorithm is used since the relative sliding between the sample and the rollers is assumed potentially non-negligible. The normal directions of the surfaces of the modelled sample and rollers are assumed to remain opposite at the contact zone throughout the bending simulation. Thus, the surface-to-surface contact implementation is preferred over the node-to-node counterpart. Tangential contact behaviour is either with friction or frictionless, depending on the study case. Details of the implementation of the penalty method with non-linear pressure-overclosure relationship are provided in Paragraph 3.1.4.

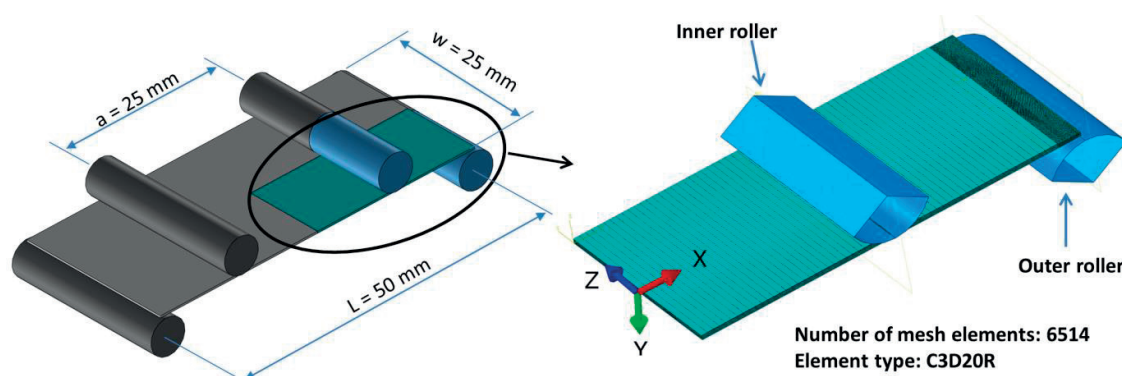


Figure 5: View of the full geometry of the 4-point bending test (left) and computational domain for the simulations (right).

The FEM model was first validated numerically. A mesh independency analysis was performed, based on the variation of the reaction force on the outer rollers computed by the model, depending upon the number of mesh elements. The analysis was performed using arbitrary sample mechanical properties and friction coefficient, i.e. elastic modulus, Poisson’s ratio and friction coefficient of 65 GPa, 0.39 and 0.8, respectively. The imposed displacement at the inner rollers was 2 mm. A set of 16 cases differing in terms of number of elements in the mesh was simulated, using all the same model implementation. Each step of mesh refinement consisted in varying the number of mesh elements simultaneously along the thickness, width and length of the sample. To limit numerical inaccuracies, the maximum aspect ratio of each mesh was lower than 30. The results are shown in Figure 6. The accuracy of the simulated reaction force rapidly increases for a number of mesh elements from 1’000 to 4’000, supposedly because finer meshes allow a more accurate tracking of the contact at the interface between sample and roller. Above 4’000 elements, variations are lower than 0.998 and monotonically decreasing.

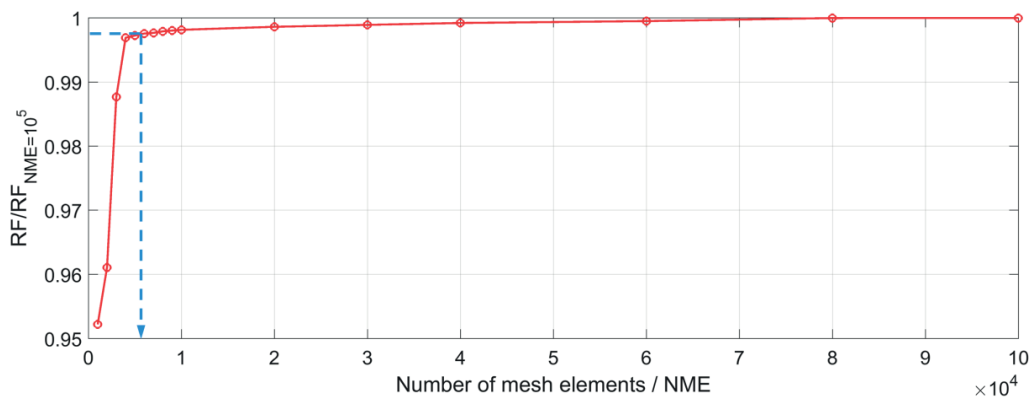


Figure 6: Mesh dependence study of the FEM model of four-point bending setup. The y-axis is the ratio between the computed reaction force at the outer rollers for each mesh and for that for the finest mesh.

The mesh selected for all the FEM simulations of four-point bending in this study comprises 6'514 elements, which appears a good trade-off between accuracy and model runtime based on Figure 6. The simulated reaction force is within 0.2% with respect to the case with the finest mesh and the computation time is about 7 min using 6 cores of a desktop computer (Intel Core i7-3930K). The selected mesh is that shown in Figure 5.

A first assessment of the inaccuracy due to the use of the analytical solution based on linear beam theory to measure the elastic properties is performed by comparing the reaction force from the analytical solution (Equation (10)) and the FEM predictions for varying coefficient of friction, FEM kinetic equations, and Poisson's ratio, whereas other material properties are kept constant. The results are shown in Figure 7.

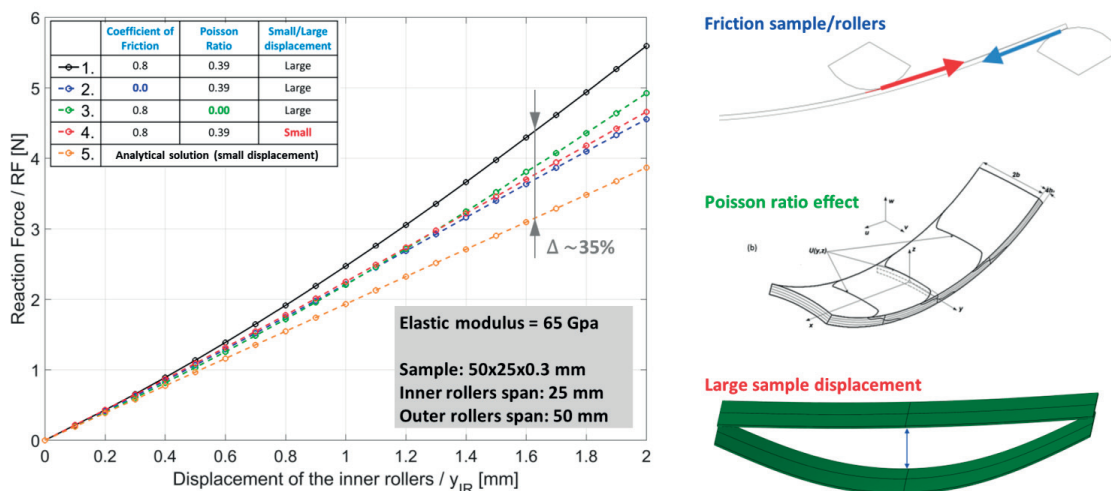


Figure 7: Comparison of the computed reaction force at the outer rollers over displacement at the inner rollers, from different simulation cases of the FEM model (curves from #1 to #4) and from analytical solution (curve #5). On the right-hand side, schematic representations of the potential analysed source of errors are shown.

The difference in the computed reaction force between the analytical solution and case #1 (i.e. FEM model including all the three measurement errors shown in Figure 7) is the highest, i.e., about 35%. Mechanical properties estimated by using the analytical solution rather than numerical models would in this case be affected by this error. The curve #2 represents the ideal limiting case for a bending test under the conditions relevant for the present study, i.e. with frictionless contact with large deformation (e.g. lubrication between sample and rollers, and sample deformed until its brittle failure). In this case, the discrepancy is the lowest (around 15%), but will still affect the accuracy of the measured mechanical properties.

2.1.2 Design of 4-point bending setups

2.1.2.1 Consideration on the sample dimensions and testing fixture

The sample dimensions, which are needed to design the testing fixture, are in this work the result of trade-offs between the inner diameter of the work-tube (of the SEP setup) and the accuracy of post-processing by both the analytical solution of four-point bending and material strength estimation by statistical methods. The estimation of the errors of the analytical solution as a function of the dimensions of both the sample and testing fixture follows analytical recommendations reported in the literature [102]. For each contribution to the error of the analytical solution of the linear beam theory, a sensitivity analysis is carried out, with the dimensions of sample and testing fixture as input variables. The sample thickness is fixed to 0.3 and 0.27 mm, respectively for Crofer and NiO/Ni-YSZ, which are imposed by the available raw materials from which the samples are cut. In the following series of sensitivity analysis of the errors, a thickness of 0.3 mm is used. The considered error metric is simply the percentage difference between the stress computed by the linear beam theory σ_{xx}^{LBT} and the true stress σ_{xx}^{True} :

$$err = 100 \left[\frac{\sigma_{xx}^{LBT} - \sigma_{xx}^{True}}{\sigma_{xx}^T} \right] \quad (11)$$

The contributions to the inaccuracy investigated in the series of sensitivity analysis are i) the friction between sample and rollers, ii) the wedging stresses, caused by the wedging effect that the inner and outer rollers lead on the sample upon bending, iii) load mislocation, caused by the fabrication tolerances of the testing fixture, and iv) Poisson's ratio effect, which leads to anticlastic curvature.

The analytical expression to estimate the error on the stress caused by the friction between sample and rollers is:

$$err_{fri} = 100 \left[\frac{\mu}{\left(\frac{L-a}{2h}\right) - \mu} \right] \quad (12)$$

A coefficient of friction of 0.5 (arbitrarily set, but plausible in case of dry contact) is used in this sensitivity analysis. The inner and outer spans are the two variables of the sensitivity analysis listed in Table 1. In practice, the measurement error caused by friction between the sample and the rollers can be minimised either by fabrication of a testing fixture with rollers freely pivoting around their axis or by applying lubricants at the contact interface. For high temperature testing, several research laboratories have attempted to interpose thin graphite sheets at the interface. In this work, pivoting of the rollers of both SEP and CRP setups is impeded by other design alternatives, and the long-term durability for high temperature questionable. A special spray lubricant was used in all tests.

Table 1: Sensitivity of the error caused by friction to the inner and outer span.

		outer span L [mm]										
		40	42	44	46	48	50	52	54	56	58	60
inner span a [mm]	15	1.21	1.12	1.05	0.98	0.92	0.86	0.82	0.78	0.74	0.70	0.67
	20	1.52	1.38	1.27	1.17	1.08	1.01	0.95	0.89	0.84	0.80	0.76
	25	2.04	1.80	1.60	1.45	1.32	1.21	1.12	1.05	0.98	0.92	0.86
	30	3.09	2.56	2.19	1.91	1.69	1.52	1.38	1.27	1.17	1.08	1.01
	35	6.38	4.48	3.45	2.80	2.36	2.04	1.80	1.60	1.45	1.32	1.21
	40	-100.00	17.65	8.11	5.26	3.90	3.09	2.56	2.19	1.91	1.69	1.52

The error caused by the wedging stress is:

$$err_{wdg} = 100 \left[\frac{-0.133}{\frac{3}{2} \left(\frac{L-a}{h}\right) + 0.133} \right] \quad (13)$$

The results of this sensitivity analysis, also in this case as function of the inner and outer spans, are listed in Table 2. The contribution of the wedging stresses to the inaccuracy is relatively low, and it decreases for large outer spans and small inner spans.

Table 2: Sensitivity of the error caused by wedging stresses to the inner and outer span.

		outer span L [mm]										
		40	42	44	46	48	50	52	54	56	58	60
inner span a [mm]	15	0.11	0.10	0.09	0.09	0.08	0.08	0.07	0.07	0.07	0.06	0.06
	20	0.13	0.12	0.11	0.10	0.10	0.09	0.08	0.08	0.07	0.07	0.07
	25	0.18	0.16	0.14	0.13	0.12	0.11	0.10	0.09	0.09	0.08	0.08
	30	0.27	0.22	0.19	0.17	0.15	0.13	0.12	0.11	0.10	0.10	0.09
	35	0.54	0.38	0.30	0.24	0.21	0.18	0.16	0.14	0.13	0.12	0.11
	40	-100.00	1.35	0.67	0.45	0.33	0.27	0.22	0.19	0.17	0.15	0.13

The error caused by the misplacement between the pairs of inner and outer rollers Δs is calculated as:

$$err_{mis} = 100 \left[\frac{2\Delta s}{L-a} \right] \quad (14)$$

In the following analysis, Δs is assumed equal to 0.5 mm, and is equal to the deviation in position of both inner rollers along the x-axis with respect to the theoretical design. A proper estimation of this

parameter may be obtained by tolerance analysis of the designed components or by direct measurements on the testing fixture. The results of the sensitivity analysis of this error as function of the inner and outer rollers span are listed in Table 3. Load mislocations are found to lead to severe inaccuracies in the stress estimation by analytical solutions. The error becomes higher if the difference between outer and inner rollers span is reduced.

Table 3: Sensitivity of the error caused by load mislocation to the inner and outer span.

		outer span L [mm]										
		40	42	44	46	48	50	52	54	56	58	60
inner span a [mm]	15	4.00	3.70	3.45	3.23	3.03	2.86	2.70	2.56	2.44	2.33	2.22
	20	5.00	4.55	4.17	3.85	3.57	3.33	3.13	2.94	2.78	2.63	2.50
	25	6.67	5.88	5.26	4.76	4.35	4.00	3.70	3.45	3.23	3.03	2.86
	30	10.00	8.33	7.14	6.25	5.56	5.00	4.55	4.17	3.85	3.57	3.33
	35	20.00	14.29	11.11	9.09	7.69	6.67	5.88	5.26	4.76	4.35	4.00
	40	#DIV/0!	50.00	25.00	16.67	12.50	10.00	8.33	7.14	6.25	5.56	5.00

The analytical solution for the estimation of the error generated by the anticlastic curvature (caused by the Poisson's ratio of the tested material) is:

$$err_{pre} = 100 \left[\frac{y_z}{y_{x,max}} \right] = 100 \left\{ \frac{\frac{1}{2} \left[\frac{h}{2\varepsilon_{zz}} - \left(\left(\frac{h}{2\varepsilon_{zz}} \right)^2 - \left(\frac{w}{2} \right)^2 \right)^{1/2} \right]}{\left(\frac{2wh^2\sigma_{xx,max}}{3} \right) \frac{2L^2 - a^2 + 2La}{8wh^3Em}} \right\} \quad (15)$$

with the transversal elastic strain ε_{zz} calculated as:

$$\varepsilon_{zz} = \frac{\nu\sigma_{xx,max}}{Em} \quad (16)$$

To perform the sensitivity analysis, the elastic modulus Em and the Poisson's ratio ν are respectively equal to 80 GPa and 0.39. In the following sensitivity analysis (see Table 4), the inner span a is set to 25 mm, whereas the maximum stress $\sigma_{xx,max}$ is set to the arbitrary value of 100 MPa. As an example, with an outer roller span of 50 mm and sample width of 25 mm, the sample deflection $y_{x,max}$ is 2.39 mm, whereas the deflection along the transversal direction is about 0.1 mm.

Table 4: Sensitivity of the error caused by anticlastic curvature to the sample width and outer span.

		outer span L [mm]										
		40	42	44	46	48	50	52	54	56	58	60
width w [mm]	10	1.28	1.17	1.07	0.99	0.92	0.85	0.79	0.74	0.69	0.65	0.61
	12	1.84	1.68	1.55	1.43	1.32	1.23	1.14	1.07	1.00	0.94	0.88
	14	2.51	2.29	2.11	1.94	1.80	1.67	1.55	1.45	1.36	1.27	1.20
	16	3.27	2.99	2.75	2.54	2.35	2.18	2.03	1.89	1.77	1.66	1.56
	18	4.14	3.79	3.48	3.21	2.97	2.76	2.57	2.40	2.24	2.11	1.98
	20	5.12	4.68	4.30	3.96	3.67	3.40	3.17	2.96	2.77	2.60	2.44
	22	6.19	5.66	5.20	4.79	4.44	4.12	3.84	3.58	3.35	3.15	2.96
	24	7.37	6.74	6.19	5.71	5.28	4.90	4.57	4.26	3.99	3.74	3.52
	26	8.65	7.91	7.26	6.70	6.20	5.75	5.36	5.00	4.68	4.39	4.13
	28	10.03	9.17	8.42	7.77	7.19	6.67	6.22	5.80	5.43	5.10	4.79
	30	11.52	10.53	9.67	8.92	8.25	7.66	7.14	6.66	6.24	5.85	5.50

Because of the Poisson’s ratio effect, the inaccuracy on the stress estimation by the analytical solution increases for both wider samples and larger outer spans. However, the effect is more pronounced by the former. The inaccuracy caused by the anticlastic curvature is highly dependent upon the value of Poisson’s ratio of the sample material: if the Poisson’s ratio is 0.26 instead of 0.39, the errors are halved.

In summary, the four sensitivity analyses showed that the accuracy of the analytical solution of four-point bending is improved if the span of outer rollers is larger compared to that of the inner rollers, and if the sample width is relatively small. In contrast, accurate measurement of the material strength by statistical methods requires that large volumes of tested material are subjected to tensile stresses. This can be achieved by wider samples and lower difference between outer and inner rollers spans. As a result, the ratio between length and width of the sample was arbitrarily fixed to 2. The samples and testing fixture dimensions are thus determined as follows:

1. The sample dimensions are maximised to fit the diameter of the work-tube with a clearance between corners of the sample and inner diameter of the work tube of approximately 8 mm. The resulting dimensions of the sample are 60x25 mm.
2. The outer rollers span is determined such that the local stresses in correspondence of the two outer rollers (because of the contact pressure) are not amplified by the edges effect. This effect can be damped out after a distance equal to that of the sample thickness. Hence, the maximum outer rollers span of samples 60 mm long and 0.3 mm thick is 59.4 mm. However, to guarantee easy handling, the overhang of the samples used in this work is 5 mm. With samples 60 mm long, this leads to an outer roller span of 50 mm.
3. The inner roller span is fixed to 25 mm, as drawback to maximise the accuracy of the strength measurement by statistical approaches (attainable by large inner rollers span) and minimise the errors on the analytical solution because of the effects of friction, wedging stresses and load mislocation, which implies minimised inner rollers span.

The error caused by the contact point tangency shift upon sample bending cannot be quantified easily by analytical solutions, because the prior knowledge of the tangency shift by either a numerical model or direct observations is required. Reduction of the rollers diameter on the one side minimises this error, on the other side increases the stresses at the contact zone. Peak of stresses in the sample in correspondence with the contact zone worsens the accuracy of the strength measurement by statistical approaches, because in the analytical solution the stress state between the two inner rollers is instead assumed uniform. The selected material of the rollers of both SEP and CRP setups is the commercial Nicrofer® 6025 HT alloy. It contains about 2% of aluminium. It forms a protective oxide scale upon the first heat-up to relatively high temperatures (e.g. 800 °C), which tightly adheres on the component surface. On the surface of the rollers, the function of this alumina layer is to lower the coefficient of friction with the sample. To fabricate the rollers, the most available commercial diameter of the rods is 6 mm. Machining is required for the fabrication of cylinders with the desired tolerance. The design roller diameter for both setups is therefore 5.70 mm.

Besides, analytical solutions encompassing a higher level of detail can take into account the effect of potential sample twisting as well as of chamfered/rounded sample cross sections. They are however not included in this analysis, which is a first analysis performed in the view of setup design. For refined analysis, the developed parameter estimation procedure presented in Chapter 2.2 can also provide detailed information.

2.1.2.2 Description of the setup for elastic and strength measurements (SEP)

The present section presents specific practical details of the SEP setup. The SEP setup was limited by space constraints for integration in the available laboratory. The height is minimised, while keeping the possibility of partial vertical opening of the furnace and the number of loaded samples maximum. The length of the linear actuator and consequently its stroke required modification. Figure 8 provides an overview of the setup. The numbering in the following text refers to this figure.

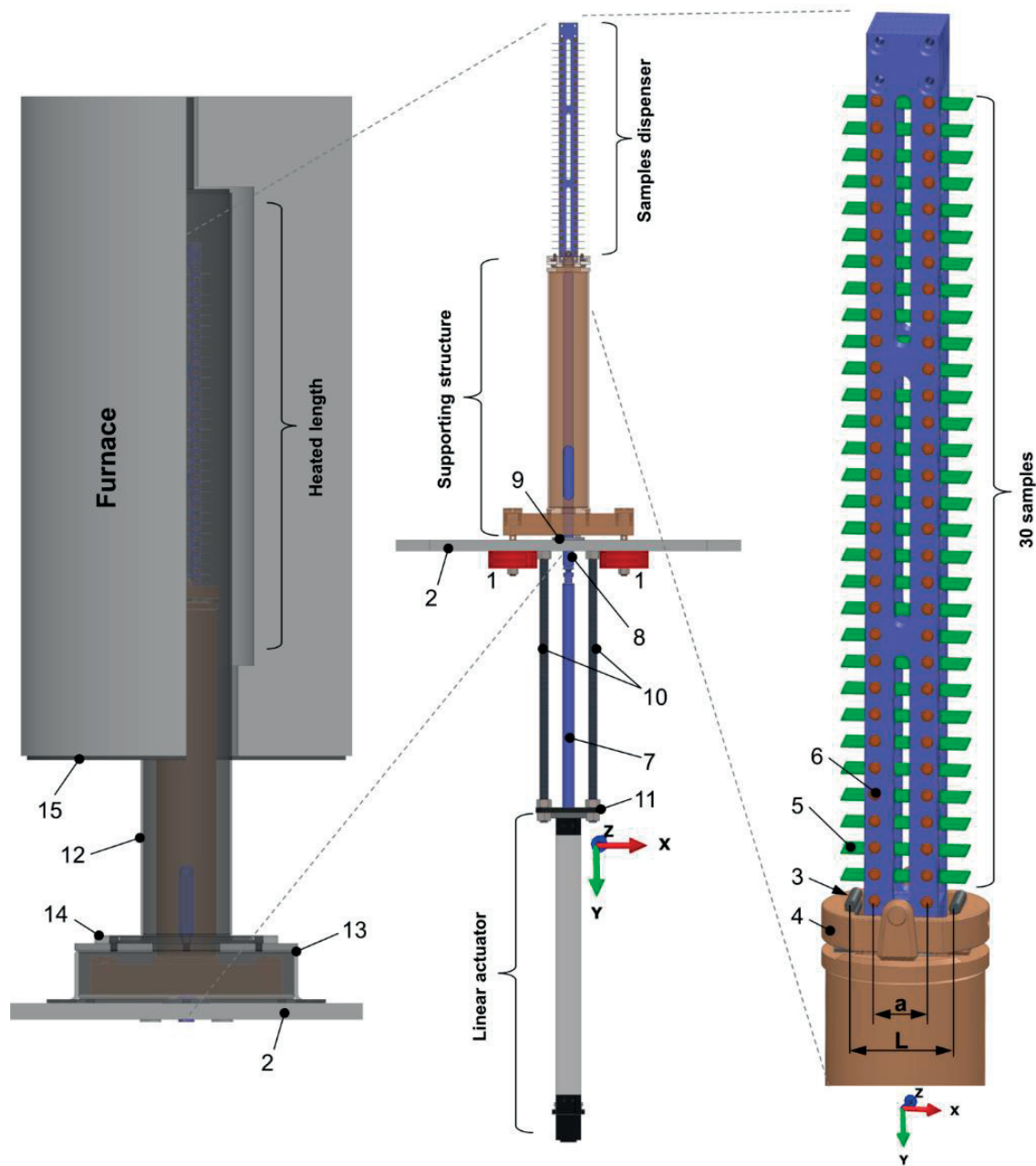


Figure 8: 3-D sketch of upper side of the SEP setup. Components in transparency are shown for reference.

The outer rollers are supported by two load cells, which do not move upon sample bending, whereas the vertical displacement of the inner rollers is controlled by a linear actuator. The lower part of the supporting structure (Figure 8) is fixed to two strain gauge load cells (1) (model K11-500N005, Transmetra GmbH) by two threaded rods, which are screwed to the threaded hole of each load cell (see Figure 9). The precise positioning of the rollers is key for the measurement accuracy. The adjustment to guarantee the symmetric position of the outer rollers with respect to the inner rollers is made by

fastening of these threaded rods. To achieve reliable measurements, distortions in mounting the strain gauge load cells must be minimised. Hence, the contact surface of the mounting plate (2) in correspondence of the load cell housings is milled to reach specified planar tolerances.



Figure 9: Representation of the load cell model (K11-500N005, Transmetra GmbH) used in the SEP setup.^e

The installed model of load cells can operate at a maximum service temperature of 70 °C. To mitigate the effect of heat conduction from the sample testing zone in the furnace to the upper zone of the SEP setup, the load cells are fixed on the bottom side of the support plate. During the validation of the setup, the temperature of the load cell was monitored to verify that the thermal conditions are adequate. Both load cells are connected to a 2 channels strain gauge amplifier (model GSV3USBx2, Transmetra GmbH), which process the signal voltage of both load cells and transmit the output digital signal to the data acquisition software.

On the top of the supporting structure, the two cylindrical outer rollers (3) are fixed on a horizontally pivoted head (4) at a centre-to-centre distance L of 50 mm. The function of the pivoting head around the z -axis (see Figure 10) is to reduce the measurement errors in the case of pre-deformed samples. Such initial deformations may arise from residual stresses in the sample or manufacturing imperfections, among others. If this compensation is not accounted for and the sample is pre-deformed, only one of the two inner rollers may be in contact with the sample, i.e. the sample is loaded on three points instead of four, leading to misleading measurement data. This capability was a design specification, but the pre-deformation of all the samples tested in this thesis proved very limited. Therefore, pivoting of the head was blocked for all the measurements.

The samples dispenser (see Figure 8) is an assembly of two steel stripes and a set of 30 pairs of both inner rollers (6) and spacing rollers. The spacing rollers, welded on the upper side of the inner rollers, maintain the stack of samples (5) separated from each other by a distance of 13 mm in the vertical direction. This distance guarantees that the left and right free extremities of the sample do not touch under bending and thus potentially misplace the next sample of the test batch. Initially, all samples are supported by the spacing rollers (Figure 10-a). Upon downwards displacement of the sample dispenser,

^e Reproduced under authorization of Transmetra GmbH, Lorenz Messtechnik GmbH.

the sample at the bottom of the batch first contacts the outer rollers (Figure 10-b), and then also the inner rollers (Figure 10-c). At this point, the 4-point testing of the sample starts, i.e. it is bent by further downwards displacement of the sample dispenser. The sequential testing of the whole batch of 30 samples requires that each sample is either bent until its failure (then, the scraps should fall down by gravity force) or manually removed after bending (which is possible only in tests at RT).

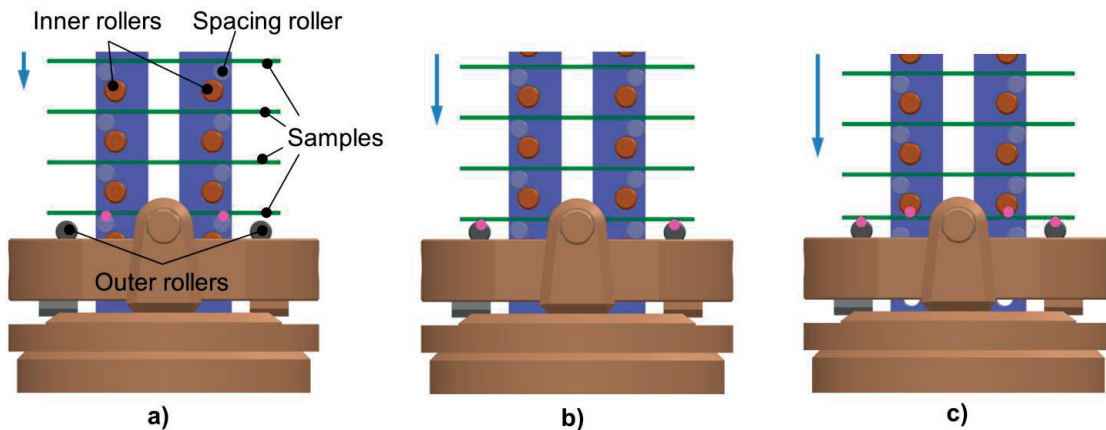


Figure 10: Tracking of the contact points (depicted by magenta points) between samples and rollers upon downwards displacement of the samples dispenser. The frontal steel strip of the samples dispenser is shown in transparency.

The maximum operating temperature of the linear actuator, including its piston (7), is 70 °C, whereas the sample dispenser is exposed at relatively high temperatures during testing (e.g. 600-900 °C). The piston is therefore fixed to the sample dispenser by a connecting rod (8) made of steel, to keep the linear actuator close to RT. Undesired bending of the assembly made of sample dispenser, connecting rod and piston around the x- and z-axis is hindered by a Teflon® O-ring (9) housed between the connecting rod and the mounting plate. The O-ring also guarantees the gas-tightness of the testing environment.

The frame of the linear actuator is fixed to the mounting plate (2) by four threaded rods (10). Controlled fastening of the calibration nuts (11) pivots the linear actuator around x- and z-axis, which allow the accurate positioning of the sample dispenser with respect to the supporting structure. Such adjustment, along with that of the treaded rods of the load cells, is performed only once after the setup is assembled. The chosen electro-mechanical linear actuator (model ETH032, Parker Hannifin Corporation) has a total stroke of 412 mm, and is provided with an anti-rotation guide of the piston. Conversion of the digital signal from the setup PC to the controlled power supply of the motor of the linear actuator is carried out by a servo drive (model Compax3, Parker Hannifin Corporation), for closed-loop control. The actual position of the piston is provided by a rotary encoder which monitors the rotation of the motor. Both the displacement and the stroke rate of the piston are controlled parameters. This means that the motor speed (and thus the stroke rate of the piston) remains constant,

independently of the reaction force generated upon sample bending. The digital communication between PC and servo-positioning drive is controlled by the user via commands that can either define the values of displacement and stroke rate or start/stop the displacement.

The supporting structure and the samples dispenser are enclosed in a gas-tight work-tube (12) to allow for high temperature measurements under controlled atmosphere. The work-tube is made of steel and housed in a tubular furnace and in a cooled chamber (13) fixed on the mounting plate. The gas-tightness of the testing environment between the work-tube and the cooling chamber is achieved by a flange (14), which is welded to the lower extremity of the work-tube. The part of the work-tube outside the furnace is coated with thermal insulation to minimise heat losses. The setup is connected to N₂, forming gas (9% H₂ - 91% N₂) and H₂ gas lines to control the testing atmosphere. All gas flows are controlled by electronic mass flow controllers, installed between the laboratory gas network and the setup. The setup gas-inlet is placed on the cooled chamber to further help the cooling of the load cells. The work-tube is sealed at its upper extremity by a circular cap. A calibrated hole is drilled on this cap as exhaust for the hot gases while maintaining the testing atmosphere slightly under pressure.

The furnace and work-tube are fastened using a circular plate (15), which is welded on the work-tube. The cylindrical furnace installed on the SEP setup (model GVC-600, Carbolite GmbH) comprises three heating zones, to help keeping a uniform temperature along the heated length. Temperature control of the furnace is provided by a PID furnace controller (model Nanodac, Eurotherm - Schneider Electric).

Lifting of the furnace and work-tube allows the preparation of high temperature tests, i.e. the samples are placed one-by-one on the sample dispenser. Then, furnace and work-tube can be lowered until the work-tube flange enters in contact with the cooled chamber. If the test is carried out at RT, furnace and work-tube are typically maintained lifted for a visual control visual of the sample testing.

It consists of a steel frame fixed to both the furnace and the work-tube, by four steel wheels which allow the vertical displacement of both the furnace and work-tube (total weight of about 140 kg) on the two lifting guides. The lifting guides are then fixed at their extremities to the setup frame. At the opposite side of the wheels, plastic rolls are used to maintain the lifting system correctly in position with the guides. Furnace and work-tube are lifted by a manual winch (not shown in Figure 11), connected to the furnace lifting system by a metallic cable.

Because of the presence of hydrogen for testing under reducing atmosphere, the setup is placed under a gas-hood during testing. This placed a height constraint for the design of the SEP setup. Any shortening of the setup would have resulted in shorter sample dispenser, i.e. less tested samples per experiment. Therefore, the height of the SEP setup and thus the length of the components (linear actuator, sample dispenser, furnace and setup frame) were maximised to fit the GEM gas-hood (setup height of 2300 mm, 2900 mm with the furnace lifted, outside from the gas hood). Figure 11 shows the fabricated setup SEP installed in the laboratory.

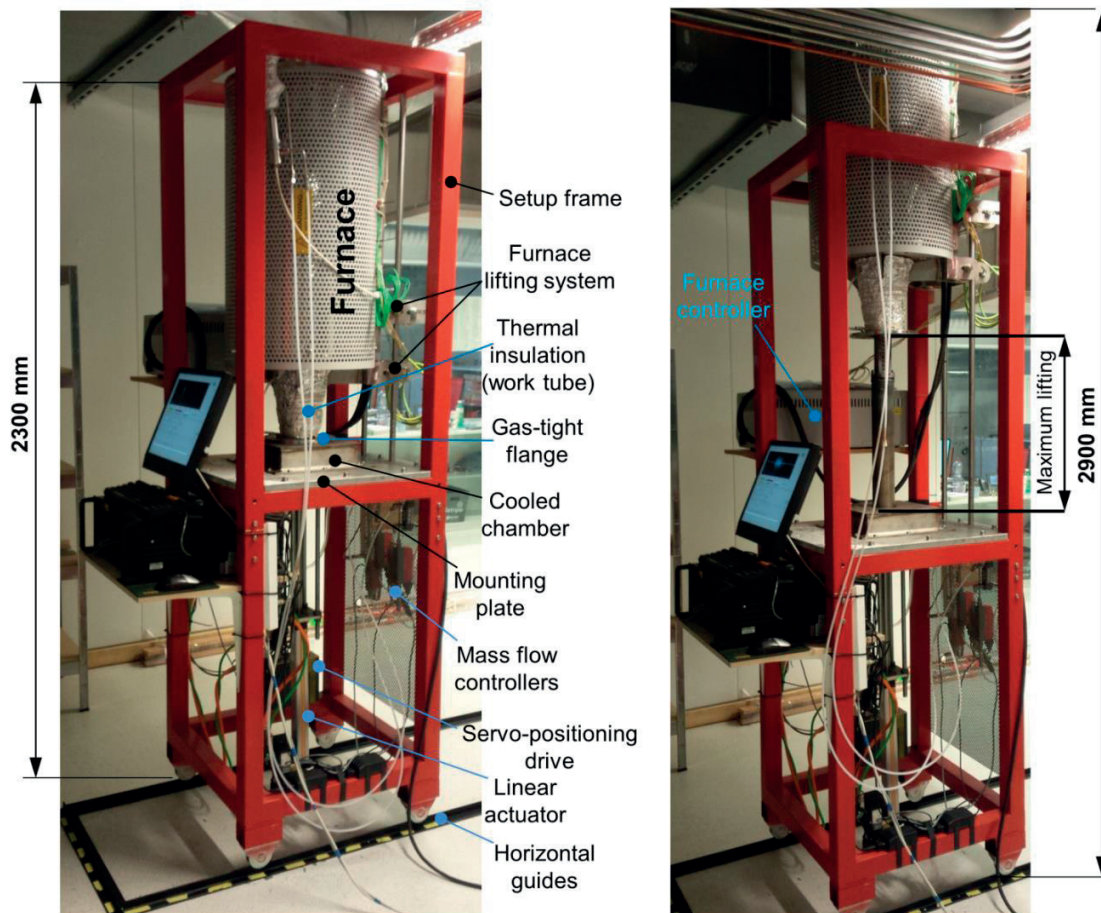


Figure 11: Overview of the SEP setup in the laboratory of GEM group (EPFL Valais-Wallis).

2.1.2.3 Creep setup

Creep testing over both the primary and the secondary regimes requires measurements of the sample deformation over prolonged periods. For example, about 100 h are expected for creep testing of Ni-YSZ (see Chapter 2.2). The creep setup design developed in this work includes four identical test slots, for testing at the same temperature but under different mechanical loads to increase the measurement throughput.

In the CRP setup, the dimensions of both the sample and of the four-point bending device are the same as in the SEP setup, i.e. the inner and outer rollers spans are equal to 25 mm (a) and 50 mm (L), respectively. Figure 12 provides a detailed scheme of the setup. The numbering in the following text refers to this figure. The outer rollers (1) are tightened to the outer rollers supports (2). The outer rollers span L of each test slot can be calibrated by screws (3). However, in all the creep tests carried out in this thesis, the same span of 50 mm as for the SEP setup is used. The outer rollers supports are

then tightened to five vertical plates (4), which are fixed with a base (5). This structure is then enclosed in a gas-tight steel box (13) and housed in a furnace (model TE10Q, Rohde GmbH).

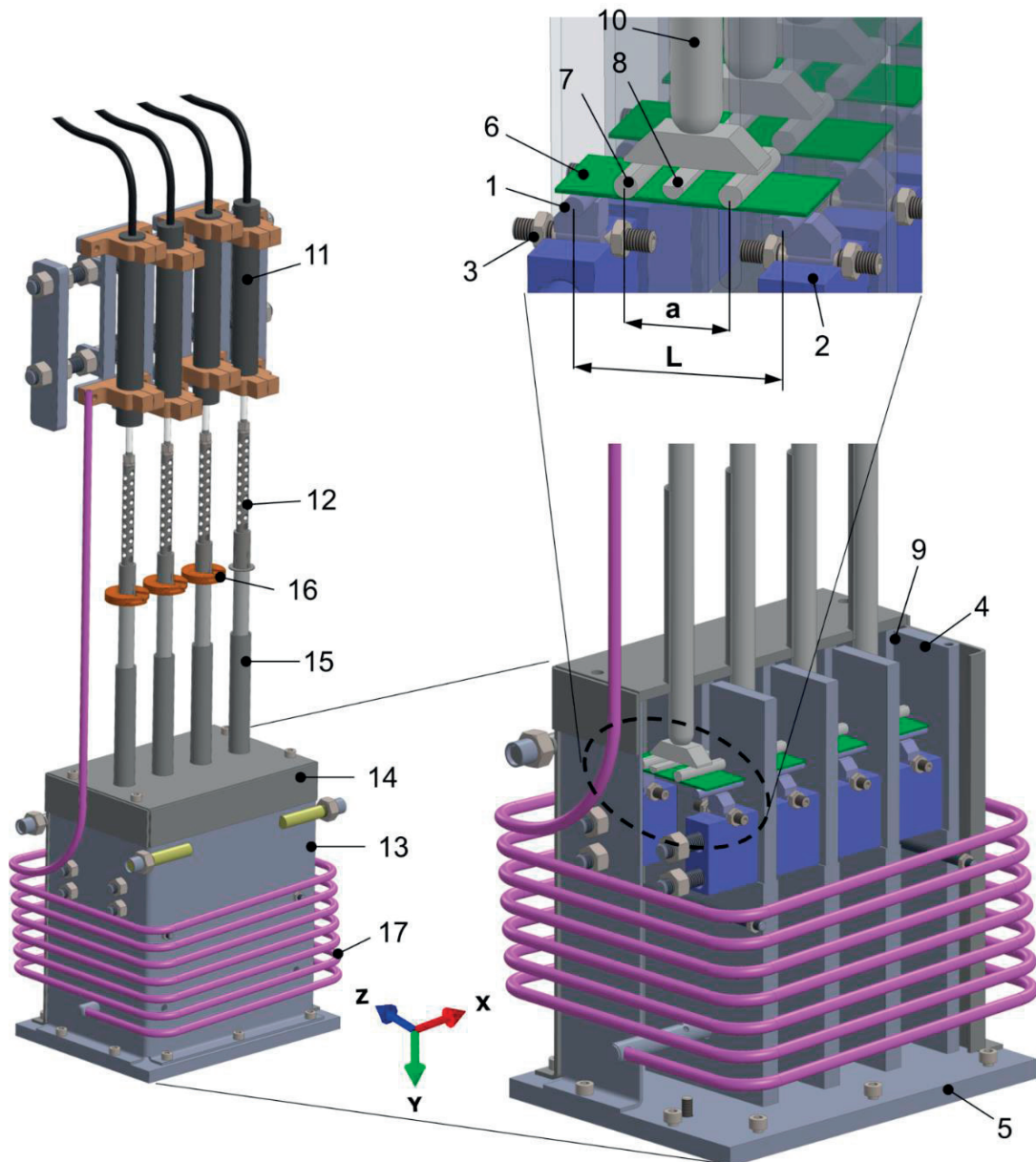


Figure 12: 3-D sketch of CRP setup and detailed views of the testing fixture.

At the beginning of a test, the sample (6) is placed on the outer rollers, but the inner rollers (7) are maintained lifted until the testing temperature is reached and, in the case of Ni-YSZ, the reduction is completed. Therefore, no mechanical load is applied on the four samples to avoid creep of the samples already during heat up, i.e. during thermal transients. Symmetric placement of the inner rollers with respect to the outer rollers is guaranteed by central rollers (8) which can slide in the grooves (9) of the

five vertical plates. The inner and central rollers of each of the four test slots are fixed to a ceramic rod (10). These ceramic rods are connected to the armature of the displacement transducers (11) by holed metallic rods (12). The use of holed rods reduces heat conduction from the testing environment (at high temperatures) to the displacement transducers, which must not be exposed to temperatures above 100 °C. They also serve as support for the additional weights (16), which are needed for testing the samples in the four test slots under different stress levels. The steel box is closed on the upper side with a lid (14). Four tubular guides (15) are welded on the lid, which house the ceramic rods. To avoid friction between the tubular guides and the ceramic rods, the clearance between their diameters is 2 mm. This relatively large clearance causes high gas leakages. Hence, in the case of testing under reducing atmosphere, the gas flow at the inlet of the setup must compensate for this leakage.

The displacement transducers installed on this setup (model ACT500C, RDP Electronics Ltd) use the linear variable differential transformer (LVDT) principle. An LVDT transducer is composed by a cylindrical frame, which contains three coils (a primary and two secondary), and a sliding rod, referred to as armature. The relative displacement between the magnetic core of the armature and the coils generates a transfer of current between the primary and secondary coils. Since the two secondary coils are connected in opposition, the resulting output voltage is zero when the armature is at the centre of the measurement stroke of the LVDT. Upon displacement of the armature caused here by the deformation of the sample the voltage increases in one secondary coil and decreases in the other one. The comparison between excitation and output phases by a signal amplifier enables the determination of the displacement direction. Over a specific displacement range of the armature, the output voltage processed by the LVDT signal amplifiers varies linearly from -14 to 14 V. Outside the range of displacement, the LVDT signal saturates, i.e. the output voltage remains essentially constant upon displacement. Hence, each of the four LVDTs was calibrated manually such that the measurement accuracy is optimal within an expected range of sample deformations of up to 10 mm. The calibration was carried out by clamping coaxially the LVDT and a depth micrometre on a fixed structure, with the rods of both the micrometre and of the LVDT maintained constantly in contact. Hence, calibration is carried out by modifying the amplification of the LVDT signal amplifiers, such that a displacement of the inner rollers of 10 mm causes a variation of the voltage between -14 and 14 V, i.e. a conversion ratio of $28 \text{ V} / 10 \text{ mm} = 2.8 \text{ V/mm}$ to determine the displacement at the inner rollers.

The LVDTs are fixed on the setup frame by mounting blocks. The position of the mounting blocks and thus of the LVDTs can be adjusted along the x- and z-axis by threaded rods. To avoid deleterious overheating of the LVDTs transducers because of heat convection from the furnace, two fans are installed in front of them. For testing in reducing atmosphere, forming gas (9% H₂ - 91% N₂) is used. The gas at the inlet of the steel box is heated up by a heating coil (17). Figure 13 provides a close-up view of the CRP setup.

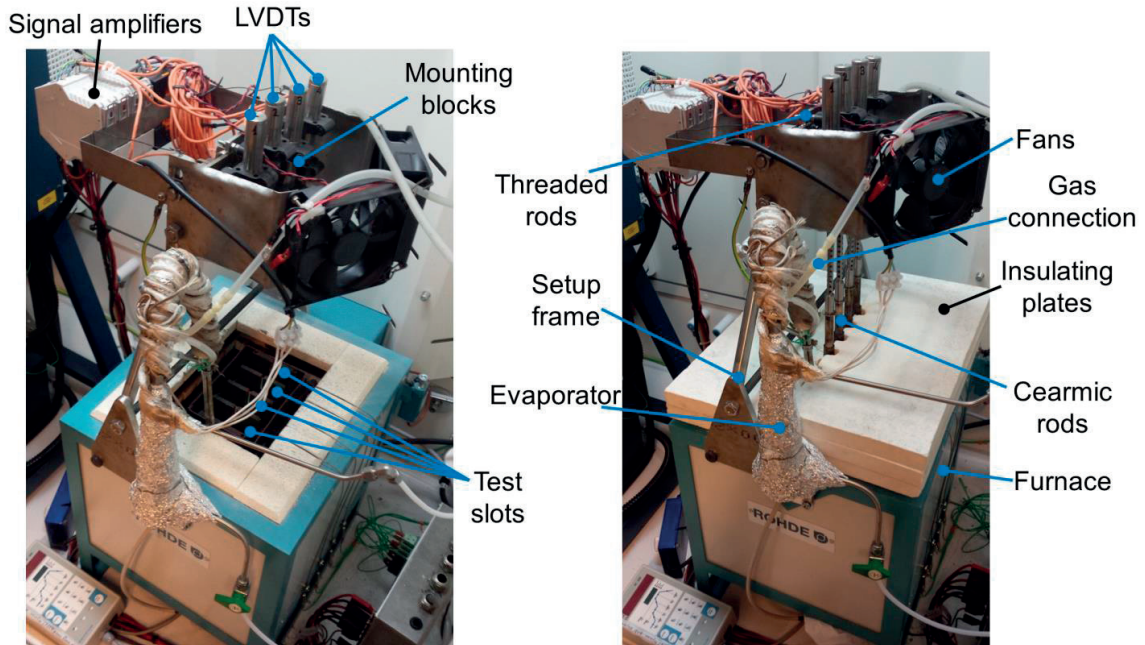


Figure 13: Overview of the CRP setup in the laboratory of GEM group (EPFL Valais-Wallis).

2.1.3 Experimental validation of the SEP and CRP setups

The SEP and CRP setups are validated by comparison between simulations with the 4-point bending FEM model (description in Paragraph 2.1.1) and measurements using materials for which several literature studies and/or datasheets on the mechanical properties are available. Crofer 22 APU was selected for the present validation. Crofer 22 APU samples with planar dimensions of 60x25 mm and a thickness of 300 μm were prepared and tested. Table 5 lists the considered properties of Crofer 22 APU, which are implemented in the FEM model.

Table 5: Elastic and creep properties of Crofer 22 APU from the literature (Ref. [103,104], tensile testing).

	Elastic properties [103]		Creep parameters [104]	
	E_m (GPa)	ν (-)	A ($\text{h}^{-1}\text{MPa}^{-n}$)	n (-)
RT	216.0	0.3	-	-
800 °C	65.9	0.3	2.30e-11	4.73

In the case of the SEP setup, the comparison between the predictions of the FEM model and experimental data is for the reaction force at the outer rollers as a function of the displacement at the inner rollers. The samples are assumed to deform within the elastic regime. The applied displacement at the inner rollers is 1.4 mm in both the experiments (displacement rate of 0.3 mm/s) and simulations. During the experiment, the effects of friction between the sample and the rollers was minimised by lubricants and frictionless contact was considered for the FEM model. The comparison between the experiments and simulation results are shown in Figure 14.

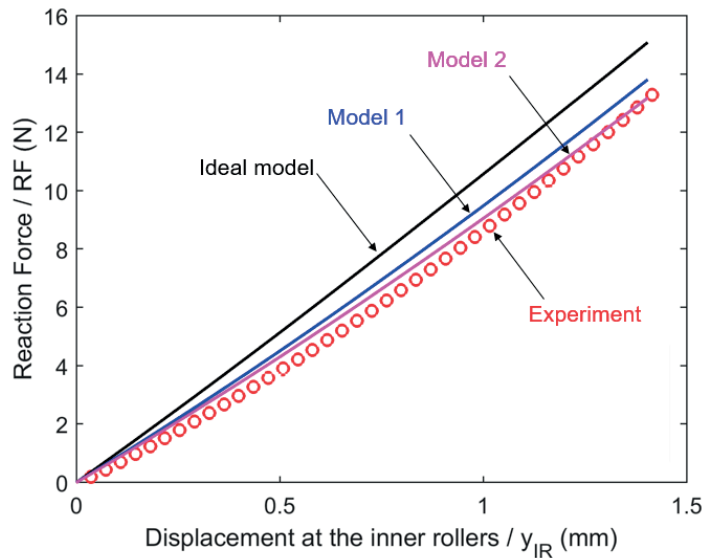


Figure 14: Reaction force versus displacement at the inner rollers measured experimentally (red circles) and simulated by the FEM model of the sample (continuous lines).

The simulation of the experiment following the approach described in Paragraph 2.1.1 and here referred to as “Ideal Model” does not predict accurately the experimental data, with an error on the reaction force of about 12%. The sources of error in the “Ideal Model” come from the assumption that i) for each pair of inner and outer rollers, the contact pressure with the sample is the same, ii) the sample is initially flat and iii) upon sample deformation, the inner rollers are allowed to move only along the y-axis. These conditions may not be met in practice, because of the effect of i) position tolerances between the inner and outer rollers, ii) initial wavy/bent samples and iii) the compliance of both the piston and the connecting rod of the SEP setup, which may bend during the sample deformation because of asymmetric reaction forces on the rollers (because of e.g. position tolerances of the rollers and/or pre-deformed samples).

The FEM model of the sample described in Paragraph 2.1.1 is modified to simulate the situation where the sample is initially not in contact with the left inner roller by an arbitrary clearance of 0.5 mm (Figure 15) and during bending the inner rollers translate along the x-axis (towards the left direction) by 0.6 mm (value estimated by visual observation of the bending of the connecting rod). This bending is caused by the component of the reaction force on the inner rollers along the x-direction, which is higher on the right inner roller. Oppositely to the “Ideal Model”, in the modified case only the symmetry along the z-axis is maintained. This modified model is referred to as “Model 1” and provides better agreement with the experimental data (Figure 14). The discrepancy between the model predictions and the measurements is now of about 5%. A last variation is considered. “Model 2” is the same as “Model 1” but a lower elastic modulus of 210 GPa is considered, instead of 220 GPa. The mismatch with the experiment is further reduced and of about 7% in the middle range of deformations.

Part of the remaining deviations between experimental and simulated data is ascribed to sample pre-deformation and variation of the sample thickness, which are not considered in the FEM models.

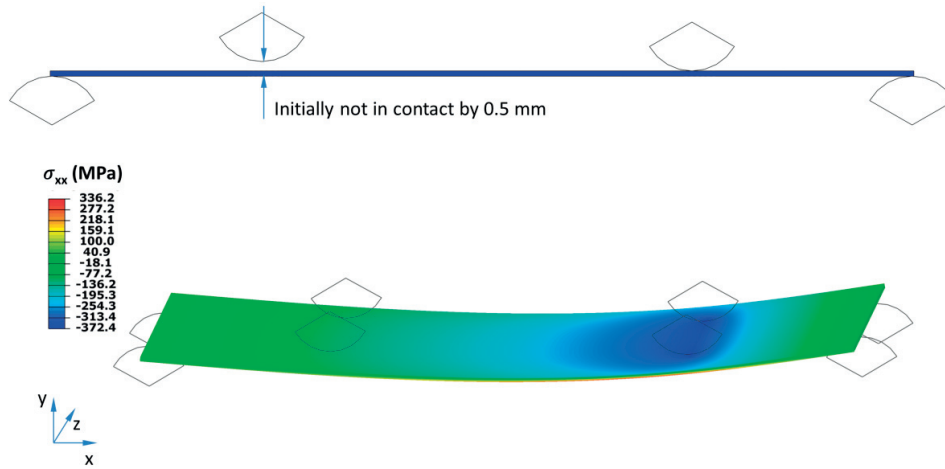


Figure 15: View of the simulated model with the left inner roller initially not in contact, and stress component along the x-direction upon bending.

In the case of the CRP setup validation, the comparison between the FEM model predictions and experimental data is performed for the displacement at the inner rollers as a function of time. Figure 16 shows the experimental results of the creep testing on the Crofer 22 APU samples at four load levels of 0.90, 1.04, 1.18 and 1.32 N. The tests were performed with the CRP setup described in Paragraph 2.1.2. The testing conditions were 800 °C and air and lubricant was not applied on the rollers.

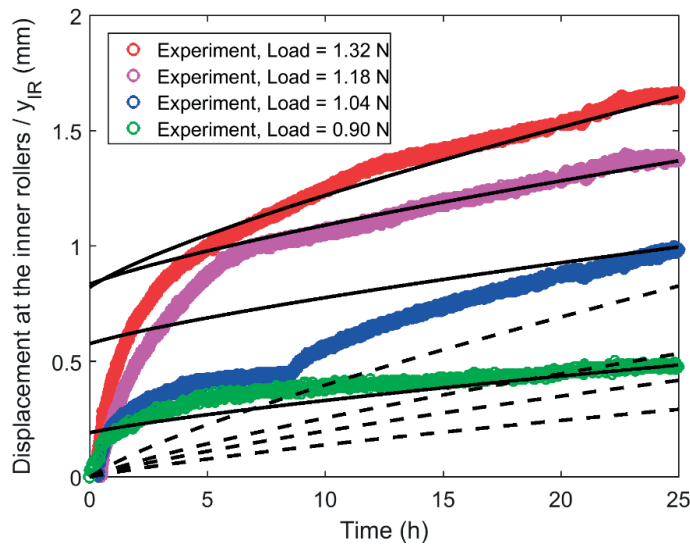


Figure 16: Displacement at the inner rollers over time during creep deformation measured experimentally (red, magenta, blue and green points) and simulated by the FEM model of the sample (black lines). The dashed lines correspond to the direct results of the simulation. The continuous lines depict the simulation data result but shifted onto the experimental curves for direct visual comparison.

The effects of primary creep of the material combined with the stress redistribution in the sample because of creep lead to a transient regime, from the beginning of the creep deformation until approximately 12 h. This regime is followed by a nearly constant displacement over time slope, which corresponds to the creep deformation caused by the secondary regime. The irregular experimental curve at the load of 1.04 N is assumed due to partial sticking between sample and rollers. The duration of the experiments was of 25 h.

The FEM model of the sample described in Paragraph 2.1.1 is used to simulate the creep deformation under the same four loads used in the experiments and elastic and creep properties for Crofer 22 APU listed in Table 5. Since the available creep parameters are valid only for the secondary regime, the comparison between the experimental and simulated data is performed by shifting of the simulated curves onto the value of the experimental displacement at 25 h. This allows the comparison only of the secondary regime, between experiments and simulations. The creep bending rates between 20 h and 25 h are listed in Table 6.

Table 6: Computed creep bending rates (in mm/h) from experimental and simulation data.

	Experiment	Simulation	error %
0.90 N	0.0038	0.0097	60
1.04 N	0.0254	0.0138	45
1.18 N	0.0140	0.0176	20
1.32 N	0.0237	0.0268	11

The error between the two data-sets is higher for lower loads. The potential reason is that for lower loads, the stress stabilisation requires more time than at higher loads, because of the dependence of the creep strain rate upon the stress. Furthermore, since the bending in the experiments is larger than that in the simulations (because of primary creep), and since in large bending the behaviour deviates from linearity, direct comparison between experimental and simulation results is not fully rigorous, and may affect the mismatch between the two data-sets.

2.2 Estimation of the mechanical properties of Ni-YSZ anode

Non-negligible errors can arise in the estimation of the elastic or creep properties using closed-form analytical solutions derived from the Euler-Bernoulli beam bending theory (see Chapter 2.1 and [105,106]). The applicability of such a simplified approach requires several conditions. The creep strain rate must have reached a steady-state regime, also referred to as secondary creep, and the stress state in the sample remains constant upon creep deformation. The deformation of the sample must also comply with the assumptions of the Euler-Bernoulli beam bending theory. The contribution of primary creep to the total creep deformation of the SOFC anode as well as the accuracy of the estimated elastic properties are expected relevant for the prediction of mechanical failures in SOFC stacks. However, non-linearity because of primary and secondary creep and of deviations of the actual bending behaviour from that predicted by the linear beam theory do not allow to estimate the mechanical properties directly from post-processing of the experimental data by analytical solutions. Most of these sources of material and geometrical non-linearity can be investigated with a finite-element method (FEM) model, but because of the model runtime, among others, the development of dedicated procedures are required for integrating such level of detail within the parameter estimation workflow. This section presents the methodology as well as the application to the experimental results from Chapter 2.1 developed in this thesis to improve the accuracy and flexibility in terms of constitutive laws for the accurate measurement of the elastic and creep properties of SOFC materials by macro-scale mechanical testing.

2.2.1 Samples for 4-point bending tests

The samples for the investigation of the mechanical properties by 4-point bending were made of NiO-YSZ and Ni-YSZ cermets, used for both the functional and supporting layers in the SOLIDpower anode-supported cells (Mezzolombardo, Italy). They were produced from the same raw materials and by the same procedures as the commercial cells, except for the co-casting of the electrolyte. The dimensions of the tested samples were 60x25 mm. The thickness of each tested sample was measured on four random points between the two inner rollers (i.e. the central region of the sample, dimensions 25x25 mm) and on two random points at each side of sample, between the inner and outer rollers. Samples exhibiting excessive waviness and/or large variability in thickness were rejected.

Subsets of the supplied batch were used for the measurement of the elastic properties (Paragraph 2.2.3) and of the strength (Chapter 2.3). A set of 14 NiO-YSZ samples was used for the elastic properties. 13 out of the 14 samples were reduced at 800 °C to obtain Ni-YSZ samples. The dimensions of the tested samples were 60x25 mm, with an average thickness of 270 µm.

The mean thickness over the whole batch of samples for the strength testing was equal to 261 μm . Part of Ni-YSZ samples were obtained by reduction at 800 $^{\circ}\text{C}$. To test the strength of the YSZ skeleton (referred to as (Ni)-YSZ), the Ni phase of 50 Ni-YSZ samples was removed by dissolution in HNO_3 . This chapter is limited to the description of the samples. Details on the testing conditions for the measurement of the elastic properties, strength measurements and 3-D imaging are provided in Chapters 2.2.3, 2.3, 2.4.1.

2.2.2 Parameter estimation

Parameters estimation is based on an optimisation algorithm for minimising the discrepancy between the experimental data and model predictions. In this thesis, a numerical workflow for parameters estimation was developed based on the FEM model of the tested sample presented in Paragraph 2.1.1 and the experimental data obtained with the two setups and measurement procedures described in Paragraph 2.1.2. The same workflow structure is used for the measurement of the elastic and creep (details provided in Chapters 2.2.3 and 2.2.4, respectively) properties, only the exchanged model parameters and responses differ. Table 7 provides the overview of the parameters of interest that are estimated from the analyses, along with the materials and conditions of reference.

Table 7: Overview of the estimated parameters, materials and reference conditions for the elastic and creep properties studies.

Case study	Material	Temperature	Estimated parameters
Elastic properties (controlled displacement) ELF	NiO-YSZ	RT	<ul style="list-style-type: none"> ➤ Elastic modulus, E_m ➤ Coefficient of friction sample/rollers, μ
		800 $^{\circ}\text{C}$	
	Ni-YSZ	RT	
		700 $^{\circ}\text{C}$	
		750 $^{\circ}\text{C}$	
		800 $^{\circ}\text{C}$	
Creep properties (constant load) CRP	Ni-YSZ	700-800 $^{\circ}\text{C}$	<ul style="list-style-type: none"> ➤ Creep pre-exponential constant, B ➤ Creep activation energy, Q ➤ Stress exponent, n ➤ Primary creep exponent, m

The developed workflow is validated for both the estimation of the elastic and creep properties (hereafter referred to as “ELF” and “CRP”), using numerical experiments with the FEM model with predefined (known) values of the set of parameters listed in Table 7. Once validated, the workflow was applied to real experimental data, to estimate the mechanical properties of the NiO/Ni-YSZ anode cermet (Paragraph 2.2.3 and 2.2.4).

The developed workflow for parameter estimation consists of the following main steps, which are described in detail in the next sections:

1. Sensitivity analysis
2. Generation of distributed meta-models
3. Optimisation based on distributed meta-models

2.2.2.1 Sensitivity analysis

A sensitivity analysis is first performed to quantify how variations in the design variables impact the model response [107]. The following description uses design and design variables, as approximately equivalent terms to e.g. sample and parameters and signals as response or model output. Correlations between the design variables are identified and quantified, and used as pre-processing information for the optimisation task. In the present sensitivity analysis, the scanning of the space of the design variables follows sampling determined by a design of experiment (DoE). The computed responses for each design consist of one or several “signals” that are then used to assess for the statistical analysis and, as it will be explained later, to generate meta-models.

Table 8: Design variables, models and computed signals in the sensitivity analysis of the ELF and CRP parameter estimations

Workflow	Sensitivity analysis		
mode	Design variables	FEM models	Signals
ELF	<ul style="list-style-type: none"> ➤ Elastic modulus, E_m ➤ Coefficient of friction sample/rollers, μ ➤ Sample thickness, h_s 	ElaDispl	<ul style="list-style-type: none"> <i>Loading</i> <i>Unloading</i> <i>Delta</i>
CRP	<ul style="list-style-type: none"> ➤ Sample thickness, h_s ➤ Elastic modulus, E_m ➤ Coefficient of friction sample/rollers, μ ➤ Creep rate constant, A ➤ Stress exponent, n ➤ Primary creep exponent, m 	<ul style="list-style-type: none"> <li style="border-bottom: 1px solid black;">CrpLoad01 <li style="border-bottom: 1px solid black;">CrpLoad02 <li style="border-bottom: 1px solid black;">CrpLoad03 CrpLoad04 	<ul style="list-style-type: none"> <i>Load01</i> <i>Load02</i> <i>Load03</i> <i>Load04</i>

The workflow is implemented in the software OptiSLang (Dynardo GmbH), a platform for sensitivity analysis and optimisation, with calls to MatLab and FEM or finite-difference codes Abaqus and gPROMS. The DoE is first performed in OptiSLang following a prescribed sampling method. The computation of each design is controlled by a Matlab routine, which (i) implements in the model the variations of the design variables prescribed by the sensitivity analysis, (ii) execute the simulation run and (iii) post-process the simulation results to generate the signals, directly or by retrieving first the required simulation results.

There is no a-priori guarantee that the numerical non-linear simulations will converge over the complete range of design variables, which may require revision of the problem formulation. A first step

in assessing the quality of the sensitivity analysis results is to verify that the converged designs are distributed with sufficient uniformity over the entire space of the design variables. In OptiSLang, plots of the probability density function and of the 2-D scatter are used for visual inspection, whereas linear or extended correlations between the design variables indicate how the variation of the i^{th} design variable affects the remaining $n-1$ design variables. Values of linear correlation close to 1 and -1 denote respectively direct and inverse relation of proportionality.

2.2.2.2 Meta-modelling

Depending upon the nature of the selected optimisation algorithm used for the parameter estimation, a relatively large number of iterations and/or demanding computation of often locally-valid sensitivity matrix is needed. As a result, the parameter estimation runtime can rapidly grow and the problem become intractable, depending upon the complexity of the FEM simulations and interactions between the design parameters. An alternative is to perform the optimisation with a meta-model of the signals generated from the responses of the simulations performed in the sensitivity analysis. This optimisation approach is faster and requires lower computational resources. A meta-model allows the computation of the signals and design variables by simpler mathematical relationships.

The meta-modelling capability of the software OptiSLang is used in the present study. Meta-modelling is performed by the Meta-model of Optimal Prognosis (MOP®). In OptiSLang, MOPs can be generated following different mathematical approaches. Those available in OptiSLang and used in the development of the workflow are polynomial least squares (PLS), moving least squares (MLS) or Kriging. In the case of polynomial least squares, the approximation function is:

$$y(x) = [y_1 \ y_2 \ \dots \ y_m]^T = P^T(x)\hat{\beta} + \varepsilon \approx \hat{y}(x) = p^T(x)\hat{\beta} \quad (17)$$

where $y(x)$ are the values at m support points, $\hat{y}(x)$ their approximated values, ε the approximation errors over all the support points m , whereas $p^T(x)$ is the global polynomial basis, which is defined as:

$$p^T(x) = [1 \ x_1 \ x_2 \ \dots \ x_1^2 x_2^2 \ \dots \ x_1 x_2 \ \dots] \quad (18)$$

P is the polynomials base computed over each support point m :

$$P = [p(x_1) \ p(x_2) \ \dots \ p(x_m)] \quad (19)$$

The coefficients $\hat{\beta}$ must be determined. They are global coefficients, i.e. their values are the same for all the support points. Once the polynomial basis p is established and P is computed, the coefficients $\hat{\beta}$ are calculated by least squares:

$$\hat{\beta} = (PP^T)^{-1}Py \quad (20)$$

In moving least squares (MLS), the approximation function is defined as:

$$y(x) \approx \hat{y}(x) = p^T(x)a(x) \quad (21)$$

where $a(x)$ are “moving” coefficients, which in contrast to the coefficients $\hat{\beta}$ of the polynomial least squares, can differ for each support point. The advantage of MLS method over polynomial least squares

is a better ability to represent arbitrary complex non-linear functions, though still continuous, and convergence to the exact solution if the number of support points increases [108]. Moving Least Squares (MLS) and Kriging methods are used in the present study for the meta-model generation, instead of polynomials for better accuracy and flexibility.

A model independent measure of the MOP quality is required and formulated as the Coefficient of Prognosis (CoP[®]) [107,108]. The total CoP (CoP_{Total}) is:

$$CoP_{Total} = 1 - \frac{SS_E^{Prediction}}{SS_T} = 1 - \frac{\sum_{i=1}^N (y_i - \hat{y}_i)^2}{\sum_{i=1}^N (y_i - \mu_Y)^2} \quad (22)$$

where N is the number of support points used in the MOP, y_i and \hat{y}_i are respectively the response value at the support point and the meta-model approximation, whereas μ_Y is the mean over all the support points. The support points are split into two subsets, one for the generation of the meta-model and another for the computation of the error $y_i - \hat{y}_i$. The CoP_{Total} ranges from 0% to 100%, indicating respectively poor and good quality. In practice and as rule of thumb, MOPs with a CoP_{Total} higher than 90% are needed for sufficient accuracy during the optimisation. The total effect sensitivity index of the i^{th} design variable is defined as:

$$S_{T_i} = 1 - \frac{V(Y|X_{\sim i})}{V(Y)} \quad (23)$$

where $V(Y)$ and $V(Y|X_{\sim i})$ are respectively the unconditional variance of the model output and the variance of Y caused by all the model inputs without X_i [109]. Multiplication of CoP_{Total} by the total effect sensitivity index of the i^{th} design variable provides the variance contribution of a single design variable CoP_i :

$$CoP_i = CoP_{Total} \cdot S_{T_i}^{MOP}(X_i) \quad (24)$$

The CoP_i quantifies the separate effect of the i^{th} design variable on the generated MOP. This parameter is used by OptiSLang to identify the design variables of lower importance (i.e. those ones giving a relatively low CoP_i), which can be excluded. This analysis therefore provides knowledge on the effects, which allows the simplification of problems involving a large number of design variables to lower the computation time, among others.

In prevision of the formulation of an objective function for parameter estimation, an intuitive approach consists in generating the MOP of the Euclidian norm of the difference between experimental and simulated loading curve, which is then minimised:

$$\min \left[\sqrt{\sum_{i=1}^{NX} (y_{exp} - y_{FEM})_i^2} \right] \quad (25)$$

y_{exp} and y_{FEM} are respectively the experimental and FEM computed values of the tested sample at n common discrete values. This standard objective function and model formulation proved inadequate for the measurement of both the elastic (ELF) and creep (CRP) properties. It did not pass the first

validation tests. The reason is the presence of local minima and inaccuracy in the MOP, which result in unreliable search of the global minimum. The issue could practically be overcome by formulation of the MOP using random fields. Figure 17 illustrates the random fields modelling principle.

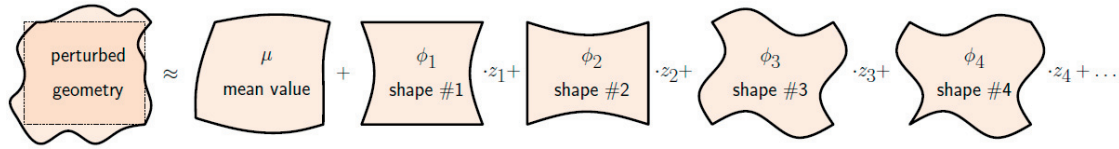


Figure 17: Representation of the perturbed geometry as a combination of shapes and amplitudes^f.

Random fields are built upon the mean μ , the array of shape functions and the corresponding array of amplitudes. The formulation of random fields proceeds as follows:

$$RF = \mu + \sum_{i=1}^n z_i \phi_i = \mu + \sum_{i=1}^n [z_1 \ \dots \ z_n] \begin{bmatrix} \phi_1 \\ \vdots \\ \phi_n \end{bmatrix} \quad (26)$$

The decomposition of a set of arbitrarily different perturbed geometries by random fields is performed by computing μ , and the summation of n shape functions ϕ , (identical for all the perturbed geometries), modulated by the corresponding amplitudes z , specific to each perturbed geometry. In the developed workflow, the random fields are computed by Statistics on Structures (Dynardo GmbH), hereafter referred to as SoS, a software for the post-processing of statistical data, which evaluates and simulates random effects. In a first step, SoS acquires the signals from the sensitivity analysis. Each group of signals is then modelled by a specific F-MOP (Field Meta-model of Optimal Prognosis) using random fields. Each F-MOP is composed by a number of MOPs that corresponds to the number of shape functions for the signals that is modelled. The number of shapes is chosen automatically by SoS to meet a desired quality of the meta-model. Afterwards, the individual MOPs are generated by computing the amplitudes as function of the design variables.

Once the meta-models are generated, the optimization task can start. It calls the generated F-MOPs instead of the FEM solver. For each iteration of the selected optimisation algorithm (y_{lte} refers to the response with the set of design variable at the iteration):

1. A set of values of the design variables determined by the optimisation algorithm is implemented in the F-MOP to compute the amplitude for the corresponding shape function.
2. Using the mean value determined by the random field simulation, the shape functions and the corresponding amplitude obtained from step 1, the random field computation (run by SoS) generates x - y_{lte} data. The abscissa x (of dimension N_X) between x - y_{lte} data and those used as experimental values in the optimisation x - y_{Exp} must be identical.

^f Reprinted with permission from Dynardo Austria GmbH

3. The objective of the optimisation is assessed over all the signals NS and then over all the simulated models NM:

$$\min_{\theta} \left\{ \sum_{k=1}^{NM} \left[\sum_{j=1}^{NS} \left(\sum_{i=1}^{NX} (y_{Ite,i} - y_{Exp,i})^2 \right) \right] \right\} \quad (27)$$

where θ is the set of parameters to estimate. In the workflow developed in this work, the optimisation processes run on the F-MOPs in either ELF or CRP mode requires only a few minutes on a desktop computer.

2.2.3 Estimation of the elastic modulus and coefficient of friction

2.2.3.1 Experimental data

For the ELF case, the experimental dataset consists of the reaction force measured on the outer rollers and generated by applying a constant rate displacement at the inner rollers in contact with the NiO/Ni-YSZ sample. In a first step, the constant rate displacement bends the sample, and consequently the reaction force increases as the sample deforms. Afterwards, the constant rate displacement at the inner rollers is applied in the opposite direction, i.e. the sample is unloaded and thus the reaction force progressively decreases up to the initial value. During both loading and unloading, the displacement rate is 0.3 mm/s. For the high temperature tests, the heat-up rate is 100 °C/h, either under reducing or oxidising atmosphere. Respectively, forming gas (N₂:90% - H₂:10%) with a flow rate of 5 l/min or natural convection is used for the two testing conditions. For each testing condition and material, five measurements (i.e. five sequences of loading followed by unloading) are performed for verifying the reproducibility. The reaction force for both loading and unloading is found to increase slightly over the five measurements (by about 0.5% per loading-unloading cycle), supposedly because the relative sliding between sample and rollers tends to remove the grease from the contact interface.

Each sample is tested sequentially at all the testing temperatures listed in Table 7 to measure the variation of the elastic modulus upon temperature. The conditions during elastic bending testing on the NiO-YSZ and Ni-YSZ samples and the measured reaction force for the displacements prescribed at the inner rollers for each experiment are provided in Figure 18. The experimental dataset shown in Figure 18 is used to estimate the elastic modulus E_m and the coefficient of friction μ . The thickness of the sample (treated as a design variable in the sensitivity analysis) is here left constant and assigned the average measured value (see Figure 18).

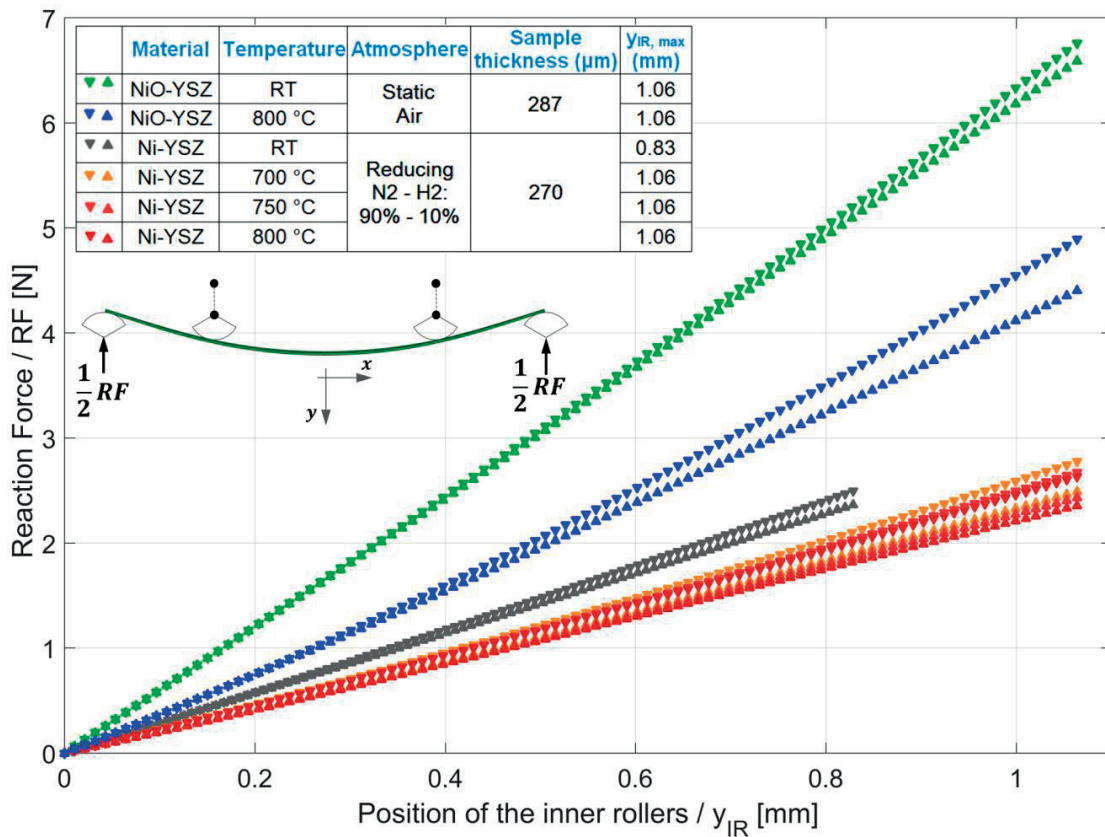


Figure 18: Reaction force measured on the outer rollers versus position of the inner rollers during bending test of NiO-YSZ and Ni-YSZ samples at RT and high temperature conditions. Downwards and upwards triangle symbols depict respectively loading (i.e. downwards displacement of the inner rollers) and unloading (i.e. upwards displacement of the inner rollers) curve.

2.2.3.2 Specific workflow description

For the estimation of the elastic properties (ELF), each design in the sensitivity analysis is simulated with the following sequence in the FEM model, which mirrors the experiments (Paragraph 2.1.1):

1. Starting with the undeformed sample (point 0, in Figure 19), a displacement is applied at the inner rollers at a constant rate, which deforms the sample elastically (from point 0 to 1a, in Figure 19). The position of the inner rollers versus reaction force corresponds to the signal "Loading".
2. Afterwards, the constant-rate displacement at the inner rollers is applied in the opposite direction. This induces a sudden drop (from 1a to 1b in Figure 19) followed by the progressive decrease of the reaction force (from 1b to 0). Since the simulated deformation is elastic, the sample returns at the end to the undeformed configuration (i.e. point 0). The signal "Unloading" is the simulated position of the inner rollers versus the reaction force from point 1b to 0.

The difference between signals “Loading” and “Unloading” yields the signal “Delta”, which is required to obtain a unique solution from the parameters estimation process, as discussed later in this section. The area 0-1a-1b-0 is equivalent to the energy dissipated by the friction between the sample and the rollers. In the FEM models of this study, the coefficient of friction is assumed independent of the sample deformation.

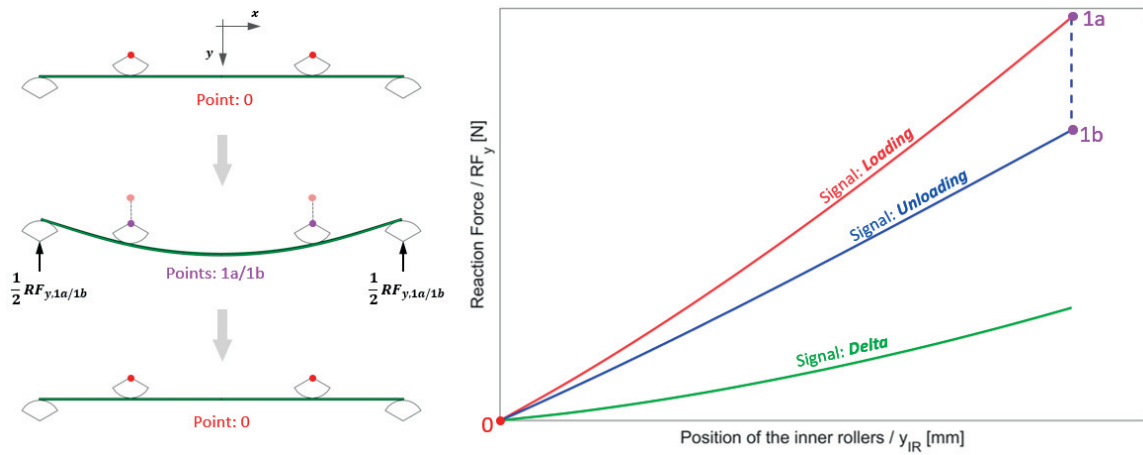


Figure 19: Simulated elastic bending (loading, from point 0 to 1a, followed by unloading, from 1b to 0) of the 3D FEM model of Paragraph 2.1.1 , with friction between the sample and the rollers. The deformation-reaction force plot (on the right hand side) depicts the three signals extracted from the output of the models.

A single global sensitivity analysis is performed covering all the variations in experimental testing conditions and expected sample properties. The range of design variable values must be therefore sufficiently wide:

- The elastic modulus E_m of Ni-YSZ reported in the literature, varies from 38 GPa (at 800°C, in reduced state) to 210 GPa (at RT, in oxidised state) [15]. Since the parameter estimation is carried out on experimental data of both oxidised and reduced state, and at both RT and HT, the selected range of the design variable E_m is [30,250] GPa.
- Mechanical tests at RT show that the loading and unloading curves are fairly close if grease is applied between the sample and the rollers, indicating that friction at the interface is limited. High temperature (e.g. 700-800 °C) however induces drying of the grease, which is expected to result in an increase of friction. Variations of the friction coefficient between the sample and rollers between 0 (i.e. frictionless) to 1 are therefore considered in the sensitivity analysis.
- The thickness of the sample, h_s , is varied between 210 and 300 μm , which exceeds the range measured on the batch of samples delivered for testing.

2.2.3.3 Numerical validation

The workflow is tested using two sampling methods, either the Full Factorial (FF) or Advanced Latin Hypercube Sampling (ALHS), to verify that the sensitivity analysis is not significantly influenced by how the space of the design variables is scanned. This verification is carried out only for the elastic bending case. The ALHS case comprises 300 designs. In the full factorial case, the closest number of designs is achieved with 7 levels, i.e. $7^3 = 343$ designs because there are three design variables (hs , E_m and μ). The purpose is not a discussion of the performance of the sampling methods, but a verification of the behaviour of the developed workflow. The validation test is passed regardless of the sampling method, i.e. the set of estimated parameter values (with the procedure explained later in this paragraph) corresponds with sufficient accuracy to that imposed in the computer-generated experiment. This test suggests that the workflow developed here is not strongly affected by the choice of a sampling method in the ELF case. All the results presented hereafter were obtained using ALHS and 300 designs.

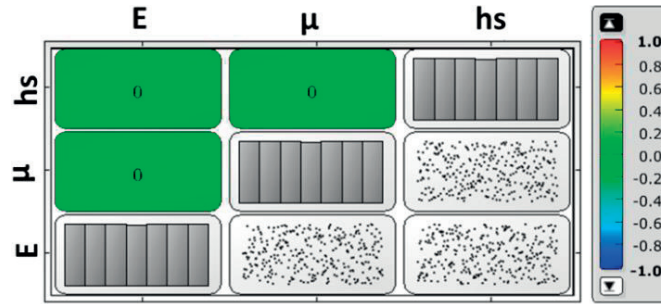


Figure 20: Extended correlation matrix of the sensitivity analysis for the ELF mode.

The extended correlation matrix for the case of elastic bending is depicted in Figure 20. There is no linear correlation between the three design variables. However, quadratic correlations may not be excluded. The probability density function of all the three design variables (plots on the diagonal) are close to uniform, and unpopulated regions are not observed in the 2-D Anthill plots, which suggests that the DoE and simulation execution is adequate.

Table 9: F-MOPs and components of the random field simulations for the parameters estimation mode ELF.

F-MOP	RF simulation (i^{th} design)	Shape functions implemented	Best MOP approach
Loading	$\mu_{\text{Loading}} + z_{1,\text{Loading}}^i \phi_{1,\text{Loading}}$	$\phi_{1,\text{Loading}}$	MLS
Unloading	$\mu_{\text{Unloading}} + z_{1,\text{Unloading}}^i \phi_{1,\text{Unloading}}$	$\phi_{1,\text{Unloading}}$	MLS
Delta	$\mu_{\text{Delta}} + z_{1,\text{Delta}}^i \phi_{1,\text{Delta}}$	$\phi_{1,\text{Delta}}$	MLS

Table 9 shows the outcome of the post-processing by SoS of the three signal types (i.e. Loading, Unloading and Delta) for all the simulated designs to generate the random fields components and thus process the corresponding F-MOPs.

The CoP matrices of the three F-MOPs (F-MOP_{Loading}, F-MOP_{Unloading} and F-MOP_{Delta}) are depicted in Figure 21. The first three columns provide the CoP_i values relative to each design variable, whereas the last column shows the CoP_{Total}.

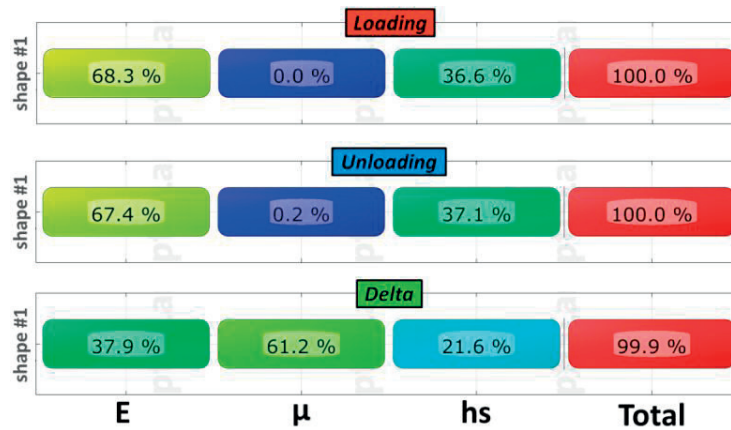


Figure 21: COP matrices of the three F-MOPs of the workflow for parameters estimation in ELF mode.

The CoP_{Total} of the three F-MOPs all reach 100%, which indicate that a meta-model of high quality could be generated. As expected, the variation of the elastic modulus E_m within the values range defined in the sensitivity analysis has the dominant effect on the response of the F-MOP_{Loading} and F-MOP_{Unloading}, since the CoP _{E_m} are about 68%. The effect of the sample thickness h_s within the range of prescribed values comes next and remains significant (i.e. CoP _{h_s} of about 37%). However, in both F-MOPs the coefficient of friction has practically no effect. Figure 22 shows the MOPs of the F-MOP_{Loading} (the MOPs of F-MOP_{Unloading} are not provided because similar). Upon variation of μ within the range of values, the response of the MOPs on both left and right hand-side of Figure 22 (respectively: z_1 as function of E_m and μ , and z_1 as function of h_s and μ) is essentially negligible, compared to that caused by the variation of either E_m or h_s . As a result, OptiSLang considers this design variable as not important, which would be automatically discarded from the optimisation task. This conclusion contradicts the observations of Paragraph 2.1.1, where a meaningful increase of the reaction force is measured when there is friction between sample and rollers.

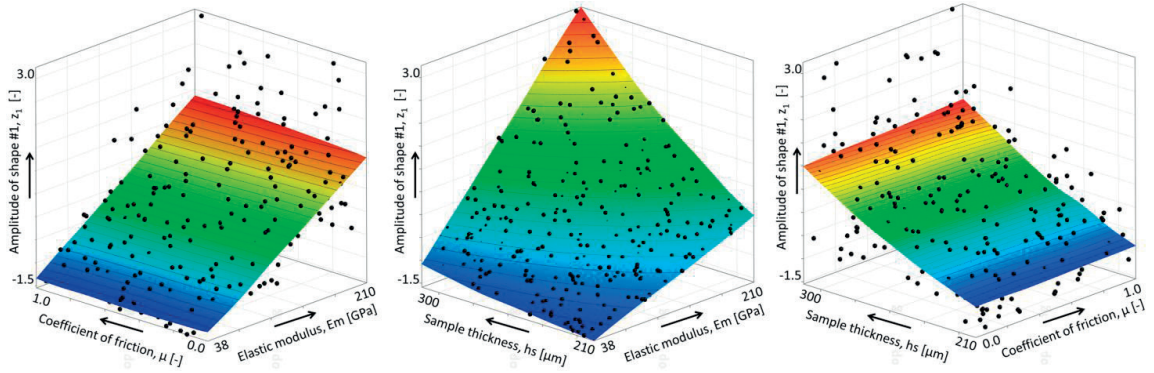


Figure 22: MOPs of the amplitude z_1 (i.e. corresponding to shape function ϕ_1) constituting the $F\text{-MOP}_{\text{Loading}}$, as a function of the three design variables Em , μ and hs .

The simplification of the problem following a standard guideline would therefore not allow capturing the effects of friction on the measurement error. The solution implemented in this study consists in adding the signal Delta, as mentioned previously. Indeed, verification of $F\text{-MOP}_{\text{Delta}}$ leads to a CoP_μ much higher than in $F\text{-MOP}_{\text{Loading}}$ and $F\text{-MOP}_{\text{Unloading}}$, see Figure 21.

In the ELF case, the objective function for parameter estimation (Equation (28)) reduces to:

$$\min_{Em, \mu} \left\{ \sum_{j=1}^3 \left(\sum_{i=1}^{40} (y_{Ite,i} - y_{Exp,i})^2 \right)_j \right\} \quad (28)$$

The validation of the parameters estimation for the ELF case is performed using a sample thickness hs of $280 \mu\text{m}$, elastic modulus Em of 100 GPa and coefficient of friction sample/rollers μ equal to 0.7 for the artificial experiment. We recall here that this choice of numerical values is arbitrary and corresponds to an initial guess. Table 10 summaries the results of the validation tests.

Table 10: Validation tests on the parameters estimation workflow, ELF case.

Sensitivity analysis	Test	Start point of optimisation			Set of parameters to estimate	
		Em [GPa]	μ [-]	hs [μm]	Em [GPa]	μ [-]
a) Advanced Latin Hypercube Sampling b) Full factorial	#1	39.0	0.05	280	100.0	0.7
	#2	209.0				
	#3	39.0	0.99			
	#4	209.0				

The convergence is tested for two optimisation starting points to assess if the problem formulation produces critical local minima or inaccuracy that affect the search for a unique optimal solution. Table 10 shows that the values of Em and μ used for the computer-generated experimental data are successfully retrieved during all the four tests, within satisfactory accuracy (3% error is estimated here acceptable). The approach is therefore considered ready for the analysis of the experimental 4-point bending data.

2.2.3.4 Parameter estimation

Figure 23 shows the estimated parameters E_m and μ as a function of temperature. The provided error bar is the standard deviation calculated using 5 repetitions of the measurements.

The estimated elastic modulus of NiO-YSZ is close to the value reported in the literature but for higher porosities (19 %), i.e. about 125 GPa and 120 GPa, respectively at RT and 800 °C [110]. The dominant contribution to the large decrease in the elastic modulus from NiO-YSZ to Ni-YSZ is mainly due to the increase in porosity, i.e. from 9% to about 29% (see also the analysis on aged samples in Paragraph 2.4.1). In part, the different elastic modulus between NiO and Ni also contributes to the reduction of the effective elastic modulus upon reduction: the elastic modulus of NiO is 277 GPa and 200 GPa as reported in Ref. [111], respectively at RT and 800 °C, whereas that of Ni is 205 and 140 GPa at the same temperatures.

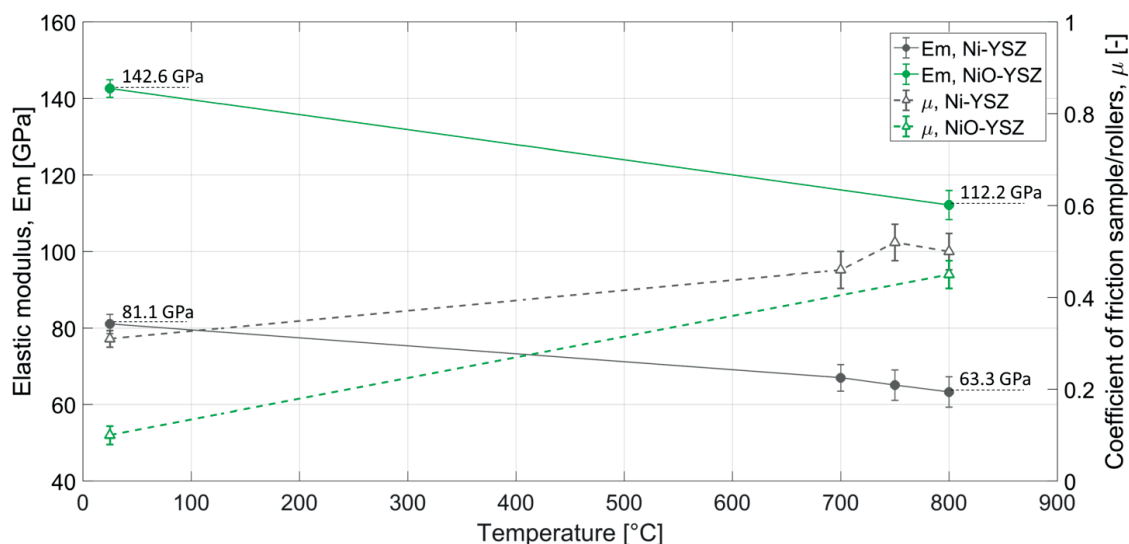


Figure 23: Estimated elastic modulus (filled circle) and coefficient of friction between the sample and the rollers (empty triangle). Green and grey refers to NiO-YSZ and Ni-YSZ, respectively. Interpolating straight lines between data points are provided as guide.

The estimated elastic modulus of Ni-YSZ at RT and 800 °C is about 81 GPa and 63 GPa, respectively. These values fall within the same range as those reported in the literature for Ni-YSZ with 39% porosity, which for the same temperatures are 73 GPa to 58 GPa [110]. The difference is likely justified by the lower porosities of the Ni-YSZ samples tested in this work (about 29%). The increase of the coefficient of friction with temperatures is attributed to the drying of the grease between sample and rollers, which at RT is fluid, whereas after heat-up to high temperatures dried and becomes a fine powder. Compared to NiO-YSZ, the higher friction coefficient when testing Ni-YSZ is probably caused by the favoured sticking of the Ni particles on the rollers (which are made of steel).

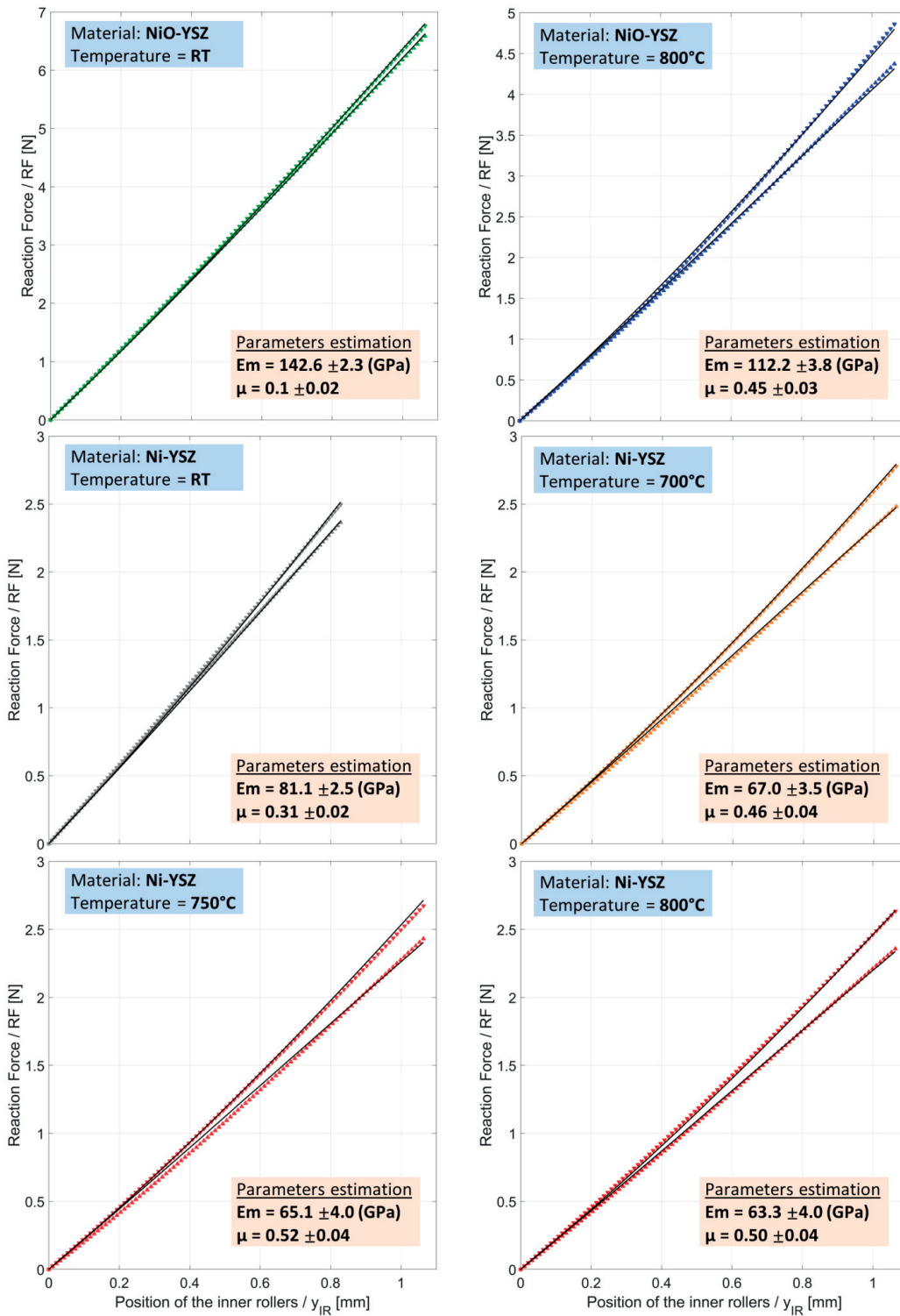


Figure 24: Plot of the responses simulated by the FEM model (black lines) of the tested sample using the parameters estimated by each data-set of mechanical tests. The experimental reaction force versus displacement at the inner rollers, already plotted in Figure 18, are here reported for comparison with the results of the simulations.

However, this cannot be confirmed, because grease should partially prevent such sticking. The mild decrease of the friction coefficient from 750 to 800 °C is unexpected, but error bars indicate that it is not significant.

The elastic modulus and friction coefficients reported in Figure 23 are used to simulate the FEM model of the sample for the six experiments. The simulation and experimental results are plotted together in Figure 24.

The experimental data shown in Paragraph 2.2.3.1 and implemented for the estimation procedure of elastic modulus and friction coefficient of NiO/Ni-YSZ samples at room and high temperature are used to estimate the elastic modulus by analytical solution (see Chapter 2.1). The results are listed in Table 11. The discrepancy between the elastic modulus measured using the meta-model parameter estimation and the analytical solution is lower than 10% for all the cases in Table 11.

The results indicate that the use of the unloading experimental data provides higher accuracy, because the component of the friction force is opposite to that of the measured reaction force.

Table 11: Comparison of the elastic modulus computed from estimation procedure and analytical solution.

		Estimation (GPa)	Analytical solution			
			Loading		Unloading	
			Em (GPa)	err %	Em (GPa)	err %
NiO-YSZ	RT	142.0	154.7	8.9	154.0	8.5
	800 °C	112.0	105.3	6.0	104.1	7.0
Ni-YSZ	RT	81.0	88.9	9.8	87.2	7.6
	700 °C	67.0	73.1	9.1	72.2	7.8
	750 °C	65.0	71.0	9.2	70.2	8.1
	800 °C	63.0	69.1	9.7	68.0	8.0

Therefore, inaccuracies in the four-point bending test measurements are partially compensated. As expected, the error scales inversely in average with the elastic modulus. Variations may be due to differences in the coefficient of friction.

Table 11 shows that for the tested Ni-YSZ samples, the error in first estimations provided by post-processing based on the analytical solution remains limited.

2.2.4 Primary and secondary creep

2.2.4.1 Experimental data

The experimental dataset in the creep (CRP) case consists of the displacement measured at the inner rollers over time during four-point bending test of the Ni-YSZ samples. It comprised testing at three different temperatures to investigate the temperature dependence of the creep parameters. In each

experiment at a determined temperature, four Ni-YSZ samples (one in each slot) were subjected to a different mechanical load, i.e. 0.9, 1.04, 1.18 and 1.32 N.

For each series of experiments, sets of four samples having a relatively low variation in thickness (see Table 12) were selected from the batch. The experimental procedure for the creep tests consisted in a first heat-up from RT to the testing temperature at a rate of 100 °C/h and under reducing atmosphere (N₂:90% - H₂:10%) with a flow rate of 2 l/min. During this stage, the mechanical loads are disabled, i.e. the four samples are subjected only to gravity body force, which is assumed to cause a negligible bending moment. After the end of the heat-up, the testing temperature (i.e. in this work 700, 750 or 800 °C) as well as the atmosphere is kept constant throughout the whole testing time. After a stabilization time of 30 minutes, the mechanical load prescribed for each sample is applied.

In the three series of tests, creep deformation is measured over a total time t of 215 h. The deformation of the samples measured at the inner rollers is plotted in Figure 25. A strong dependence of the creep strain rate on temperature is already observed by comparing series of curves at the three different testing temperatures, but same set of loads.

Table 12: Overview of the creep test conditions at the three testing temperatures.

Material	Atmosphere	Temperature (°C)	Sample thickness (µm)		Load (N)	Initial max stress (MPa)
			Experiments	FEM model		
Ni-YSZ	Reducing N ₂ - H ₂ : 90% - 10%	700	267	267	0.90	18.9
			266		1.04	21.9
			267		1.18	24.8
			268		1.32	27.7
		750	261	262	0.90	19.6
			262		1.04	22.7
			263		1.18	25.7
			262		1.32	28.8
		800	278	278	0.90	17.4
			278		1.04	20.2
			279		1.18	22.9
			278		1.32	25.6

It is here further worth mentioning that thicker samples were used for the experiment at 800 °C compared those at 700 °C. Hence, if the samples had had the same thickness over all the experiments, the dependence of the temperature on the creep strain rate would have been visually higher.

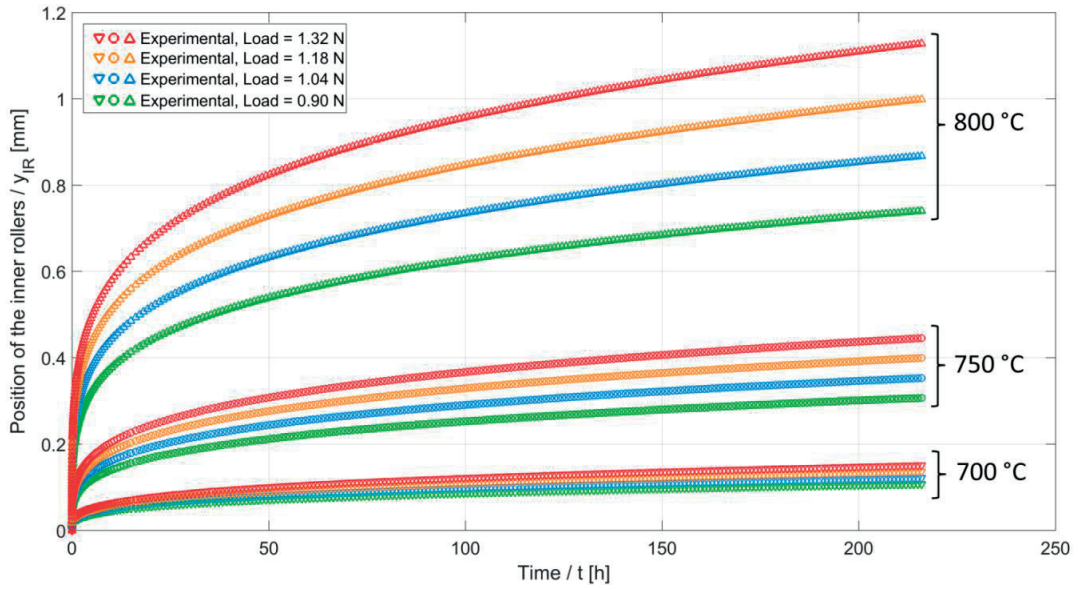


Figure 25: Displacement at the inner rollers over time for the four mechanical loads, caused by creep at the three testing temperatures (the initial elastic deformation caused by the application of the load on the sample is here not plotted). Upwards and downwards triangle symbols depict respectively experimental data at 800 and 700 °C, whereas circle symbols are for the test at 750 °C.

2.2.4.2 Specific workflow description

For the estimation of the creep properties by bending tests (CRP), each design of the sensitivity analysis contains four models. The parameter varied is the constant applied force on the inner rollers. Four discrete values are considered and correspond to the experiment, 0.90, 1.04, 1.18 and 1.32 N (see Table 12). For each design in the sensitivity analysis, the simulation with the 3-D FEM model therefore comprised four runs each consisting of the following sequence:

1. The force in the experiments is applied on the inner rollers of each model. Only elastic deformation is first allowed in the model during this first simulation step.
2. The force is then maintained constant and creep deformation is enabled in the model. The sample deforms because of creep for a defined time duration, see time-deformation curves 0-1 (Load01), 0-2 (Load02), 0-3 (Load03), 0-4 (Load04) in Figure 26.

First tests showed that the agreement between the experimental and simulated response is better with the strain-hardening version of power-law as the creep constitutive law:

$$\dot{\epsilon}_{ij}^{crp} = \frac{3}{2} s_{ij}^{m+1} \sqrt{A[(m+1)\epsilon_{eq}^{crp}]^m (\sigma_{eq})^{n-1-m}} \quad (29)$$

A, n and m are first estimated for each testing temperature separately and their temperature dependence then investigated, i.e. the parameters B and Q corresponding to the pre-exponential factor and activation energy are determined.

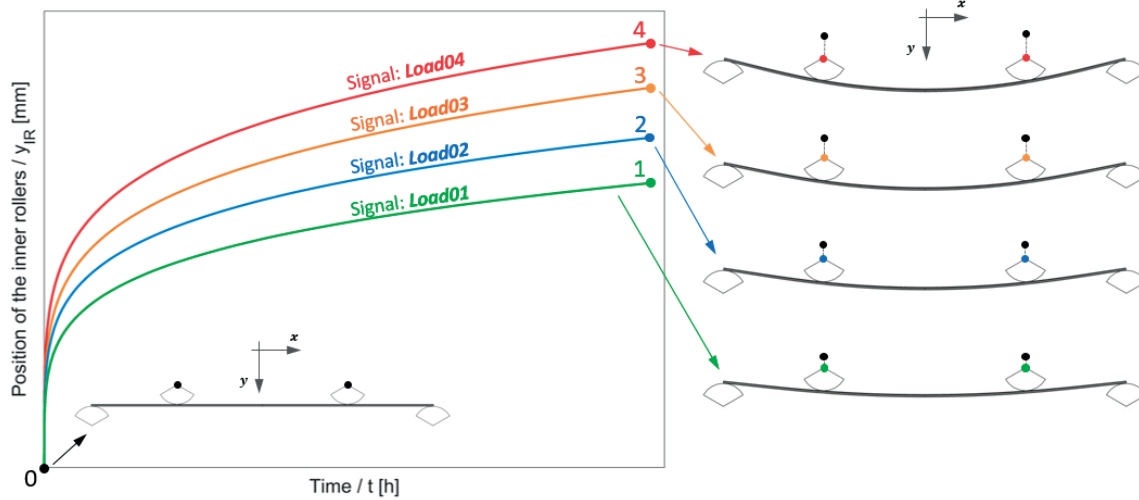


Figure 26: 4-point bending creep experiment with the 3-D FEM model.

The design variables in the sensitivity analysis are the three parameters of the strain-hardening creep power law A , n and m as well as the elastic modulus E_m , the friction coefficient between sample and rollers μ and the thickness of the sample h . In the optimisation step, the estimated parameters are A , n and m , whereas the last three design variables are assigned constant values:

- The temperature-dependent values estimated in Paragraph 2.2.3 (ELF case, Ni-YSZ) are used for E_m and μ (see Table 7).
- h_s is assigned the mean (i.e. Sample thickness - FEM model, in Table 12) of the thickness measurement for the corresponding series of four tested samples at a given temperature (Sample thickness - Experiments, in Table 12). The reason is that for each run of the optimisation step, the thickness is a constant.

Similarly to the ELF case, a global sensitivity analysis is first performed for the CRP case. All the creep parameter estimations in this study are therefore based on the same metamodel. This approach is selected to reduce the runtime of the sensitivity analysis, which is the most demanding. Because the creep properties of the Ni-YSZ anode cermet are not known a priori, sampling is performed over a highly conservative range to ensure that the optimization is not limited by the search space. However, the drawback is that the generation of a F-MOP of sufficient accuracy over a larger range of design variables typically requires a higher number of design evaluations. Therefore, the adequate ranges of variation for each design variable are estimated based upon physical considerations for the Ni-YSZ case. Creep in ceramic materials is expected to occur by vacancy diffusion, either along the grain boundaries (i.e. Coble creep) or by bulk diffusion (i.e. Nabarro-Herring creep). The stress exponent for this creep mechanism is typically slightly higher than unity [106]. In this study, a conservative range spanning from 0.5 to 2.5 is therefore used for the design variable n .

The parameter m relates to the primary creep regime. For physical reasons, it assumes values between -1 (high primary creep deformation) and 0 (no primary creep). However, numerical convergence with the 3-D FEM model of the tested sample with values of m lower than -0.8 proved difficult for sets where the values of A and n are relatively high. This numerical issue is attributed to the relatively high creep strain rates occurring with such values. Therefore, the range for the design variable m is between -0.8 and 0, to prevent unpopulated regions because of simulation failures in the workflow.

The parameter A is dependent upon temperature and topological, morphological and crystallographic properties of the material microstructure. Generalized scaling laws are to our knowledge not available for first-estimations. Therefore, the limits of the adequate range of values for the sensitivity analysis are determined by comparison between the experimental results with a few runs with the FEM model of the tested sample:

- FEM simulations were performed with n and m equal respectively to 2.5 and -0.8 (upper and lower bounds imposed in the sensitivity analysis, respectively) and increasing values of A until the simulated response is sufficiently close to the experimental curve with the lowest creep strain among those used for the parameters estimation, i.e. the curve measured under a load of 0.90 N at 700 °C, see Figure 25. The value of A thus determined is then used as the lower bound in the sensitivity analysis.
- Similarly, FEM simulations were performed with n and m equal respectively to 0.5 and 0 (lower and upper bounds imposed in the sensitivity analysis, respectively) and decreasing values of A until the simulated response is sufficiently close to the experimental curve with the highest creep strain among those used for the parameters estimation, i.e. the curve measured under a load of 1.32 N at 800 °C, see Figure 25. The value of A thus determined is then used as higher bound in the sensitivity analysis.

Concerning the design variables E , μ and h_s , the same ranges as for the ELF parameters estimation are used.

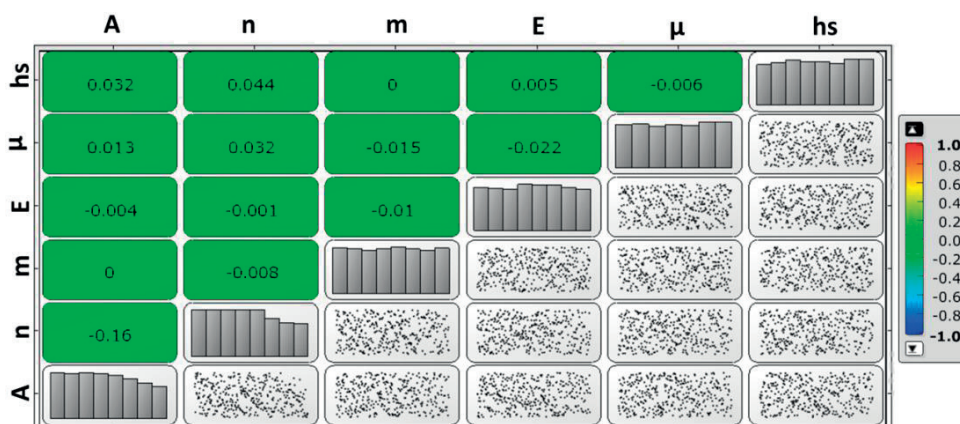


Figure 27: Extended correlation matrix of the sensitivity analysis of the workflow for parameters estimation in CRP mode.

The sensitivity analysis for the CRP parameter estimation comprises more than 400 design evaluations. Figure 27 shows the extended correlation matrix. Mild linear correlations are observed in this configuration. This suggests that more than one signal may be required to obtain a unique solution, which is in line with the expected behaviour. The sample distribution is less uniform for the design variables A and n, in particular close to the upper bounds, (see the lower density on the right-hand side of the probability density function for A and n). Therefore, the Anthill plot of A with respect to n exhibits a blank region in the top-right hand- side, i.e. for values of A and n close to their upper bound. This is due to simulation failures, because combined high values of A and n lead to higher creep strain rates and thus complicate numerical convergence.

Each of the four series of signals Load01, Load02, Load03 and Load04 is used to generate the respective F-MOP, i.e. F-MOP_{Load01}, MOP_{Load02}, MOP_{Load03} and MOP_{Load04}, see Table 13. Each F-MOP contains as many MOPs as the quantity of shape functions implemented by SoS for simulation by random fields. Simulation by random fields of the series of signals of both Load01 and Load02 requires two distinct shape functions. The following upfront words of caution are worth mentioning:

- the shape functions #1 used here in all four F-MOPs are not necessarily the same as for the ELF case.
- shape functions with the same index but referring to distinct F-MOPs are not necessarily the same, e.g. $\phi_{1,Load01}$ and $\phi_{1,Load02}$ may be different.

Table 13: F-MOPs and components of the random field simulations for the parameters estimation mode CRP.

F-MOP	RF simulation (i^{th} design)	Shape functions implemented	Best MOP approach
Load01	$\mu_{Load01} + z_{1,Load01}^i \phi_{1,Load01} + z_{2,Load01}^i \phi_{2,Load01}$	$\phi_{1,Load01}$	MLS
		$\phi_{2,Load01}$	Kriging
Load02	$\mu_{Load02} + z_{1,Load02}^i \phi_{1,Load02} + z_{2,Load02}^i \phi_{2,Load02}$	$\phi_{1,Load02}$	MLS
		$\phi_{2,Load02}$	Kriging
Load03	$\mu_{Load03} + z_{1,Load03}^i \phi_{1,Load03}$	$\phi_{1,Load03}$	MLS
Load04	$\mu_{Load04} + z_{1,Load04}^i \phi_{1,Load04}$	$\phi_{1,Load04}$	MLS

Figure 28 depicts the CoP matrices of the four F-MOPs (F-MOP_{Load01}, F-MOP_{Load02}, F-MOP_{Load03} and F-MOP_{Load04}). The first six columns provide the CoP values of each design variable, whereas the last column shows CoP_{Total}. For F-MOP_{Load01} and F-MOP_{Load02}, two shape functions are required. Therefore, the lower and upper line of the CoP matrices corresponds respectively to shape #1 and shape #2. The CoP_{Total} of the four F-MOPs with respect to shape #1 all reach 100%, which denote a MOP of high quality. The quality is also very high for F-MOP_{Load01} and F-MOP_{Load02} using shape #2. For the four F-MOPs with respect to shape #1, the creep parameters A and n are the most important factors

influencing the response of the meta-model (about respectively to 55% and 43%). The importance of the primary creep exponent is captured only by F-MOP_{Load01} and F-MOP_{Load02} computing the shape #2, leading for both MOPs to a COP_m of more than 93%. This means, that to estimate the parameter m (in addition to A and n), the optimisation must comprise at least the F-MOPs Load01 and Load02. In this work, the optimisation step uses all the four F-MOPs.

The design variables Em, μ and hs have a limited effect on the response of all the four F-MOPs, since their COP_i are close to 0%. If they were part of the design variables to optimise, the optimisation task would have discarded them. In this study, they are however set as constant values.

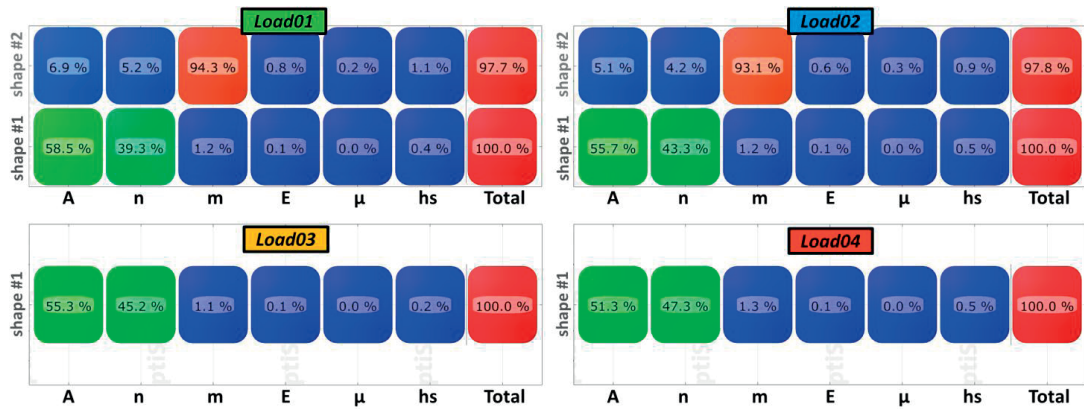


Figure 28: COP matrices of the four F-MOPs of the workflow for parameters estimation in CRP mode.

In the CRP case, each design requires four model runs, to retrieve one signal. Discretisation of each signal is carried out over 40 equidistant points on the abscissa, i.e. in this case the range of time t, from 0 to 215 h. The objective function for the CRP case is computed as follows:

$$\min_{A,n,m} \left\{ \sum_{k=1}^4 \left[\sum_{i=1}^{40} (y_{ite,i} - y_{Exp,i})^2 \right]_k \right\} \quad (30)$$

which is very similar to Equation (28). The validation of the workflow for the CRP case consisted of the 8 tests listed in Table 14. Two distinct artificial experimental dataset were generated for test #1 to #4 and #5 to #8, respectively.

Table 14: Overview of the tests for the numerical validation of the parameters estimation, CRP case.

Sensitivity analysis	Test	Start point of optimisation						Set of parameters to estimate		
		A [h ⁻¹ MPa ⁻ⁿ]	n [-]	m [-]	Em [GPa]	μ [-]	hs [μm]	A [h ⁻¹ MPa ⁻ⁿ]	n [-]	m [-]
a) Advanced Latin Hypercube Sampling	#1	1.28E-07	0.55	-0.05	100	0.7	280	8.00E-07	1.5	-0.3
	#2	4.80E-06	2.4							
	#3	1.28E-07	0.55	-0.78						
	#4	4.80E-06	2.4							
	#5	1.28E-07	0.55	-0.05	200.0	0.1	220	2.00E-06	2.0	-0.7
	#6	4.80E-06	2.4							
	#7	1.28E-07	0.55	-0.78						
	#8	4.80E-06	2.4							

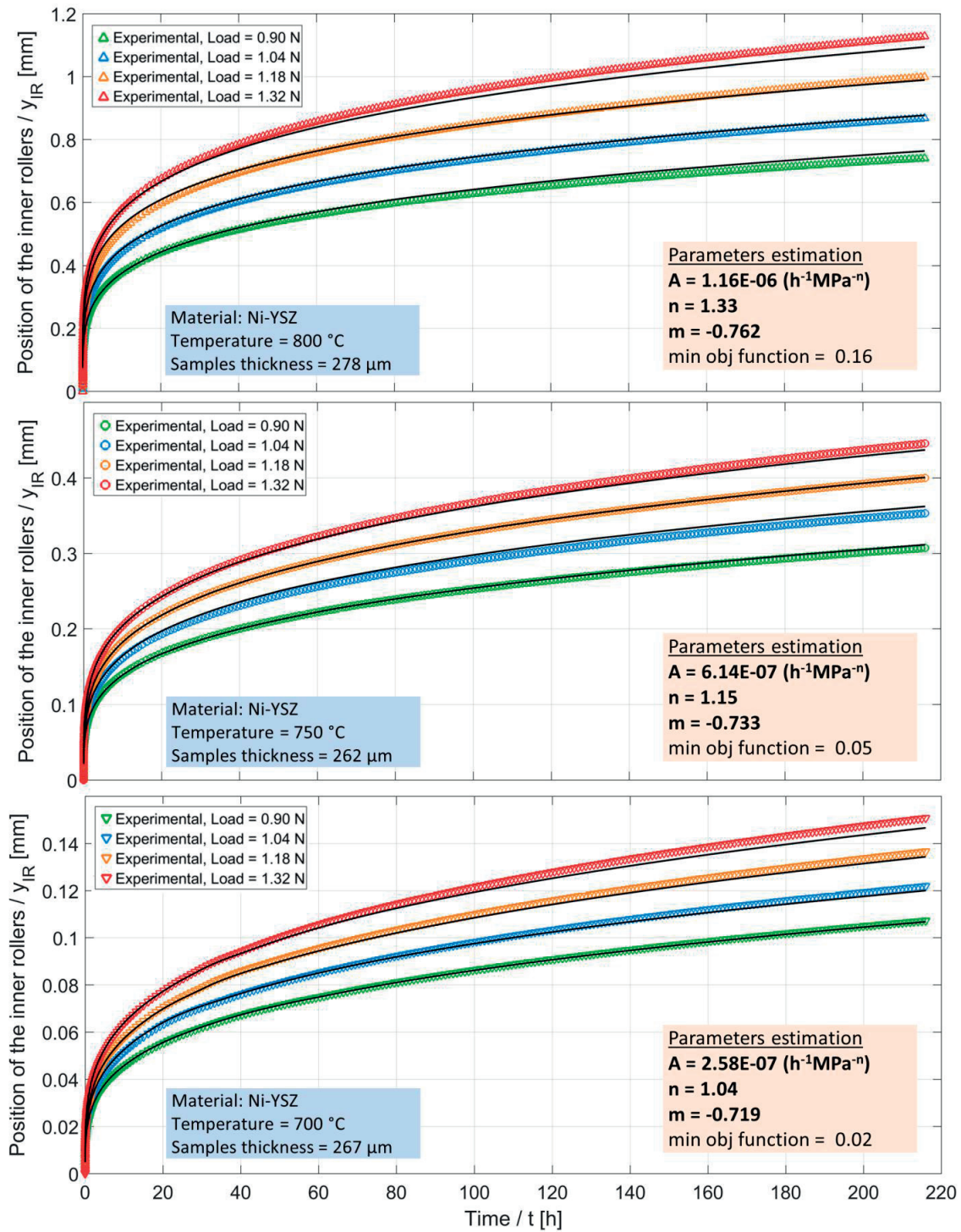


Figure 29: Plot of the experimental (green, blue, orange and red markers) and simulated (black lines) displacement at the inner rollers (black lines) over time for the four mechanical loads. Simulated curves are computed using the parameters estimated by the workflow. Top, middle and bottom plot are referred respectively to testing at 800, 750 and 700 °C.

Two sets of values for A, n, m, Em, μ and hs within their range of allowed variation discussed previously are implemented in the FEM model to simulate the responses CrpLoad01, CrpLoad02, CrpLoad03 and CrpLoad04, and obtain the computed set of signals, i.e. Load01, Load02, Load03 and Load04, which together form the artificial experimental data-set.

For each set of parameters to estimate, four optimisation tests with varying start point are performed, as a first verification that the search of the optimal solution is not strongly affected by local minima. The validation test for each study case is considered successful if the workflow retrieves with adequate accuracy (3% error is estimated here acceptable) the set of predefined parameters values used in the computer-generated experiments. This is the case for all the 8 cases in Table 14 and the workflow therefore considered adequate for the study of the creep behaviour of Ni-YSZ.

2.2.4.3 Estimated parameters

Figure 29 depicts the displacement at the inner rollers over time simulated by the FEM model and the experimental data. The set of creep parameters estimated and used for the simulation of each series of tests is included in Figure 29 for each temperature. The sample thickness is the same as listed in Table 12 (values for FEM model).

The stress exponents estimated from creep testing between 700 and 800 °C are close to unity and thus suggest a diffusion mechanism.

Table 15: Creep parameters A, n and m of Ni-YSZ at 700, 750 and 800 °C obtained from estimation procedure.

Material	Temperature (°C)	A (h ⁻¹ MPa ⁻ⁿ)	n (-)	m (-)
Ni-YSZ	700	2.58E-07	1.04	-0.719
	750	6.14E-07	1.15	-0.733
	800	1.16E-06	1.33	-0.762

Assuming Arrhenius law, the creep pre-exponential factor B and the creep activation energy Q are estimated from the measurement of the creep rate constants at 700, 750 and 800°C. B and Q are further assumed constant over the tested range of temperatures, leading to Equation (31):

$$A = B e^{-Q/RT} \rightarrow \ln(A) = -\frac{Q}{R} \frac{1}{T} + \ln(B) \quad (31)$$

The logarithmic form yields a linear equation, i.e. $y = ax + b$, where the slope and interception point provide the activation energy Q and the pre-exponential factor B. The Arrhenius plot is shown in Figure 30. The values of B and Q estimated by linear fitting are respectively 2.75 h⁻¹MPa⁻ⁿ and 130.7 kJmol⁻¹. Morales-Rodriguez et al. [112,113] investigated the steady-state creep properties of Ni-3YSZ (40 vol.% Ni) anode cermet by compressive testing between 950 to 1250 °C, yielding n = 2.5, Q = 640 (kJ mol⁻¹)

and $B = 1.04E+20$ ($h^{-1}MPa^{-n}$). These parameters were negligibly affected by the Ni content, it was therefore inferred that the YSZ phase controlled the creep deformation of the cermet.

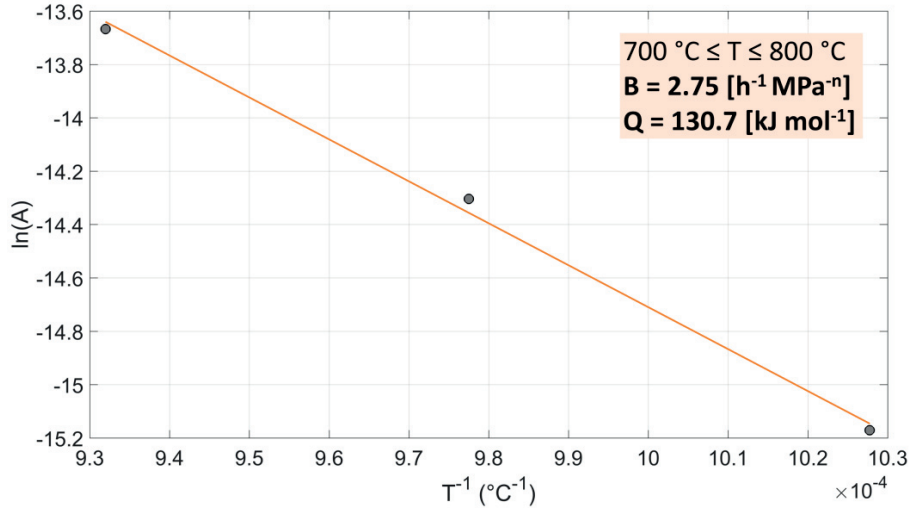


Figure 30: Arrhenius plot of the natural logarithm of the estimated creep rate constant A from the experiments at 700, 750 and 800 °C. The values of B and Q reported on the plot are obtained from the linear fitting.

This also justified the observed decrease of the stress exponent upon temperature increase, because the stress exponent of the Ni phase ($n=4.7$) is higher than that of the YSZ and the contribution of the Ni phase to the apparent creep strain of the cermet is expected lower at higher temperatures. Due to the significantly higher testing temperature, comparison with the results obtained in this work is not fully representative, because of the dependence upon temperature of both stress exponent and creep activation energy [15]. The steady-state creep of Ni-8YSZ (56 wt.% NiO) anode cermet was studied by four point bending and analytical solutions in ref. [106]. The porosity of the tested samples was $\sim 43\%$, which is higher than that of the samples tested in the present work, i.e. $\sim 29\%$. If the same strain rate is applied to two identical phases differing in porosity, the effective stress remains the same, but local higher stresses can be expected in the material with a higher porosity. The increase of the value of creep stress exponent upon increase of strain rate (and thus of generated stress) is reported [114]. This may partially explain the higher stress exponent in Ref. [106], i.e. $n=1.7$ at 800 °C, compared to the value estimated in this work, at least for the testing temperature of 800 °C. Both Ref. [106] and this work observe an increase of the stress exponent upon temperature increase: in both studies, n increases respectively by 0.6 and 0.18 over a temperature increase from 750 to 800 °C. This trend, opposite to that reported by Morales-Rodriguez et al. [112,113], requires further investigations.

To our knowledge, data on the primary creep exponent of Ni-YSZ is very limited. For 8YSZ, the primary creep exponent is around -0.67 [115] and is constant over the range of testing temperature, i.e. between 600 and 1000 °C. The primary creep exponent values obtained in this work are slightly higher,

supposedly because of i) different material microstructure than that in Ref. [115] and ii) a contribution of the Ni phase on the apparent primary creep strain.

The measured creep activation energy of 130 kJmol⁻¹ is fairly close to that reported in Ref. [106] (i.e. 115 kJmol⁻¹). The reason is that at temperatures lower than ~1100 °C, the favoured mass transport mechanism in polycrystalline YSZ is diffusion along the grain boundaries (i.e. Coble creep), whereas at higher temperatures the dominant mechanism is bulk diffusion (i.e. Nabarro-Herring creep). The dependence of the activation energy upon the creep mechanism is confirmed by several studies: between 800 and 1100 °C, it varies between 104 and 190 kJmol⁻¹ for 8YSZ [116,117], and between 114 and 134 kJ mol⁻¹ for 7YSZ [118,119], whereas it increases up to 440-460 kJmol⁻¹ (for 8YSZ) for higher temperatures, i.e. in the range of 1100-1300 °C [120,121]. The creep strain rate in ceramics is determined by the diffusion of the slowest species, Zr⁴⁺ cations in YSZ [106,116].

Due to mostly the different microstructure, the creep pre-exponential constant estimated in this study, i.e. 2.75 h⁻¹MPa⁻ⁿ, is higher than that of Ref. [106], which is equal to 0.037 h⁻¹MPa⁻ⁿ. The creep pre-exponential constant expressed as function of the grain size is:

$$B = \frac{B'}{d^g} \quad (32)$$

where B' is a material parameter independent of the grain size, d is the grain size and g the grain size parameter. In Coble and Nabarro-Herring creep mechanisms, g is equal to 3 and 2, respectively. Assuming that in both this work and in the measurements in Ref. [106] Coble creep is the dominant mechanism (i.e. $g=3$) and that the values of B' are similar, the YSZ grain size of the Ni-YSZ tested in this work is approximately four times lower than the one in Ref. [106]. The trend corresponds to that of the mean of the YSZ phase size distribution (approximately 1.1 and 0.37 μm, i.e. ratio of 3), but requires confirmation by a direct measurement of the grain size.

2.2.4.4 Comparison with analytical solution

The three sets of experimental data at the three testing temperatures, i.e. displacement at the inner rollers over time over four mechanical loads, are also used to estimate the creep parameters A and n by analytical solutions reported in the literature and based on the linear beam theory [105,106], for comparison with the metamodel-based parameter estimation. The approach consists in interpolating the displacement rate at the inner rollers upon the steady-state deflection regime over the set of mechanical loads by the following equation:

$$\ln(\dot{y}_{IR}) = n \ln(P) + \ln \left\{ \frac{A}{(2I_{crp})^n} \left(\frac{L-a}{2} \right)^n \left[\frac{L^2 - a^2}{8} + \frac{L-a}{2} \left(\frac{n(a-L)}{4(n+2)} \right) \right] \right\} \quad (33)$$

This logarithmic form yields a linear equation, i.e. $y = ax + b$, where the slope provides the stress exponent n . The moment of inertia with the contribution of creep is calculated as:

$$I^{crp} = \frac{2wn}{1+2n} \left(\frac{h}{2}\right)^{\frac{2n+1}{n}} \quad (34)$$

The creep constant A is then calculated from the interception point of the fitting equation.

By visual examination of the plots in Figure 25, the start of steady-state creep rate is estimated after 180 h. The analytical solution is therefore applied for the range of displacements at the inner rollers between 180 h and end time of testing (i.e. 216 h).

Table 16: Displacement rates at the inner rollers obtained from linear fitting of the experimental data (see Figure 25).

Temperature (°C)	Sample thickness, h (μm)	Load, P (N)	Displacement rate inner rollers, \dot{y}_{IR} (mm/h) $\times 10^{-4}$
700	267	0.90	1.50
		1.04	1.70
		1.18	1.92
		1.32	2.09
750	262	0.90	3.87
		1.04	4.36
		1.18	4.98
		1.32	5.57
800	278	0.90	7.90
		1.04	9.14
		1.18	10.63
		1.32	11.84

The displacement rates at the inner rollers, \dot{y}_{IR} , obtained from the linear fitting of the displacement at the inner rollers after 180 h, are listed in Table 16. By linear fitting with Equation 33 of the four displacement rates at the inner rollers for each testing temperature, the parameters A and n are calculated. They are listed in Table 17 (the values obtained from the estimation procedure are reported for comparison).

Table 17: Creep parameters A and n obtained from the estimation procedure and from the analytical solution.

Temperature (°C)	A ($\text{h}^{-1}\text{MPa}^{-n}$)		n (-)	
	Estimation	Analytical	Estimation	Analytical
700	2.58E-07	6.82E-09	1.04	0.88
750	6.14E-07	1.43E-08	1.15	0.96
800	1.16E-06	2.54E-08	1.33	1.07

For the material, sample dimensions and testing conditions investigated here, the analytical solution underestimates both the stress exponent n and the creep constant A by about 18% and by two orders of magnitude, respectively. These deviations are attributed to the limitations of the analytical solution and to the use of the simple beam theory.

2.3 Strength of NiO/Ni-YSZ anode cermet

The effects of material flaws is typically reduced because of plasticity in metals and polymers [80]. For such materials, the scatter in the measured strength is usually limited, indicating that there exists at a first appraisal a load level (and thus a stress state) above which mechanical failure by cracking always occurs. Hence, deterministic approaches are applicable for practical failure analysis of structures made of such types of materials [122]. Plastic deformation in ceramic materials is in most cases negligible and therefore the size and spatial distribution of geometrical flaws and material defects can lead to a significant scatter of the failure load measured on components made of a same ceramic material. The strength in ceramics is therefore not an intrinsic material property, because it depends on the quality of the component, therefore on the manufacturing parameters, among others. For this reason, statistic approaches instead of deterministic were proposed to estimate the mechanical reliability of ceramics. A summary of standard concepts is provided hereafter.

The most common statistical approach for analysing the failure probability of ceramics is based on the Weibull distribution. The concept originates from the “weakest-link” model, which approximates the component as an in-series assembly of links, with the weakest one governing the apparent strength. The derivation yields an expression containing the probability of a volume failing at a given stress, for which Weibull proposed a simple parametric solution. Inserting into the weakest-link expression yields the probability that a component fails as (without lowest threshold):

$$P_f(\sigma) = 1 - \exp \left[- \left(\frac{\sigma_{max}}{\sigma_0} \right)^m \right] \quad (35)$$

where σ_0 is the value of the characteristic strength (value corresponding to a failure probability of 63.2%), σ_{max} is the stress at which failure occurs, and m is known as the Weibull modulus, a reciprocal indicator of the scatter in the sample strength measurements. The rationale behind the choice of Weibull parameters is not based on physical considerations, but they intuitively express the effects of the size and spatial distribution of the defect population.

Standard Weibull analyses are typically based on the principle of independent actions. It postulates that the components of the principal stress contribute to crack propagation independently in each corresponding principal direction. However, it cannot be rigorously excluded that a combination of principal stresses in multiaxial stress states contribute together to crack propagation. For this reason, and as observed experimentally [96], Weibull statistics is not necessarily a conservative approach to estimate the failure probability of components. The limitation of this approach is thus the prediction of failure in components with multiaxial stress states. Extensions of the approaches are available, such as the Batdorf theory [123], which is however less extensively used, because despite the increase in the complexity of the mathematical treatment requiring numerical analysis, limitations remain.

Equation (35) is limited to the calculation of the probability of failure of identical components and made of the same material, subjected to different stresses. Because the Weibull approach aims at including

the effects of defect distribution, the failure load of ceramics is expected dependent upon the size of the component, since the probability that large flaws or inclusions are present scales with the volume of material subjected to stress:

$$P_f(\sigma, V) = 1 - \exp \left[-\frac{1}{V_0(\sigma_0)^m} \int_V \sigma^m dV \right] = 1 - \exp \left[-\frac{V}{V_0} \left(\frac{\sigma}{\sigma_0} \right)^m \right] \quad (36)$$

The stress σ is the subset in tension, because in ceramics the strength measured in compression is about three times higher than that in tension. The reason is that failure in tension is caused by crack propagation in the direction perpendicular to that of tensile stress, whereas in compression the sample failure often comes from the friction between setup and sample, i.e. the compression stress in the sample generates transversal stress in tension (i.e. along the compressive force direction) which are much lower than the compressive stress. Hence, failure of ceramics under compression occurs for significantly higher compressive stresses.

The knowledge of the effective volume is also needed for the application of the Weibull approach to structures. In the case of mechanical testing different from uniaxial tension, it accounts for the fact that i) only a part of the tested volume is under tensile stresses and ii) the tensile stress is not uniform. Depending upon the nature of the defect, a surface-based equivalent version of Equation (35) is sometimes used.

2.3.1 Experimental data processing

In the mechanical tests carried out in this study, the standard approach to estimate the Weibull parameters consisted in fracture testing of a batch of samples. Standards for the calculation of the two Weibull parameters are described in ASTM C1239-13. Post-processing is typically based on the linearized form of Equation (35), leading to Equation (37), which neglects the volume correction. It applies if the spatial and size distribution of flaws as well as the geometry of the domain subjected to stress are similar in each sample. Hence, the samples must be produced with the same manufacturing process.

$$\ln \left(\ln \frac{1}{1 - P_f} \right) = m \ln \frac{\sigma_{max}}{\sigma_0} \quad (37)$$

To apply this linearized form, the values of stress at which failure occurred are ranked in ascending order. Respecting the same order, the cumulative population failure $P_{f,i}$ is assigned to each sample [122]:

$$P_{f,i} = \frac{i - 0.3}{N + 0.4} \quad (38)$$

where N is the total set of measurements. The Weibull modulus m and the characteristic strength σ_0 are then calculated from the slope and interception point of the regression line fitting the data from Equation (37). In four-point bending, the effective volume V_0 corresponds to the volume of an equivalent sample tested in uniaxial tension and subjected to a uniform equivalent stress σ_{tens} , with

the same probability of failure as the tested sample and undergoing a maximum stress at the fracture point equal to $\sigma_{max} = \sigma_{tens}$.

$$V_0 = \frac{1}{(\sigma_{max})^m} \int_V \sigma^m dV \quad (39)$$

In four point bending, the reference volume is computed as [100]:

$$V_0 = \frac{whL(2+m)}{4(m^2+2m+1)} \quad (40)$$

Assuming that the sample dimensions are constant, a decrease of m corresponds to an increase in the reference volume, because if the distribution of the heterogeneous flaws is larger (i.e. if m is lower), the equivalent volume tested in uniform tensile stress is higher.

The Weibull analysis can be applied also on the stress state computed from numerical simulations of the FEM model of the sample (see Paragraph 2.1.1) rather than by analytical solution. In this way, the accuracy of the obtained Weibull parameters is increased. The cost in terms of efforts is higher but not expected critical because a numerical simulation is required for each tested sample. Such a procedure would consist in a routine which modifies the FEM model for each tested sample: i) the thickness of the sample is the same as in the test and ii) the displacement at the inner roller is the same to that obtained from the testing setup at the point where the sample failed. The first principal stresses computed by FEM simulation of each sample are post-processed. The failure probability of a component under multiaxial stress state is defined as:

$$P_f(\sigma) = 1 - \exp \left[- \frac{(\sigma_1)^m + (\sigma_2)^m + (\sigma_3)^m}{(\sigma_0)^m} \right] \quad (41)$$

Afterwards, the reference volume is computed from the output of the numerical simulation as:

$$V_0 = \int_V \left(\frac{\sigma_1}{\sigma_{max}} \right)^m + \left(\frac{\sigma_2}{\sigma_{max}} \right)^m + \left(\frac{\sigma_3}{\sigma_{max}} \right)^m dV \quad (42)$$

where σ_{max} corresponds to the maximum simulated stress in the sample, i.e. the maximum value of the first principal stress.

2.3.2 Experimental

Batches of the NiO-YSZ, Ni-YSZ and YSZ scaffold (referred to as (Ni)-YSZ) samples described in Paragraph 2.2.1 were used for the strength measurements. Before testing, the laser-cut edges of the samples were polished by P1200 sandpaper, to minimise the effects of edge defects. The testing consisted in the four-point bending of the samples at a constant displacement rate at the inner rollers (0.3 mm/s). For high temperature testing, this displacement rate was assumed sufficiently high for negligible stress relaxation by creep upon sample bending. The effect of creep is i) the increase of the plastic zone at the flaws tips, hence higher external work (i.e. higher sample deformation until failure) is needed to break the sample and ii) the reaction force measured by the setup is lowered. From the practical standpoint of macro-scale deformation, if the post-processing of the experimental data is based on the sample

deflection at failure (i.e. the procedure described in the previous section for the FEM model-based post-processing), creep is expected to result in an overestimation of the apparent strength, whereas if the post-processing uses the value of force at failure (i.e. with the analytical solution), the apparent strength is underestimated.

The reaction force of the load cells was recorded at a frequency of 100 Hz. The value of force at the point where the sample failed RF_{fail} (detected visually) was then used to calculate the maximum stress at failure by the analytical solution of force-maximum stress derived from the linear beam theory:

$$\sigma_{max} = 1.5 \frac{(L - a)RF_{fail}}{wh^2} \quad (43)$$

For h , the averaged value of 261 μm was used. L and a were equal to 50 and 25 mm, respectively.

Since the Weibull approach is based on the statistical distribution of flaws in the material, the uncertainty on the parameters σ_0 and m depends upon the number of samples tested. Figure 31 illustrates how the errors on these two parameters vary as a function of the number of tested samples, reproduced from ASTM C1239-13. The accuracy on the Weibull modulus is much lower than on the characteristic strength. It can be deduced that the testing of a small batch of samples (e.g. <30) would lead to significant errors on the obtained Weibull statistics parameters. This is a practical difficulty in the application of the Weibull theory, since the testing of large batches of samples using conventional mechanical test setups is time consuming and guarantying identical conditions throughout the measurement campaign is challenging.

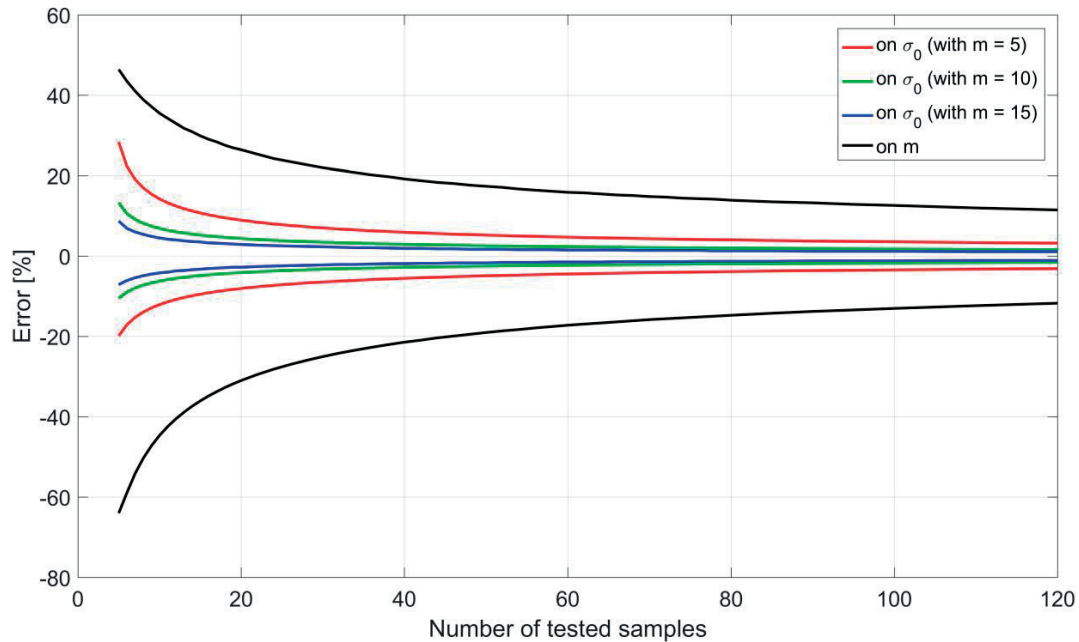


Figure 31: Plot of the error on the characteristic strength (red, green and blue lines, for different Weibull moduli) and on the Weibull modulus (black line) as a function of the number of tested samples. The curves are generated using the 90% confidence interval.

The aim of the present analysis is however not to provide exact values of the probability for design guaranteeing a target probability of survival, but to understand the risks of failure in a stack by comparative analysis (Chapter 3.4).

The SEP setup fabricated at GEM (see Paragraph 2.1.2) is designed to test up to 30 samples in one heat up stage. This quantity was determined based upon practical considerations including expected target properties of the materials to be tested, space constraints in the laboratory and required accuracy for qualitative comparative analyses. In this work, for each experimental condition a batch of 50 samples was tested. Since the capability of the SEP setup is of 30 samples, two heat-ups with 25 samples each were performed. The testing temperatures were RT and 800 °C, whereas the testing atmospheres were air for the testing of NiO-YSZ and (Ni)-YSZ samples, and reducing for Ni-YSZ samples (forming gas 9% H₂ - 91% N₂).

2.3.3 Results and discussion

Figure 32 shows Weibull plots from the four-bending measurements of NiO-YSZ, Ni-YSZ and (Ni)-YSZ both at RT and 800 °C. Table 18 summarises the measured Weibull parameters, together with the confidence interval and sample batch size. The Weibull statistic parameters σ_0 and m are calculated using the procedure based on the analytical solution of linear beam bending, see Paragraph 2.1.1. The range of error does not account for the effects of imprecisions in the elastic properties or simplified post-processing using analytical solutions (see Paragraph 2.1.1). The probability of failure computed using the measured properties are shown in Figure 32 as a guide for the eye. The measurements seem to follow a Weibull distribution, but stronger deviation is observed for NiO-YSZ at room temperature. The typical strains at failure are low as expected, for NiO-YSZ at RT and 800 °C about 0.3% and 0.25% and they fall within similar range for Ni-YSZ, i.e., 0.47% at RT and 0.25% at 800 °C. This suggests that the amount of plastic deformation is limited at high temperature for the tested Ni-YSZ material. The Weibull moduli of all the tested materials are overall low. A value of 10 is usually considered a threshold for technological materials, but the primary function of the Ni(O)-YSZ is not of mechanical nature.

The characteristic strength and Weibull modulus of NiO-YSZ are respectively 449.7 MPa and 8.5 at RT, whereas at 800 °C they decreased by about 37% and 46%, which is larger than the decrease in the elastic modulus of 21% measured in Figure 32. Opposite dependence upon temperature is observed for the characteristic strength and Weibull modulus for Ni-YSZ. A temperature increase from RT to 800 °C decreased (increased) the characteristic strength (Weibull modulus) by about 60% (35%). For comparison, the measured decrease of the elastic modulus is of about 21 %, similar than that of NiO-YSZ (Figure 32).

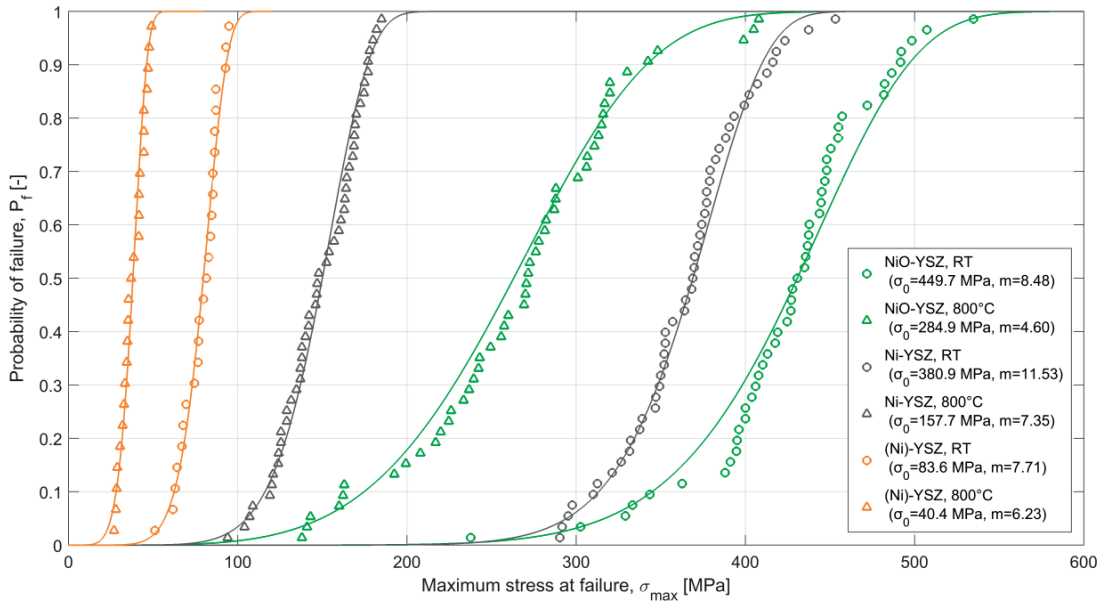


Figure 32: Measured strength of NiO-YSZ (green), Ni-YSZ (grey) and (Ni)-YSZ (orange) at RT (circles) and 800 °C (triangles). The Weibull failure probabilities calculated with the estimated parameters are plotted for reference in continuous lines.

Table 18: Weibull statistics parameters estimated from the RT and 800 °C testing.

Material	Temperature	Samples	Characteristic strength σ_0 (MPa)	Weibull modulus m (-)	Reference volume V_0 (mm ³)
NiO-YSZ	RT	50	449.7 [436.5; 463.3]	8.48 [7.22; 10.47]	9.51 [7.73; 11.12]
	800 °C	50	284.9 [269.6; 301.0]	4.60 [3.92; 5.68]	17.17 [14.04; 19.95]
Ni-YSZ	RT	50	380.9 [372.6; 389.4]	11.53 [9.82; 14.24]	7.03 [5.70; 8.23]
	800 °C	50	157.7 [152.4; 163.2]	7.35 [6.26; 9.08]	10.94 [8.90; 12.78]
(Ni)-YSZ	RT	25	83.6 [79.7; 87.6]	7.71 [6.24; 10.56]	10.44 [12.82; 7.67]
	800 °C	25	40.4 [38.1; 42.8]	6.23 [5.04; 8.53]	12.84 [15.74; 9.46]

Upper and lower bounds: 90% confidence interval

The strength of the zirconia scaffold obtained from the dissolution of the Ni phase of Ni-YSZ samples is considerably lower than that of the corresponding Ni-YSZ samples at the same testing conditions. At RT and 800 °C, it is lower by about 78% and 75%, respectively. The temperature dependence is the same for the characteristic strength and Weibull parameter, which decrease by about 52% and 19%. The inspection of the confidence intervals indicates that the changes are overall significant, with the exception of that of the Weibull modulus of the YSZ scaffold.

Ni(O)-YSZ is a porous heterogeneous material designed to provide a variety of functions, such as gas and ion and electron solid-phase transport to a high density of electro-catalytic sites. Material features spanning across varying length scales that are relevant to the primary purpose of the electrode material can therefore represent material flaws from a mechanical standpoint. The size of the critical defects can be estimated assuming that the crack propagates only in mode I, from the estimated fracture toughness K_{Ic} and the stress at failure σ_{max} as:

$$a_c = \frac{2}{\pi} \left(\frac{K_{Ic}}{\sigma_{max}} \right)^2 \quad (44)$$

For K_{Ic} in the range of 1-2 $\text{m}^{0.5}\text{MPa}$ [124] for NiO-YSZ and a characteristic strength of 450 MPa, the estimate of the critical flaw size ranges from approximately 3 to 10 μm . Direct application of the estimate is not expected to break down for highly porous materials. Indeed, using K_{Ic} of YSZ equal to 1 to 1.80 $\text{m}^{0.5}\text{MPa}$ [125], the flaw length for a stress of 83.6 MPa (e.g. characteristic strength of (Ni)-YSZ) yields 90 μm to 0.3 mm. Correction based on the volume fraction of YSZ measured by 3-D electron microscopy yields smaller values of 16-52 μm . For the Ni-YSZ, the estimate is in the range of 2-8 μm . Critical crack sizes computed for Ni-YSZ and NiO-YSZ using volume fraction correction and the highest fracture stress for each batch yields a flaw size of 1.5-2 μm . For comparison, the phase size distribution measured by ray-tracing on volume samples obtained by 3-D focused-ion beam – scanning electron microscopy (FIB-SEM) serial sectioning extends up to approximately 2.5-3 μm , but the median and modal values in pristine state are all smaller than 1 μm . Care is therefore required when drawing conclusions. The results suggest that the strength of the tested material is primarily limited by defects from production that are still slightly larger than the features that provide to Ni-YSZ its electrochemical activity. This is further supported by the relatively low Weibull modulus, but not directly by the variation upon temperature. The difference between the estimate and the measured size distribution is less than one order of magnitude, which is low, owing to the uncertainty on the fracture toughness and stress distribution in a reticulate structure, among others. The analysis suggests that the factors that control the strength of the tested material cannot be investigated in the views of defects in a continuum, but that the stress state in the different phases plays a role. The comparison between the difference in strength and elastic properties at high and room temperature further support this first conclusion, except for the YSZ scaffold ((Ni)-YSZ).

Table 19: Thermo-elastic and strength properties of NiO and YSZ.

		Em (GPa)	Strength (MPa)	CTE (800 to RT) (K^{-1})
NiO	RT	277	40	13.5e-6
	800	200	30	
YSZ	RT	205	400	12.2e-6
	800	163	165	

Care is however required in the application of Weibull theory in the case the defect size is similar to that of the phase size distribution, i.e. distribution close to uniform. Table 19 lists the material properties of the phases in NiO-YSZ to support the discussion hereafter. Residual stress builds-up in the Ni(O)-YSZ upon manufacturing. Both NiO and YSZ phases are stress-free at the sintering temperature of about 1400 °C in this work. During the cool down to RT, the mismatch of CTE between these two phases (13.5E-06 and 12.2E-06 between 800 °C and RT, for NiO and YSZ respectively) generates residual stresses in both phases. An offset in apparent zero-stress temperature is expected because of significant creep relaxation upon cool-down. Hence, the stress-free temperature depends on the highest creep strain rate among the phases. At 800 °C, these residual stresses are still present in both phases but their magnitude is less. In all cases, the higher thermal shrinkage of the NiO is constrained by the YSZ. As a result, on average, the NiO withstands tensile stress whereas the YSZ is in compression. A calculation assuming linear elasticity indicates that the expected magnitude of the stress is in the range of 182 MPa, neglecting microstructural effects. The fracture of NiO-YSZ anode occurs because of that of both the YSZ and NiO phases, which are ductile at room temperature. Indeed, NiO fails by brittle failure until 300 °C, ductile failure above 500 °C [111]. At high temperature, the NiO yield strength is in the range of 25 MPa, the fracture strength 30 MPa and the elongation rupture larger than 25%. The difference in the characteristic strength of 37% between RT and 800°C that exceed the change in elastic modulus is therefore the results of a decrease of the strength and of the compressive stress in YSZ with temperature. The failure is expected to initiate in the NiO phase at room temperature. Clear conclusion cannot be provided at 800°C, because of the NiO plasticity, which should partially balance the more detrimental situation in the YSZ. The ductility of NiO at high temperature is expected to increase the apparent strength of Ni-YSZ, because of the hardening effect before failure, even though the strength of both phases decreases with temperature. This analysis does not account for microstructural effects. The median neck size of Ni and YSZ and pore were measured by 3-D imaging, but not that of NiO. However, since the median neck size of YSZ and Ni are similar, that of NiO is expected only slightly larger than YSZ. The significant decrease in temperature of the Weibull modulus may be explained in the case the phase where the failure is initiated changes from NiO to YSZ, from the perspective of defects of a size similar to the phase size distributions, but not necessarily in the case of larger isolated defects.

Macro-scale fracture of Ni-YSZ anode also requires the cracking of both YSZ and the Ni phases. The YSZ fails by brittle failure, whereas Ni is expected to fail in the plastic regime over the whole investigated temperature range. The comparison of the strength measurements between Ni-YSZ and (Ni)-YSZ (the YSZ scaffold) provides several informations. The characteristic strength of Ni-YSZ is higher than that of the YSZ scaffold (by about 78%) and the Weibull modulus follows similar trends. There is therefore a clear beneficial effect of the Ni phase. The expected beneficial effects are residual stress in the brittle YSZ phase and increased resistance to crack propagation because of plasticity. From the latter

standpoint, the Weibull modulus of Ni-YSZ is also higher than that of NiO-YSZ. The CTEs of Ni and YSZ between RT and 800°C are respectively 16.2×10^{-6} and 12.2×10^{-6} . Assuming a stress-free temperature around the reduction temperature and an elastic modulus of 200 GPa for both phases, the magnitude of the stress is expected in the range of 320 MPa. The compressive stresses in YSZ are beneficial and a calculation without considering microstructural effects and creep relaxation suggests that plastic deformation already occurs in Ni. The yield strength of Ni is about 150 MPa at room temperature, and rupture occurs at 430 MPa. In a simplified view, the Ni phase is expected to start failing for an applied stress of 110 MPa. For a corresponding increase in stress in the YSZ initially in compression, failure does not occur, but the failure of the Ni is expected to alter the residual compressive stress in the YSZ. The failure of Ni however occurs at high elongation, up to 40%, a behaviour that is difficult to integrate in the present reasoning. The strength of the YSZ phase should be around 90 GPa to withstand such elongation.

The results suggest that the dependence upon temperature of the Weibull modulus, and the higher value compared to that of (Ni)-YSZ is partly due to the compressive residual stress in YSZ. Even if Ni is in traction, the effect of flaws on stress concentration can be alleviated by plasticity. The Weibull modulus is therefore highest at room temperature and higher than that of (Ni)-YSZ. At 800°C, the compressive stress is released (in contrast to NiO-YSZ) and only the beneficial effect of Ni plastic deformation remains. This may explain why the difference between the apparent strength at room and high temperature is the highest for Ni-YSZ, among all the three tested materials. The offset between the Ni-YSZ and (Ni)-YSZ curves in Figure 32 indicates that Ni plasticity still improves the strength at high temperature, i.e. both the characteristic strength and the Weibull modulus. The effects of changes in flaw geometry because of a lower porosity are likely less for such a fine heterogeneous microstructure. The dependence upon temperature for (Ni)-YSZ is however unexpected. It does not follow most of the published work on either dense 3YSZ or 8YSZ, which report usually an increase, because creep can to some extent lower the stress at the crack tip generated because of the flaws. A comprehensive analysis of the (Ni)-YSZ dataset therefore requires further analyses to explain the reasons for the discrepancy.

2.4 Computational homogenisation

The purpose of computational homogenisation is the measurement of effective properties based on the concept that the macroscopic material properties are related to the volume average of the microscopic fields. For the computation of effective mechanical properties, modelling a domain of material of sufficient size and with adequate spatial resolution to be representative is performed and the relationship between the volume-averaged values of simulated strains and stresses and macro-scale counterpart used to obtain a measure of the effective mechanical response of the heterogeneous material in a macroscopic sense [126].

Computational homogenization based on 3-D imaging is complementary to mechanical testing methods, such as presented in Chapter 2.1. The microstructural metric and topological parameters of the material of the samples for the mechanical testing must be as similar as possible as those of the real components, ideally identical. This requires production using the same manufacturing route, because modifications of the process parameters to e.g. increase the thickness of the deposited layer may lead to changes in the material microstructure. This is a practical difficulty for characterisation as a key factor for the performances of the SOFC systems is the thickness of the SRU components: cell electrodes and interconnects with reduced thickness have a lower ohmic resistance because of the shorter current transport path, as long as sufficient in-plane conductivity is maintained. Similarly, electrolytes with reduced thickness have a lower ionic resistance thanks to the shorter ionic transport path. Besides, the reduction of the thickness of the SOFC stack components is also dictated by market requirements, since thinner layers reduce the usage of raw material and lower ohmic and ionic resistances help reducing the operating temperature of SOFC stacks, enabling the use of cheaper steels for the metallic interconnects and balance-of-plant (BoP) components, among others.

Conventional macro-scale mechanical testing of ceramic and cermet materials used in SOFCs does not inform alone about the relationships between the material's microstructure and mechanical properties. Moreover, there are practical difficulties when macro-scale mechanical testing is used on relatively thin samples, because i) the brittleness of ceramic materials complicates the handling of the samples ii) the dimensional and geometrical tolerances can hardly be scaled down with the reduction of the thickness of the deposited layer, leading to higher uncertainties in the quantification of the thermo-mechanical properties.

SOFC stacks comprise several components made of heterogeneous materials. For example, the common anode material is a three-phase material containing metallic, ceramic and pore phase. Further, GDLs are often domains comprising a metallic and a pore phase. The characteristic length of the geometrical features relevant for understanding the mechanical behaviour therefore ranges approximately from 100 nm (e.g. mean phase diameter of the electrode material phases) to a few mm (e.g. typical GDL channel size). Modelling with such varying level of detail is demanding in terms of computational requirements. A practical workaround is the use of effective (volume-averaged)

properties. In the case samples of the material of adequate size can be produced, direct measurement of the properties by mechanical testing is preferable. Alternatively, computational homogenisation enables the estimation of the mechanical properties at the continuum macro-scale by solving a boundary values problem at the micro-scale, using as computational domain either the computer-aided design (CAD) geometry for stack sub-assemblies or 3-D imaging for complex heterogeneous materials. Computational homogenization requires attention to two main requirements on the size and level of details of the computational domain. A definition of a representative volume element (RVE) is provided by Kanit et al. [127] as *“a volume V of heterogeneous material that is sufficiently large to be statistically representative of the composite, i.e., to effectively include a sampling of all microstructural heterogeneities that occur in the composite. This is generally the principle adopted, and it leads to the fact that the RVE must include a large number of the composite micro-heterogeneities (grains, inclusions, voids, fibres, etc.)”*. However, the fulfilling of the two requirements is limited by the available computing resources. Further, the two requirements are in a simple sense opposite requirements.

Computational homogenisation has already been used for investigating the mechanical properties of SOFC materials or artificial reconstruction equivalent. For instance, Johnson and Qu [128] determined the elastic modulus and CTE of the Ni-YSZ anode cermet at RT. The domain was an artificial microstructure made of Ni, YSZ and pore, generated by a three-dimensional reconstruction method. The size of RVE and voxels affects relevantly the elastic properties (the value of elastic modulus converges for small voxel sizes and large RVEs). Delette et al. [129] reconstructed a Ni-YSZ functional layer and LSCF cathode microstructure respectively by X-ray holotomography and FIB-SEM serial sectioning. The two modelled microstructures were simulated by FEM to determine the elastic properties and CTE of the materials at RT. Recommendations were provided in terms of discretization refinements and size of the RVE. Conventional mechanical testing of these two layers is typically difficult, since they are thin and brittle, which illustrates the relevance of the method.

Two homogenization studies were performed in this study. Paragraph 2.4.1 presents the application of standard elastic homogenization for computing the thermo-elastic properties of Ni-YSZ. In Paragraph 2.4.2, the elastic and creep behaviour of single-solid phase gas diffusion layers is investigated.

2.4.1 Thermo-elastic properties of NiO/Ni-YSZ

In this study, the Hill-Mandel [130] method for the homogenization of the thermo-elastic properties has been implemented. Grid and volume independence studies have been performed to estimate the required spatial resolution and volume for the accurate measurement of the thermo-elastic properties of the studied Ni-YSZ electrode. The computed thermo-elastic properties then have been compared to dilatometry and four-point bending measurements of the pristine anode. Once validated, the effects of short-stack operation on the mechanical properties were analysed for comparison with the improved accuracy provided by the meta-model parameter estimation (Paragraph 2.2.3).

2.4.1.1 3-D imaging and characterization

Imaging was performed on Ni-YSZ anode samples similar to those described in Paragraph 2.2.1. A reduced cell was kept un-operated to measure the properties in the pristine state, while other cells were operated in a 6-cell short stack for 4700 h fed with air and dry H₂. Testing was performed at a current density of 0.4 A cm² and a furnace temperature of 780°C. Both pristine and aged cells were fractured to expose the interface between the anode and the YSZ electrolyte and impregnated. The samples were polished first mechanically, then by ion-milling for preliminary 2-D SEM observations. The region close to the interface with the electrolyte was then imaged by FIB-SEM serial sectioning. Before the acquisition, fiducial marks were milled to adjust the position of the FIB beam and maintain the thickness variation of the slices below the nanometer level. The acceleration voltage was of 1.7 kV and data from both the energy selective backscatter (ESB) and in-lens secondary electron detector were recorded. The pixel size and slice thickness were respectively of 10 nm and 15 nm for the aged sample, and set equal to 7 nm for the pristine cell. The sections were aligned with a Fiji [131] script using the marks, which consisted of grooves orthogonal to the imaged plane. The reconstruction of the aged stack was resampled at an isometric voxel size of 10 nm.

The imaging data consist of two 3-D reconstructions of 17x18x10 μm³ for the pristine cell and of 21x13x19 μm³ for the aged cell. A bilateral filter was applied before combining the data from the ESB and in-lens detector to remove artefacts caused by imperfect impregnation. The segmentation of the data, which consists in assigning to each voxel belonging to a same material phase the same label, has been performed using Matlab routines with calls to Avizo [132] for image gradient and watershed transform computations.

The volume fractions, the contiguity, and the total and connected triple-phase boundary length are computed using standard methods implemented in Matlab [133]. The phase size distributions are measured based upon the concept of the phase volume that can be filled with overlapping mono-sized spheres, as described in e.g. [134]. The Matlab code reproduces the process of filling a phase with spheres of decreasing radii by repeatedly thresholding the phase distance map and then dilating for corresponding values of the distance map. The neck size distribution is determined on a discrete representation of the heterogeneous material provided by skeletonization of the phase volume followed by partitioning into transport channels [135],[135]. The cross-sections are measured at each skeleton point. The smallest cross-sectional area in each channel is recorded and the corresponding size of the neck is set as the radius of a circular section of the same area.

The two segmented stacks were re-sampled at a same voxel size of 15 nm. The volume fractions, contiguity, phase size distributions and total and effective triple-phase boundary length measured before and after resampling did not differ significantly.

For the grid independence study two volume samples were prepared. They were cubes of 2.25 μm³ and 6.75 μm³ extracted from the reconstruction of the pristine and aged cell, respectively. The volume was

resampled at 11 and 7 voxel sizes ranging from 20 nm to 200 nm and 50 to 200 nm, respectively for the first and second volume. Ten volume samples have been generated for the volume independence study by expanding a core of $2.25 \mu\text{m}^3$ in the aged cell to differing sizes, up to $8.25 \mu\text{m}^3$, with a constant voxel size of 75 nm.

2.4.1.2 Homogenization

Computational homogenization enables the determination of properties at the continuum macro-scale by solving a boundary value problem at the micro-scale on a representative volume element. The macroscopic homogeneous strain and stress tensor are the volume average of their microscopic counterparts, and the problem complies with the Hill lemma, an additional equation that expresses volume averaging of the virtual work. The deformations simulated by the boundary values problem must not be inelastic. The convergence behaviour as a function of the domain size varies depending upon the applied boundary conditions. Static and kinematic uniform boundary conditions respectively underestimate and overestimate the apparent elastic modulus of the composite for sizes smaller than the RVE, but asymptotic convergence is obtained in all cases to the same limit for ever increasing sizes. They can therefore be practically seen as approximate upper and lower bounds. With periodic boundary conditions, the convergence of the apparent elastic modulus is usually faster.

For evident reasons in the case of a non-periodic porous computational domain, kinematic uniform boundary conditions are applied in the present study for the measurement of the linear elastic properties [127]. Linear relationships $u_i = E_{ij} x_j$ are enforced between the displacements u_i and the macroscopic homogeneous strain E_{ij} at locations x_j on the sample volume boundaries. Within this framework, the components of the stiffness tensor are determined from six simulations, one for each column. The effective CTE is computed by enforcing that opposite faces remain parallel and flat. The expansion of the sample volume along the 3 directions caused by a uniform change of temperature is measured.

Macro-strain and macro-stress tensor are conveniently expressed in the array form as:

$$E_{ij}^{el,LD} = \frac{1}{V_{RVE}} \int_V \varepsilon_{ij}^{el,LD} dV = \frac{1}{V_{RVE}} \sum_{n=1}^N \varepsilon_{ij}^{el,LD} V_n \quad (45)$$

$$\Sigma_{ij}^{LD} = \frac{1}{V_{RVE}} \int_V \sigma_{ij}^{LD} dV = \frac{1}{V_{RVE}} \sum_{n=1}^N \sigma_{ij}^{LD} V_n \quad (46)$$

where V_{RVE} is the total volume of the RVE (i.e. including also potential unmeshed domains), V_n is the integration volume of the n_{th} mesh element, N is the number of mesh elements in the RVE, ε_{ij}^{LD} and σ_{ij}^{LD} are the component ij respectively of the elastic strain tensor and stress tensor in the n_{th} mesh element for the loading configuration LD .

The segmented and resampled 3-D reconstructions are meshed by converting the voxels into 8-node linear brick elements. The material properties, boundary conditions and thermal loads are then applied, depending upon the property to be measured. All the pre- and post-processing steps are implemented in Matlab routines. A rapid test of the consistency is performed by retrieving the properties of homogeneous volume sample with linear elastic properties assigned arbitrarily. The phase properties for the computational homogenization of the properties of the Ni-YSZ electrode material are listed in Table 20. The Poisson ratio is assumed temperature independent.

Table 20: Thermo-elastic properties of Ni and YSZ at room temperature and 800°C.

		Em (GPa)	ν (-)	CTE _{25-800°C} ($10^{-6}K^{-1}$)
Ni	RT	207	0.29	16.2
	800	140		
YSZ	RT	205	0.32	10.4
	800	163		

2.4.1.3 Volume and grid independence study

The elastic modulus and CTE measured on a $2.25 \mu\text{m}^3$ cubic sample for voxel sizes ranging from 20 to 200 nm are shown in Figure 33-a. Changes in the phase volume fractions can be non-negligible during the resampling of a brick mesh and were monitored. Variations are less than 1.5% for all the phases (0.2% for the pore phase) once the voxel is smaller than 100 nm (not shown). The average elastic modulus stabilizes at a similar value of the voxel size and the variations are then lower than 1%. The dependence of the CTE is less pronounced. Part can be ascribed to an artefact of the resampling. Within the variations of the volume fraction of 1.5%, the Ni volume fraction with a higher CTE monotonically decreases for decreasing voxel sizes, which is mainly mirrored by an increase of the YSZ volume fraction. At a voxel size lower than 100 nm, the error is estimated acceptable. The trends in the grid independence study performed on a sample volume of $6.375 \mu\text{m}^3$ are similar (Figure 33c-d). In this case however, the resampling does not cause variations of the volume fraction exceeding 0.07%. For voxels smaller than 100 nm, the variation in the averaged Young modulus is apparently negligible for the Young modulus and the CTE (both below 0.1%).

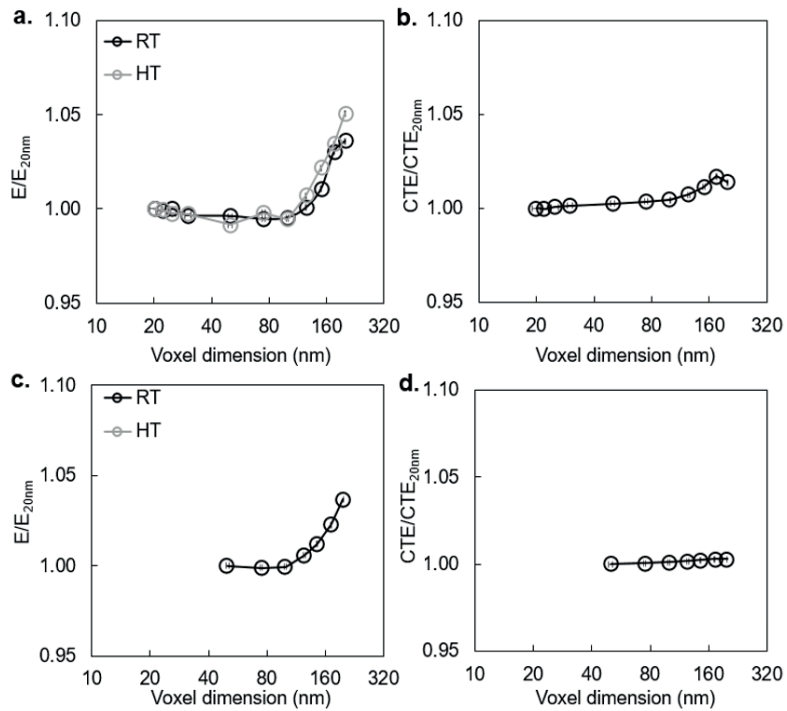


Figure 33: Grid independence of (a) the Young modulus and (b) CTE on a $2.25 \mu\text{m}^3$ sample; (c) Young modulus and (d) CTE on a $6.375 \mu\text{m}^3$ sample.

The volume independence study shown in Figure 34 is performed with a voxel size of 75 nm based upon the results of the grid independence study. The convergence behaviour is expected for kinematic uniform boundary conditions. The bars correspond to the scatter between the three directions, assuming an isotropic behaviour. For volume samples larger than $6.5 \mu\text{m}^3$, the variations of the average Young modulus are within 1.3% and 0.6% for the CTE, which is smaller than the scatter among the directions. The trend is the same for the measurements at room temperature and 800°C.

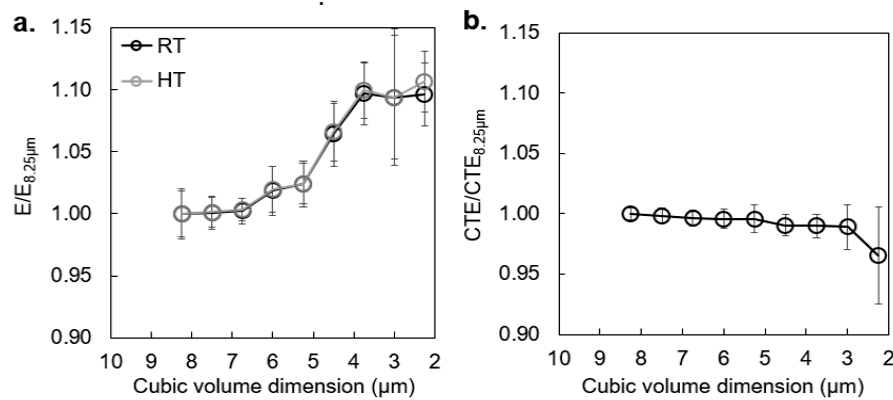


Figure 34: Volume independence study based on growing cubic samples for: (a) the Young modulus and (b) the CTE.

2.4.1.4 Results and discussion

Based upon the results of the grid and volume independence studies, homogenization calculations were performed with a voxel size of 75 nm and a volume size of $9^3 \mu\text{m}^3$. Table 21 shows that the results for the pristine sample from homogenization are close to the four-point bending and dilatometry measurements, but the remaining discrepancy requires further investigations.

Table 21: Young modulus and CTE obtained by experimental methods and 3-D imaging.

	Em (GPa)		CTE _{25-800°C} (10^{-6}K^{-1})
	RT	800 °C	
Dilatometry	-	-	12.4
Four-point bending	81±3	63±4	-
Computational homogenisation	91±1	67±2	12.8±0.05

The Ni-YSZ electrode is known to evolve upon operation. A discussion of Ni coarsening is outside the scope of the present study, e.g. [136],[137], which aims at quantifying the effects of microstructural changes on the thermo-elastic properties. The evolution of the metric and topological properties upon short stack operation follows expected trends. Table 22 lists the properties of the Ni and pore phases, which undergo the largest microstructural changes, whereas the volume fraction and coordination number of the YSZ do not vary significantly (not listed). In a simplified view, the evolution of the Ni phase is mirrored by that of the pore phase. Upon coarsening of the Ni phase indicated by the increase of the median phase diameter D₅₀, the contiguity and the intra-phase coordination number decrease. The trends in the pore phase are opposite, but the magnitude of the changes is smaller for most of the metrics. The connected and accessible TPB lengths concurrently decrease (not shown) which is detrimental for the electrochemical performance.

Table 22: Metric and topological properties of the pristine and aged Ni-YSZ volume samples.

	Pristine			Aged		
	Pore	Ni	Solid (Ni and YSZ)	Pore	Ni	Solid (Ni and YSZ)
Volume fraction	0.281 (0.009)	0.290 (0.008)	0.719 (0.009)	0.302 (0.010)	0.266 (0.009)	0.698 (0.010)
Contiguity	0.957 (0.012)	0.960 (0.011)	1.000 (0.000)	0.991 (0.004)	0.878 (0.055)	1.000 (0.000)
Average intra-phase coordination number	3.2 (0.1)	3.2 (0.1)	6.6 (0.0)	3.8 (0.1)	2.8 (0.1)	6.4 (0.0)
D ₅₀ (μm)	0.385 (0.009)	0.443 (0.014)	0.619 (0.017)	0.408 (0.012)	0.593 (0.024)	0.681 (0.016)

Because the contrast between the elastic modulus of Ni and YSZ remains small at room and high temperature (Table 20), microstructural quantifications were performed considering the composite as a porous single-solid phase material (Ni and YSZ together) to simplify the analysis. The microstructure of the solid phase also changes upon operation. The effects of the coarsening of the Ni phase on the lumped solid phase remains significant, as indicated by the increase of the median diameter and the

decrease of the coordination number (Table 22). Figure 35 further indicates that the neck size decreases. This overall follows the behavior expected during topological coarsening, where the solid structure network comprises larger particles connected by narrower necks, because of progressive pinching-off of the Ni phase.

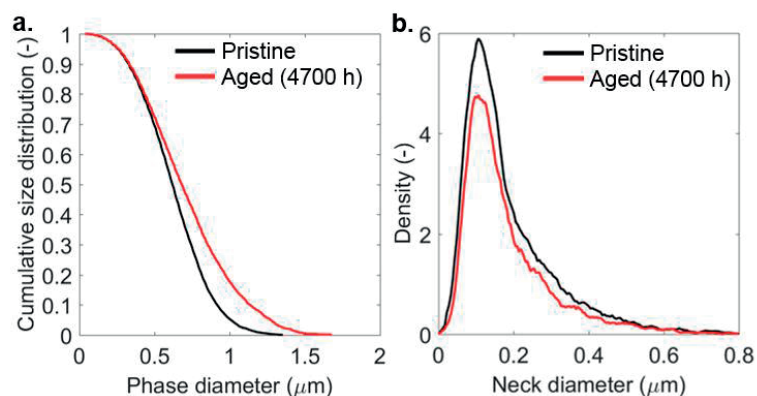


Figure 35: (a) Phase and (b) neck size distribution of the solid phase (Ni and YSZ together) before and after aging.

Figure 36a-b shows that the computed mean Young modulus decreases after 4700 h, by 8.4% and 7.8% at room temperature and at high temperature, respectively. The bars correspond to the standard deviation among the 4 samples of $9^3 \mu\text{m}^3$. The slight difference between RT and HT is due to the temperature dependence of the elastic properties of Ni and YSZ, which influences the effects of the microstructural changes. At 800°C, the contrast between the elastic properties of YSZ and Ni is larger than at room temperature (see Table 1).

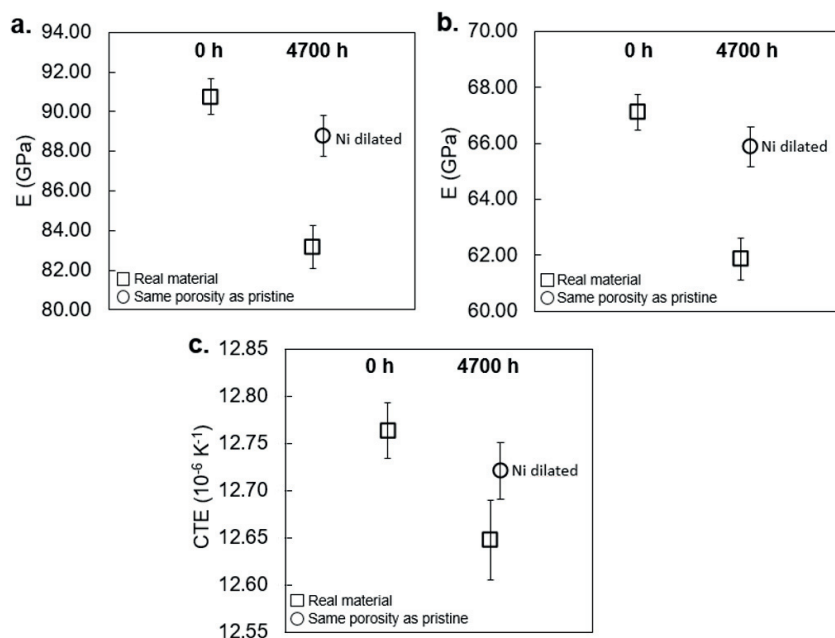


Figure 36: Ageing study of: (a) Young modulus at room temperature, (b) Young modulus at 800°C and (c) CTE.

The YSZ phase that undergoes limited morphological and topological changes during aging consequently influences the cermet elastic behaviour to a larger extent. This results in a smaller decrease of the Young modulus at high temperature. The CTE slightly decreases upon aging by less than 1% (Figure 36c). The elastic properties of the Ni-YSZ cermet are known to depend upon porosity. The measured volume fractions suggest a mild loss of Ni, which results in an increase of the porosity (Table 22). This observation has consequences for the long-term stability of the Ni-YSZ material, but the available data is not sufficient to support a detailed analysis. For the present study, the quantification of the separate effects of variations of the material volume fraction and of morphology and topology has been performed by manipulating the 3-D reconstructions of the aged samples. The Ni phase was dilated to maintain the average volume fraction (solid phase) constant between the aged and pristine samples. The results for the manipulated aged Ni-YSZ volume samples are included in Figure 36 by circles.

Figure 36a-b indicate that a variation of porosity lower than 2% modifies the Young modulus by 6.2% and 6% at room and high temperature, respectively, and the CTE by approximately 0.6%. The slight difference is consistent, because the Ni phase contributes less at high temperature. Apart from the measured mild loss of Ni, the changes in the morphology and topology quantified by the decrease of the coordination number and neck size distribution therefore contribute together to approximately one fourth of the decrease of the Young modulus caused by aging. Similarly, their effect on the limited decrease of the CTE is estimated of 40%.

The detected changes in the mechanical properties upon aging captured by homogenization are consistent with the microstructural analysis. However, their magnitude remains limited and the effects on the stack reliability may not be significant after 4700 h of SOFC operation. The measurement errors listed in Table 21 suggest that ascertaining such changes using four-point bending and dilatometry may be practically challenging.

2.4.2 Homogenised elasto-viscoplastic behaviour

The knowledge of the effective creep properties of GDLs in SOFC stacks is essential to investigate thermo-mechanical issues by numerical models, because creep deformations in GDLs are expected to alter the contact pressure on the active area (Chapter 3.3 and 3.4). Since GDL geometries are typically complex, discretisation of the domains in full detail is not possible in terms of computational requirements and simulation run-time. The replacement of the details of the geometry with a continuum domain to which effective creep properties are obtained by homogenization is instead more efficient. In this Chapter, the approach followed by Tsuda et al. [138] has been implemented. The properties were then used in the “Model v2” in Chapter 3.1, which is dedicated to the analysis of stack thermo-mechanical failures. We emphasise here that the application of homogenization to stack GDL as performed in the present study is not fully rigorous, but a practical approach, because in a simplified

view, a volume sample of the same size as that used as “RVE” sampled anywhere in a stack will likely contain e.g. the cell, or higher volume fraction of MIC, etc.

A 2-D simplification of the theory was used by Molla et al. [31] to analyse the creep behaviour of a generic metallic SOFC GDL design. The micro-model was a 2-D RVE of the GDL in frictionless contact on the upper and lower side by mechanical contact with two rigid surfaces, which represent respectively the cell and the MIC. The study aimed at describing the initial non-linear macro-strain upon applied mechanical load by a dimensionless function that accounts in an averaged manner for the dimensional and geometric changes of the structure.

The present study follows the 3-D implementation presented by Tsuda et al. [138], without determination of the dimensionless function by Molla et al. [31]. Besides the geometry of the GDL of the stack design modelled in Chapter 3.1, a test case was used for the validation of the creep macroscopic constitutive model. Once the computational homogenization process is validated by comparison with the published results, the approach is used to simulate and post-process the micro-model simulations of the SOFC GDLs, to determine their anisotropic creep properties.

2.4.2.1 Macroscopic constitutive modelling of creep behaviour

The analysis starts with the homogenization of the elastic properties following the description in Paragraph 2.4.1. A summary of the approach proposed by Tsuda et al. [138] for the creep behaviour is provided in this section. Local small deformations are assumed for the identification of the parameters of the material constitutive law, which does however not prevent that the large dimensional changes occur in the structure upon applied deformation. The possibility for structural instabilities at the RVE scale such as buckling is not considered. The material constitutive law of the dense material is linear elasticity without rate-independent plasticity, and creep following Norton law, which applies only to the secondary creep regime (i.e. primary creep is not considered). The approach is based on the quadratic strength function, which is an extension of Hill’s orthotropic incompressible yield function and is valid for a porous single solid phase material. This means that the approach presented in this section cannot be applied directly to the case of heterogeneous materials comprising solid phases that exhibit differences in creep behaviour, such as SOFC electrodes. Residual stresses in the modelled parts, generated e.g. by the manufacturing, are also neglected.

$$\dot{\varepsilon}_{ij}^{crp} = \frac{3}{2} A (\sigma_{eq})^{n-1} s_{ij} \quad (47)$$

where $\dot{\varepsilon}_{ij}^{crp}$ is the creep strain rate tensor, s the deviatoric part of the stress tensor, A and n are material properties, namely the creep power law multiplier and the stress exponent of the bulk material. The equivalent Von Mises stress σ_{eq} is defined as:

$$\sigma_{eq} = \sqrt{\frac{3}{2} s_{ij} s_{ij}} \quad (48)$$

The macroscopic constitutive model here developed uses the macro-stress and macro-strain computed from six FEM simulations to provide the anisotropic creep properties of the homogenised material. The computed macro-strain E_{ij}^{tot} is defined as the sum of elastic macro-strain E_{ij}^{el} and creep macro-strain E_{ij}^{crp} :

$$E_{ij}^{tot} = E_{ij}^{el} + E_{ij}^{crp} \quad (49)$$

Calculation of the equivalent macro-stress in the presence of anisotropy is introduced by Tsai and Wu [139], who have developed a formulation for the computation of the strength in anisotropic solids. This formulation has then been applied as plastic flow rule for metallic sandwich core structures [140] and open-cell nickel foams [141] as well as for developing macroscopic models of anisotropic creep [138,142]. It is expressed as:

$$\Sigma_{eq} = \sqrt{\frac{3}{2} \Sigma_{ij}^T M_{ij} \Sigma_{ij}} \quad (50)$$

where M_{ij} is a matrix containing the anisotropy factors. Using Equation (50) as expression of the equivalent stress, and including the deviatoric operator factors into M , the modification of Equation (47) for the creep macro-strain becomes:

$$\dot{E}_{ij}^{crp} = \frac{3}{2} A (\Sigma_{eq})^{n-1} M_{ij} \Sigma_{ij} \quad (51)$$

If the domain of the macro-model is isotropic and incompressible, M reduces to the deviatoric operator I_d , expressed as:

$$I_d = \begin{bmatrix} 2/3 & -1/3 & -1/3 & 0 & 0 & 0 \\ -1/3 & 2/3 & -1/3 & 0 & 0 & 0 \\ -1/3 & -1/3 & 2/3 & 0 & 0 & 0 \\ 0 & 0 & 0 & 2 & 0 & 0 \\ 0 & 0 & 0 & 0 & 2 & 0 \\ 0 & 0 & 0 & 0 & 0 & 2 \end{bmatrix}$$

The matrix M is independent of the applied macro-strain rate \dot{E}^{tot} , elastic modulus and creep power law multiplier A of the base material. It is in contrast dependent upon the geometry of the structure and creep exponent of the base material. Calculation of the terms of each line of the matrix M require the simulation of the six micro-models under respectively loading mode uniaxial XX, YY, ZZ and shear XY, XZ, YZ. The conditions are listed in Table 23, and the applied macro-strain rate \dot{E}^{tot} is the same for all loading modes.

Table 23: Kinematic equations of the boundary conditions at the RVE for the six loading modes.

uniaxial XX	uniaxial YY	uniaxial ZZ
$u_x^i = \frac{x^i}{L_x} E_{xx}^{el}$	$u_x^i = 0$	$u_x^i = 0$
$u_y^i = 0$	$u_y^i = \frac{y^i}{L_y} E_{yy}^{el}$	$u_y^i = 0$
$u_z^i = 0$	$u_z^i = 0$	$u_z^i = \frac{z^i}{L_z} E_{zz}^{el}$
shear XY	shear XZ	shear YZ
$u_x^i = \frac{y^i}{L_y} E_{xy}^{el}$	$u_x^i = \frac{z^i}{L_z} E_{xz}^{el}$	$u_x^i = 0$
$u_y^i = 0$	$u_y^i = 0$	$u_y^i = 0$
$u_z^i = 0$	$u_z^i = 0$	$u_z^i = \frac{y^i}{L_y} E_{yz}^{el}$

From each simulation of the six loading modes, the macro-stress is calculated as:

$$\Sigma_{ij}^{LD} = \frac{1}{V_{RVE}} \int_V \sigma_{ij}^{LD} dV = \frac{1}{V_{RVE}} \sum_{n=1}^N \sigma_{ij}^{LD} V_n \quad (52)$$

The macro-stress for each loading mode is then used to compute the components of the matrix M as follows (compare with Equation (51)):

$$M = \begin{bmatrix} \frac{2}{3} \left(\frac{1}{\Sigma_{xx}} \right)^2 \left(\frac{\Sigma_{xx} \dot{E}_{xx}^{crp}}{A} \right)^{\frac{2}{n+1}} & \frac{\dot{E}_{yy}^{crp}}{\dot{E}_{xx}^{crp}} M_{11} & \frac{\dot{E}_{zz}^{crp}}{\dot{E}_{xx}^{crp}} M_{11} & 0 & 0 & 0 \\ \frac{\dot{E}_{xx}^{crp}}{\dot{E}_{yy}^{crp}} M_{22} & \frac{2}{3} \left(\frac{1}{\Sigma_{yy}} \right)^2 \left(\frac{\Sigma_{yy} \dot{E}_{yy}^{crp}}{A} \right)^{\frac{2}{n+1}} & \frac{\dot{E}_{zz}^{crp}}{\dot{E}_{yy}^{crp}} M_{22} & 0 & 0 & 0 \\ \frac{\dot{E}_{xx}^{crp}}{\dot{E}_{zz}^{crp}} M_{33} & \frac{\dot{E}_{yy}^{crp}}{\dot{E}_{zz}^{crp}} M_{33} & \frac{2}{3} \left(\frac{1}{\Sigma_{zz}} \right)^2 \left(\frac{\Sigma_{zz} \dot{E}_{zz}^{crp}}{A} \right)^{\frac{2}{n+1}} & 0 & 0 & 0 \\ 0 & 0 & 0 & \frac{2}{3} \left(\frac{1}{\Sigma_{xy}} \right)^2 \left(\frac{\Sigma_{xy} \dot{E}_{xy}^{crp}}{A} \right)^{\frac{2}{n+1}} & 0 & 0 \\ 0 & 0 & 0 & 0 & \frac{2}{3} \left(\frac{1}{\Sigma_{xz}} \right)^2 \left(\frac{\Sigma_{xz} \dot{E}_{xz}^{crp}}{A} \right)^{\frac{2}{n+1}} & 0 \\ 0 & 0 & 0 & 0 & 0 & \frac{2}{3} \left(\frac{1}{\Sigma_{yz}} \right)^2 \left(\frac{\Sigma_{yz} \dot{E}_{yz}^{crp}}{A} \right)^{\frac{2}{n+1}} \end{bmatrix}$$

The procedure described above has been implemented to determine the components of the matrix M of a test case geometry first for validation, then for stack GDL sub-assemblies.

2.4.2.2 Validation of the homogenisation implementation

As verification of the developed homogenisation workflow, the geometry of the micro-model of the RVE is reproduced with few simplifications from Ref. [138] and is shown in Figure 37. It consists in a brazed plate-fin stack used as compact heat exchanger.

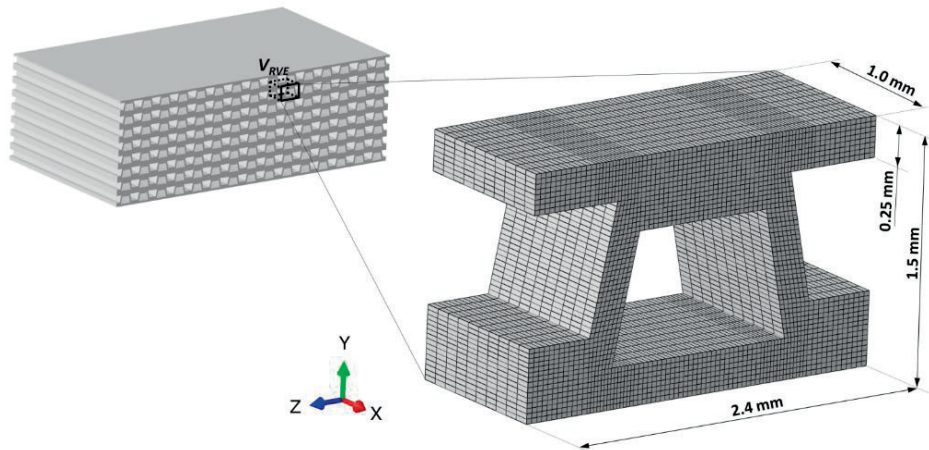


Figure 37: Periodic structure considered in this study and analysed RVE.

The simulation of the RVE consisted in imposing the boundary conditions listed in Table 23 and applied strain rate of 0.001 s^{-1} . The Von Mises stresses for the six cases are shown in Figure 38.

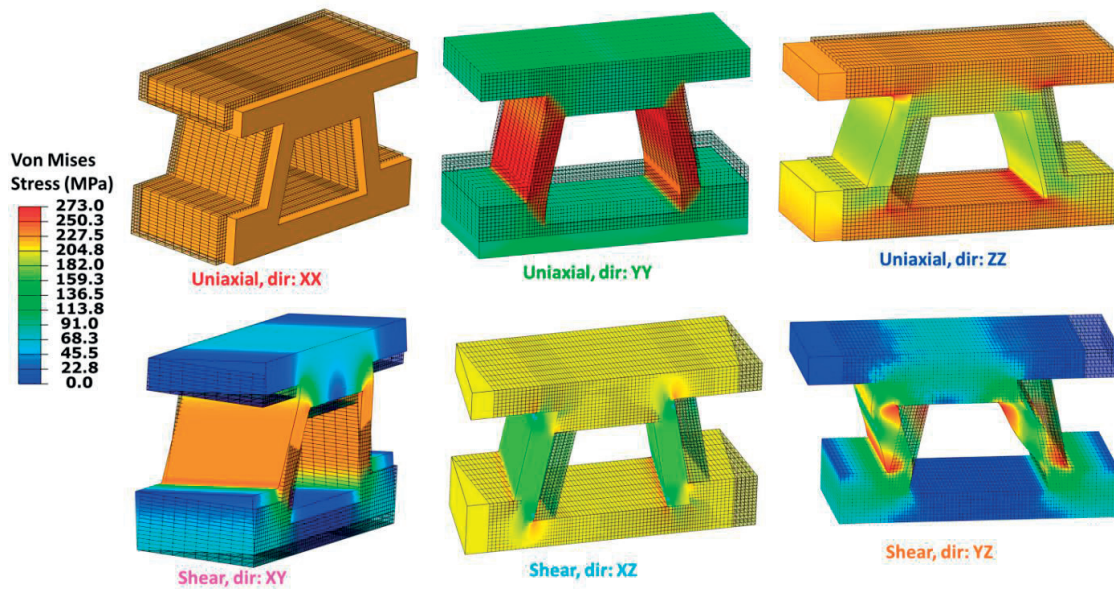


Figure 38: Von Mises stress in the analysed RVE for the six cases of loading. Meshes correspond to the undeformed configuration.

From the six simulations, the parameters of the M matrix are computed and plotted in Figure 39. For simplicity, only the diagonal terms are shown. The terms of M vary over the applied total macro-strain because of the change of the structure geometry upon deformation. It is worthwhile highlighting that in this study the creep constitutive law implemented in the micro-model is limited to the secondary regime. The approach formulation does not allow including primary creep, but it is expected that the initial non-linearity of the terms of M as a function of macro-strain capture only part of the behaviour in the reality.

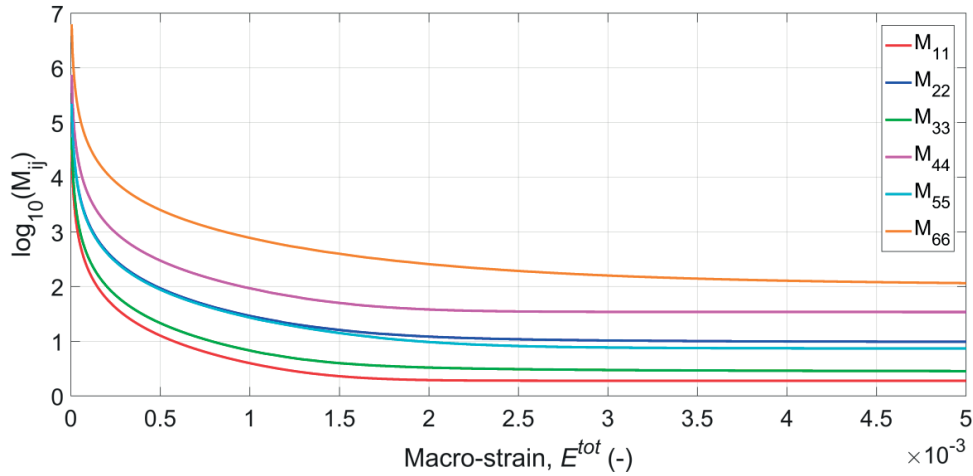


Figure 39: Values of diagonal terms of M matrix over applied macro-strain computed from this study.

In the present study, the initial non-linearity is neglected, following the approach by Tsuda et al. [138]. The matrix M is therefore determined when the terms M_{ij} become constant over macro-strain. From Figure 39, they can be considered constant starting from a value of macro-strain E^{tot} of 0.005. Figure 40 shows the macro-stress Σ as a function of macro-strain for each micro-model simulation (see Figure 40). At the value of macro-strain of 0.005, the macro-stress becomes also constant. From Equation (50) and (51), it can be inferred that Σ_{eq} does also not change and thus \dot{E}^{crp} is constant. The values of the M matrix computed for the present verification case are reported in black as follows, whereas the values in red correspond to the results published in Ref. [142] are shown for comparison:

$$M_{Valid} = \begin{bmatrix} \frac{1.90}{(1.94)} & \frac{-0.95}{(-0.97)} & \frac{-0.95}{(-0.97)} & 0 & 0 & 0 \\ -0.26 & 9.32 & -0.54 & 0 & 0 & 0 \\ \frac{-0.65}{(-0.97)} & \frac{-1.47}{(-1.82)} & \frac{2.80}{(2.18)} & 0 & 0 & 0 \\ 0 & 0 & 0 & \frac{33.75}{(44.28)} & 0 & 0 \\ 0 & 0 & 0 & 0 & \frac{7.32}{(7.08)} & 0 \\ 0 & 0 & 0 & 0 & 0 & \frac{94.32}{(78.05)} \end{bmatrix}$$

A further test was performed in the view of the implementation in the stack thermo-mechanical model (Chapter 3.1). A macro-model consisting in a simple rectangular hexahedron with the same dimensions as the RVE of the micro-model was simulated with the six loading modes and same prescribed macro-strain rate. The elastic stiffness matrix of the homogenised structure has been calculated according to the procedure described in Paragraph 2.4.1, using PBC as boundary condition. The obtained parameters

of the stiffness matrix (in GPa) are given as follows (black: values obtained in this work, red: values from Tsuda et al. [138]):

$$D_{valid} = \begin{bmatrix} 79.88 & 9.78 & 20.30 & 0 & 0 & 0 \\ 79.59 & 9.78 & 22.39 & 0 & 0 & 0 \\ & 23.82 & 8.79 & 0 & 0 & 0 \\ & 21.01 & 11.60 & 0 & 0 & 0 \\ & & 58.87 & 0 & 0 & 0 \\ & & 63.06 & 0 & 0 & 0 \\ & & & 11.01 & 0 & 0 \\ & & & 10.34 & 0 & 0 \\ & sym & & & 22.63 & 0 \\ & & & & 23.40 & 0 \\ & & & & & 3.14 \\ & & & & & 4.73 \end{bmatrix}$$

The parameters of the stiffness matrix here calculated are in good agreement with those reported by Tsuda et al. [138]. The creep behaviour predicted by the macro-model (homogeneous cubic computational domain) and the micro-model were compared and are shown in Figure 40. The macro-model and the values reproduced from Ref. [138] are included as well in Figure 40. The relatively large difference in macro-stress between the curves of the six loading modes indicates a significant anisotropy of the analysed structure. Furthermore, the relevantly lower macro-stress in XX, YY and ZZ compared to the base material tested in uniaxial loading mode, and XY, XZ and YZ compared to the base material tested in shear loading mode, show how the geometry significantly increases the creep compliance of the structure.

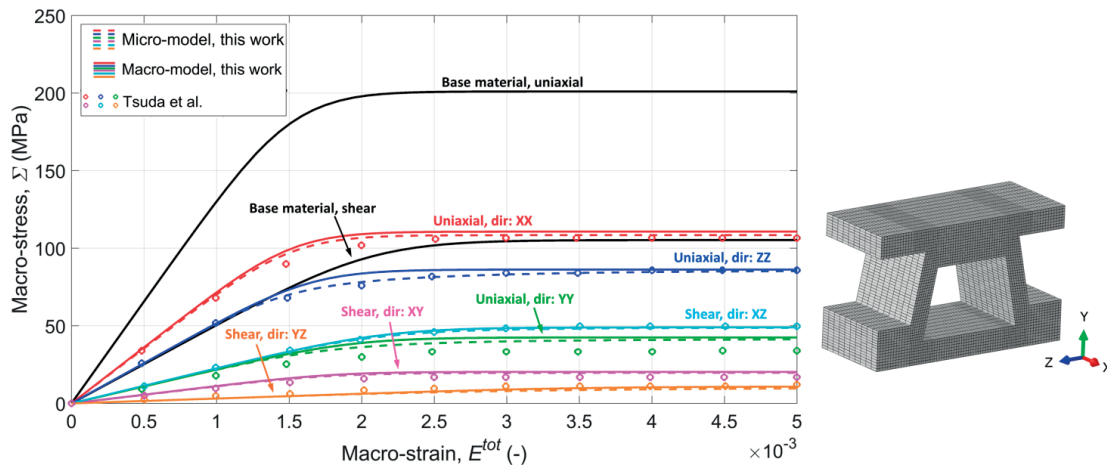


Figure 40: Macro-stress versus Macro-strain computed from micro- and macro- model simulations (in dashed and continuous line, respectively). Data points, reproduced from Tsuda et al. [138], and the simulated mechanical behaviour of the base material (in black continuous lines) are plotted for comparison.

2.4.2.3 Application to SOFC GDLs

The validated homogenisation workflow is used to determine the homogenised creep properties of different GDL geometries for implementation in the SOFC stack design analysed in Chapter 3.1. The geometries of the micro-models of the GDLs are here not reported because they are proprietary. Temperature-dependent elastic and creep properties of the bulk materials were implemented in the micro-model and simulation runs performed for the six independent loading cases, using a prescribed macro-strain of 0.001 s^{-1} . The anisotropy matrix M was computed for each GDL geometry by using the macro-stress and macro-strain computed by the six simulations following the approach described previously. The results of the computations are provided hereafter for different geometries and implemented into the stack model.

$$M_1 = \begin{bmatrix} 2.60 & -1.29 & -1.30 & 0 & 0 & 0 \\ -0.54 & 11.38 & -4.16 & 0 & 0 & 0 \\ -0.24 & -3.59 & 5.34 & 0 & 0 & 0 \\ 0 & 0 & 0 & 18.78 & 0 & 0 \\ 0 & 0 & 0 & 0 & 10.78 & 0 \\ 0 & 0 & 0 & 0 & 0 & 11.26 \end{bmatrix} \quad M_3 = \begin{bmatrix} 1.79 & -0.74 & -0.80 & 0 & 0 & 0 \\ -0.76 & 1.52 & -0.76 & 0 & 0 & 0 \\ -0.76 & -0.72 & 2.61 & 0 & 0 & 0 \\ 0 & 0 & 0 & 4.77 & 0 & 0 \\ 0 & 0 & 0 & 0 & 5.41 & 0 \\ 0 & 0 & 0 & 0 & 0 & 5.24 \end{bmatrix}$$

$$M_2 = \begin{bmatrix} 1.75 & -0.87 & -0.86 & 0 & 0 & 0 \\ -0.86 & 1.72 & -0.86 & 0 & 0 & 0 \\ -0.00 & -0.86 & 1.81 & 0 & 0 & 0 \\ 0 & 0 & 0 & 5.17 & 0 & 0 \\ 0 & 0 & 0 & 0 & 6.11 & 0 \\ 0 & 0 & 0 & 0 & 0 & 5.20 \end{bmatrix} \quad M_4 = \begin{bmatrix} 1.30 & -0.64 & -0.64 & 0 & 0 & 0 \\ -0.64 & 1.29 & -0.64 & 0 & 0 & 0 \\ -0.00 & -0.64 & 1.30 & 0 & 0 & 0 \\ 0 & 0 & 0 & 3.90 & 0 & 0 \\ 0 & 0 & 0 & 0 & 4.05 & 0 \\ 0 & 0 & 0 & 0 & 0 & 3.89 \end{bmatrix}$$

3 Thermo-mechanical modelling of SOFC stacks

3.1 Model description

The stack design analysed in this study is based on planar anode supported SOFC and is operated within the intermediate-temperature range, i.e. between 600 and 800 °C. The series of thermo-mechanical investigations presented in this Chapter uses an uncoupled thermo-electrochemical and thermo-mechanical approach. The 3-D temperature field over the computation domain during polarization is first simulated using a thermo-electrochemical model for a variety of operation conditions, then imported into the FEM thermo-mechanical model [12,143–145]. The computational domain corresponds to a complete repeating unit in a stack. The stack assembly is simulated first as an initialisation sequence, followed by long-term constant polarisation combined with thermal cycling. The information exchanged between the thermo-electrochemical and thermo-mechanical analyses is the 3-D spatial distribution of the temperature under SOFC polarisation. In the present work, the emphasis was placed on the thermo-mechanical reliability. The thermo-mechanical model was implemented in the commercial FEM code ABAQUS [60]. The control of material and interface property changes upon assembly, the importation of the temperature profile and the post-processing of the results is implemented in Matlab with calls to Python routines.

The development of the model required the testing of variations in the modelling assumption, following the progresses on the other aspects of this thesis. Two versions of the thermo-mechanical model are presented in this Chapter. They differ in terms of slight modifications of the geometry, mechanical properties of the material and mechanical interactions between the components. Hereafter, they are referred to as “Model v1” and “Model v2”, respectively.

3.1.1 Geometry and mesh

The study is focused on the SOFC stack design currently produced by SOLIDpower S.p.A (Italy). A repeating unit is the elementary item that is piled to obtain a SOFC stack that meets a target nominal power.

The repeating units in a stack are geometrically identical. Thus, with adequate simplifications, a subset of repeating units rather than the entire stack may be modelled to reduce significantly both the computational requirements and the simulation runtime. With the appropriate set of boundary conditions, the outcome of the stress analysis of a single repeating unit (SRU) will be relevant for a large part of the stack.

The geometry of the analysed SRU is shown in Figure 41. The planar anode-supported cell is composed of a NiO/Ni-YSZ anode approximately 270 μm thick. The YSZ electrolyte with a thickness of approximately 10 μm , and the 40 μm thick LSCF cathode are separated by a GDC compatibility layer approximately 5 μm thick. The electrolyte covers the whole area on the upper face of the anode (y -direction in Figure 41), whereas the footprint of both the GDC and cathode layers is the same and

corresponds to the active area. The inactive area, i.e. the region of the cell that is not covered by the GDC and the cathode, is approximately 4 mm wide. In the SRU model, the cell comprises the anode, electrolyte and compatibility layer, whereas the cathode is not considered. Its stiffness is lower than that of the other cell layers and the cathode layer has therefore a lower effect on the cell curvature and residual stress, including that of the other stack components.

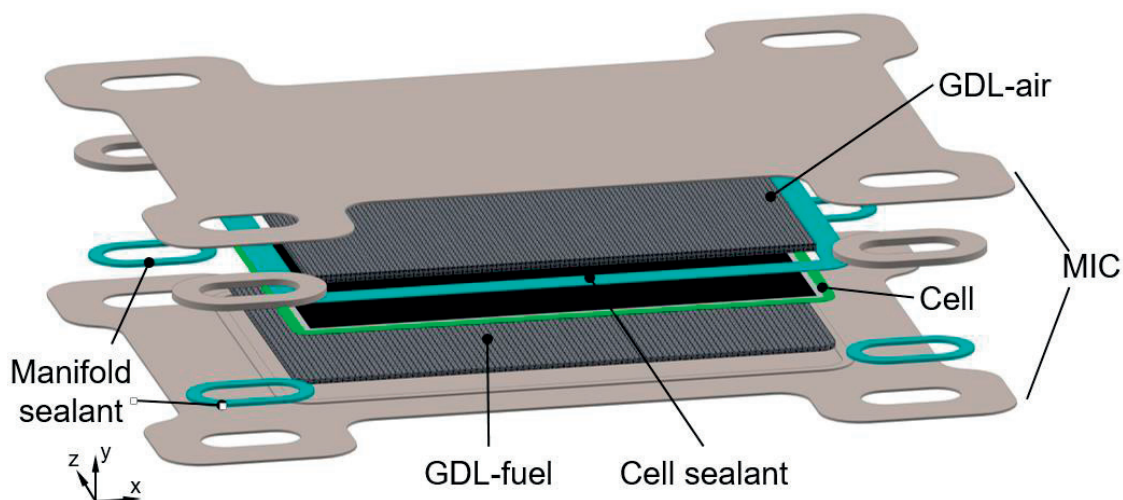


Figure 41: Exploded view of the geometry of the SRU^g.

The MIC is made of metal. This stack design uses an integrated manifold configuration: in co-flow, the two manifolds on the left and right hand side (see Figure 41 for reference) are respectively the incoming and exhaust fuel streams; the opposite in counter-flow. The air stream is provided externally, from the left to the right hand side of the SRU. To ensure the electrical contact between the MICs and the cell, as well as the distribution of gas over the active area, two pairs of GDLs are inserted, each of them on the two sides of the cell. In the present study, each pair has a first layer in contact with the cell electrodes and another for gas distribution on the MIC side. In Figure 41, the GDL pair on the cathode side is referred to as “GDL air”, whereas that on the anode side as “GDL fuel”. Contact pastes are usually deposited on the contact interfaces of the GDLs before the assembly of the stack. In this work, the mechanical properties of such interlayer with unknown properties were approximated as contact interface instead of solid elements (see Paragraph 3.1.4 for the details on the numerical implementation).

The repeating unit comprises two sealing geometries to seal the two gas compartments: the cell sealant, joining the inactive area of the cell with the MIC, and the manifold sealants, placed between

^g Reproduced with permission from J. Electrochem. Soc., 78, (2017). Copyright 2017, The Electrochemical Society.

two contiguous MICs. They are both made of a barium-calcium-aluminosilicate glass-ceramic type material (BCAS).

In “Model v1”, the upper layer of the “GDL air” has the footprint as the active area. This means that the assembly load is supported by the manifold sealants and by the cell active area. To study the effect of design variations on the stack reliability, the “Model v2” considers a larger “GDL air” plate, which can go in contact with the cell sealant. This entails that part of the assembly load may be supported also by the cell sealant. For further modelling assumption discussions are provided in Paragraph 3.1.4.

In the implemented geometries of both SRU model versions, the computer-aided design (CAD) geometry is slightly simplified for tractable meshing of the parts. The influence of such simplified details on the simulation results is expected to be negligible. Furthermore, the in-plane dimensions of the porous layer of “GDL fuel” were slightly adjusted to prevent numerical issues in the contact simulation, i.e. scratching between layers with contrast in stiffness, which may cause numerical issues.

A main effort in the present study was the investigation of the effects of component geometrical imperfections. A workflow, the mesh and modelling assumption, among others, were developed to perform simulations with idealised as well as geometrically imperfect SRU components. In the idealised case, the model comprises one SRU, to reduce the computational requirements and the simulation runtime. In the second case, two identical SRUs are modelled, to investigate the effects of the component with dissimilar shapes over the two SRUs. The details of the implementation of the component geometrical imperfections are provided in Paragraph 3.1.5. The model with one SRU is composed of approximately 350'000 mesh elements, whereas the number of mesh elements is almost doubled for the model with two SRUs. The number of elements may seem low, but the margin for refinement is low for tractable runtime, which are currently in the range of 1-2 days (on 1 node cluster: 14 cores each, 2.2 GHz, 128 Gb RAM), because of the many interfaces. The mesh and the element types used to discretise the components of the SRU models of this work are shown in Figure 42. The rationale behind the choice of the different element types is discussed hereafter.

To compute the stresses with adequate accuracy, the aspect ratio of the mesh elements (i.e. the ratio of the longest to the shortest dimension of the element) must be maintained within reasonable limits. However, meshing of the thinnest components in the SRU model (i.e. electrolyte, compatibility layer and cathode) by solid elements would lead to a mesh excessively fine and thus to increased computational requirements. In the present SRU models, conventional shell elements were used to discretise these thin layers. Conversely to solid elements, the thickness is not modelled in conventional shell elements, but defined as element property. They possess six nodal degrees of freedom (translation and rotation along the three directions). In this work, the type of selected shell elements was second-order, reduced integration, for improved accuracy and reduced computational requirements, respectively. The aspect ratio issue is less severe for the anode, because it is thicker.

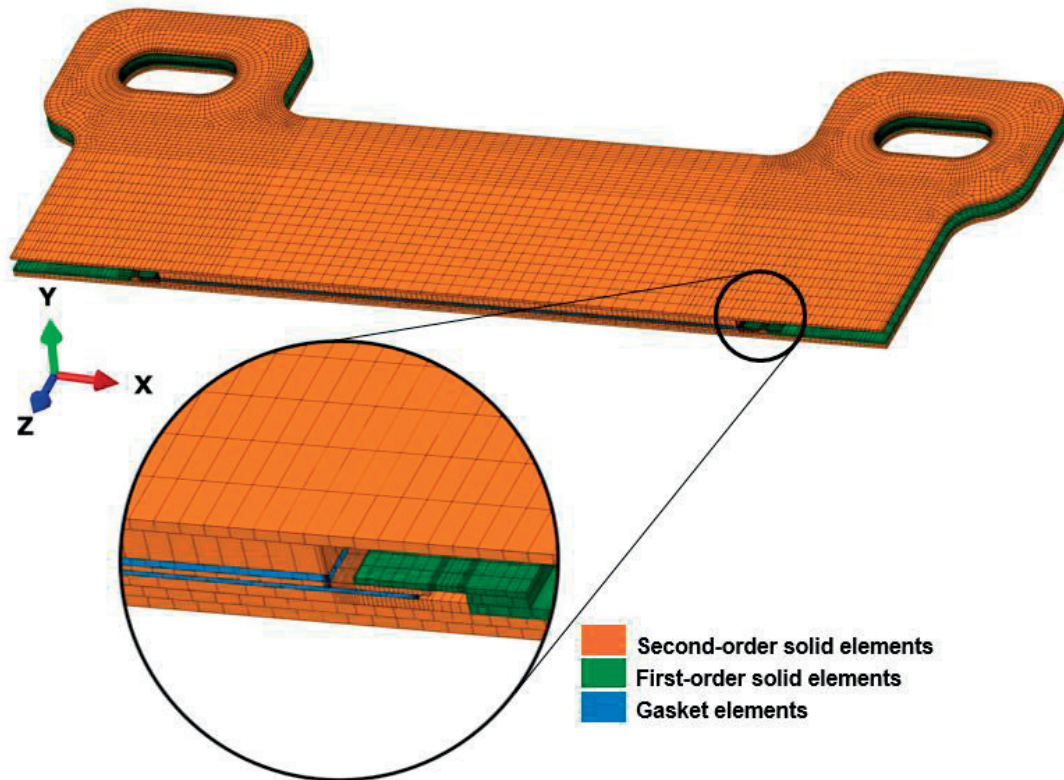


Figure 42: Overview of the mesh.

In this work, the reduction strain of the anode was simulated by imposing an artificial volumetric shrinkage, which requires solid mesh elements. In addition, since the cell bends upon thermal cycling, the use of second-order mesh elements is recommended for improved accuracy of the computed stresses. Hence, the anode was meshed with 3-D second-order, reduced-integration solid elements. Simulation tests comprising MIC geometrical imperfections showed that the use of first-order, reduced integration solid elements for both the MICs and the GDLs leads to severe numerical inaccuracies on the computed contact pressure on the active area. The best trade-off between computational requirements and accuracy was obtained by discretising the MIC and the GDL plates (both on the air and fuel sides) with 3-D second order, reduced integration, solid elements, whereas 3-D gasket elements were used for the second GDL layers. In gasket elements, the in-plane and through-the-thickness mechanical behaviour are uncoupled (for further details, see Chapter 1.5). Since the GDLs transmit the contact pressure between the MICs and the cell, gasket elements used for meshing such layers must include the through-the-thickness mechanical behaviour. The in-plane mechanical behaviour (also known as membrane behaviour) is included for those GDLs that can withstand shear and tensile/compressive stresses along the in-plane direction caused e.g. by the mechanical interaction with the interfaced components, at the cost of higher computational requirements. In the present two SRU model versions, the gasket elements used to mesh the GDL fuel included both mechanical

behaviours, whereas only the through-the-thickness mechanical behaviour was enabled for the mesh elements of the GDL air.

Very similar results were obtained during comparative simulations between first- and second-order solid elements for the sealants, the metal spacers and the metallic frame. However, the simulation runtime was higher by about 20% for the case with second-order solid elements. This was mostly due to the several contact interfaces (sealants with the metallic parts and the cell), which in the case of second-order elements require solving a higher number of equations by the contact algorithm. Hence, first-order, reduced integration, solid elements were selected to mesh the sealants, and the adjacent metallic parts.

Significant reduction of the computational requirements and simulation runtime was achieved by a careful assignment of the “master” and “slave” definition of the surfaces involved in the contact interface (see Chapter 1.5) and by the adequate mesh refinement of the parts in contact. In the contact pairs over the cell area of the SRU models, the master property was assigned to the stiffer materials, i.e. the cell and the GDLs channelled plates, whereas the slave property to the GDLs porous layers.

The current understanding of the mechanical failure of sealants during combined long-term operation and thermal cycling is largely imperfect. Failures can arise because of a combination of microstructural changes in or near the sealant (both bulk and interfaces), mismatches in the coefficients of thermal expansion of the joined layers, accumulation of plastic strain in the stack components and stack-scale external loading. A decrease of the thickness of the sealant reduces the stored energy and hence the driving force for crack propagation. Procedures that automatically modify the component dimensions were developed using Matlab routines to study such effects. The variations in the thickness of the sealant were compensated by that of the other components to maintain the total thickness of the SRU constant.

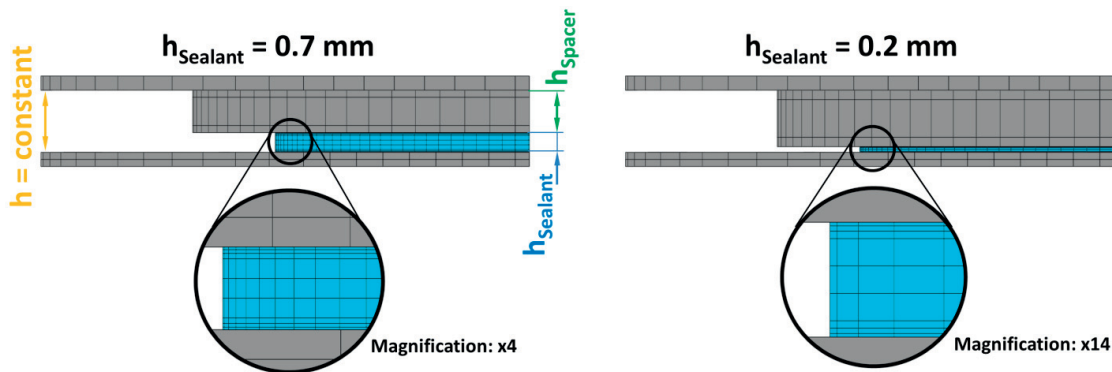


Figure 43: Close-up view of a sealing region, where the mesh is automatically adjusted to modify the component thickness.

Figure 43 illustrates the two cases used here to investigate the failure at the interfaces (see Chapter 3.4). The cases were successfully tested to ensure that the modification of the thickness does not alter the tracking of the surfaces at the interfaces. The mesh shown in Figure 42 is already fine, but not yet

sufficient and to allow capturing adequately singularities at biomaterial interfaces and e.g. simulate the propagation of a crack. Tests showed that it is sufficient for investigating the effect on the overall SRU deformation and comparative studies of the stress fields.

3.1.2 Mechanical properties of the materials

The thermo-mechanical properties of the materials in the SRU are listed in Table 24 and 25, for “Model v1” and “Model v2”, respectively. The Young’s modulus, E_m , is mainly dependent upon the porosity p of the material and temperature T . The symbols ν , σ_y and ε_{red} refer to respectively the Poisson’s ratio, yield strength and reduction strain. Table 24 and 25 provide only values at room temperature and 1073 K, but the values implemented in the FEM model include temperature dependence over the full range for most of the materials (except for the elastic properties of NiO/Ni-YSZ in “Model v2”).

All ceramic components and sealants are assumed to follow a linear elastic behaviour, whereas plasticity with a isotropic hardening law is used for the metallic parts. In this work, creep was implemented in all SRU materials. The model used as constitutive law for creep is the Norton power law expression [81], which correlates the stress σ_{ij} to the creep strain rate $\dot{\varepsilon}_{ij}^{crp}$ as:

$$\dot{\varepsilon}_{ij}^{crp} = B e^{(-Q/RT)} \left[\frac{3}{2} (\sigma_{eq})^{n-1} s_{ij} \right] \quad (53)$$

where B , Q , T , R and n are respectively the pre-exponential factor, the creep activation energy, temperature, universal gas constant and stress exponent. The creep parameters for the strain-hardening form of the creep constitutive law (which includes both primary and secondary creep regime) were measured for the Ni-YSZ anode, see Chapter 2.2. However, numerical convergence of the SRU model with the implementation of the creep constitutive law and the estimated parameters proved unsuccessful, despite several tests. Numerical failure occurred at the early stages of stresses relaxation by creep in the anode, i.e. right after the simulated reduction. Potential sources of numerical issues are the relatively fast and large deformations caused by the primary creep. The analysis of the topic remains of interest, which warrants dedicated future efforts. Therefore, for both “Model v1” and “Model v2” the creep properties of the Ni-YSZ anode were taken from literature data [112].

Potential shrinkages of YSZ, GDC, LSCF and that of the anode upon thermal cycling were not implemented in the SRU models of this work. A reason is that the outcome of the first analysis performed previously at the present scale suggests that the effect of at least a uniform shrinkage may be assessed separately [56].

The CTE values correspond to the total form, i.e. to the thermal expansion between the reference and a given temperature. The reference temperature for the CTE data is set to RT in the SRU models. Table 24 and 25 list the CTE values for all the materials in the SRU at the temperature of 1073 K (reference temperature: RT), but the model implementation comprises the temperature dependence over the complete range.

Table 24: Thermo-mechanical properties of the materials of the SRU for “Model v1”. Data from Ref. [15,68,103,104,110,112,121,128,146–155].

	T (K)	p (%)	ϵ_{red} (%)	E_m^a (GPa)	ν^a (-)	σ_y^a (MPa)	CTE ^a ($\times 10^{-6} \text{ } ^\circ\text{C}^{-1}$)	B (h^{-1}MPa)	Q (kJ mol^{-1})	n (-)
<i>Anode (oxidised)</i> (NiO-YSZ)	RT	19	-	124.9	0.39	-	12.37	-	-	-
	1073			119.9						
<i>Anode (reduced)</i> (Ni-YSZ)	RT	39	-0.01	72.5	0.39	-	12.41	1.040e+20	640	2.5
	1073			58.1						
<i>Electrolyte</i> (8YSZ)	RT	0	-	196.3	0.32	-	10.21	1.836e+07	320	0.5
	1073			148.6						
<i>Compatibility layer</i> (GDC)	RT	0	-	196.3 ^d	0.32 ^d	-	12.63	6.768e+04	264	1.0
	1073			148.6 ^d						
<i>Cathode contact layer</i> (LSCF)	RT	29	-	10 ^b	0.32	-	15.34	5.551e+10 ^e	392 ^e	1.7 ^e
	1073			10 ^b						
<i>MIC</i> (Crofer 22APU)	RT	0	-	216.0	0.3	248	12.80	1.222e+06	344	4.73
	1073			65.9		35				
<i>GDL fuel</i>	RT	93	-	0.37	0.1 ^b	0.9	16.20	7.170e+10	284	4.6
	1073			0.25		0.26				
<i>GDL air</i>	RT	93	-	0.39	0.1 ^b	1.7	12.80	3.380e+13	344	4.73
	1073			0.12		0.25				
<i>Sealants</i> (G18 ^f)	RT	0	-	67.4 ^c	0.28	-	11.10	1.627e+10	283	1.59
	1073			14.4 ^c		-				

^a Temperature-dependent values implemented in the model. Linear interpolation between available data points.

^b Assumed value

^c Arbitrary value of 0.2 GPa before sealing procedure

^d Values for YSZ

^e Values for dense LSCF

^f BCAS, glass-ceramic material

Table 25: Thermo-mechanical properties of the materials of the SRU for “Model v2”. Data from Ref. [15,68,103,104,110,112,121,128,146–155].

	T (K)	p (%)	ϵ_{red} (%)	E_m^a (GPa)	ν^a (-)	σ_y^a (MPa)	CTE ^a ($\times 10^{-6} \text{ } ^\circ\text{C}^{-1}$)	B (h^{-1}MPa)	Q (kJ mol^{-1})	n (-)
<i>Anode (oxidised)</i> (NiO-YSZ)	RT	9	-	142.6 ^g	0.39	-	12.37	-	-	-
	1073			112.2 ^g						
<i>Anode (reduced)</i> (Ni-YSZ)	RT	29	-0.01	81.1 ^g	0.39	-	12.41	1.040e+20	640	2.5
	1073			63.3 ^g						
<i>Electrolyte</i> (8YSZ)	RT	0	-	196.3	0.32	-	10.21	1.836e+07	320	0.5
	1073			148.6						
<i>Compatibility layer</i> (GDC)	RT	0	-	196.3 ^d	0.32 ^d	-	12.63	6.768e+04	264	1.0
	1073			148.6 ^d						
<i>Cathode contact layer</i> (LSCF)	RT	29	-	10 ^b	0.32	-	15.34	5.551e+10 ^e	392 ^e	1.7 ^e
	1073			10 ^b						
<i>MIC</i> (Crofer 22APU)	RT	0	-	216.0	0.3	248	12.80	1.222e+06	344	4.73
	1073			65.9	35	35				
<i>GDL fuel</i>	RT	93	-	CmpHmg	CmpHmg	0.9	16.20	CmpHmg	CmpHmg	4.6
	1073					0.26				
<i>GDL air</i>	RT	93	-	CmpHmg	CmpHmg	1.7	12.80	CmpHmg	CmpHmg	4.73
	1073					0.25				
<i>Sealants</i> (G18 ^f)	RT	0	-	67.4 ^c	0.28	-	11.10	1.627e+10	283	1.59
	1073			14.4 ^c						

a Temperature-dependent values implemented in the model. Linear interpolation between available data points.

b Assumed value

c Arbitrary value of 0.2 GPa before sealing procedure

d Values for YSZ

e Values for dense LSCF

f BCAS, glass-ceramic material

g Linear interpolation between RT and 1073 K (NiO-YSZ) and RT and 973 K (Ni-YSZ). Data from results in Chapter 2.2.3.

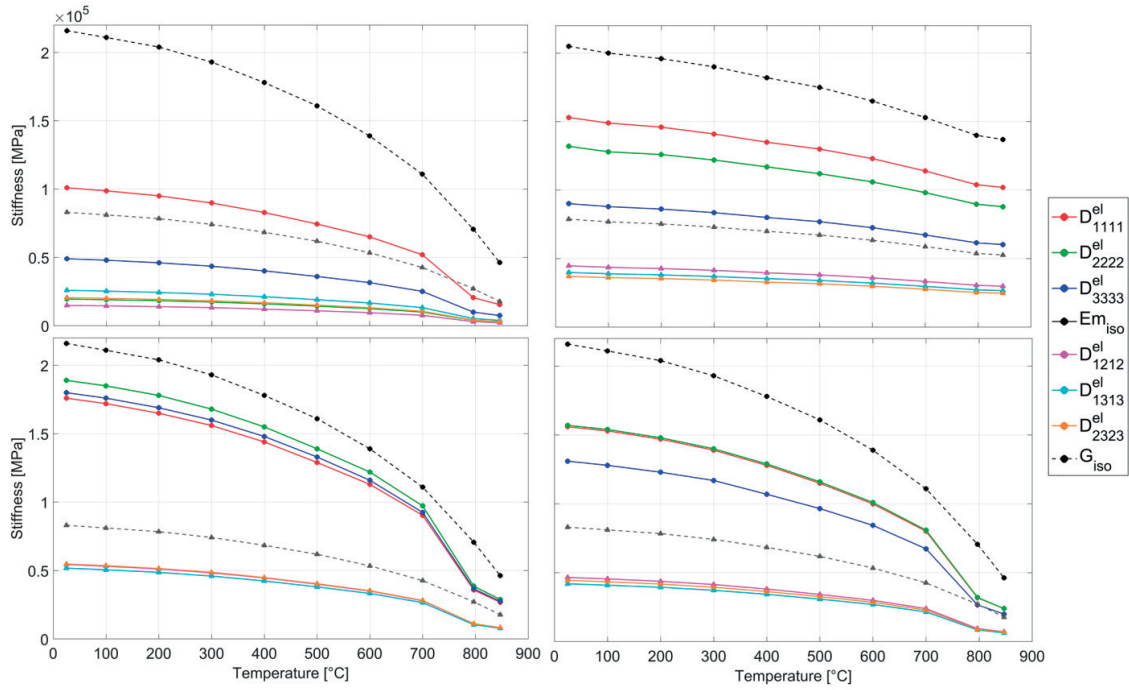


Figure 44: Temperature dependence of the anisotropic elastic properties of the GDLs materials obtained from computational homogenisation and implemented in the stack model.

The model version “Model v1” and “Model v2” differ in terms of level of refinement in the estimation of the mechanical properties of the GDLs. In the “Model v1”, the mechanical properties of the layers of both GDL air and fuel were estimated by expressions which scale the properties of the dense material. These laws provide reasonably accurate estimations for periodic material structures and isotropic behaviour at the macro-scale. Significant anisotropy was observed in the mechanical properties of the GDLs layers obtained by computational homogenisation, see Chapter 2.4. However, for first analysis and comparisons, these layers were all assumed isotropic in the “Model v1”. First estimate of the elastic modulus of the porous layers was obtained using Equation (54) [156]:

$$Em = 0.28(1 - \alpha)^2 Em_d \quad (54)$$

where Em_0 is the elastic modulus of the dense material, and α the porosity.

To estimate the creep properties of the Norton power law expression (i.e. valid only for the secondary creep regime) it was assumed that the struts of the porous layers deform in compression. In this case, Equation (55) has been proposed in the literature for calculating the effective creep strain rate of the porous media [157]:

$$\dot{\varepsilon}_{ij}^{crp} = B_d e^{(-Q/RT)} \left[\frac{3}{2} (\sigma_{eq})^{n-1} s_{ij} \right] \left(\frac{1 - \alpha}{3} \right)^{-n} \rightarrow B = B_d \left(\frac{1 - \alpha}{3} \right)^{-n} \quad (55)$$

The creep pre-exponential constants B_0 and B are here referred to the dense and porous materials, respectively. The effective mechanical properties were estimated using dense Crofer 22 APU [146] and

Nickel [158], respectively. The computed elastic modulus, yield strength and creep parameters are reported in Table 24. The Poisson's ratio was set at an arbitrary value of 0.10 (relatively high compressibility, because of the porous structures). In the "Model v2", the anisotropic elastic and creep properties of the GDLs layers were obtained from computational homogenisation, see Chapter 2.4, and indicated in Table 25 as CmpHmg (see Figure 44 for anisotropic elastic properties).

The elastic properties of the NiO/Ni-YSZ anode in "Model v1" and "Model v2" were respectively taken from literature data and measurements in Chapter 2.2. In the second case, the model uses data from linear interpolation between the values at RT and 800 °C, for NiO-YSZ, and between the values at RT and 700 °C, for Ni-YSZ (see also Figure 23), because in Chapter 2.2 no mechanical testing was carried out at intermediate temperatures. However, especially for NiO-YSZ a remarkable non-linear temperature-dependence of the elastic modulus is reported [110,159], because of the antiferromagnetic to paramagnetic structural transition of NiO at the Néel temperature of 250 °C. This behaviour may affect the conclusions from the simulation of the first stack heat-up, and should be considered in future studies.

For the anode material tested in this work, the reduction strain and the CTE were assumed the same as the literature data. For the glass-ceramic material, an artificial relatively low elastic modulus is implemented before the sealant curing, to minimise the contribution of the glass-ceramic pastes on the stresses in the SRU, because the glass-ceramic material is not yet crystallised. The elastic modulus of the glass-ceramic material is then changed throughout the simulation, see Paragraph 3.1.6 for further indications. ABAQUS allows the control of each set of material mechanical properties by a field variable which can be used as a flag. For the same material, switches or variation between sets of mechanical properties, such as caused by microstructural changes, e.g. Ni to NiO reduction or crystallization, can be implemented. Hence, by manipulating the field variables over the simulation steps, the modification of the mechanical properties can be controlled by the user. This modification was applied for instance to the simulation of anode reduction, i.e. the mechanical properties of the anode domain changed from those of NiO-YSZ to those of Ni-YSZ. Specific details about the numerical simulation of the anode reduction are provided in Paragraph 3.1.6.

3.1.3 Boundary conditions

The stack design considered here typically comprises around 70 cells. Therefore two limiting cases were treated to investigate the conditions of units or a cluster of units close to the middle of the stack or to the end plates. The first case is that of a stack made of an infinite number of repeating units, without variations in gas flow among the height i.e., approximating a real situation where (i) the analysed SRU is far from the end-plates (ii) the stack is relatively large (iii) the temperature profile is close to symmetric across the z direction and (iv) the loading system can accommodate differences in expansion along the

flow path. An intuitive approach for simulating such situation consists in enforcing modified periodic boundary conditions (referred hereafter as PBC) [19,56].

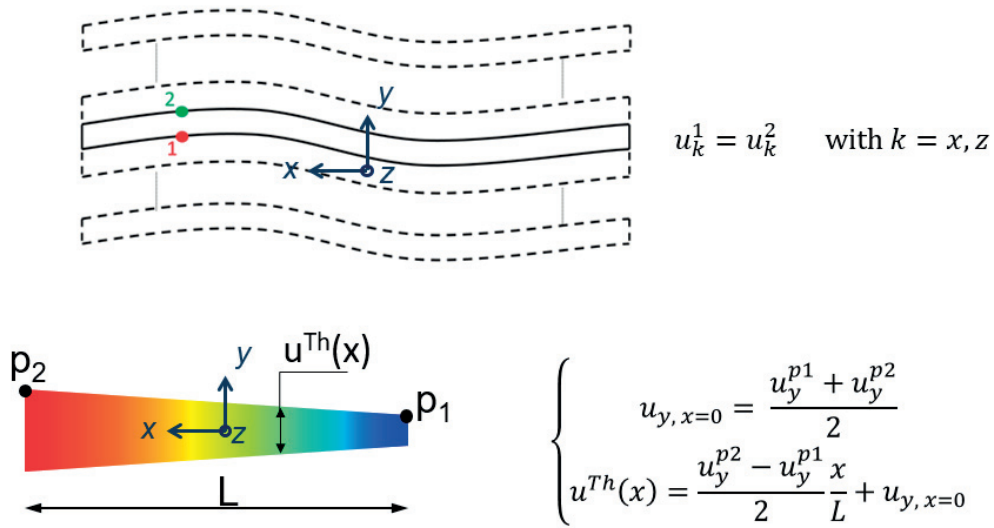


Figure 45: Schematic of the modified periodic boundary conditions applied on the lower and upper node sets of the repeating unit, and linear multi-point node equations involving nodal displacements (u) implemented in the model. The temperature increase along the flow path (positive x direction) is depicted qualitatively by a colour scale from blue to red.

With these boundary conditions, the periodicity of the displacements on the in-plane directions is enforced, whereas the respective nodes on the lower and upper MIC are allowed to rotate around the z -axis, as shown in Figure 45. This relative rotation is constrained to be the same for all nodes on which the PBCs are applied. In the case of SRUs, the temperature difference along the gas flow path causes the outlet air side of the stack to be hotter and thus to expand more than at the inlet.

The second case is that of SRUs close to the end plates or approximating a real situation closer to that of a short stack. Oppositely to the case of modified PBC, here the upper and lower MICs of the SRU are enforced to remain flat (FBC), whereas their rotation around the z -axis is allowed.

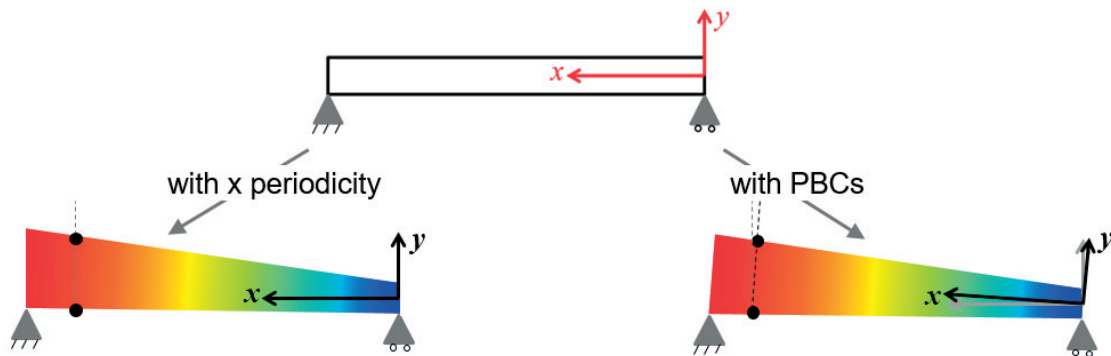


Figure 46: Schematic of the limitations using simple in-plane periodicity on the modelled SRU (on the left-hand side), and simplified configuration using modified PBC (on the right-hand side).

Figure 47 shows two simulated cases of SRU deformation with enforced MIC flatness (FBC) and modified periodic boundary conditions (PBC). In “Model v1” only PBC were implemented. To compare the effects of the position of the SRU in the stack, the “Model v2” was modified to consider either FBC or PBC.

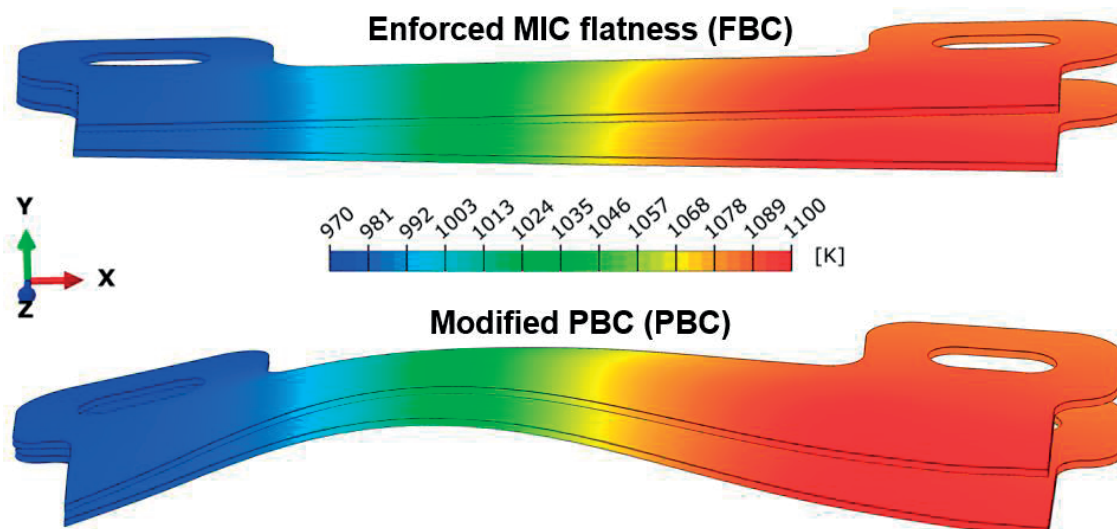


Figure 47: Representation of the simulated displacement of the upper and lower MICs of one SRU using enforced MIC flatness (FBC, on the top) and modified periodic boundary conditions (PBC, at the bottom).

In this work, considerable reduction of the computational requirements and simulation runtime was achieved because of the assumed symmetry of the stack along the z direction in terms of i) SRU geometry ii) temperature field under polarisation with co- and counter-flow configurations and iii) geometrical imperfections (see Paragraph 3.1.5).

3.1.4 Modelling of the mechanical interactions between the SRU components

The mechanical interactions between the components in a stack are complex. The properties are known to differ for the several interaction pairs that exist in a repeating unit and further, evolve during the assembly, manufacturing and most likely operation of the stack. The characterization of the several interaction properties is far-reaching and the dissemination of the results subject to confidentiality issues. The current knowledge on the interfacial properties is not yet sufficient for full detail simulation. Assumptions based on expected behaviour, assembly and testing experience and inspection of intermediate model results were used for the development of the SRU model. A reason for the distinction between “Model v1” and “Model v2” is the investigation of differences in the implemented interaction properties.

In this study, the mechanical interactions between two or more parts are approximated using either tie or contact. The tie (on surfaces $\partial\Omega_T$) consists in a surface-based constraint, which enforces identical displacements of the mesh nodes of the two surfaces throughout the whole simulation. This mechanical interaction is set to the interfaces between MICs parts and between the MICs and a face of both the GDL air and fuel.

The contact mechanical interaction comprises both a normal and a tangential behaviour model. In this study, the normal behaviour follows a “softened” non-linear pressure-overclosure relationship. The enforcement of this relationship is approximated by the penalty method, resulting in a contact force that is proportional to the penetration distance, hence allowing a certain inter-penetration of the contacting surfaces.

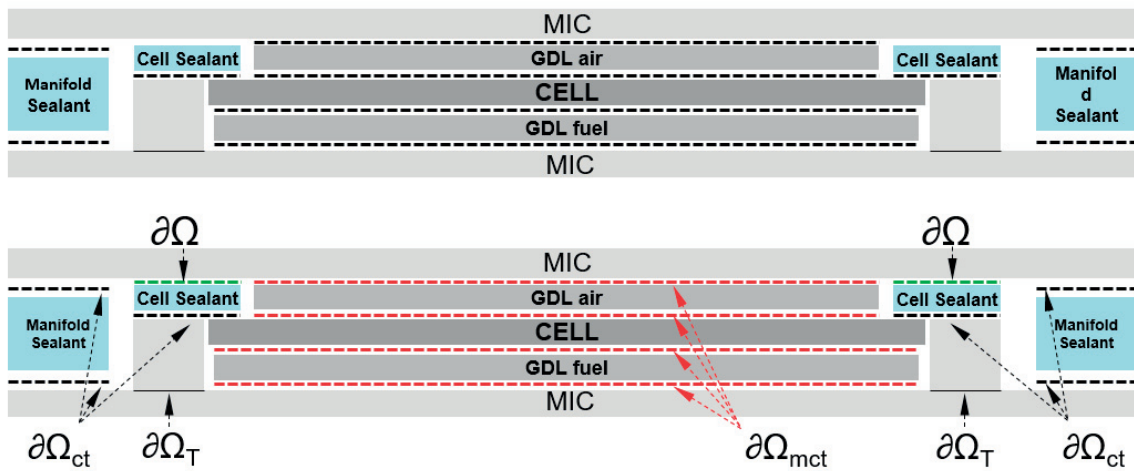


Figure 48: Schematic view of the mechanical interactions (shown in dashed lines) between the components for “Model v1” (upper) and “Model v2” (lower). Black solid lines ($\partial\Omega_T$): tie contact. Black dashed lines ($\partial\Omega_{ct}$): default non-linear pressure-overclosure relationship. Red dashed lines ($\partial\Omega_{mct}$): modified non-linear pressure-overclosure relationship. Green dashed lines (depicted by $\partial\Omega$): frictionless contact with detachment throughout the whole simulation.

In practice, the non-linear form of the pressure-overclosure relationship allows a better convergence and an acceptable overclosure as the contact pressure builds up. In both “Model v1” and “Model v2”, the pressure-overclosure relationship does not include separation behaviour of the contact surfaces (except for the interface between the MIC and cell sealant, in “Model v2”, see below), to reduce the computational requirements and the simulation runtime. Mechanical contacts were set for the interfaces within the GDLs layers and with the cell active area, between the cell sealant, the cell inactive area and the metallic frame, and for the interface of the manifold sealant with the spacer and the MIC, see Figure 48.

In the “Model v2”, the possibility for mechanical interaction between the upper MIC of each SRU and the cell sealant (domain $\partial\Omega$ in Figure 48) was investigated (see also Paragraph 3.1.1). This mechanical interaction was modelled by frictionless contact with detachment allowed.

For the interfaces of the GDL porous layers with the channelled plates and the cell active area, the default pressure-overclosure relationship (on surfaces $\partial\Omega_{ct}$ Figure 48 and Figure 49, black lines) was used in “Model v1”, which entails that independently of the potential tensile stresses generated at the contact interfaces, no separation is simulated. The slopes K_i and K_f refer to the initial and final penalty stiffness, respectively. K_f is equal to the material stiffness of the most compliant material between the two components in contact, whereas K_i is in the default relationship two orders of magnitude lower than K_f . Between the two linear trends, the contact pressure varies by a quadratic function. In the “Model v2”, K_i was reduced by about 8 orders of magnitude with respect to K_f (see Figure 48 and Figure 49, red lines). Implementing very low initial penalty stiffness, the simulated tensile stresses at the contact interface in the case of interface separation are negligible. This partially overcomes the need for expensive computation of the separation behaviour. In order to achieve numerical convergence with the modified pressure-overclosure relationship, the clearance at zero contact pressure is set to 0.005 mm. Matching of the two pressure-overclosure relationships was not carried out. However, the maximum deviation of the contact pressure (i.e. in the final penalty stiffness) between the two relationships is about 15%.

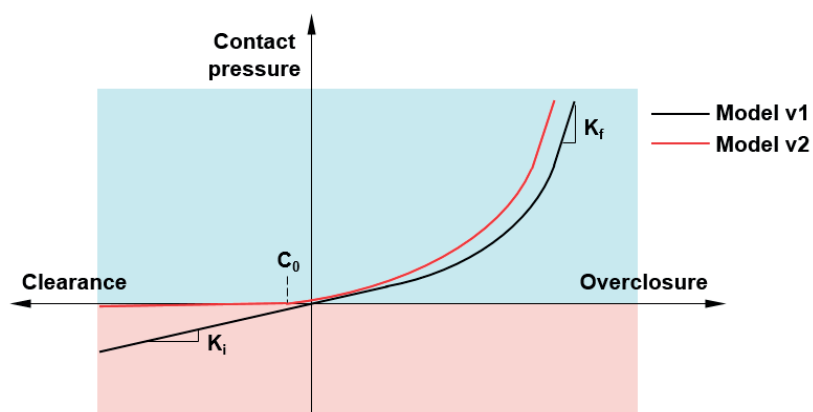


Figure 49: Non-linear pressure-overclosure relationships for “Model v1” (black line) and “Model v2” (red line).

The discretisation of the contact follows a surface-to-surface approach, because the normal directions of the surfaces in contact in the SRU are expected to remain close to opposite throughout the whole simulation. The surface-to-surface approach enforces contact conditions in an average sense over regions nearby the slave mesh nodes rather than only at individual slave nodes. Thus, large undetected penetrations of the master nodes into the slave surface are mitigated [60].

In the present analysis, the sliding between the components in contact is dominated by i) mismatches in thermal expansion and ii) the accommodation of the parts during the assembly of the stack with pre-deformed components (i.e. the MIC in this study). The magnitude of the relative sliding is expected to be of the same order as the characteristic mesh element length. Under this condition, the small instead of the large sliding formulation is preferred because computationally less expensive. In the small-sliding

tracking approach, a local tangent plane on the master surface of the contact pair is associated to the region nearby the slave node. This entails that the contact algorithm does not need to monitor the whole set of slave nodes for possible contact along the master surface [60].

For the tangential contact behaviour, the model uses a frictionless sliding approach until the end of the first heat up. Compared to other works where coefficients of friction of $0.1\div 0.2$ were used [19,54], this study therefore assumes that interfaces with e.g. contact or sealing pastes do not constrain the relative sliding of the parts in contact. Once the simulated temperature reaches the crystallisation temperature of the glass-ceramic sealants, i.e. at the end of the first stack heat-up (see Paragraph 3.1.6), a no-sliding condition was enforced for all contact interfaces (except for the interface between the MIC and cell sealant, in the “Model v2”), which aims at simulating the bonding caused by the sintering of both the contact pastes and the glass-ceramic sealants.

3.1.5 Implementation of component geometrical imperfections

The variations in the shape of the SRU components because of imperfections in their manufacturing or design alternatives are simulated by applying artificial deformations to the component. The developed procedure for implementing imperfections of the MICs in terms of flatness is illustrated in Figure 50. The implementation of the initial deformations requires first the measurement of the deflection of the MIC as a function of the in-plane directions (x and z, see step a. in Figure 50). A separate FEM model (hereafter referred to as “MIC model”) including only the metallic components of the SRU as the computation domain was implemented (see step b) in Figure 50) is then needed to compute artificial stress under deformation for importation in the full SRU model. The displacements along the y-axis (measured in step a)) are applied on each mesh node of the “MIC model” but in the opposite direction and the stresses computed (see step c) in Figure 50). Because the stress field has the only purpose of generating a deformation, the MIC model assumes linear elastic behaviour without plasticity for all the components. The implemented workflow approach then consists in the importation of the stresses from the “MIC model” into the homologous components of the SRU model. In the SRU model i) the parts are in their reference state at the start of the simulation, i.e. they are all un-deformed and defined by the ideal CAD geometry, and ii) the boundary condition of imposed displacement at the mesh nodes (like in step c) in Figure 50) is not imported. To fulfil the force equilibrium of the model, each metallic component deforms following the shape measured experimentally (step a) in Figure 50). From this point on, the simulation of the SRU model is continued with the initialisation sequence (see Paragraph 3.1.6).

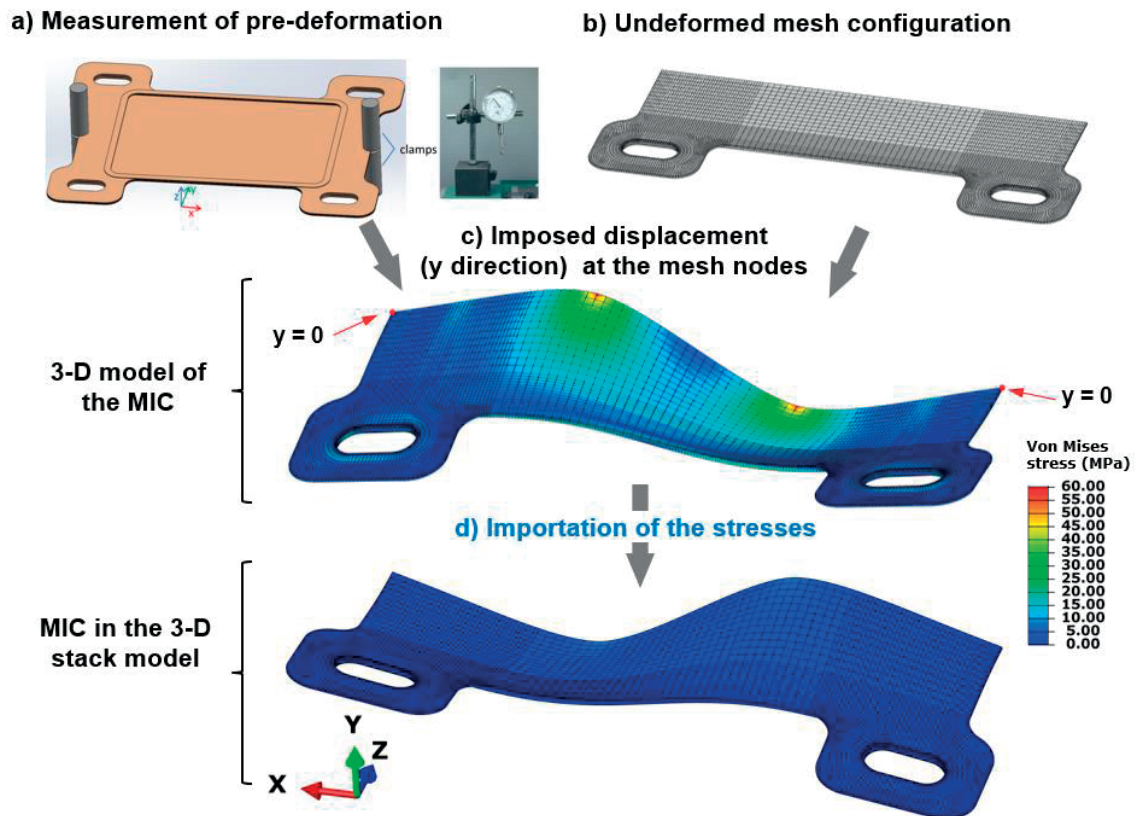


Figure 50: Schematic view of the steps in the approach for modelling the pre-deformation of the components in the stack simulations.

There are caveats to the proposed approach: i) plastic deformations and ii) residual stresses cannot be imported, which in reality can develop in the metallic components, e.g. upon their fabrication, are not considered. Instead, in the present approach, the MIC is assumed stress-free under deformation.

Since in this work half of the SRU geometry is modelled (see Paragraph 3.1.3), the pre-deformations measured experimentally (step a) in Figure 50) are assumed symmetric along the z-axis. This temporary restriction does however not prevent investigating the effect of pre-deformation on selected cases.

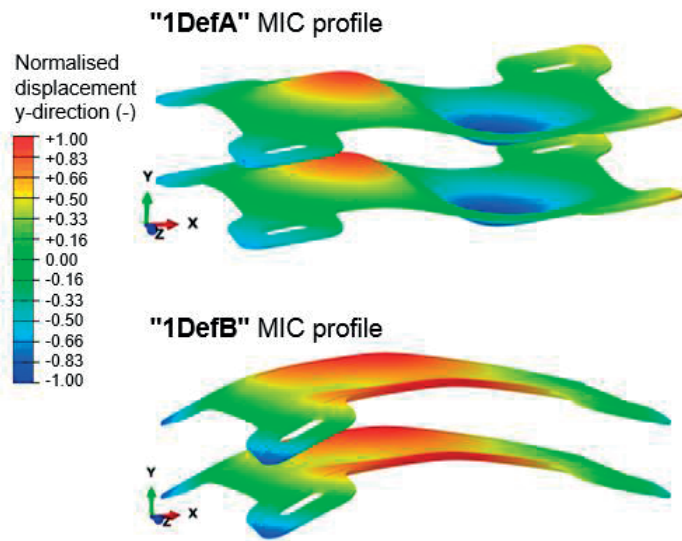


Figure 51: View of the initial deformation profile of the two MICs used in the stack model comprising 1 SRUs. For illustration purpose, the deformation is magnified. GDLs, cells and sealants are not represented.

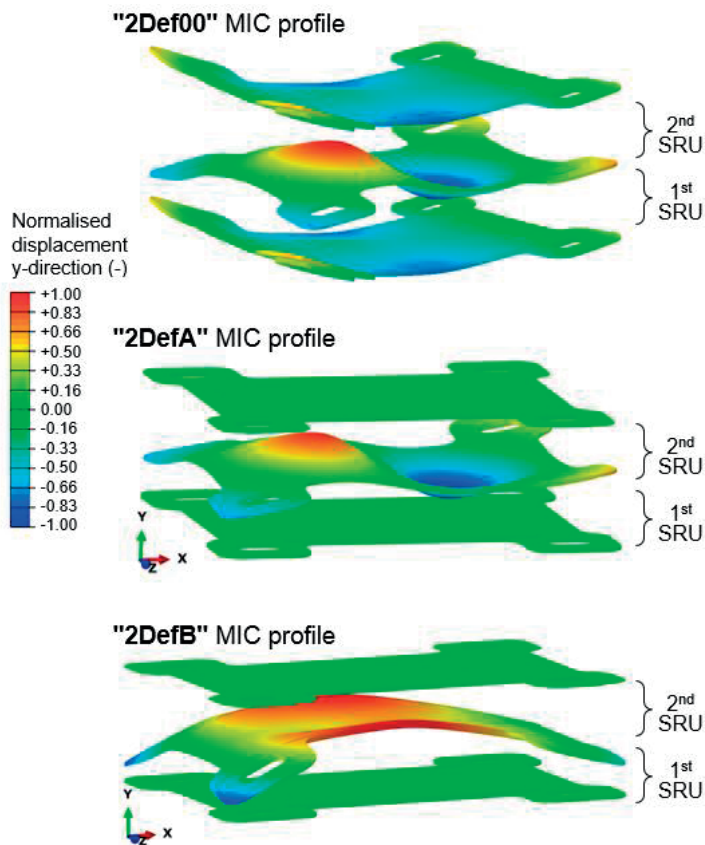


Figure 52: Plot of the initial deformation profile of the three MICs used in the stack model of two SRUs. For illustration purpose, the deformation is magnified. GDLs, cells and sealants are not represented.

Indeed, a multitude of combinations of pre-deformations can be imagined and their effects investigated to understand how imperfect components must be selected and assembled to minimize the risks of thermo-mechanical issues, which largely exceeds the available computational resources. The present study was limited to a few cases, requiring including in the computational domain of the SRU model 1 or 2 units. In the case of modified periodic boundary conditions, the simulation results therefore correspond to the periodic stacking of such a combination of imperfect components. Figure 51 and Figure 52 show the series of deformed shapes of the metallic components implemented in the SRU models comprising 1 and 2 SRUs, respectively. The 1 SRU simulation cases correspond to the situation where the MICs are imperfect but all identical, whereas 2 SRU models were performed to investigate the effect of assembling components with different shapes.

3.1.6 Simulation procedure

The SRU thermo-mechanical analyses performed in this work comprise a first set of simulation steps defined as the “initialisation sequence”, and a second set where the operating conditions are simulated, i.e. polarisation or operation combined with thermal cycling. An overview of the simulation sequence is provided in Figure 53. The presentation of the results in Chapters 3.3 and 3.4 is organized using the steps shown in grey in Figure 53, i.e. “A1”, “A2”, “A3” for the assembly, “HT 0 h”, “HT 10 h”, “HT 10 kh” for operation under constant thermo-electrochemical conditions, “RT 0 h” and “RT 10 kh”, for thermal cycles, for the “Model v2”.

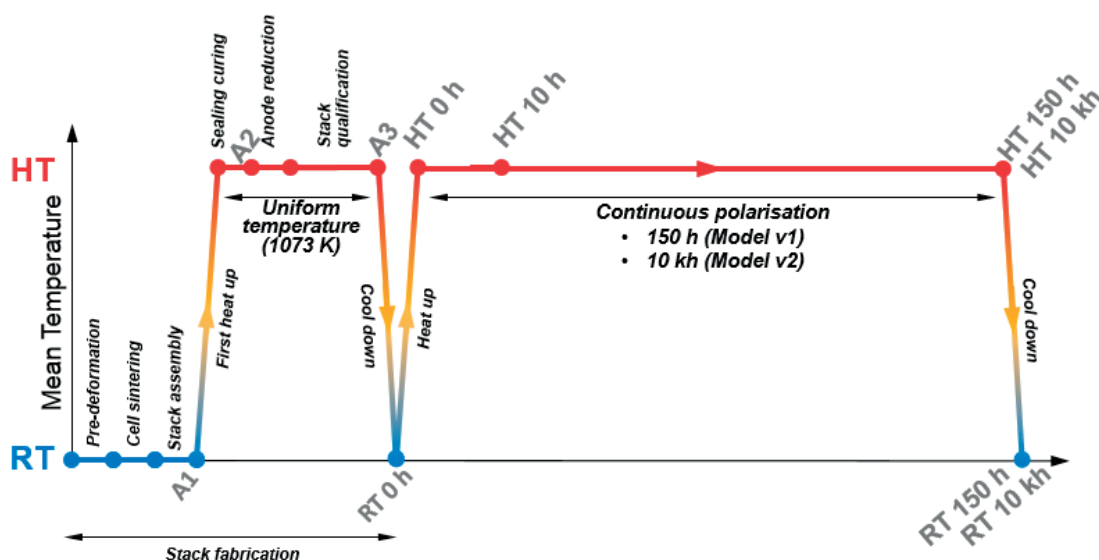


Figure 53: Overview of the simulation sequence. Points from “A1” to “RT 0 h” comprise the phases of the stack production and qualification, including the first thermal cycle (“A3” to “RT 0 h”). Points “HT 0 h” to “HT 150 h” (“Model v1”) and to “HT 10 kh” (“Model v2”) correspond to operation under constant thermos-electrochemical operation, which is followed by a second thermal cycle (“HT 150 h” to “RT 150 h” in “Model v1”, “HT 10 kh” to “RT 10 kh” in the “Model v2”).

The sequence is the same for the “Model v1”, except that the simulation duration under constant thermo-electrochemical conditions is shorter (150 h). The simulation of the initialisation sequence for 1 and 2 SRU models is respectively about 15h and 25h, respectively, whereas for the simulation of polarisation combined with thermal cycling they are about 20h and 30h, respectively for 1 and 2 SRU models. These computation runtime are referred to 1 node cluster, with 14 cores each, 2.2 GHz, 128 Gb RAM.

The output of the initialisation sequence is required for the simulation of the operating conditions. As long as constant stack design, material properties and manufacturing specifications are considered, a single initialisation sequence is simulated and used for the analysis of all the thermo-electrochemical operation scenarios. In contrast, any modification in steps up to A3, such as in modelling assumptions (e.g. “Model v1” and “Model v2”) or component pre-deformation require running a dedicated initialisation sequence.

In this study, the detail of the evolution of the temperature profile during cool downs and heat-ups of the stack (in Figure 53, the intervals A1-A2, A3-RT 0 h, RT 0 h-HT 0 h and HT 10 kh-RT 10 kh) are not considered. Linear variation from the high to the low temperature profile point is implemented. The time-scale is also assumed much smaller than the processes at steady-state temperature (i.e. in Figure 53, the intervals A2-A3 and HT 0 h-HT 10 kh). To reduce the simulation runtime, creep in all materials is disabled during these steps. From these two perspectives, the present simulation of the thermal cycling conditions intuitively corresponds to a worst-case.

3.1.6.1 Initialisation

The initialisation sequence aims at calculating the stress in the stack during its manufacturing and conditioning. This sequence comprises both the simulation of real production steps and artificial numerical procedures to approximate the reality. A description of each step is provided hereafter.

Simulation of components pre-deformation. At the first step of the initialisation sequence, the position of the upper and lower MICs of the SRU is constrained along the y-axis and the stresses from the MIC model (if the analysis includes pre-deformed components) imported in the homologous components of the SRU model (see also Paragraph 3.1.5). Since this step is an analysis and not a manufacturing procedure, irreversible deformation (i.e. plasticity and creep) are disabled in all materials using switching of field variables (see Paragraph 3.1.2 for more details).

Cell sintering. The residual stresses caused by the sintering of the cell layers, i.e. anode, electrolyte, compatibility layer (the cathode layer is not considered in the SRU model), are reproduced in the stack model by simulating artificial thermal strains. These thermal strains are generated by assigning an artificial CTE for each material of the cell layers corresponding to an increase of the temperature of the

whole cell of 1 °C. The reason for this 1 °C increment is the reduction of convergence difficulties because of relative sliding. The artificial CTEs are calculated using an Euler-Bernoulli 1-D model [41] including elasticity and creep, which simulates the residual stresses during the cool-down from the sintering temperature of each layer to RT. The artificial CTE of the electrolyte and compatibility layer were computed with respect to the anode. For the present cell, the computed values for the anode, electrolyte and compatibility layer are 0.00, 2.12E-03 and 1.55E-04, respectively. At the end of this simulation step, the CTE of the NiO-YSZ, YSZ and GDC is changed from the artificial to the real values by switching of field variables.

Stack assembly force. The displacement of the MIC along the y-axis is in this step removed, and an assembly force is applied on the SRU. In the model, this force is applied on the stack using multi-point constraint (see Figure 45). At the end of this step, plasticity was enabled in all the materials.

First heat-up (after point “A1”). The stack is heated up from RT to a uniform temperature of 800 °C. At the end of this simulation step, the tangential contact behaviour at the contact interfaces depicted by black and red dashed lines in Figure 48 is switched from frictionless to no-sliding condition (see Paragraph 3.1.4), for both “Model v1” and “Model v2”.

Sealants curing. This step aims at including the change of mechanical properties of the glass-ceramic material (i.e. of the sealants) because of its crystallisation. The dominant change in mechanical properties upon crystallisation is the increase of elastic modulus, from the artificial initial value of 0.2 GPa, up to 14.4 GPa (see Tables 24 and 25 and Paragraph 3.1.2). However, until this simulation step, the sealants in the SRU model are elastically deformed and the strains relatively large (i.e. about 4%, mostly because of the applied assembly force on the SRU as well as to accommodate the pre-deformation of the MICs). Once the stiffness of the glass-ceramics is increased in the model, relatively high stresses are generated in the sealants and in the interfaced components. These stresses are artificial and are relaxed by simulating artificial creep strains only in the sealants, because in reality the glass-ceramic pastes likely deforms plastically until crystallisation. Ideally, at the end of this simulation step, the sealants should be intuitively stress-free, from a macro-scale perspective. In reality, the simulation step is stopped when the stress became negligible, e.g. lower than a threshold of 0.5 MPa. At the beginning of this simulation step, creep and plasticity material behaviours are disabled in all materials (except for the creep in the glass-ceramics) and re-enabled at the end of the step, to avoid unrealistic inelastic deformations in the SRU components because of glass-ceramics stiffening.

Anode reduction (point “A2”): the physical modifications in the anode upon its reduction are the changes in mechanical properties and the shrinkage (see Tables 24 and 25 and Paragraph 3.12), which

occur together. In this work, the mechanical properties of the anode material is changed from NiO-YSZ to Ni-YSZ by manipulation of the field variables, whereas for the reduction strain and the compensation of the CTE change, with respect to the reference temperature, was applied using artificial isotropic shrinkage.

Stack qualification (point “A3”, followed by “RT 0 h”). A stack is usually not cooled-down right after anode reduction, because of first tests and mild IV-characterization. In the present study, a uniform temperature of 800 °C is maintained for 10 h, during which creep relaxation of the stress in all the SRU parts takes place. At the end of the 10 h, the stack was cooled down to RT. This is the first thermal cycle of the stack.

3.1.6.2 Operation

The baseline case considered in the present study is prolonged operation under constant conditions followed by a thermal cycle. The stress computed by the initialisation sequence, i.e. at the end of the first thermal cycle, is used as the restart point for the SRU thermo-mechanical simulations of operation cases, which consists in prolonged continuous polarisation in either co- or counter flow configuration, see Table 26 for an overview of the operation conditions. The hold time under constant polarization differs in “Model v1” and “Model v2”, respectively 150 h and 10’000 h. At the end of the polarisation, the stack is cooled-down to RT, which represents the second thermal cycle of the stack (point HT 10 kh - RT 10 kh).

A thermo-electrochemical model is used for computing the 3-D spatial distribution of temperature in the repeating unit in operation, for importation into the 3-D FEM thermo-mechanical model. The thermo-electrochemical model was developed in the GEM-EPFL group in parallel to this Thesis. The work performed here consisted in implementing the interfaces in Matlab for the importation of the temperature profile.

The requirement for the thermo-mechanical analysis is the accurate prediction of the 3-D temperature profile, over the range of operation conditions relevant for the SOLIDpower stack. While the local electrochemical model provides local information such as the spatial distribution of electrostatic potentials in the electrolyte as well as single solid phase or composite electrodes, a discussion of the modelling assumptions is outside the scope of the thesis. In a simplified view, the requirement is here limited to the reasonable prediction of the sink/source terms for CFD computations. A brief description of the thermo-electrochemical modelling approach is therefore provided hereafter.

The approach consists in coupling a fast thermo-electrochemical model with detailed electrochemistry [143,144] with a 3-D computational flow dynamic (CFD) model that comprises adequate level of geometrical detail for the thermo-mechanical simulations. In the active area of the SOLIDpower stack

design, the temperature and current density profiles are close to one-dimensional. The modelling approach is based upon this quality. A simplified open loop interface provides a model runtime that allows tractable sensitivity analysis for e.g. meta-modelling [160]. The heat transport and gas flow governing equations are solved in 3-D in all domains, except in the cell where the sink/source terms are provided by a finite-difference model, implemented in gPROMS, an equation-oriented process modelling tool based on the finite-difference/orthogonal collocation on finite-element method.

The information flow is summarized in Figure 54. The transport of electrons and ions and gas species along with chemical and electrochemical reactions is first solved by gPROMS in all the cell layers, assuming one-dimensional gas and temperature profiles along the air flow direction. The 3-D CFD model then solves the transport of mass, heat, and species, with the species and heat source (sink) along the flow direction computed by gPROMS, after projection and interpolation on the active area of the 3-D model. The procedure is implemented in Fluent by programming User-Defined Functions (UDFs).

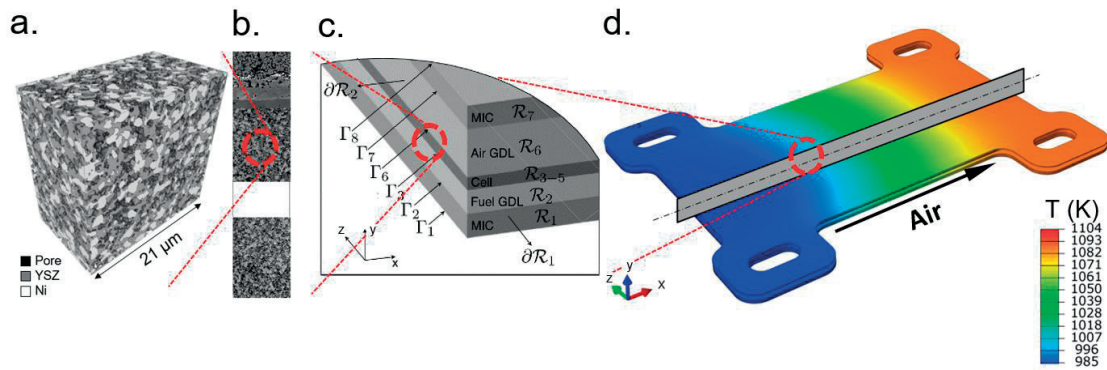


Figure 54: Schematic view of the information flow in the thermo-electrochemical model. (a) 3-D imaging for the computation of the effective transport and electrochemical properties of the heterogeneous electrode materials using methods equivalent to the computational homogenization presented in Chapter 2.4. (b) Micrograph showing the layers discretized in 1-D in the local gPROMS electrochemical model. (c) 1-D discretization in the finite difference gPROMS stack model. (d) Importation of the species source and sink terms in the Fluent CFD model (only the subset of the computational domain that comprises the SRU solid parts is shown).

To reduce complications due to round off errors and interpolation during the importation of the temperature profile into the thermo-mechanical model, the solid parts are modelled with the same level of detail in the CFD and FEM models. Compared to the SRU thermo-mechanical models, the CFD model comprises additional computational domains, such as the thermal insulation and both the air and fuel domains. Periodic thermal boundary conditions are implemented in the CFD model in the y-direction. The compatibility of the meshes between CFD and thermo-mechanical models is facilitated by guaranteeing that the number of cells in the y-direction in the CFD model equals or exceeds that in the thermo-mechanical model, to allow fast 2-D interpolation layer-by-layer of mesh nodes in the thermo-mechanical model. Routines were developed for the automatic importation of the temperature

profile computed by the CFD simulations into the thermo-mechanical model. With the implemented gPROMS-Fluent procedure, a simulation requires about 45 min per core (Intel Core i7-3930K) to achieve sufficient convergence. The CFD computations imported in Chapter 3.2 consisted of 700 iterations, which proved conservative. The simultaneous gPROMS solver allows determining the air flow need to maintain a constant maximum solid temperature in the stack, and constant surface specific power density (including an estimate of the ancillary consumption of the air blower) for investigating the thermo-mechanical effects of differences in features in the temperature profiles.

Table 26: List of selected thermo-electrochemical conditions

	PR	U (V)	j (A cm ⁻²)	Air Ratio	P (W cm ⁻²)	Steam to carbon ratio	T _{air,inlet} (K)	T _{max} (K)	FU
Co-flow	0.50	0.74	0.48	5.5	0.33	2	973	1100	0.85
Counter-flow	0.10	0.76	0.47	4.1					
	0.50	0.76	0.48	6.1					
	0.99	0.75	0.49	8.4					

3.1.7 Post-processing of simulation results

3.1.7.1 Evolution of the contact pressure

The interface between the cell and the gas diffusion layers in the active area is central for the stack performance. Achieving and maintaining a low ohmic resistance is not straightforward in a stack, which is a multilayer. In a simplified view, a state-of-the-art 70 cell stack comprises more than 500 interfaces that must have the lowest possible resistance to electron transport, among which approximately half have usually low but inaccurately known mechanical properties. The mitigation of imperfect or altered contact is often addressed on a trial and error basis, since predictive approaches have not yet been established. The tolerance on component quality is a first aspect that can be considered, but the experimental identification of the adequate trade-off between performance, durability and costs is far reaching. Intuitively, the statistical variability in shape and dimensions caused by the manufacturing tolerances is expected to detrimentally affect the uniformity of the contact pressure at the interface. The relationships between the electrical contact resistance and the applied contact pressure were investigated by Dey et al. [17]. The material for the studies on the cathode side was LSM. They observed that since the cathode has the characteristics of semiconductor, the contact resistance on the cathode side decreases with the increase in temperature. Conversely, the contact resistance on the anode side increases with the increase in operating temperatures and is approximately one order of magnitude lower than that of the cathode. The results highlight the dependence between the applied load and the contact resistance. The situation corresponds to that of a sintered screen-printed or tape-cast electrode

in contact with a MIC, which therefore depends on the surface quality and cannot be generalized for all stack situations. The relationships shown in Figure 55 were therefore not used quantitatively for the present study.

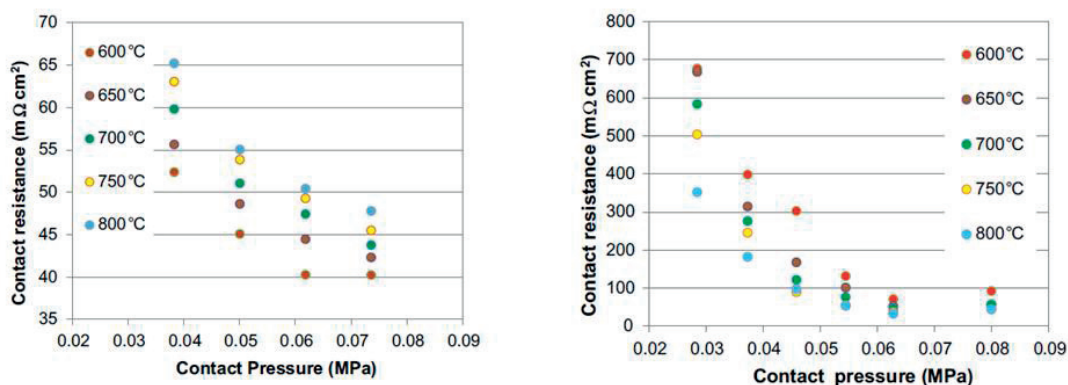


Figure 55: Contact resistance as a function of the contact pressure for the anode (left-hand side) and cathode (right-hand side) interfaces. Plots reproduced from Ref. [17]^h.

The quantitative prediction of the interfacial electrical resistivity in the long-term and under varying operation conditions requires first the knowledge of the contact status and pressure and second of the relationship between the contact status and the effective interface conductivity. The present studies are focused on the first aspect, within the limits discussed in Paragraph 3.1.4. Therefore, there is no feedback from the thermo-mechanical simulation results to the thermo-electrochemical mode.

From the mechanical standpoint, the phenomena that can result in a history-dependent contact status in the model are the effect of history on the stress state, in a simplified view. In contrast, the possibility for the damage of the contact interfaces is not simulated. This is because the contact formulation allows any region of discretized surface that underwent zero or tensile contact pressure or opening to fully recover its original contact properties at any time, which is unlikely the case in reality.

Contact issues differ whether the anode/GDL-fuel or the cathode/GDL-air interface is considered: the cathode has a lower electric conductivity and thickness than the anode, therefore the effects of current constrictions at the scale of the interconnection system are more severe on the cathode/GDL-air interface [19]. Post-test disassembly further shows that the strength of the cathode side interface is also lower. In the present study, both contact interfaces are investigated. The contact pressure computed by Abaqus is positive (negative) if the interface is under compressive (tensile) stress.

^h Reprinted from Journal of Power Sources, 233, Tapobrata Dey, Debanand Singdeo, Manaswita Bose, Rajendra N. Basu, Prakash C. Ghosh, Study of contact resistance at the electrode-interconnect interfaces in planar type Solid Oxide Fuel Cells, 290-298, 2013, with permission from Elsevier.

The evolution of the contact is quantified by computing the probability density function of the contact pressure at the interfaces. The binning of the contact pressure data is performed using as weight the corresponding element surface area.

The “Model v1” and “Model v2” comprise 2 repeating units for the analysis of the pre-deformation profiles “2Def00”, “2DefA” and “2DefB” (see Figure 52). The spatial distribution of the contact pressure is not identical within the two pairs of cathode or anode interface. For comparison with the reference 1 repeating unit model, the equivalent contact pressure is calculated for each mesh element on the same interface of both SRUs. This post-processing choice therefore places the emphasis on the probability of interface separation at either one or both SRUs, which may cause alteration of the electrical field. The discrepancy in contact pressure within pairs of same GDL is of interest, but not discussed quantitatively using a dedicated metric. It is analysed qualitatively by visual comparison of the computed contact pressure spatial distributions.

3.1.7.2 Cell Failure

The probability that a cell in the stack fails is of little interest, which does not correspond to the computational domain. In this study, the probability of failure is computed over the volume of anode materials of all the 70 SRUs of the considered stack.

For the computation of the failure probability in the anode, the Weibull statistics parameters of NiO-YSZ and Ni-YSZ obtained from four-point bending tests and at room and high temperature are used (see Chapter 2.3). Confidence intervals on the failure probability are computed using the lowest and upper bound of the 90% confidence interval values on Weibull modulus, characteristic strength and reference volume. The mesh of the cell is considered fine enough for comparative studies. Therefore, the principal stress distribution computed in the cell sub-domain of the full stack model is used for the probability, i.e. displacement-driven submodelling of the cell is not performed for achieving a higher accuracy of the stress computation. The probability of failure is computed by integration over the volumes of the mesh elements of the cell layer, following the standard expression assuming the principle of independent action:

$$P_{f,i} = 1 - \exp \left\{ -\frac{1}{V_0 \cdot (\sigma_0)^m} \cdot ncells \cdot \int_{V_i} \left[\sum_{ps=1}^3 (\sigma_{ps})^m \right] dV_i \right\} \quad (56)$$

where V_0 is the reference volume, m the Weibull modulus, σ_0 the *characteristic* strength of the material, $ncells$ the number of cells in the stack and σ_{ps} the principal stress with $ps = 1, 2, 3$ which indicates the first, second and third component of the principal stress. The integral can be evaluated for each volume of material i in the SRU, with $i = anode, electrolyte, compatibility\ layer$. Only positive (tensile) values of the principal stress are used for calculating the probability of failure.

The Weibull parameters measured in Chapter 2.3 and usually found in the literature correspond to the strength for the pristine material. Microstructural changes were observed for the present anode under SOFC operation. An effect on the strength cannot be excluded. Therefore, the direct comparison of the simulations at the start and end of operation requires some care. The analysis based on computational homogenization in Chapter 2.4 however shows that the change in the thermo-elastic properties due to changes in the morphology and topology are limited. The variations in the strength are therefore likely limited if the degradation does not affect the volume fraction of the phases.

3.1.7.3 Failure of the sealing

A technological difficulty with ceramic materials is that they tend to be much more brittle compared to metals. Therefore, the effects of geometrical and material singularities that trigger damage by cracking, because of localised high stress that exceeds the strength of the material [161]. Failure occurs in the elastic deformation regime with limited possibility for plastic deformation at the crack tip, which entails that the crack process zone is negligibly small. The analysis of failure in ceramics therefore typically starts with linear elastic fracture mechanics (LEFM) theory. The fracture mechanics problem has been historically tackled from two perspectives provided by stress or energy balance of a system comprising a pre-existing crack.

The stress intensity approach is based upon the analysis of the stress field near the crack tip. The inspection of analytical solution for the stress field derived by Irwin [162] shows that each component of the stress tensor is proportional to a constant, which therefore represents a stress-intensity factor. The analysis holds for different loading, referred to as Mode I (opening), Mode II (sliding) and Mode III (tearing), which yields the stress intensity factors K_I , K_{II} and K_{III} . Failure corresponds to a critical stress intensity factor, which is a measure of the material resistance.

The concept in the energy balance approach introduced by Griffith roots from the first law of thermodynamics, i.e. crack extension occurs when the energy available in the system exceeds the resistance of the material, because energy is required to break the atomic bonds. The nature of the relevant processes that dissipate energy upon crack extension differ depending on the material, but for evident reasons, always comprise the generation of new surfaces. The energy balance for an infinitesimal crack growth provides the energy release rate (ERR), which must exceed a critical value that is a measure of the toughness of the material.

The inspection of the expressions derived from the energy and stress analysis approaches for a crack in the bulk of a linear elastic material, yields a relationship between the energy release rate and stress intensity factor, indicating that for such a case the two approaches are equivalent.

A simplified approach based upon energy considerations has been implemented as a post-processing procedure of the stack simulations to inform qualitatively and comparatively about the risk of failure of

the sealant. Standard expressions for the energy-based approach are therefore briefly presented hereafter. For the simplest case, the energy balance for an infinitesimal crack growth is:

$$dW - dU_{el} = -d\Pi = d\Gamma \quad (57)$$

Where Π is the potential energy, W is the external work dependent upon the displacement at the boundaries of the system δ and the applied forces F . For example, the infinitesimal external work provided to a system by a constant dead load F and causing an infinitesimal deformation δ at the application point of the load is:

$$dW = \frac{1}{2}F d\delta \quad (58)$$

The infinitesimal stored elastic energy of the system is the product between an infinitesimal volume of the considered system and the elastic strain energy density φ in the same volume:

$$dU_{el} = \varphi d\Pi \quad \text{with} \quad \varphi = \int_0^{\varepsilon_{max}} \sigma_{ij} \cdot d\varepsilon_{ij} \quad (59)$$

Independently of compressive or tensile stresses, the elastic strain energy density φ is always a positive quantity.

The energy to create free surfaces by crack propagation is linearly dependent on the extension of the created surface and by the specific surface energy γ , which is either a material or an interface property, respectively if the crack develops within one material or at the interface between different materials. In infinitesimal terms, the free surface energy $d\Gamma$ to generate a surface dS is expressed as:

$$d\Gamma = \gamma dS \quad (60)$$

By differentiating the condition for crack propagation (Equation (57)) to the surface generated by the cracking process, we obtain:

$$\frac{dW}{dS} - \frac{dU_{el}}{dS} = -\frac{d\Pi}{dS} = \frac{d\Gamma}{dS} = G(a_c) \quad (61)$$

where G is defined as energy release rate (units of Jm^{-2}).

A failure mode of interest in multilayer assemblies is the delamination at the interface between the dissimilar materials. The analysis usually starts by considering failure at the interfaces, which are often preferred locations for delamination because of their lower fracture toughness than the bulk materials. Furthermore, since the two interfaced materials have often different compositions, residual stresses build-up after manufacturing or usage and imperfections at the interface act as notches where stress singularities develop.

In SOFC stacks, stable short cracks or delamination not affecting the gas-tightness of the two gas compartments are of interest for a full understanding of failure and lifetime analysis, but at the present stage of the analysis, the emphasis is placed on the complete detachment at the interface between the MIC and the manifold sealants. The approach is based upon that used by Sørensen et al. [163] for the analysis of delamination in multilayer plates, along pre-defined paths. The layers are treated as continuum media, i.e., the microstructural features in the glass-ceramic and MIC must be sufficiently

smaller than the layer thickness. The approach schematized in Figure 56 “bypasses the complexities of the stress field at the crack tip” by performing an energy balance using the Euler-Bernoulli beam theory. The calculation of the energy release rate then simply consists in the variation of the stored elastic strain energy between far behind and upfront the crack tip position (Figure 56), i.e.:

$$G_{ss} = U_{el}^{III} - U_{el}^I \quad (62)$$

The considerable decrease of the problem complexity comes at the cost of several limitations. First, the crack faces downstream the tip position do further not enter into contact, i.e., the crack remains open upon its propagation. However, the energy release rate if delamination occurs with complete separation of the interface is expected higher than in the case the delaminated layers establish contact, leading to a likely overestimation of the risks of failure. The second restrictions are on the geometry and dimension of the samples. The stripe shown in Figure 56 is a typical case for which the assumptions apply. The crack length must be however sufficiently small compared to the stripe length, but larger than the multilayer assembly. The analysis is also restricted to the regime of steady-state crack propagation during which the energy release rate is independent to the crack length. For the stripe, the crack length must be sufficiently larger than the width of the stripe, because the transition zone where the curvature changes between that with and without the crack is typically a few times larger than the stripe width.

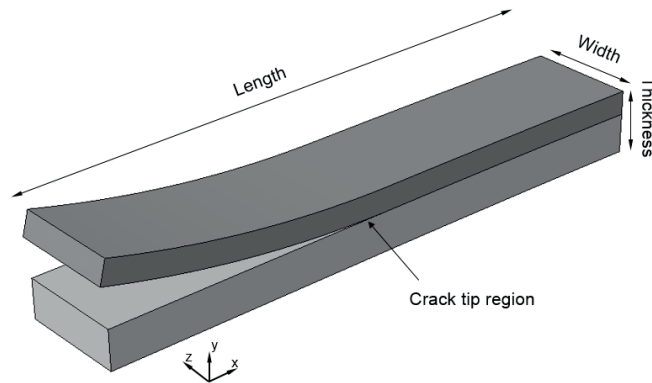


Figure 56: Schematic of the multi-layer stripe used for the description of the energy-based analysis of the failure of the manifold sealants.

The procedure for the energy-based analysis of the failure of the sealing at the stack scale consists in applying Equation (62), using for the state III the end of a simulated sequence point (RT 0 h and RT 10 kh, in Figure 53), where all the sealing interfaces have retained their integrity. An additional simulation step is then performed, during which the interaction at the interface of interest is disabled, i.e., full delamination occurred, which corresponds to state I in Equation (62). Therefore, an additional interaction release step is performed for each investigated interface and sequence point. Two types of releases are considered for the comparative analysis of the risks of failures upon stack operation. In the first case, the contact interaction is simply removed, which does not guarantee that the crack faces

inter-penetrate. Therefore, a second set of simulations is systematically performed by removing the joining contact interface by a frictionless contact, which is closer to a real full delamination situation.

The application of the procedure on the computational domain shown in Figure 41 has several practical implications, in particular in the case of modified periodic boundary conditions (Paragraph 3.1.3). A detachment simulation corresponds to the simultaneous failure of all the corresponding interfaces in the stack and on both sides of the symmetry axis. Therefore, the situation rigorously differs for the cases with one or two computational domains, i.e. failure occur in all, respectively each two similar interfaces in the stack.

Numerical crack propagation simulations were performed to test the effect of geometry and that the order of magnitude of the ERR estimated from stack simulations falls within meaningful limits. The virtual crack closure technique (VCCT) is an established approach to compute the components of the strain energy release rate (G) from finite-element simulations e.g. in Ref. [164–166]. The VCCT was however not available in commercial software until fairly recently. Abaqus implementation aims at simulating crack propagation along pre-defined paths using a mixed-mode fracture criterion within or at interface between parts. The computation is based on surface discretization and tracking algorithm in a similar way as contact interactions (see Paragraph 3.1.4).

The discussion of the known caveats of the VCCT for advanced applications is beyond the scope of the present analysis. A typical example is the appropriate normalization to ensure a breakdown of the total energy release rate G_{tot} into G_I and G_{II} components for biomaterial interfaces that is independent of mesh size [165], because of oscillations in the analytical solution for the stress at bi-material interfaces. The present analysis is based only on the G_{tot} . The complexity of the simulations is reduced by preventing crack propagation using arbitrarily large critical energy release rates in the software failure criterion.

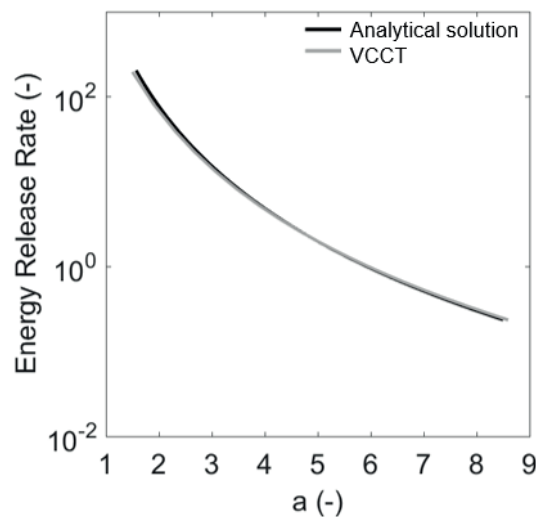


Figure 57: Comparison between VCCT computation and the analytical solution for the energy release rate as a function of crack length for a single material double cantilever beam (DCB).

Instead, a Matlab routine sequentially manipulates the node and element sets, as well as surface definition from a template Abaqus input file to control the position of the crack tip and perform one VCCT simulation per crack extension. 2-D plain strain, generalized plane strain and axisymmetric geometries are meshed with full integration first order elements. The full crack path at the interface between two parts is enclosed in sub-partitions to ensure that the mesh for the VCCT calculation is similar and made of square elements, with a constant size ranging from 0.05 to 0.125 mm, depending on the study case. Geometrical non-linearity is disabled. The Matlab-Abaqus VCCT procedure is first tested on a benchmark case consisting of a single material double cantilever beam (DCB) subjected to displacement controlled boundary conditions. The agreement with the analytical solution is satisfactory for the present analysis, as shown in Figure 57. The applicability of the approach proposed by Sorensen et al. [163] is formally limited to stripe-like shape. A generalized plain strain simplification of the manifold sealing region as a three-layer stripe was first implemented and the total strain energy release rate computed as a function of the crack length (Figure 58-a). The second model consisted in an axisymmetric simplification of the sealing region (Figure 58-b). In both cases, the MIC and glass-ceramic elastic properties and coefficient of thermal expansion are those used for the stack simulations and listed in Table 25.

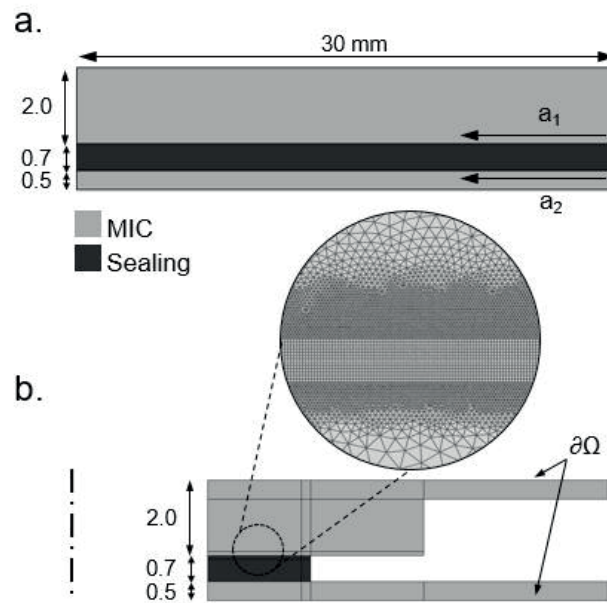


Figure 58: Schematic of the stripe (a) and axisymmetric (b) simplification of the manifold sealing region (not to scale). The crack propagation directions and interfaces are indicated by a_1 (upper) and a_2 (lower).

The assemblies are stress-free at 1073 K and cooled-down to room temperature, and the VCCT processing is then enabled. The boundary conditions are free standing. For the axisymmetric simplification, an additional case is considered consisting of periodic boundary conditions on $\partial\Omega$ with a compression load close to that computed by the stack imposed using multi-point linear constraints.

3.2 Temperature profiles in operation

This section provides a discussion based on visual inspection of the temperature profile computed by the gPROMS-Fluent thermo-electrochemical model (Paragraph 3.1.6) for the conditions listed in Table 26. The discussion is limited to aspects relevant to thermo-mechanical analysis. Test simulations were first performed to verify that the thermo-mechanical simulations converged with the imported 3-D temperature profiles. Minor issues during the interpolation related to round-off of the node positions between the thermo-electrochemical output and the thermo-mechanical input had to be solved. The inspection of the test results did not highlight issues except if local discontinuities in the temperature field occur. Figure 59 shows the computed 3-D temperature profiles considered for the thermo-mechanical analysis in the following sections. The profiles in co- and counter-flow with a same fraction of pre-reformed methane (PR) are similar (see a. and b. in Figure 59). However, as expected, the thermal gradients in counter-flow are higher in the z direction. A further relevant difference is observed on the air outlet side, near the fuel manifold. The in-plane thermal gradients are also higher in counter-flow, because of cooling by the endothermic steam-methane reforming reaction, which also moves the peak of temperature in the active area towards the air inlet, compared to the co-flow case.

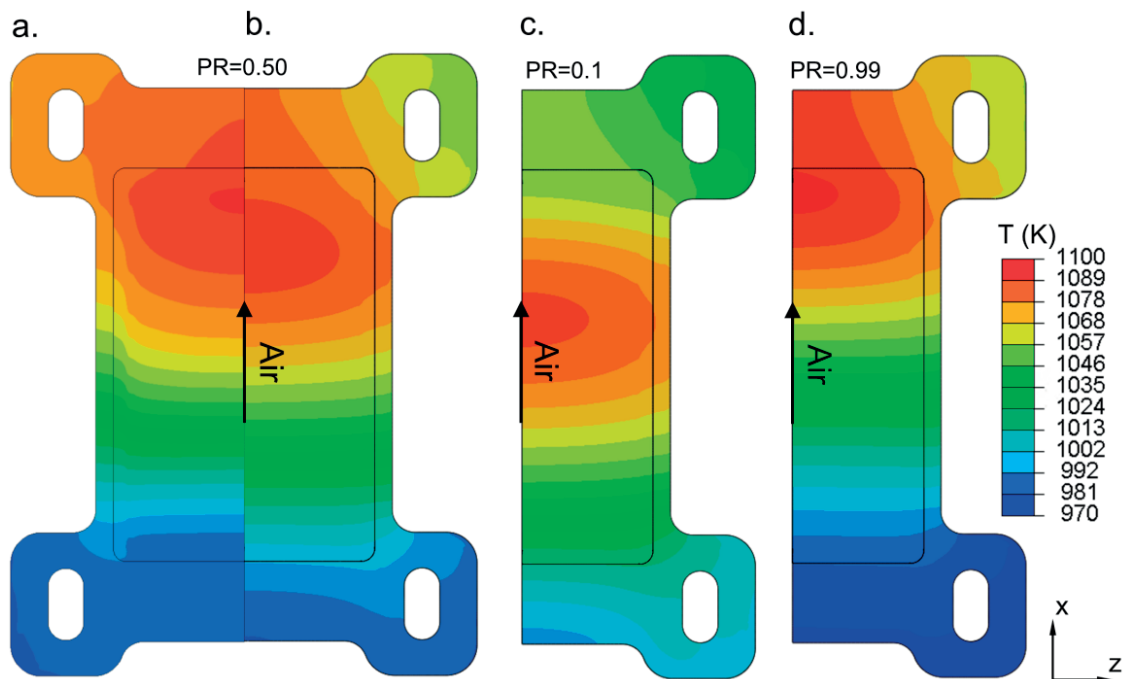


Figure 59: Simulated temperature profiles for the conditions listed in Table 26: co-flow and fraction of pre-reforming (PR) of 0.5 (a), counter-flow and fraction of pre-reforming of 0.5 (b), 0.1 (c) and 0.99 (d). Only the lower MIC and cell are shown for illustration purpose.

In a simplified view, the position of the peak of temperature along the air flow path in SOFC mode follows a balance between internal sources due to electrochemical and chemical reactions and thermal

management by the air flow. It therefore differs in co- and counter-flow and depends on the fraction of methane pre-reforming (PR). In counter-flow, it moves towards the air inlet for decreasing fractions of methane pre-reforming, because the steam-reforming reaction is endothermic (see b, c and d in Figure 59). In co-flow, the steam-methane reforming can result in a minimum of temperature away from the air inlet. This is not observed in the present simulated case with a pre-reforming fraction of 0.5. Higher fractions of pre-reformed fuel also result in an increase of the footprint of the regions of high temperatures, which is also higher in co-flow than in counter-flow, because cooling by air and steam methane reforming occur on the same side.

First assessments of the risks of mechanical failures often rely on the analysis of the thermal gradients. Inspection of the simulated maximum in-plane thermal gradients in the cell shows that they do however not simply correlate with flow configuration and amount of methane pre-reforming. The absolute values of the thermal gradients in the cell for the four temperature profiles are listed in Table 27. The maximum value is observed in co-flow in the air flow direction, whereas in counter-flow, it scales proportionally (inversely) with the amount of pre-reforming in the z (x) direction.

Table 27: Maximum thermal gradients in the cells along the x and z directions for the four temperature profiles.

	Co-flow PR 0.5	Counter-flow PR 0.5	Counter-flow PR 0.1	Counter-flow PR 0.99
$ \partial T/\partial x _{\max}$ (K/mm)	1.6	1.7	2.2	1.3
$ \partial T/\partial z _{\max}$ (K/mm)	3.0	2.2	1.3	2.5

The peak of the temperature is dependent on the profile of the current density. In a simplified view the latter is governed by a balance between the local temperature and the fuel depletion along the path [19].

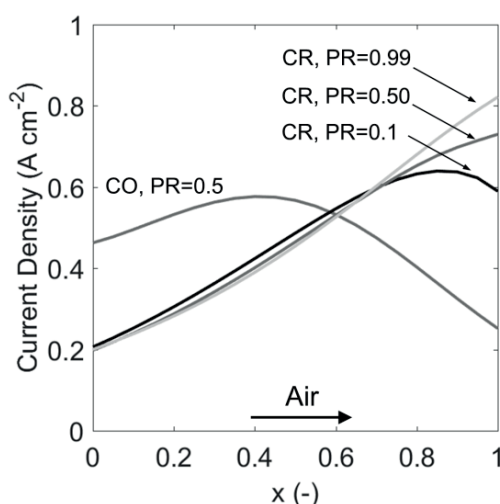


Figure 60: Current density in operation computed along the symmetry lines corresponding to the temperature profiles shown in Figure 59.

Figure 60 shows the current densities upon polarisation corresponding to the four temperature profiles of Figure 59. In co-flow, because of the trade-off between temperature (i.e. highest at the air outlet) and rich fuel mixture (i.e. highest at the air inlet), the highest current density is localised near the middle of the active area. Conversely, in counter-flow and with PR of 0.5 and 0.99, the peak of current density is in the region of the cell active area that is at high temperature, because the electrochemical reactions are there facilitated by the hydrogen-rich fuel mixture together with the high temperature. In counter-flow with a low fraction of pre-reformed methane of 0.1, the cooling effect is sufficient to lower the temperature at the fuel inlet. Hence, the maximum current density is shifted towards the centre of the active area.

Electrochemical degradation during operation at constant current density is not enabled in the thermo-electrochemical model for the present study. The computed temperature profile therefore remained constant over the simulated continuous polarisation. Another study [56] investigated the effects of variations in the spatial distribution of temperature caused by electrochemical degradation. The results suggest that the effects of electrochemical degradation on the thermo-mechanical behaviour of the stack remain limited, compared to variations in the operation conditions during load following or that expected from imperfect components, at least when the operation conditions are manipulated to control the maximum solid temperature.

The thermo-electrochemical simulations show that variation of the operation conditions have a strong effect on the features of the temperature profile, even with manipulation of the air flow to control the maximum solid temperature that is in practice difficult to achieve.

3.3 Overview of the thermo-mechanical results

This section provides a first overview of the simulation results. Trends qualitatively observed in all simulated cases are presented using as reference the case of co-flow operation with modified periodic boundary conditions and an ideal initial MIC geometry (“CO 0.5” “PBC” “Ideal MIC” and “Model v2”). The results are presented for each component separately. The interactions and the effects of boundary conditions, MIC pre-deformation, operating conditions and variations in modelling assumptions are discussed in detail in Chapter 3.1.

3.3.1 Stress in the cell

The overall trends observed in the evolution of the stress in the cell layer during the simulated sequence shown in Figure 53 are discussed. The 1st principal stress computed in the anode is shown in Figure 61. The effect of i) the anode reduction and ii) the constraint of the sealant and GDL-fuel on the cell leads to relevant changes in the stress in the anode between the points A1 (stack assembly) and RT 0 h (i.e. end of the first thermal cycle). The computed stress state in the anode evolved from tensile (about +20 MPa) to stress-free condition. The stress state at the end of the first and second thermal cycle (points RT 0h and RT 10 kh, respectively) also remains similar. This result indicates that the effects of thermal cycling dominate that of history during long-term polarisation. From a material viewpoint, the stress state in the anode is less affected by creep than by the mismatch in CTE between the cell and the other stack components.

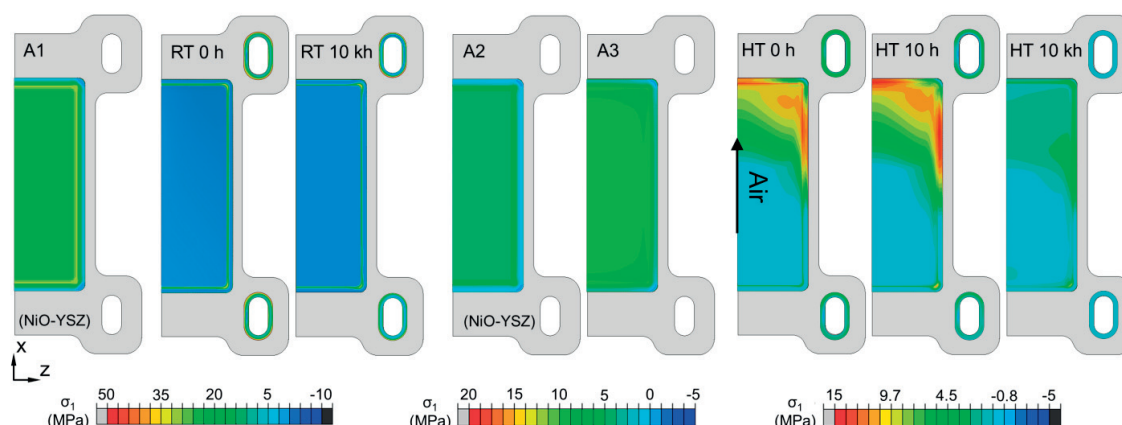


Figure 61: Evolution of the first principal stress (σ_1) in the anode (GDL-fuel side) and the manifold sealing during stack assembly (A1-A3), thermal cycling (RT 0 h, RT 10 kh) and operation in co-flow with a fraction of pre-reforming of 0.5 (HT 0 h, HT 10 h, HT 10 kh).

The first principal stresses in the active area of the anode increase upon reduction (points A2 and A3, respectively for anode in oxidised and reduced state), from about +5 MPa to +9 MPa. This stress increase is caused mostly by the interactions with the joined parts (i.e. the GDL-fuel and the MIC, on the

lower side, and the electrolyte with the compatibility layer, on the top side) and the isothermal shrinkage of the anode. Conversely, in the inactive region of the anode, the constraint of the GDC is not present, hence the increase of stress is less pronounced.

Under polarisation, the stress state in the anode is a modulation of the point A3 by the inhomogeneous spatial temperature distribution. Compared to A3 (uniform temperature of 1073 K), the region at the air outlet (inlet) is higher (lower) in the point HT 0 h, i.e. at the start of the polarisation in co-flow. Because i) of the constraint of the anode with the GDL-fuel and ii) the CTE of the GDL-fuel material which is higher than that of Ni-YSZ, the higher thermal expansion of the GDL-air was constrained by the anode. Hence, since the inlet region is colder at the point HT 0 h than in A3, the tensile stresses in the anode are lower. The higher tensile stresses, i.e. at about +15 MPa, are located in the cell inactive area surrounding the hottest region of the temperature profile in co-flow (see Figure 61). The reason is that the surrounding inactive area is colder, and thus constrains the higher thermal expansion in the active area.

Creep does not yield a monotonic relaxation of the stress in the anode. At the operation point HT 10 h, the first principal stress in the anode first increases, since the SRU bent downwards as a consequence of the different in-plane creep strain rates in the bonded components, see Paragraph 3.3.2, and this increased the stresses in the lower face of the anode. Over the long-term, the stress in the anode is however relaxed. The creep strain rate depends on stress and temperature.

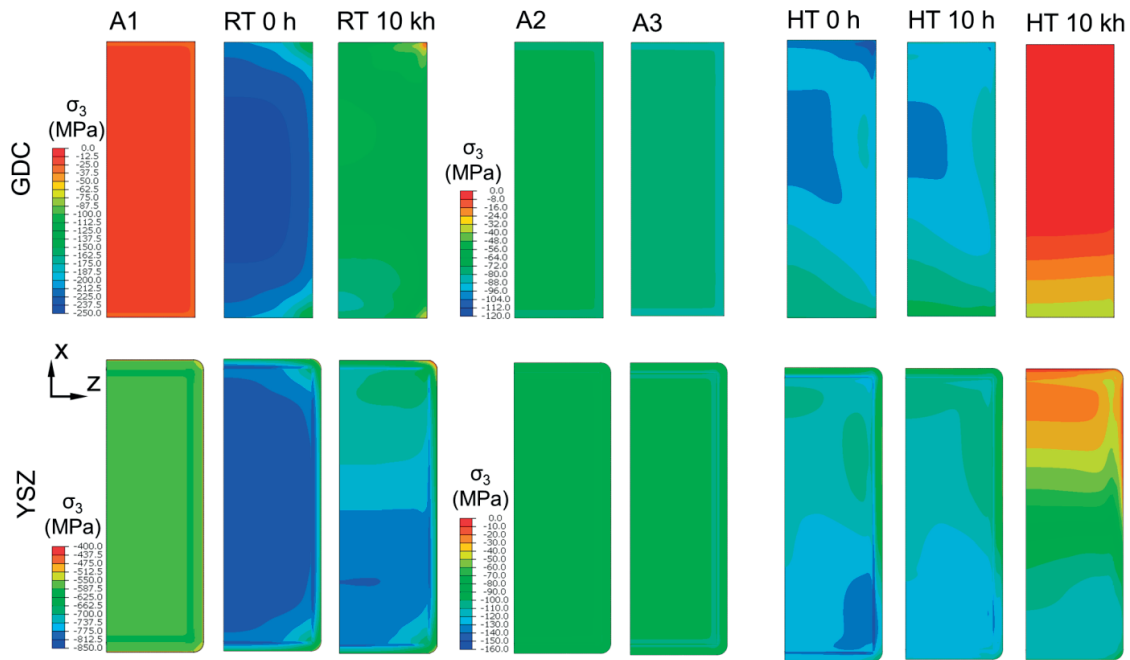


Figure 62: Evolution of the third principal stress (σ_3) in the YSZ electrolyte and GDC compatibility layer during stack production (A1-A3), thermal cycling (RT 0 h, RT 10 kh) and operation in co-flow with a fraction of pre-reforming of 0.5 (0 h, 10 h, 10 kh).

Therefore, the larger stress relaxations occurred in the regions of highest stress and temperatures over the long-term polarisation, which are on the air outlet side. In the anode-supported cell configuration, the thin YSZ and GDC are subjected to compressive shielding stress. Figure 62 provides an overview of the effects of i) the assembly process (A1, A2 and A3) and ii) long-term polarisation in co-flow (HT 0 h to HT 10 kh) and iii) thermal cycling (RT 0 h and RT 10 kh) on the third principal stresses in the electrolyte and in the compatibility layer.

After the cell sintering (point A1 in Figure 62), both the electrolyte and compatibility layer are under compressive stresses, of about -600 and -20 MPa, respectively. The increase in tensile stress in the anode upon its reduction (stress states A2-A3 shown in Figure 62) is compensated by a limited increase of the compressive stresses in both the electrolyte and compatibility layer, by comparing the stress state in points A2 and A3.

Upon polarisation, the compressive stresses decrease (increase) in the electrolyte (compatibility layer) in the hottest region of the cell (i.e. at the outlet), see point HT 0h in Figure 62. The effects of creep are relevant already during the first 10 h of polarisation. Then, the compressive stress in both layers are largely relieved during the long-term polarisation, see point HT 10 kh in Figure 62. In this situation, the compatibility layer is under compression only in a restricted region at the inlet, where creep strains were limited by the lower temperatures, whereas the rest of the layer undergoes very low tensile stresses (red region in point HT 10 kh in Figure 62). On the contrary, the compressive stresses in the electrolyte are not completely relieved after the 10 kh under polarisation.

Since the CTE of Ni-YSZ is higher than that of both YSZ and GDC, the higher thermal shrinkage of the anode upon cool down (i.e. from A3 to RT 0 h, and from HT 10 kh to RT 10 kh) results in beneficial compressive stresses in the electrolyte and compatibility layer for the RT conditions. The magnitude of the stress is however lower than initially.

The simulated tensile stress in the anode is low and not expected to lead to a high initial probability of failure (see Paragraph 3.4.2), or long-term problems since microstructural analysis suggest that the mechanical properties are expected to vary mildly upon aging (see Chapter 2.4). From a proof-testing perspective, the pattern of the stress in operation does not change significantly and while the magnitude of the stress increases during the beginning of operation, a strong dependence on operation history is not observed for the simulated conditions. The decrease of the shielding stress in the YSZ electrolyte and GDC compatibility layer is in contrast detrimental, but the present analysis does not highlight a critical situation. The results however suggest that the vulnerability towards re-oxidation or rapid changes in operation conditions may be practically lowered, which warrants follow-up studies.

3.3.2 Deformation profiles and stress in the MIC

The failure of the MIC itself is believed unlikely. This component still requires attention, because of its contribution to the deformation of the repeating unit, therefore indirect contribution to contact or

sealing issues. The MICs do not necessarily enforce the flatness of the repeating unit. Figure 63 shows the simulated deformations in the y-direction along the symmetry line of the SRU during the initialisation sequence (Figure 63-a) and the long-term polarisation in co-flow (Figure 63-b). After the stack assembly (point A1), the SRU is slightly bent upwards because of the initial cell curvature resulting from sintering. As described in Paragraph 3.1.4, the GDL-fuel and the MIC constrain the isothermal shrinkage of the anode during its reduction. The in-plane stiffness of the GDL-fuel with the MIC is higher than that of the bilayer electrolyte-compatibility layer. The shrinkage of the anode bent the SRU downwards, compare point A2 (anode oxidised) with point A3 (anode reduced) in Figure 63.

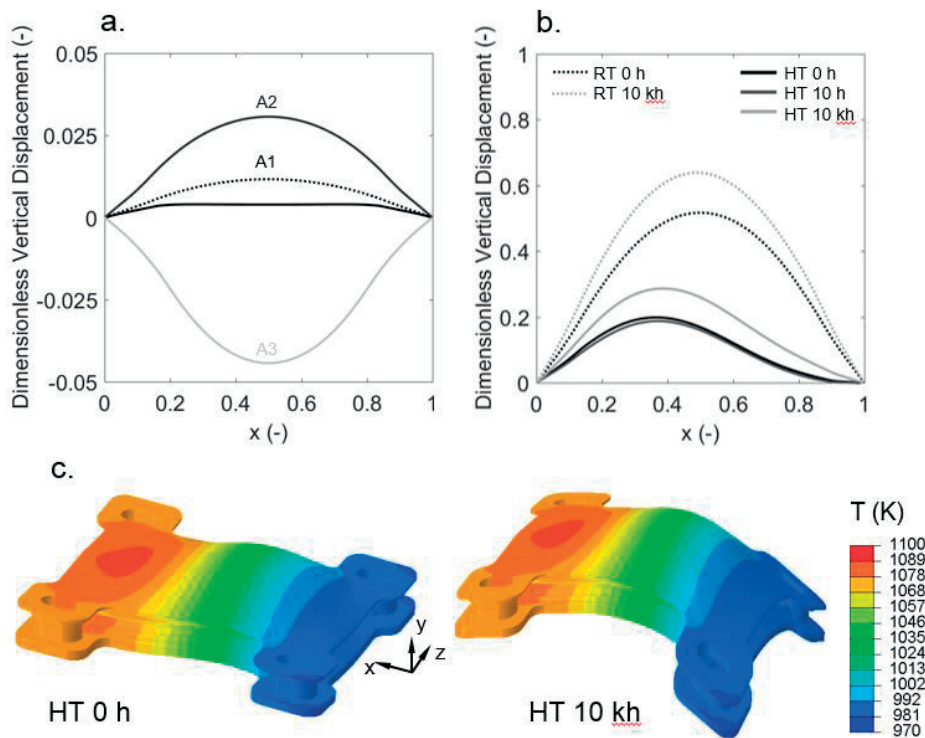


Figure 63: Evolution of the displacement in the y-direction along the x-axis (symmetry line) on the lower MIC during stack assembly (a) and operation (b). (c) Schematics showing highly magnified view of the y-deformation at the start and after 10 kh of operation, with color-coded temperature.

The lower face of the anode is tied to the porous layer of the GDL-fuel. The CTE of the material of this layer is higher than that of Ni-YSZ. The contact GDL layer is also tied with the GDL gas distribution, made of Crofer 22 APU, which has a CTE lower than that of the contact layer, but higher than that of Ni-YSZ. Upon cool down, the thermal shrinkage of the overall GDL-fuel is higher than that of the cell. Consequently, the simulated SRU bent upwards, see point RT 0 h in Figure 63-b. Considering the higher CTE of Ni-YSZ with respect to that of both YSZ and GDC, this upwards bending is further promoted. This effect is observed not only during deep thermal cycles, but also for intermediate temperatures between 1073 K and RT (e.g. in the regions with temperatures below 1073 K in operation). It is worth mentioning

that in this work, the gasket elements in cathode GDL account for only the through-the-thickness mechanical behaviour, unlike the gasket fuel GDL (see Paragraph 3.1.1). The bending behaviour of the SRU induced by mismatches in in-plane thermal expansions is thus governed by the components on the fuel side.

The uneven spatial distribution of temperature during polarisation influences the bending of the SRU along the flow path (i.e. x direction in Figure 63). In the region colder than 1073 K, i.e. for dimensionless x between 0 and 0.6, approximately, the SRU bends upwards, because of the same effect described before for thermal cycling. For dimensionless x between 0.6 and 1, the temperatures are higher than 1073 K. Hence, the effect of the CTE mismatch is reversed compared to that described upon thermal cycling, and the SRU tends to bend downwards. The bending effect is not linear with temperature: for example at x=0.3, the temperature difference between 1073 K and temperature profile at polarisation is about 5%, whereas the y-displacement at the point HT 0h is 45% of that at RT 0h (Figure 63-b). This nonlinearity is caused supposedly by the temperature-dependence of the thermo-elastic properties of the SRU materials and the modified periodic boundary condition formulation.

Creep in the SRU materials modifies the deformation profile during long-term operation. However, after the first 10 h of polarisation, the y-displacement decreases by about 5%, followed by an opposite trend in the long-term, i.e. the y-displacement increases by 50%. This behaviour is ascribed to the different in-plane creep strain rates of the bonded components (because of contrast in material properties), which relaxes the stresses in the components at different rates. Since creep was disabled for thermal cycling, the evolution of the y-displacement between the heat-up from the point RT 0 h to HT 0 h and the cool down from point HT 10 kh to RT 10 kh is symmetric but offset by the increase of y-displacement upon long-term polarisation (compare points RT 0h and RT 10kh in Figure 63).

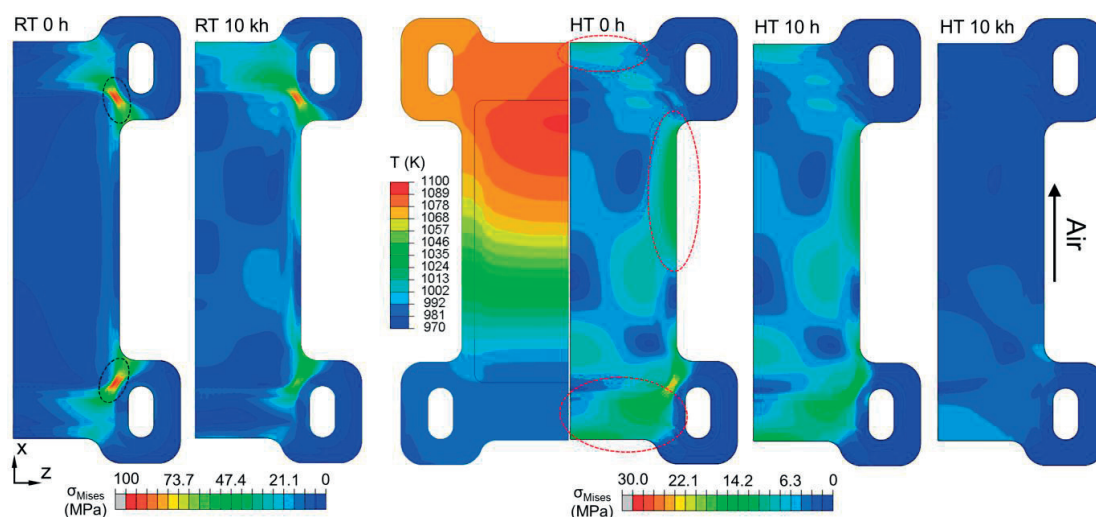


Figure 64: Evolution of the von Mises stress (σ_{Mises}) in the lower MIC during thermal cycling (RT 0 h-RT 10 kh) and operation in co-flow with a fraction of pre-reforming of 0.5 (HT 0 h, HT 10 h, HT 10 kh).

For all the simulated cases, rate-independent plastic deformation is not observed in the dense metallic components of the modelled SRU. The Von Mises stresses for both RT conditions, i.e. 0h and 10kh (see Figure 64) are well below the yield strength of the Crofer 22 APU (248 MPa at RT). In these conditions plastic deformation is very unlikely to occur, even with potential changes or variations in mechanical properties or operating conditions compared to those implemented in the SRU model. Similarly, under polarisation in co-flow, the maximum Von Mises stress is approximately half of the yield strength of Crofer 22 APU at the maximum stack temperature of 1100 K (39 MPa). The Von Mises stresses in the MICs upon the initialization sequence were lower than the values shown in Figure 64, thus not shown. The peak of stress at RT 0 h (see black circles in Figure 64) arise from different effects of the cell and sealants on the MIC, because the upwards bending of the cell upon cool down deforms the MIC on the corresponding region, whereas the bending of the fuel manifold region is constrained by the manifold sealants. Upon polarization in co-flow, the region at highest temperatures, i.e. at the outlet, undergoes compressive stresses, because the higher thermal expansion of this MIC region is constrained by the colder neighbouring regions. As a consequence, tensile stresses develop in these colder regions (see red circles in Figure 64). Conversely, the stresses in the hottest region are not significantly high because of i) lower elastic modulus, due to the higher temperature and ii) high temperatures spread over a relatively large region. The inhomogeneous Von Mises stress pattern was not analysed in detail, because it is not believed to result in mechanical issues. It may arise from the strong dependence between temperature and elastic modulus of metals.

Creep relaxed the stresses in the metallic components during polarisation. After 10 h (point HT 10h in Figure 64) the stresses decrease slightly. However, the creep constitutive law implemented in the SRU model included only the secondary regime. Hence, it is expected that in reality the contribution of primary creep would have relaxed the stresses by a larger amount. At the end of the long-term polarisation (point HT 10 kh in Figure 64) the stresses in the metallic components are almost completely relaxed. Because of the strong dependence of temperature on creep strain rate, the stress relaxation is larger in the hottest region.

3.3.3 Contact pressure at the interfaces between the cell and

GDLs

Contacting imperfections are likely to occur in a large SOFC stack and affect the performance. The capability for the quantifying and predicting of partial loss of electrical contact on the long-term performance is to our knowledge not yet established, but believed to be of central relevance. The following discussion is based on the analysis of the evolution of the contact pressure during the simulated sequence. The contact pressure simulated at the interface between the cell and the fuel and

air GDJs is shown in Figure 65. The contact pressure on both interfaces is the combination of both the assembly force and interaction with the manifold sealants.

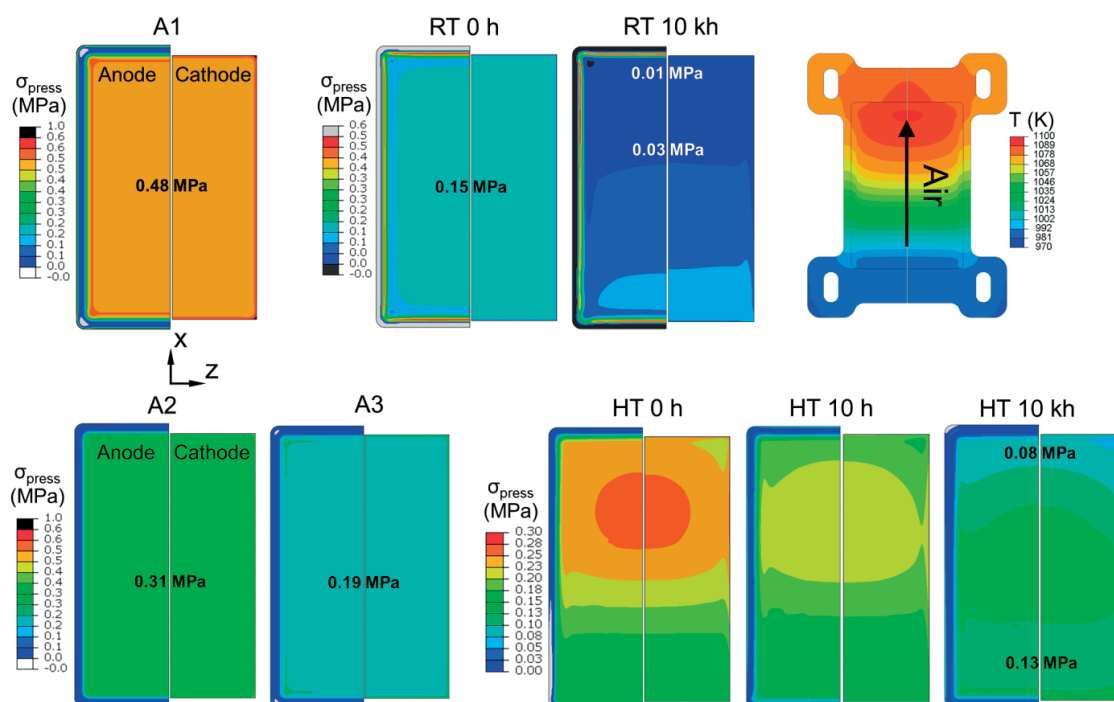


Figure 65: Evolution of the contact pressure (σ_{press}) on the anode (left) and cathode (right) sides during stack assembly (A1-A3), thermal cycling (RT 0 h, RT 10 kh) and operation in co-flow with a fraction of pre-reforming of 0.5 (HT 0 h, HT 10 h, HT 10 kh). The temperature profile is shown at the top right.

As expected and desired, the spatial distribution of the contact pressure computed for the cathode side mostly mirrors that for the anode side. The slight variations near the cell edges are due to the mechanical interaction with the cell sealing.

The contact pressure on the active area after the application of the assembly load is about 0.48 MPa. Under these conditions, the manifold sealants are in mild traction. This situation is a modelling artefact, because the pressure-overclosure relationships in “Model v2” include a clearance at zero contact pressure, which causes an artificial opening of the contact interfaces on the active area between the GDJs, cell and MICs. The contact pressure at the interface between manifold sealant and MIC at the condition A1 is about -5 MPa (interface in traction).

After the sealants curing in the initialization sequence (see Paragraph 3.1.6), the artificial creep strain relaxes the stresses in the manifold sealants, leading to a contact pressure at the interface between the manifold sealant and MIC of about -2 MPa (interface in traction). This reduction is also due to a modification of assembly force (see Paragraph 3.1.6). In these conditions, the contact pressure on the active area was 0.31 MPa. In the point A3, i.e. after anode reduction and 10 h at 1073 K, creep relaxed further the artificial stresses in the manifold sealants, and the contact pressure on the sealants became

about -1.5 MPa. In these conditions, the contribution of tensile stresses in the manifold sealants on the contact pressure on the active area is still not negligible, i.e. the contact pressure on the active area (about 0.19 MPa) is supplied both by the manifold sealants and by the assembly force. Contact pressure simulated in steps A1-A3 are therefore an overestimation of the reality, but the main outcome is that the design does not result in strong in-homogeneity of the contact pressure in the contact area during the assembly and heat-up, despite the bending of the SRU (see Paragraph 3.3.2) which is beneficial for the last step of the stack fabrication.

After the first thermal cycling to RT, the contact pressure on the active area (on the manifold sealants) decreases (increases) from 0.19 to 0.14 MPa (from -1.5 MPa to -0.8 MPa). These variations are caused by the CTE mismatch between the glass-ceramic (i.e. the manifold sealants), the GDLs and the cell (see Paragraph 3.1.1 for the values of CTE). Assuming that at the point A3 (1073 K) the thickness of the manifold sealant is equal to the sum of the thicknesses of both GDLs and cell, upon cool down to RT (point: RT 0 h) the GDLs shrink by a larger amount than the sealant, see Figure 66.

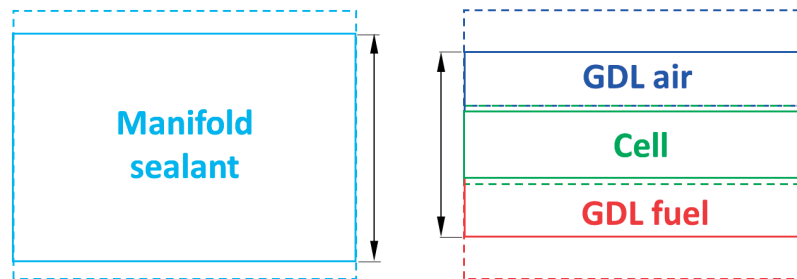


Figure 66: Schematic of the thickness variation of the manifold sealant, GDLs and cell because of thermal shrinkage upon cool down. Dashed and continuous line depicts the components at HT and RT conditions, respectively.

Since the assembly force on the stack remains unchanged, the different thermal shrinkages caused the contact pressure to decrease on the active area (see Figure 65) and to increase on the manifold sealants. Regions of high contact pressure (in Figure 65, the red ribs of about 0.5 MPa) are found on the edges of the anode contact interface, after both the first and the second thermal cycles. This is ascribed to a change in cell curvature in the inactive transition region between the active and sealing area, because the upwards bending of the cell upon cool down is constrained on the inactive area by the cell sealant.

Upon polarisation in co-flow, the thermal expansion of the GDLs is higher than that of the manifold sealants at both the air inlet and outlet regions, because i) the CTE of the GDLs materials are higher than that of the glass-ceramics and ii) the active area is hotter than the manifold regions. These two contributions control the contact pressure on the active area upon polarisation, because in comparison with the condition A3 (uniform temperature of 1073 K) the contact pressure increases at the outlet (i.e. $T > 1073$ K), whereas it decreases at the inlet (i.e. $T < 1073$ K). However, the zones of highest contact pressure at HT 0 h do not correspond to the highest temperature, because of the trade-off between the

decrease of the elastic properties with the temperature increase and higher contact pressures for larger mismatches of thermal expansion. In these conditions, the contribution to the higher contact pressure at the outlet is given in part by the assembly force, and in part by the manifold sealants in tension. Upon long-term polarisation, creep in both the glass-ceramic and in the GDLs materials, among others, monotonically relax both the compressive stresses in the GDLs and the tensile stresses in the manifold sealants. The decrease of contact pressure is significant in the first 10h of polarisation, see point HT 10 h in Figure 65. However, this decrease would be expected faster if primary creep was included in all the material constitutive laws of the SRU model.

Because of the strong dependence of the creep strain rate on the temperature, the contact pressure decreases more rapidly near the air outlet than the inlet region: after 10 h of polarisation, the contact pressure at the outlet is already similar to that at the inlet. In the long-term i) the higher creep strain rates because of the higher temperature lead to contact pressure at the outlet region lower than at the inlet, i.e. the opposite pattern from the start of the polarisation (point: HT 0 h), and ii) the mean contact pressure on the active area would converge to the value given by only the assembly force without the effect of the sealants, around 0.12 MPa.

After the second thermal cycling (point RT 10 kh) the contact pressure decreases, for the same reasons as in the first thermal cycling (point: RT 0 h). However, the contact pressure before the cool down was lower in HT 10 kh than in A3. As a result, in the second thermal cycle the contact pressure in RT 10 kh was almost lost on a large region of the active area. This showcases an undesirable situation, because the region affected first by a loss of contact pressure corresponds to that of highest current density (see Chapter 3.2). Compared to RT 0 h, the contact pressure is also less uniform at RT 10 kh. The reason is that, similarly to the heat-up for the start of polarisation (point: HT 0h), the difference in thermal shrinkage upon cool down between the GDLs and the manifold sealants is larger at the outlet, because the outlet of the active area is hotter than the inlet. As a result, the outlet region is at lower contact pressure than at the inlet, and the manifold sealants support about 80% of the assembly force.

The simulations indicate that ensuring a constant and uniform contact pressure at the interface between the cell and GDLs is a challenge. The effect of history is observed and suggests that the risk of contact issue can be expected to increase upon operation, during thermal cycling.

3.3.4 Sealing

The achievement of gas tightness throughout the whole life of a stack remains a challenge. Glass-ceramic materials provide better sealing performance, at the cost of increased risk of failure, in particular during thermal cycling. The evolution of the sealing stress state at room temperature is discussed in the present section using the cumulative density function of the opening and shear component of the stress tensor at the interfaces. The cumulative density function of the simulated opening and norm of the shear stress components in the manifold sealing during thermal cycling are

shown in Figure 67. Before the simulation of the long-term polarisation (i.e. until point RT 0 h), the temperature over the whole SRU is uniform. Hence, the stress cumulative distributions are identical for both the inlet and outlet manifold sealants, because they share the same geometry and mechanical properties. In contrast, the temperature at the outlet manifold sealant is higher than that at the inlet side during operation, thus also the stresses and the creep strains differ between the two manifold sealants. Before the first thermal cycling, the stack is at the uniform temperature of 1073 K. Upon cool down to RT, the opening stresses increases both in compression and in tension, respectively from -6 MPa to + 13 MPa. This tensile stress is well below the normal strength measured experimentally for G18 [147], i.e. about 79 MPa at RT. The tensile and compressive stress are located respectively at the inner and outer side of the manifold sealant, and they vary monotonically along the sealant width. The tensile stresses are caused by the local bending of the MIC in the region at the interface with the manifold sealant.

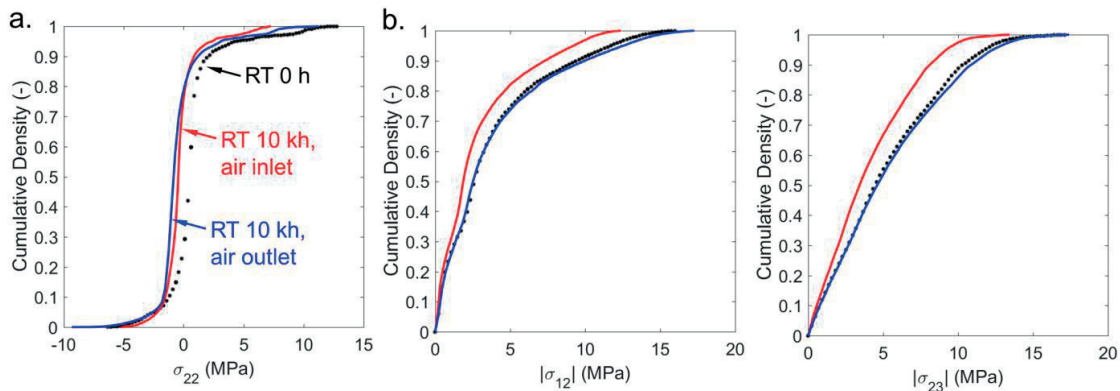


Figure 67: Cumulative density functions of the opening (a) and norm of the shear components (b) of the stress at the interface between the manifold sealing and the MICs during thermal cycling. Dots: RT 0 h, inlet and outlet, red: RT 10 kh air inlet, blue: RT 10 kh air outlet. Co-flow, fraction of pre-reforming of 0.5.

The two components of shear stresses at the interface between the manifold sealing and MICs (σ_{12} and σ_{23}) are expected very similar, because they both root from the CTE mismatch between the glass-ceramic and Crofer 22 APU. The pattern of the cumulative density functions of both the opening and shear stress components between the first and second thermal cycle are very similar. This suggests that the stresses in the manifold sealants are not substantially affected by the long-term polarisation; rather the mismatch in thermal expansion from operation to room temperature controls the stress state. The two shear stress components are however lower for the manifold sealant interface at the inlet side. The reason is that upon cool down (during the second thermal cycling RT 10 kh), the temperature variation between polarisation condition and RT is higher for the hotter air outlet manifold sealant, consequently the difference in thermal shrinkage between the MIC and sealant is higher. However, the shear stresses for the outlet side manifold sealant between RT 10 kh and RT 0 h (both manifold sealants) are very similar, because the elastic modulus of the materials decreases with temperature

increase. Hence, at higher temperatures the CTE mismatch between the materials affects the stresses by a lower extent.

Figure 68 shows the cumulative density functions of the uniaxial stress components along the x (σ_{11}) and z (σ_{33}) directions in the manifold sealants. At RT, both manifold sealants undergo high compressive stresses, because the CTE of glass-ceramic is lower than Crofer 22 APU. For the same reason as for the shear stress components, also the uniaxial stress components for the outlet side manifold sealant between RT 10 kh and RT 0 h (both manifold sealants) are similar.

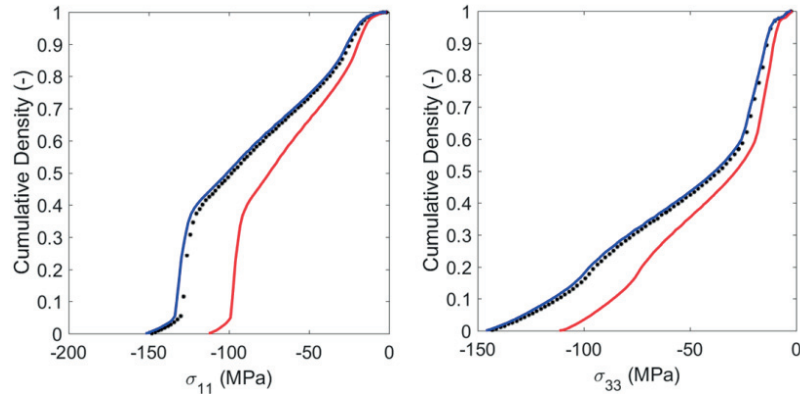


Figure 68: Cumulative density functions of the uniaxial components of the stress in the manifold sealing during thermal cycling. Dots: 0 h, inlet and outlet, red: 10 kh air inlet, blue: 10 kh air outlet. Co-flow, fraction of pre-reforming of 0.5.

At 1073 K, both the shear stresses at the interface with the MICs and the opening component of the stress are similar. However, upon polarisation the inlet and outlet manifold sealants are exposed respectively to lower and higher temperatures than 1073 K. These temperature variations from the 1073 K condition result in the shear and opening stresses shown in Figure 69 for the HT 0 h condition. At the point 3 (1073 K), the shear and opening stress components are between the red and blue dots. The magnitude of these stresses is however relatively low.

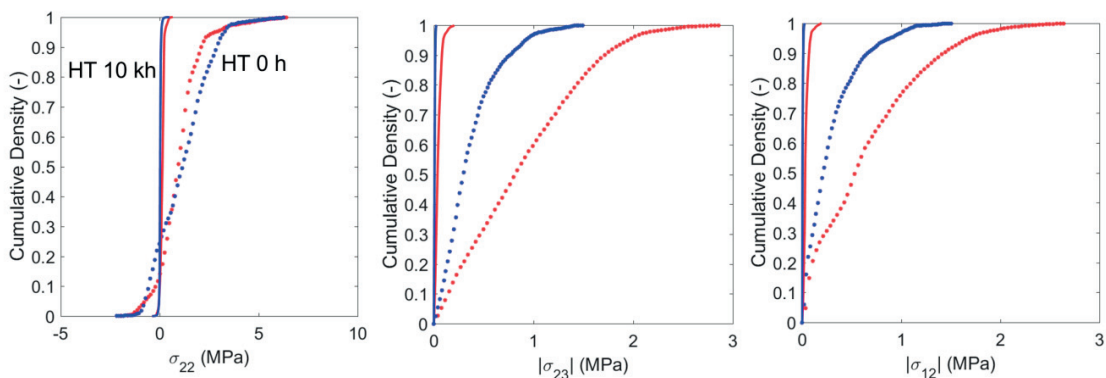


Figure 69: Cumulative density functions of the opening (a) and norm of the shear components (b) of the stress at the interface between the manifold sealing and the MICs during long-term polarisation in co-flow. Dots: HT 0 h, red: air inlet, blue: air outlet. Continuous lines: HT 10 kh. Co-flow, fraction of pre-reforming of 0.5.

Upon constant long-term polarisation, creep relaxes the stresses, and the manifold sealants become practically stress-free (see HT 10 kh condition in Figure 69). Figure 70 shows the cumulative density functions of the opening and of the norm of the shear stress components in the cell sealant. The cell sealant bonds on one side the MIC and on the other the inactive area of the cell, thus it constrains these components predominantly along the in-plane directions. The opening stress component increases slightly between the first (RT 0 h) and second thermal cycle (RT 10 kh). However, the locations where the stress increases are the fillets of the sealant, where the accuracy of the numerical solution may have been affected by relatively high aspect ratio of the mesh elements in that region.

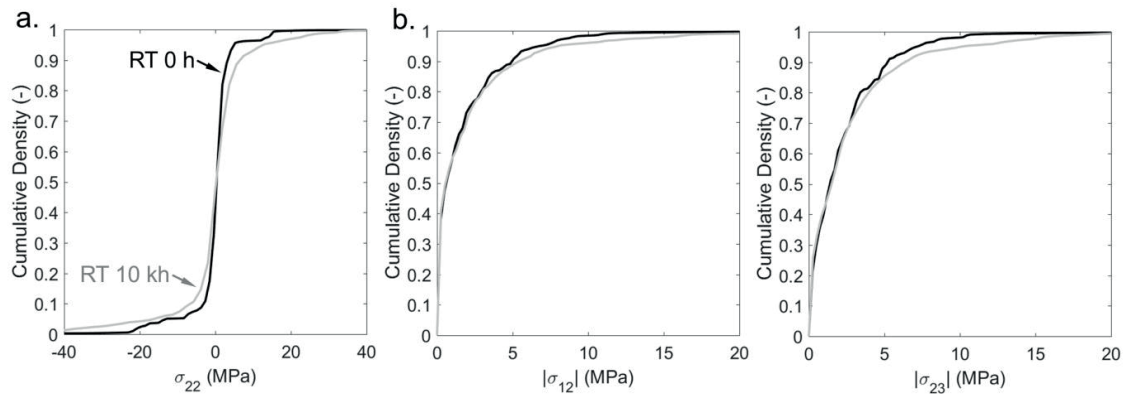


Figure 70: Cumulative density functions of the opening (a) and norm of the shear components (b) of the stress at the interface between the cell sealing, the MICs and the cell during thermal cycling. Black: RT 0h, grey: RT 10 kh air. Co-flow, fraction of pre-reforming of 0.5.

The two shear stress components between the interface of the cell sealant with the MIC and the cell do not show significant variation between the two thermal cycles. Similarly to the manifold sealants, the stresses in the cell sealant are not affected significantly by the constant long-term polarisation. The interface between cell sealant and MIC induced higher shear stresses than at the interface between cell sealant and cell, because the CTE mismatch between glass-ceramic and Crofer 22 APU is larger than that between glass-ceramic and Ni-YSZ.

The present analysis based on averaged metrics does not detect a worsening of the stress state at the sealing interface, therefore of the risk of failure assuming that the bulk and interfacial properties do not degrade significantly. In the case of uniform property degradation, the situation is expected more critical for the air outlet manifold sealing, which has oppositely lower (critical) implication in co-flow and counter-flow, in the case anode-gas recovery is not needed.

3.4 Analysis of the effects of pre-deformation, operation conditions and model formulation

This section extends the overview provided in Chapter 3.3 for a single model version (“Model v2” with modified periodic conditions) and operation (co-flow with a fraction of pre-reforming of 0.5). The discussion is extended to the effects of MIC pre-deformation (Paragraph 3.1.5), variation in the operation conditions (Paragraph 3.1.6) and variations in model assumptions and formulation (Paragraph 3.1.4).

3.4.1 Contact pressure

3.4.1.1 Difference between model assumptions

The cumulative density function of the contact pressure at the interface between the anode and fuel GDL during operation combined with thermal cycles is shown in Figure 71 for the operating points of the long-term polarisation combined with thermal cycling.

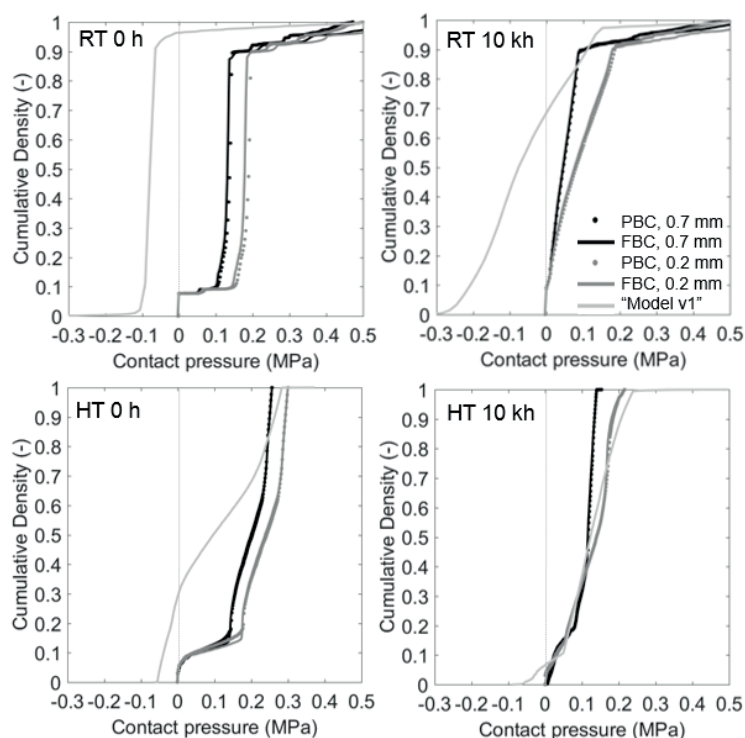


Figure 71: Cumulative density functions of the contact pressure at the interface between the anode and fuel GDL for the points RT 0 h (end of first thermal cycle), HT 0 h (start of polarisation), HT 10 kh (end of long-term polarisation) and RT 10 kh (end of second thermal cycle after long-term polarisation in co-flow with a fraction of pre-reforming of 0.5). The model version is “v2” if not indicated. Case of ideal MICs

The effects of the differences between “Model v1” and “Model v2” in terms of boundary conditions and sealant thickness are presented. Before the first thermal cycle (point A3, i.e. at a uniform temperature of 1073 K), the mean contact pressure at the anode contact interface computed by the “Model v1” is 0.15 MPa. This contact pressure is completely supplied by the assembly force. In the case of “Model v2”, the artificial residual stresses in the manifold sealants are not completely relaxed, despite the hold time, thus the mean contact pressure for 0.7 and 0.2 mm thick sealant is 0.19 MPa and 0.21 MPa, respectively.

After the first thermal cycle (point RT 0h), the contact pressure distribution shifts towards negative values for both the “Model v1” and “Model v2”. The larger decrease of contact pressure for the “Model v1” was unexpected, since almost the whole cell interface undergoes tensile stresses. The difference compared to “Model v2” is the elastic properties of the GDLs. In particular, all GDLs in “Model v1” used the arbitrary value of 0.1 as isotropic Poisson’s ratio. Instead, the anisotropic Poisson’s ratios of the GDLs materials in “Model v2” obtained from computational homogenisation are very close to that of the bulk material, i.e. around 0.3. Because of the SRU bending upon cool down, the GDL air and the GDL fuel are respectively in compressive (about -15 MPa) and tensile stresses (about +15 MPa) along the in-plane directions. Since the GDL-air is 40% thicker than the GDL-fuel, along the y-direction (i.e. stacking direction) the elastic expansion of the GDL-air is larger than the elastic shrinkage of the GDL-fuel, and this contributes to increase the contact pressure on the active area. Because of the lower Poisson’s ratio in “Model v1” (compared to “Model v2”), the elastic expansion of the GDL-air along the thickness upon cool down is lower. Hence, the elastic expansion of the GDL-air along the thickness is not sufficient to compensate the difference in thermal expansion between the GDLs and the manifold sealants caused by the cool down. As a result, the loss of contact pressure is higher than in “Model v2” and equal to about 0.25 MPa. The “kinks” observed in the cumulative density functions at high contact pressure are found only on the second version of the SRU model. They arise from the change in cell curvature in the transition zone from the inactive zone (bonded to the cell sealant) to the active area (see Chapter 3.3), which is pronounced in the second version of the model because of a through-the-thickness stiffness component of the material of the fuel GDL about four times higher than in the first version of the SRU model.

In the “Model v2” the reduction of sealant thickness is implemented without modifying the SRU thickness. Since the CTE of Crofer 22 APU is higher than that of the glass-ceramic, the difference in the through-the-thickness thermal shrinkage between the manifold sealants region and the GDLs upon cool down from point A3 to RT is lower when the thickness of the manifold sealants is 0.2 mm instead of 0.7 mm. It results in a contact pressure on the anode about higher 0.05 MPa for the case of 0.2 mm thick manifold sealants.

Upon heat-up to the temperature profile of polarisation (Figure 59), the mean contact pressure as well as the spread in distribution computed by “Model v1” and “Model v2” increase, because the difference

of the through-the-thickness thermal shrinkage between manifold sealants and GDLs differs between the outlet and inlet sides, see discussion in Chapter 3.3. About 70% of the contact interface in “Model v1” switches from negative to positive contact pressure (see Figure 71 and Figure 82), which is beneficial, even though the initial situation (RT 0 h) is undesirable. The tensile stresses at the interface are located in the inlet region.

During long-term polarisation (150 h and 10 kh for “Model v1” and “Model v2”), stress relaxation by creep in all materials redistributes the contact pressure at the cell surfaces. As a result, the negative contact pressure simulated in “Model v1” is almost completely recovered, whereas in the case of the “Model v2”, the contact pressure decreases by about 40% compared to HT 0 h. After the second thermal cycle to RT, after HT 150 h and HT 10 kh for “Model v1” and “Model v2”, respectively, about 70% of the anode side interface is under tensile stress, located in the middle and outer regions, i.e. where the temperature upon polarisation is the highest (see Figure 82). The larger difference in mean contact pressure between 0.2 and 0.7 mm thick manifold sealants is caused, similarly to the first thermal cycle, by the larger thermal shrinkage with thinner sealant and thicker metallic spacer.

For all operation points, the effects of the boundary conditions on the distribution of the contact pressure are close to negligible, by comparing the contact pressure distributions between PBC and FBC in Figure 71. This result suggests that the variations in the magnitude and shape of the y -deformation of the repeating unit are not sufficient to change the main effects that govern the distribution of the contact pressure. A further consequence is that as discussed in Chapter 3.3, the discussions apply to the contact pressure on the cathode side, which mirrors that on the anode side.

3.4.1.2 Effect of operation conditions

The effects of variations in the operation conditions on the distribution of the contact pressure at the interfaces between the anode and the fuel GDL and between the cathode and air GDL are shown in Figure 72 for the points HT 0 h (start of polarisation), HT 10 kh (end of long-term operation) and RT (thermal cycle at the end of long-term polarisation). The cumulative distribution of the contact pressure distribution for the RT 0 h is shown as reference in the RT plots in Figure 72.

Since upon heat-up the cell deflection decreases (as explained in Paragraph 3.3.2) and the thickness of the GDL-fuel increases because of thermal expansion, the contact pressure between the inactive area of the cell (constrained by the cell sealant) and the GDL-fuel is partially recovered, compare plots for the anode side between RT and HT 0 h for values of the contact pressure close to zero.

The trends observed for the other points are discussed with the help of Figure 73, which provides the evolution of the mean and standard deviation of the contact pressure at the interface between the cathode and air GDL. The values of mean contact pressure at about 0.31 MPa (the first two points) and at point A3 (i.e. start of the first thermal cycle) were discussed in Paragraph 3.3.3 and affected by

modelling artefacts. Since the temperature is uniform until the point RT 0 h, the contact pressure on the active area is practically homogenous.

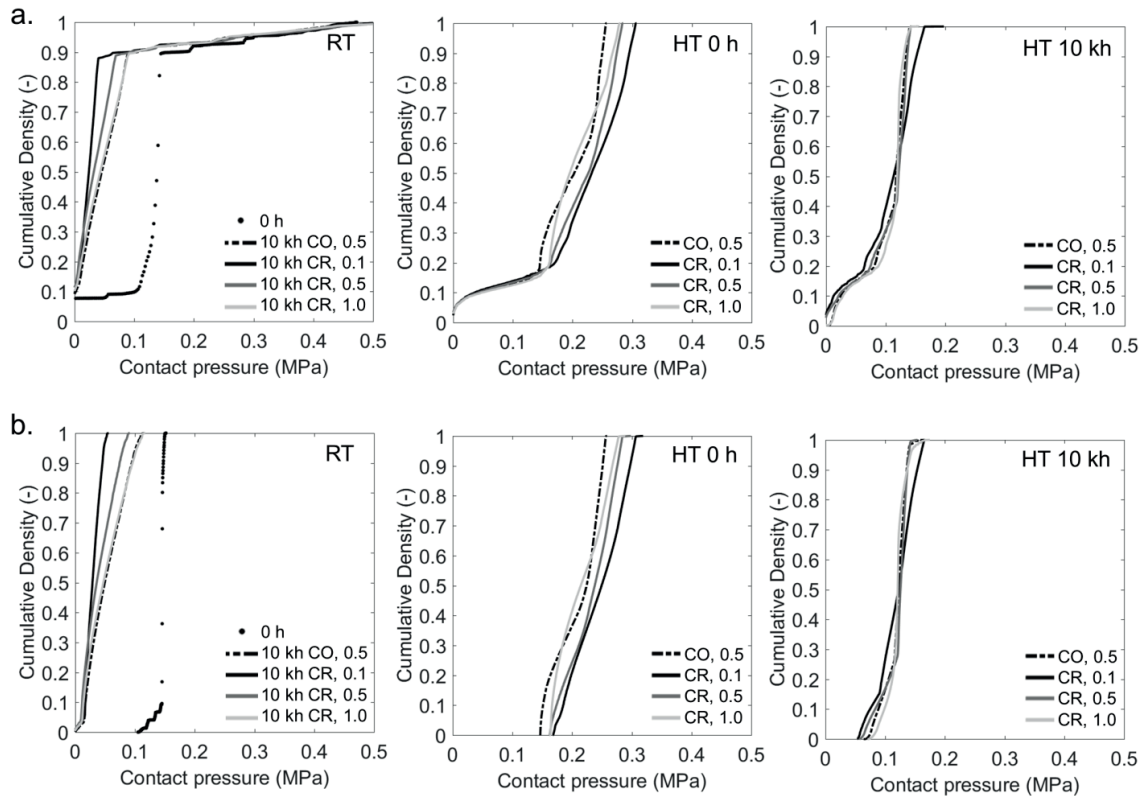


Figure 72: Cumulative density functions of the contact pressure at the interface between (a) the anode and the fuel GDL and (b) the cathode and the air GDL for the four considered operation conditions, at the operating points at RT (end of both first and second thermal cycles), HT 0 h (start of polarisation), HT 10 kh (end of long-term polarisation). Case of ideal MICs, modified periodic boundary conditions, "Model v2" with 0.7 mm sealants.

Upon heat-up to the temperature profiles of polarisation, i.e. from RT 0 h to HT 0 h, the contact pressures on both the anode and cathode sides become less homogenous, see Figure 72 and the standard deviation in Figure 73. Since the contact pressure during polarisation is largely governed by the difference in the through-the-thickness thermal expansion between the manifold sealants and the GDLs, at the start of polarisation (HT 0 h) the highest mean contact pressure on the active area occurs in counter-flow with PR=0.1, because compared to the other polarisation conditions, the difference between the mean temperature on the active area and that on the manifold sealants is the largest (in practice, this is the case where the manifold sealants are much colder than the active area), see Figure 74. For four investigated thermo-electrochemical operation conditions, the mean of the contact pressure decreases and converges in the long-term to a value of about 0.12 MPa, which is close to a contact pressure corresponding to the assembly force on the stack considered for the simulation, i.e.

the contribution of the manifold sealants on the contact pressure is negligible, because of creep relaxation in the materials.

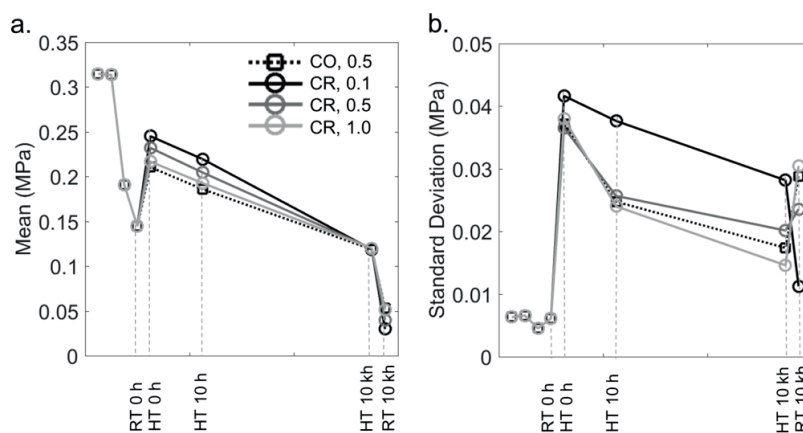


Figure 73: Evolution over the operation points of the mean (a) and standard deviation (b) of the contact pressure at the interface between the cathode and air GDL during assembly (A1-A3), operation (HT 0 h – HT 10 kh) and thermal cycling (RT 0h, RT 10 kh) for the four considered operating conditions cases (co-flow with PR=0.5, counter-flow with PR=0.1, 0.5 and 1.0). Case of ideal MIC, modified boundary conditions, “Model v2”.

For the same reason, the standard deviation of the contact pressure also decreases, but more rapidly in co-flow with PR of 0.5 and counter-flow with PR of 0.5 and 1.0, because the higher temperature at the outlet manifold sealants facilitates stress relaxation by creep in the glass-ceramic material. This behaviour towards convergence for the mean, accompanied with a decrease in standard deviation is also apparent in Figure 73.

In the second thermal cycle from HT 10 kh to RT 10 kh, the mean contact pressure decreases for all four cases of polarisation, approaching a zero contact pressure condition at the interface. For the same but reversed reasons explained above for the heat-up from RT 0 h to HT 0 h, the decrease of the contact pressure after the second thermal cycle is the highest for the counter-flow case with PR of 0.1. In the same operation condition, the difference in the mean temperature between inlet and outlet manifolds is lower than in the other polarisation cases. As a consequence, the contact pressure becomes more homogenous upon the second thermal cycle from HT 10 kh to RT 10 kh.

The relationship between polarisation conditions and simulated mean contact pressure on the active area is illustrated in Figure 74. The four investigated cases of polarisation conditions (CR 0.1, CR 0.5, CO 0.5 and CR 1.0) yield variations in the difference between the mean temperature in the active area and the manifold regions. With increase of the fraction of methane pre-reforming (for the three counter-flow cases), the mean temperature between the active area and manifold sealants decreases. As a result, the mean contact pressure on the active area at the start of polarisation decreases.

The metric is as expected limited to first estimate discussion. The results for the co-flow case with PR=0.5 deviate from the trend observed in the three cases on counter-flow. A main reason is that this

polarisation condition results in a difference between the mean temperature between outlet manifold and active area lower than in the analogous case of counter-flow (i.e. with PR=0.5).

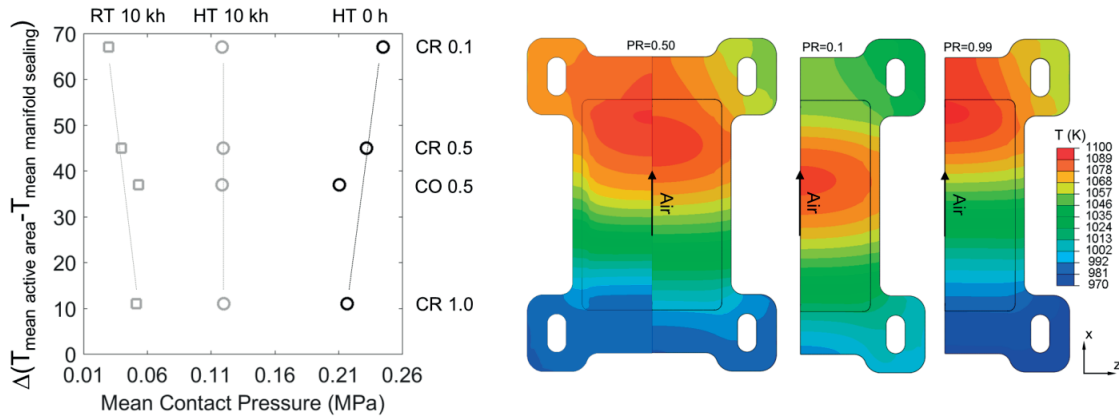


Figure 74: Relationship between the mean of the contact pressure on the cathode gas diffusion layer and the difference between the mean temperature in the active area and manifold sealant for varying operating conditions during thermal cycling (RT) and operation (HT 0 h and HT 10 kh). The dashed lines are not computed but provided as visual guides. Modified periodic boundary conditions, case of ideal MICs. The temperature profiles on the right are repeated from Figure 59.

This is noticeable by the lower ΔT for the co-flow case compared to counter-flow with PR=0.5, see Figure 74. As a result, the difference in the through-the-thickness thermal expansion between the outer manifold sealants and outer region of the GDLs is lower and so the mean contact pressure.

During long-term polarisation, the tensile stresses in the manifold sealants, generated by the difference of the through-the-thickness thermal expansion upon heat-up between manifold sealants and GDLs are relaxed by creep in both the glass-ceramic and GDLs materials. Hence, in the long-term polarisation (see point HT 10 kh in Figure 74) the mean contact pressure on the active area (0.12 MPa) is not affected by the manifold sealants, and converges to that equivalent to the assembly load.

After the second thermal cycle (point: RT 10 kh), the mean contact pressure for the four polarisation cases decreases, because the through-the-thickness thermal shrinkage of the GDLs is higher than that of the manifold sealants, and thus, compared to the condition HT 10 kh, part of the assembly force is transferred to the manifold sealants. The SRU simulations do not take into account creep deformation upon heat-ups and cool downs. This explains the symmetry in trends in the evolution of the mean contact pressure on the active area between HT 0 h and RT 10 kh conditions.

The tensile stress on the manifold sealants is caused by the difference in the through-the-thickness thermal expansion between manifold sealants and GDLs during the heat-up from RT to the temperature profile of polarisation, which is not the same at the inlet and outlet. Figure 75 shows the contact pressure at the interface between manifold sealants and MIC for the point HT 0 h, which directly affects the through-the-thickness stress component of the manifold sealants, for both co-flow and counter-flow cases, with PR equal to 0.5 and 0.1, respectively.

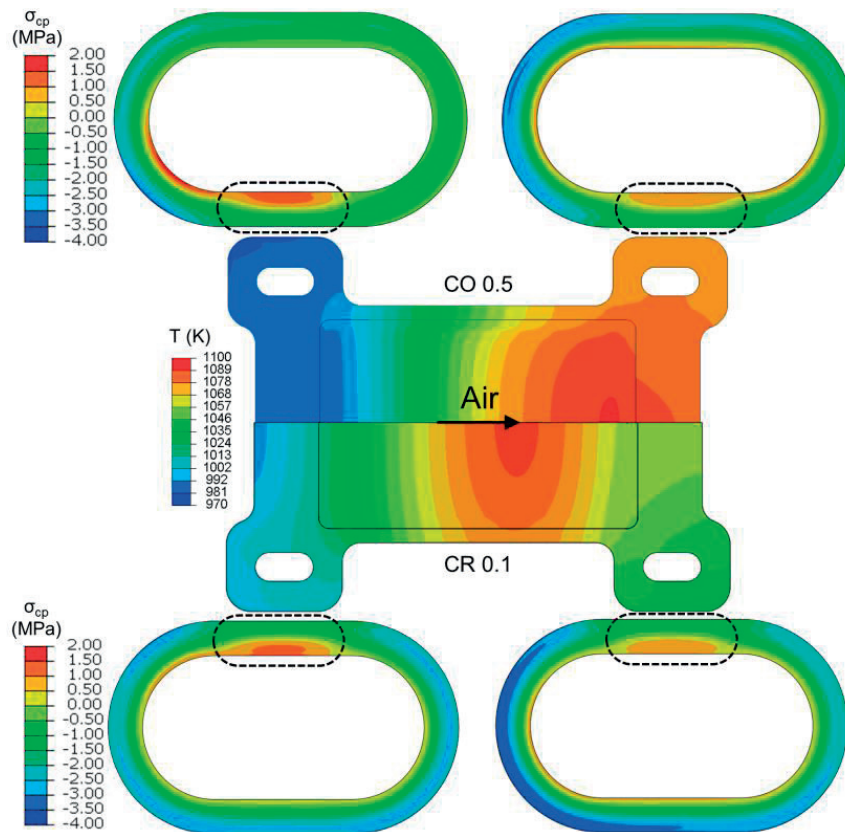


Figure 75: Contact pressure on the air inlet (left) and outlet (right) manifold sealants at the start of operation in co-flow with a methane pre-reforming fraction of 0.5 (upper) and counter-flow with a pre-reforming fraction of 0.1 (lower). Modified periodic boundary conditions without MIC pre-deformation.

The region of the MIC corresponding to the manifold sealant is unconstrained along the stacking direction, and can thus bend. Upon heat-up, the manifold sealants are subject to tension, thus the local bending of the MIC is the cause of negative (positive) contact pressure at the outer (inner) side of the manifold sealant, as shown in Figure 75.

3.4.1.3 Effect of MIC pre-deformation

The previous discussions apply for the case of ideal MIC, i.e. that has an initial geometry identical to the computer-aided design model. The present section analyses the effect of pre-deformation, following the description of the cases in Paragraph 3.1.5.

The deformations simulated by the SRU models comprising as computational domains two units and the MIC pre-deformation profiles (2Def00, 2DefA and 2DefB) are illustrated in Figure 76 in highly magnified 3-D views (for the cases 2DefA and 2DefB, only the PBC model versions are shown). The shape follows overall that of the pre-deformation (compare with Figure 52). Figure 77 further provides 2-D time-lapse plots of the evolution of the SRU deformation profile along the symmetry line until the

first thermal cycling for the simulations comprising the pre-deformed MIC profiles. That of simulated for ideal MICs is provided for comparison.

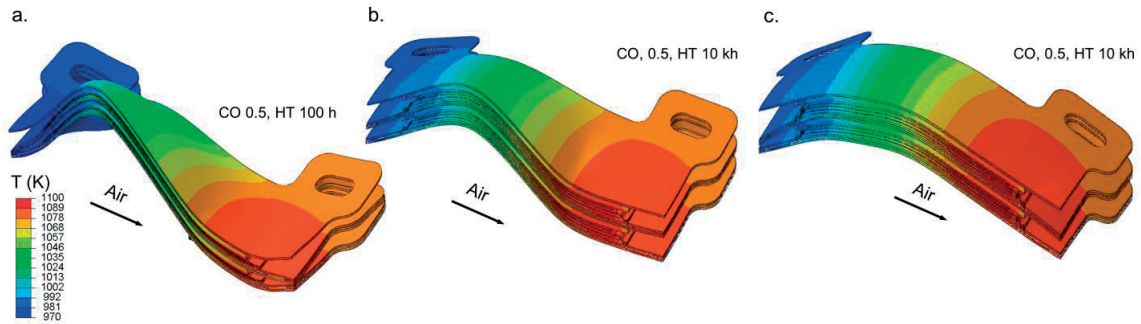


Figure 76: Highly magnified view of the simulated deformation with different MIC pre-deformation profiles. Two units computational domain, co-flow operation with a methane pre-reforming fraction (PR) of 0.5 and modified periodic boundary conditions. Pre-deformation profiles (a) 2Def00 after 150 h of operation (“Model v1”), (b) profile 2DefA, (c) profile 2DefB, both 10 kh of operation in “Model v2”.

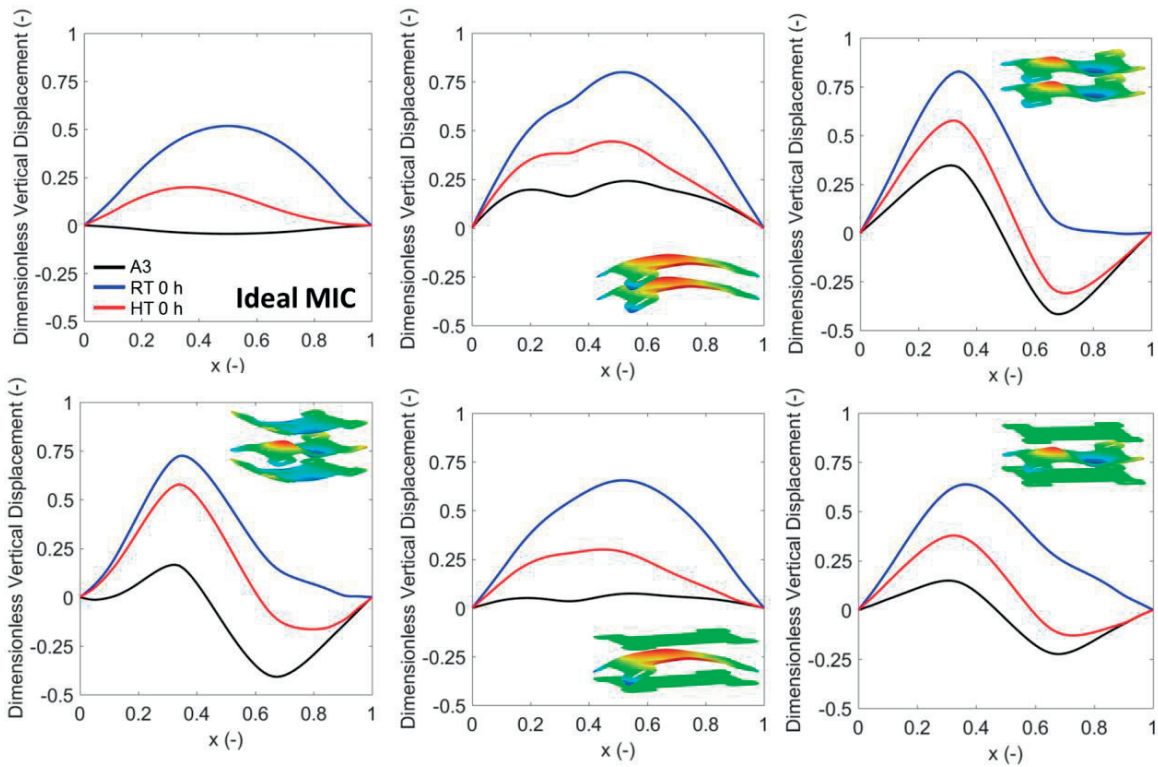


Figure 77: Evolution of the displacement in the y-direction along the symmetry line, before (A3) and after (RT 0 h) the first thermal cycle and at the start of operation in co-flow with a methane pre-reforming fraction of 0.5 (HT 0 h) for varying MIC pre-deformations (shown in inserts), PBC. The first plot refers to the ideal (flat) MIC case.

The y-deformation behaviour of the repeating unit does not show evolution in the same pattern during operation point (A3, RT 0 h and HT 0 h). The observation applies for all MIC shapes, whereas the

amplitudes vary differently upon thermal cycling. The largest variation occurred in the 2DefB case, possibly because the initial shape of the middle MIC favours the downwards bending of the SRU. Since at the start of polarisation (point HT 0 h) the outlet side of the SRU is hotter, and the elastic properties of the materials decrease with the temperature increase, the displacement in the y-direction in that region approaches that of the A3 condition by a larger extent, compared to the inlet side. Compared to the SRU models with ideal MIC, MIC pre-deformation results in changes in the shape of the distribution of the contact pressure but not in the mean value (not shown).

Before the first thermal cycle, the distribution of the contact pressure simulated by the SRU models for the MIC pre-deformation profiles 1DefA and 1DefB corresponds to that computed with ideal MICs (see Figure 78), because i) the lower stiffness of the GDLs at high temperature flattens the peaks of contact pressure at the interface and ii) the bending stiffness of both the cell and GDLs is relatively low. At the same operating point, the distribution of the contact pressure simulated by the SRU models with MIC pre-deformation profiles 2DefA and 2DefB is slightly more spread than that computed with ideal MIC (see Figure 78). Here, the lower stiffness of the GDLs at high temperature is also expected to flatten the peaks of contact pressure at the interface. For this point, the effect of the shape of the pre-deformed MICs on the contact pressure remains practically limited. The spread of the distribution of the contact pressure on the active area for the simulations of the “Model v1” with pre-deformed MIC profile 2Def00 is relatively large and comparable with those simulated by “Model v2”. The mean contact pressure is however lower, despite the higher assembly load, because in the case of “Model v2” the artificial residual stresses in the manifold sealants are not completely relaxed (see Paragraph 3.3.3), hence they contributed to increase the contact pressure.

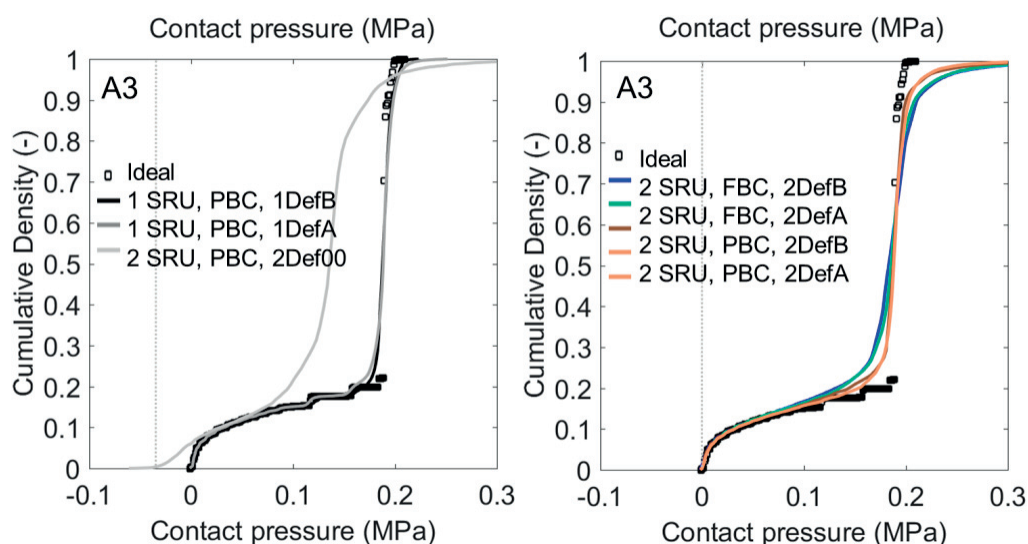


Figure 78: Cumulative density functions of the contact pressure at the interface between anode and GDL-fuel before the first thermal cycling (point: A3) for (left) a computational domain comprising on unit, pre-deformed MICs and modified PBC and (right) two units computational domain, pre-deformed MICs, modified PBC and enforced flatness (FBC).

Figure 79 shows the distribution of the contact pressure on the anode side after the two thermal cycles (i.e. RT 0 h and RT 10 kh). In the case of SRU models with one unit computational domain and identical MIC pre-deformation on the upper and lower MICs (i.e. cases 1DefA and 1DefB), the contact pressure distribution is practically unaffected by the imposed MIC pre-deformation (compared with the ideal MIC case), because the bending stiffness of both the cell and GDLs is relatively low. Increased deviations between the ideal and MIC pre-deformation cases are observed after the 1st thermal cycle. The cumulative density of the contact pressure distribution is noticeably modified in the case of SRU models with two units computational domain and MIC pre-deformation. In the “Model v1” with the MIC pre-deformation 2Def00, the spread of the distribution at the point RT 0 h is much larger than at the point A3 (Figure 78). However, the contact pressure is lost on about 30% of the active area, whereas in the case of ideal MIC the loss was on the whole interface. After polarisation followed by shut down, the distribution becomes narrower than that after the first thermal cycle, because of creep during polarisation.

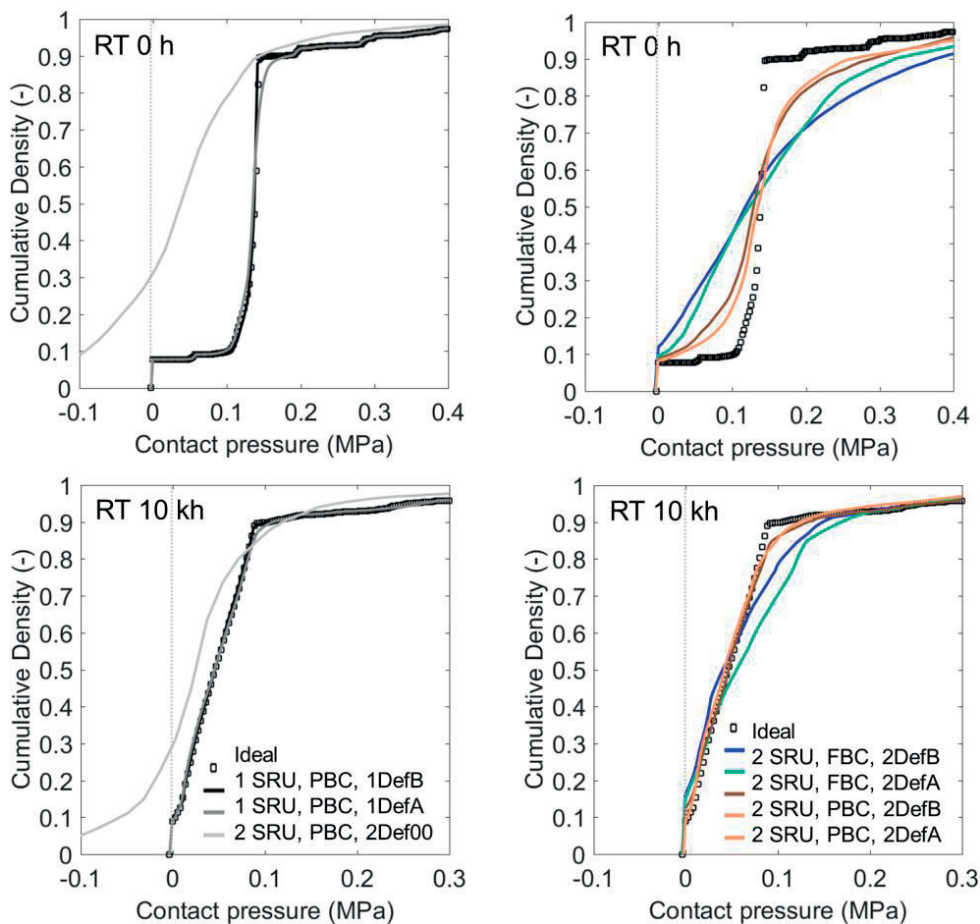


Figure 79: Cumulative density function of the contact pressure at the interface between anode and GDL-fuel before the first thermal cycle (point: A3) for (left column) one unit computational domain, pre-deformed MICs and modified PBC and (right column) two units computational domain, pre-deformed MICs, modified PBC and enforced flatness (FBC).

The effect of the pre-deformed MIC shape (2SRU-Def01 and 2SRU-Def02) is more pronounced with enforced flatness than modified periodic boundary conditions, because the periodicity between upper and lower MIC seems to help accommodating for the MIC pre-deformation. Figure 80 aims at quantifying the changes in distribution that can be assessed qualitatively in Figure 79. In the SRU models 1SRU-Def01 and 1SRU-Def02 the standard deviation of the contact pressure is negligibly affected by the MIC pre-deformation, see Figure 80 (left-hand side), as a consequence of the bending compliance of both the cell and GDLs. In contrast, the standard deviation of the contact pressure simulated for the pre-deformation profiles 2SRU-Def01 and 2SRU-Def02 are initially higher than for the ideal MIC case, but then, oppositely to the ideal MIC case, decrease during polarisation in co-flow. This effect is ascribed to the reduction of the GDLs stiffness with the temperature increase, thus upon heat-up high values of contact pressure in some regions of the active area (caused by the pre-deformed MIC) are lowered because the GDLs are more compliant. During long-term polarisation, the trend in the evolution of the standard deviation of the contact pressure follows that of the ideal MIC case. After the second thermal cycle (i.e. point RT 10 kh) the scatter of the contact pressure is lower than at the point RT 0 h, because creep deformation over the long term-polarisation compensates for the geometrical imperfections.

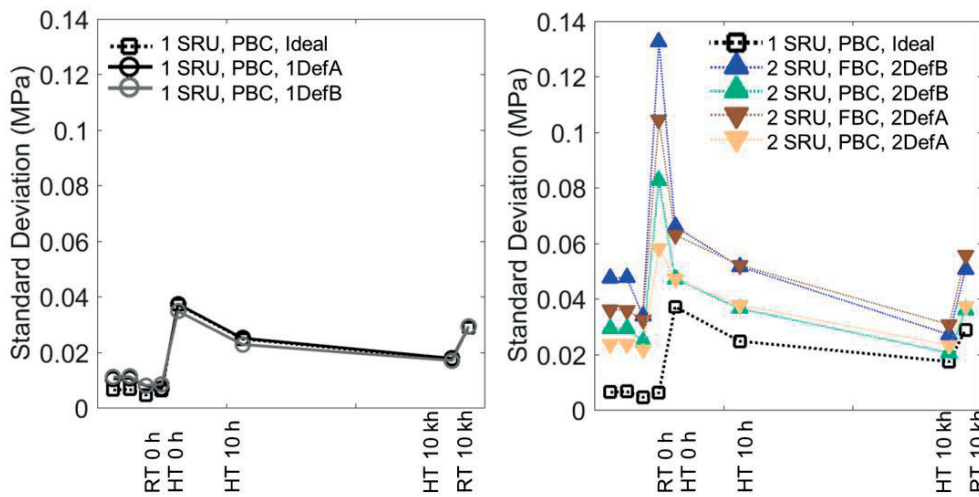


Figure 80: Evolution over the operation points of the standard deviation of the contact pressure at the interface between cathode and GDL-air for the four polarisation cases (co-flow with PRF=0.5, counter-flow with PRF=0.1, 0.5 and 1.0). Modified periodic boundary conditions without MIC pre-deformation.

The analysis of the contact pressure cumulative density function indicates that at RT 0 h, the uniformity of the contact pressure is altered by the MIC pre-deformation. Figure 81 provides the detail of the spatial distribution of the contact pressure for a selected case. As expected, in the case of MIC pre-deformation, the contact pressure does not only vary depending on the region of the active area, but also among repeating units in the stack. The profiles of the contact pressure computed for the first and

second unit are overall mirrors before operation. The quantification of the detrimental effect requires the knowledge of the relationship between contact pressure, including history, and electrical resistance. However, the results suggest that the effect on performance can be higher than anticipated from an inspection of a pre-deformation profile. The extent of the effect of alteration of the electrical contact is also expected to depend on the in-plane conductivity.

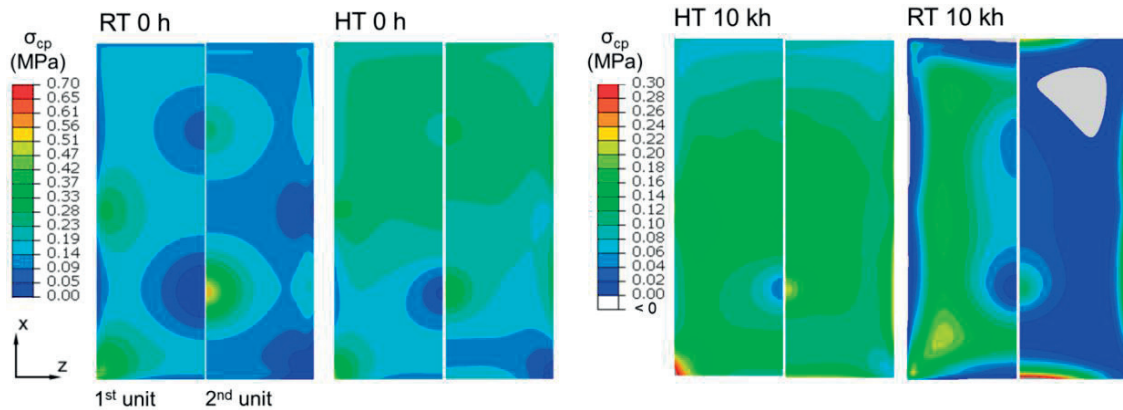


Figure 81: Evolution of the contact pressure on the cathode gas diffusion layer and discrepancy between the first and second unit, during thermal cycling (RT 0 h and RT 10 kh) and operation in co-flow with a methane pre-reforming fraction of 0.5. Modified periodic boundary conditions, MIC pre-deformation profile 2DefB. For comparison, the corresponding reference case with ideal MIC is shown in Figure 65.

Upon long-term polarisation the effect of MIC pre-deformation on the contact pressure becomes less and dominated by that of the temperature profile (at HT 0 h) and of creep (at HT 10 kh). For these operation points, the pattern of the contact pressure distribution is very similar to that shown in Figure 65; the contact pressure at the start of polarisation is higher at the central-outlet region of the active area, and decreases in the long term near the outlet. After the thermal cycle RT 10 kh, the pattern of highest contact pressure on the first unit corresponds to that of lowest contact pressure on the second unit, where complete loss of contact is detected at the outlet side. The situation is qualitatively worsened, compared to the first thermal cycle (RT 0 h).

Among the investigated cases, the largest extent of loss of contact pressure on the active area is predicted with the “Model v1”, with either ideal or pre-deformed (2Def00) MICs. Figure 82 shows in white colour the regions of the active area where the model computes a loss of compressive contact pressure. During thermal cycling, several regions of the active area are affected by a loss of contact pressure, in particular near the region of highest current density in co-flow but also counter-flow. The severity of the detrimental effect may however remain limited, as long as damage does not occur. In operation, the extent of the zone is less and the pattern is similar in the case of MIC pre-deformation. The contact pressure at the inlet is partially recovered because of creep, which also relaxes the tensile stresses at the interface. The evolution of the contact pressure on the cell between “Model v1” and

“Model v2” was shown to be considerably different. The effect was ascribed to the mechanical properties of the GDLs, which differed between the two models.

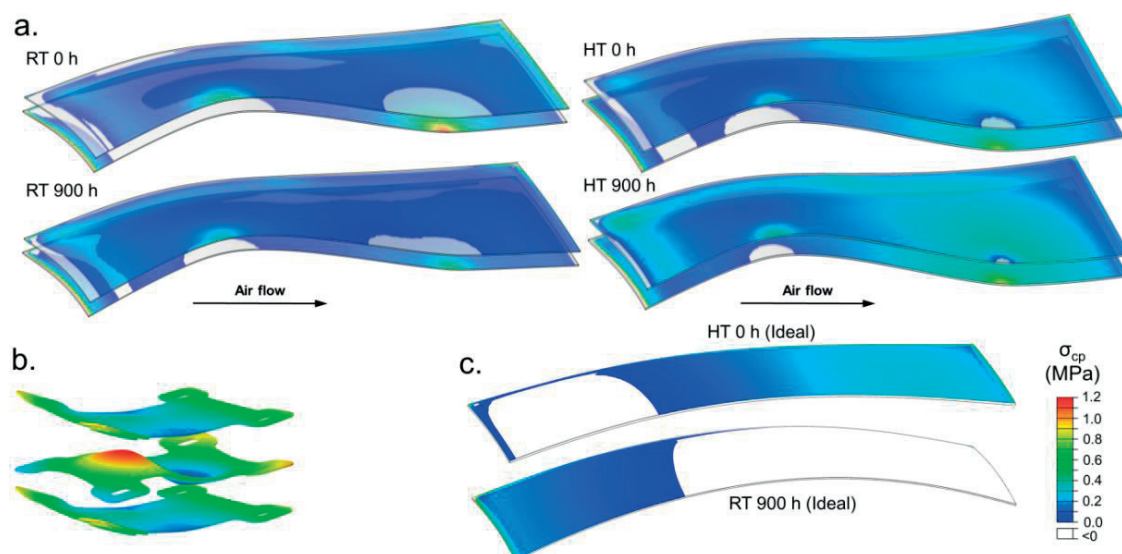


Figure 82: (a) Evolution of the contact pressure on the cathode gas diffusion layer and discrepancy between the first and second unit. During thermal cycling (RT 0 h and RT 900 h) and operation in co-flow with a methane pre-reforming fraction of 0.5 (HT 0 h and HT 900 h). Modified periodic boundary conditions, MIC pre-deformation profile 2Def00 insert in (b), the corresponding reference case without MIC pre-deformation is shown in (c).

The contribution of the design variations, i.e. in this work the possibility of contact between the cell sealant and the MIC at the interface $\partial\Omega$, was considered negligible for the effects on the contact pressure.

3.4.2 Failure of the cell

This section extends the overview of the results in Chapter 3.3 based on the visual inspection of the stress fields in the cell layers. A Weibull analysis is performed to compute the probability of failure using parameters measured in Chapter 2.3, as a metric for comparison between operation points and identifying the most detrimental effects. Chapter 3.3 showed that relevant tensile stresses are predicted only in the anode. Therefore, the probability of failure provided in the present section corresponds to that computed only for the anode. The contributions of the other layers to the total probability of failure are insignificant. The error bars correspond to the 90% confidence interval of the characteristic strength and Weibull modulus obtained from the experiments in Chapter 2.3. The upper (lower) bound of the cell failure probabilities is calculated using the lower (upper) bound Weibull parameters.

3.4.2.1 Effect of boundary conditions

Figure 83 depicts the evolution of the probability of failure of the anode during initialisation sequence and stack polarisation combined with thermal cycling for the two boundary conditions FBC and PBC applied in the “Model v2”. The latter were implemented as intuitive limiting cases corresponding to a unit near the end or the middle of a large stack, respectively. FBC conditions yield an anode probability of failure higher than PBC by a factor 1-2 under uniform temperature conditions, i.e. during assembly and thermal cycling.

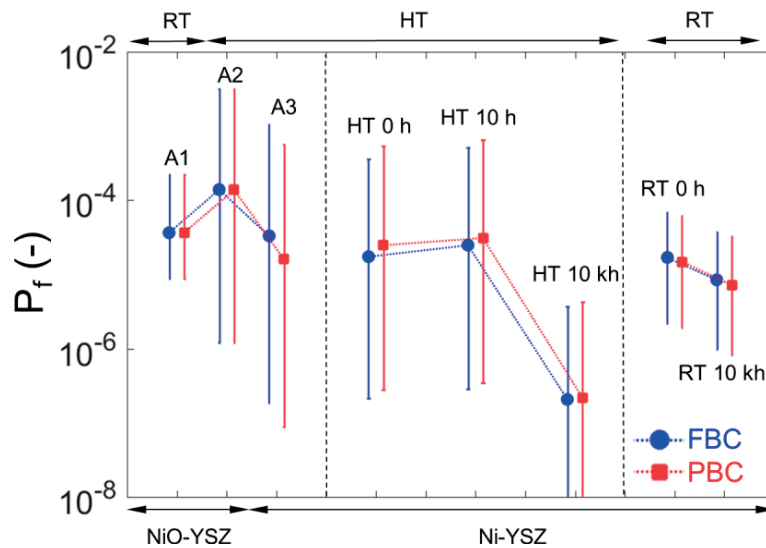


Figure 83: Effect of boundary conditions (FBC, PBC) on the probability of failure of the anode computed for a 70-cell stack (P_f) during the assembly steps (A1-A3), operation in co-flow with a methane pre-reforming fraction of 0.5 (HT 0 h – HT 10 kh) and thermal cycling (RT 0 h and RT 10 kh). Case of ideal MIC, “Model v2”.

The trend is opposite in operation, where the probability of failure with FBC is smaller than PBC, by a factor ranging from 0.7-0.94 (monotonic variations from HT 0 h to HT 10 kh).

After the sintering, the cell curvature is low (see Figure 63), hence the stresses in the anode are not strongly modified by the cell flattening during the assembly of the stack. This means that at point A1 the failure probability is governed mostly by the residual stresses after cell sintering, and equal to about 5×10^{-5} . During the first stack heat-up (anode still in oxidised conditions) the cell bends slightly downwards (see Figure 63, with simulated periodic boundary conditions). Hence, the failure probability between PBC and FBC is the same. However, it increased up to 2×10^{-4} , which is the highest value over all the analysed points in Figure 83. Anode reduction affects the failure probability differently in PBC and FBC, because the shrinkage bends the SRU downwards in the former (see Figure 63), whereas the SRU is constrained to remain flat in the latter. Consequently, the stress state in the reduced anode slightly differs in the two conditions (see Figure 84). Compared to point A2, the failure probability of the anode at the point A3 for FBC and PBC decreases to 5×10^{-5} and 2×10^{-5} , respectively.

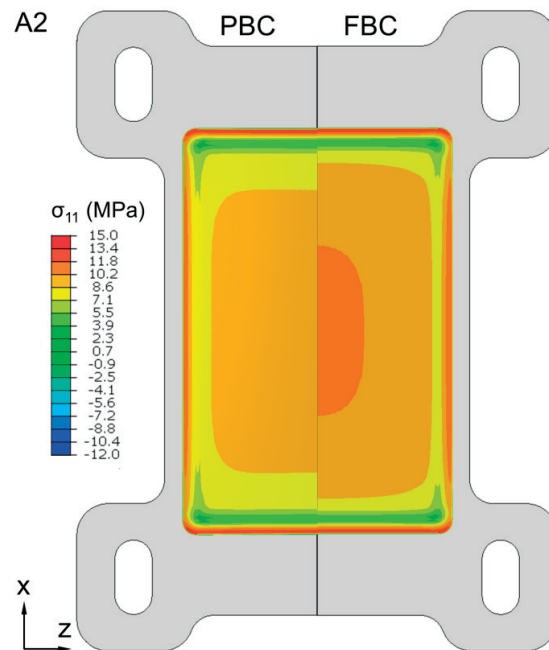


Figure 84: View of the stress σ_{11} in the anode at the end of the assembly process (A3) for modified periodic (PBC, left) and enforced flatness (FBC, right) boundary conditions, with ideal MICs.

Part of the reason of this decrease is the reduction of the elastic modulus upon reduction. The ensuing decrease in stress is balanced by a change in Weibull strength parameter, but in the present case, the former effect is dominant.

After the first thermal cycle, the failure probability does not follow the anticipated trend. As shown in Figure 61, the first principal stresses in the anode volume corresponding to the active area are highly reduced, but the probability of failure does not change significantly. Furthermore, the strength of Ni-YSZ is higher at RT. The reason is that upon cool-down, the CTE mismatch between the Ni-YSZ and the glass-ceramic induces tensile stresses in the inactive area of the anode of about 25 MPa. The heat-up from RT 0 h to the temperature profile of co-flow polarisation changed relevantly the stress in the anode, compared to the previous HT condition, i.e. at the point A3. Nonetheless, upon co-flow polarisation the lower stress at the inlet is compensated by higher stress at the outlet, especially in the colder regions surrounding those at higher temperatures, see Figure 85. As a result, the anode failure probability at the start of polarisation (point HT 0 h) is similar to that before the first thermal cycle (point A3). For this condition, the difference of anode failure probability between FBC and PBC is opposite compared to that at point A3. The reason is that, oppositely to the FBC case, in PBC the cell is less constrained to bending in the direction along the flow path. Hence, in the highest region the SRU bends more than in A3 (because here the temperature under polarisation is slightly higher than 1073 K), and this increases the magnitude of the tensile stresses in the anode, near the interface with the electrolyte.

At the beginning of the polarisation, the anode failure probability increases in both FCB and PBC cases. This is apparently due to the different in-plane creep strain rates of the joined components (because of contrast in material properties), which relaxes the stresses in the components at different rates. The increase of failure probability is less pronounced in the PBC case, possibly because slight variations in the SRU bending can partially compensate for the difference in creep strain rates, as discussed in Paragraph 3.3.2. In this work, the only intermediate time for which the probability of failure is computed is 10 h of polarisation. Therefore, the peak of highest failure probabilities upon polarisation is likely higher and might exist before or after.

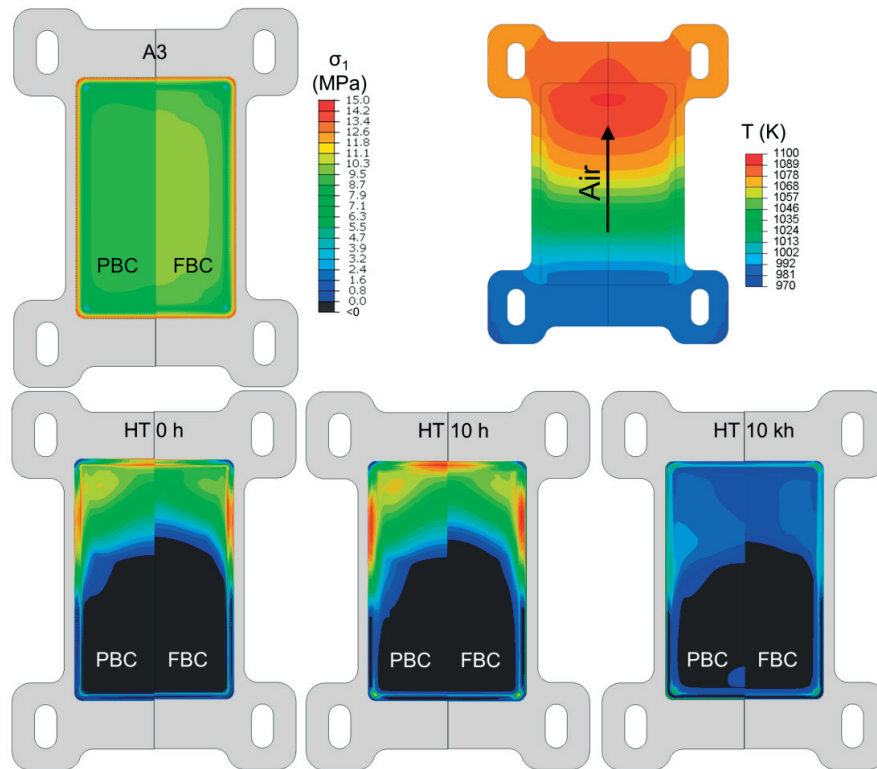


Figure 85: Evolution of the 1st principal stress σ_1 in the anode from the end of the assembly process (A3, upper left) and after up to 10 kh of operation (HT 0 h to HT 10 kh, lower serie of figures) for modified periodic (PBC, left) and enforced flatness (FBC, right) boundary conditions. Operation in co-flow with a fraction of pre-reformed of 0.5 (upper right: temperature profile repeated from Figure 59) and case of ideal MICs.

During long-term polarisation, creep in all materials significantly relieves the stresses in the anode in both FBC and PBC, see Figure 85. Consequently, at the point HT 10 kh, the failure probability is the lowest of the simulated scenarios. In this study, the dependence of the Weibull statistics parameters on the microstructural changes upon ageing is not considered, which may change the computed values of anode failure probability after the long-term polarisation. The trend between FBC and PBC is similar between the first and second thermal cycle. The probability of failure is reduced during the second

thermal cycle, because the cool down to RT started from a temperature higher (lower) than 1073 K at the outlet (inlet) region. Consequently, the difference in thermal shrinkage between the cell sealant and anode is lower at the inlet, compared to RT 0h, and hence the stress in the anode. At the outlet, the difference in thermal shrinkage between cell sealant and anode is slightly higher than in the first thermal cycling. However, the elastic modulus of the glass-ceramic is relatively low at high temperatures, thus at the outlet region the effects on the stresses of the CTE mismatch between cell and sealant are reduced at the beginning of the cool down.

3.4.2.2 Effect of operation conditions

Figure 86 provides a comparison of the probability of failure of the anode computed for the four cases of polarisation analysed in this work, followed by thermal cycling to RT. The “Model v2” is here considered, with PBC and with ideal MIC. The comparison of Figure 86 with Figure 59 highlights the strong dependence of the failure probability on the shape of the temperature profile during operation. A relevant aspect is the location of the region of highest temperature in the cell, because the cell regions surrounding the hottest zone constrain the higher thermal expansion and thus are subjected to tensile stress. Therefore, the operation with the conditions CR 0.1 is the most critical (see Figure 87), yielding a probability of failure between 0-1. In the long-term, creep relaxes the stresses in all materials. Since the creep strain rate is strongly dependent upon temperature and stress, the stress relaxation is the highest under the conditions CR 0.1. As a result, the cell failure probability for this polarisation condition is reduced drastically after 10 kh of operation, which even turns out being the safest condition among the conditions shown in Figure 86.

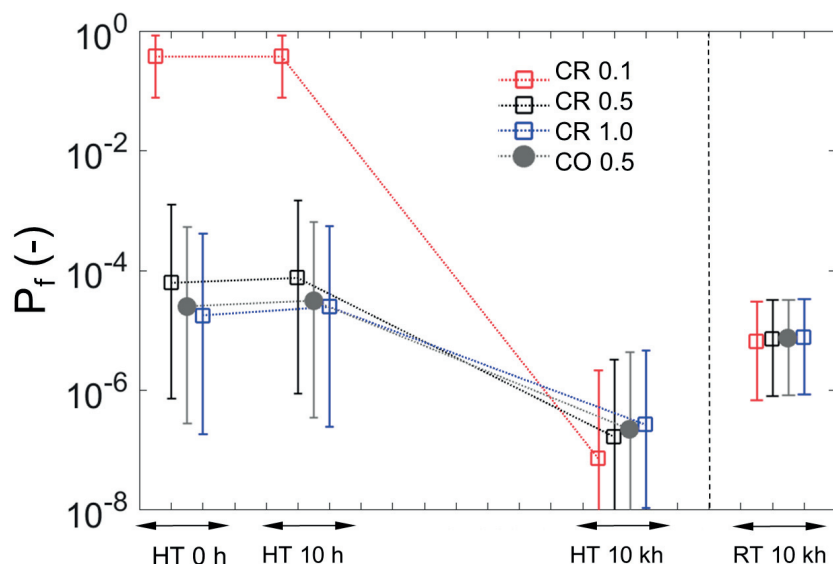


Figure 86: Effect of the operation conditions (co- and counter-flow and varying methane pre-reforming fractions) on the probability of failure computed for a 70-cell stack (P_f). Case of ideal MIC with modified periodic boundary conditions (PBC).

The sensitivity of the anode failure probability to the polarisation conditions is predominant for high fractions of internal reforming: by increasing the PR (in counter-flow) from 0.1 to 0.5, the cell failure probability is reduced in the short-term polarisation by almost four orders of magnitude.

The shape of the temperature profile exhibits similar patterns in CO 0.5 and CR 1.0, which results in similar anode failure probability.

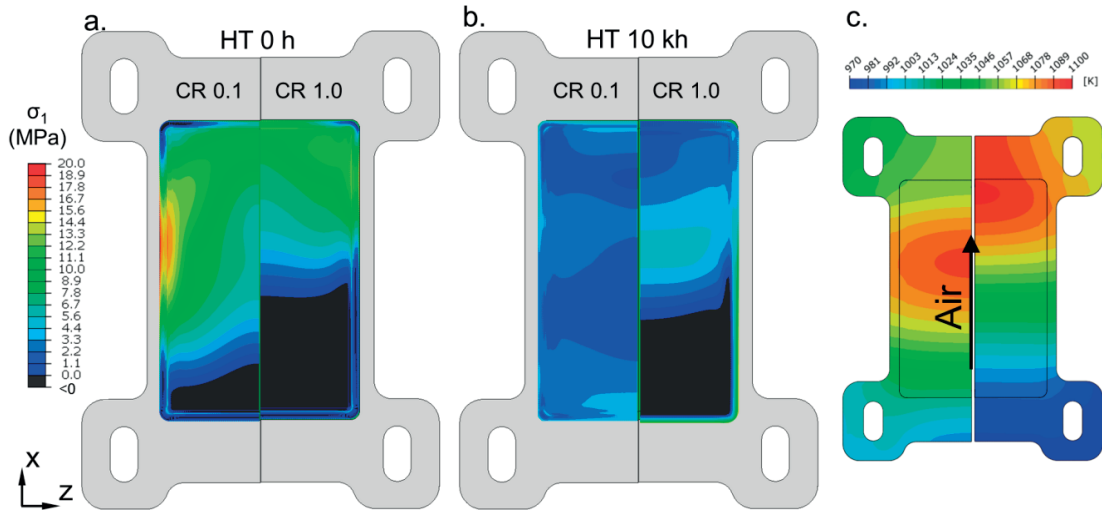


Figure 87: Evolution of the 1st principal stress σ_1 in the anode during operation from 0 h (a) up to 10 kh (b), in counter-flow with a fraction of pre-reformed methane of 0.1 (left side) and 1.0 (right side). (c) Corresponding temperature profiles repeated from Figure 59. Case of ideal MICs with modified periodic boundary conditions (PBC).

The anode failure probability after the second thermal cycle is practically unaffected by the temperature profile and thus by the polarisation conditions. The reason is that the difference between the mean temperature of each temperature profile and RT is much larger than the temperature variations of the four temperature profiles. Hence, thermal cycling effects dominate over those of thermal gradients.

3.4.2.3 Component pre-deformation

The effects of the cell vertical deformation on the failure probability caused by the assembly using pre-deformed MICs are discussed here. For the cases where the computational domain comprises a single unit and in the case of modified PBC, MIC pre-deformation increases the probability of failure during the assembly (up to A3) by a factor ranging from 1÷3 for “1DefA” and by 1.05÷1.4 for “1DefB”. The effect remains of the same order of magnitude during operation in co-flow with PR=0.5 but the trend is opposite. The probability of failure is decreased by factors spanning from 0.94-0.98 “1DefB” and 0.84-0.88 “1DefA”, but in the case “1DefB”, it slightly increases after 10 kh, by a factor up to 1.3. Therefore, the profile “1DefB” yields slightly better (worse) conditions at uniform (operation) temperature,

compared to the profile 1DefA". The changes in the first principal stress in the anode between ideal and pre-deformed MICs are subtle and cannot be clearly seen from the inspection of in Figure 88 (0 h). After the two thermal cycles, the failure probability is very similar and no clear trend is observed compared to the case of ideal MIC (factors ranging from 0.98-1.07).

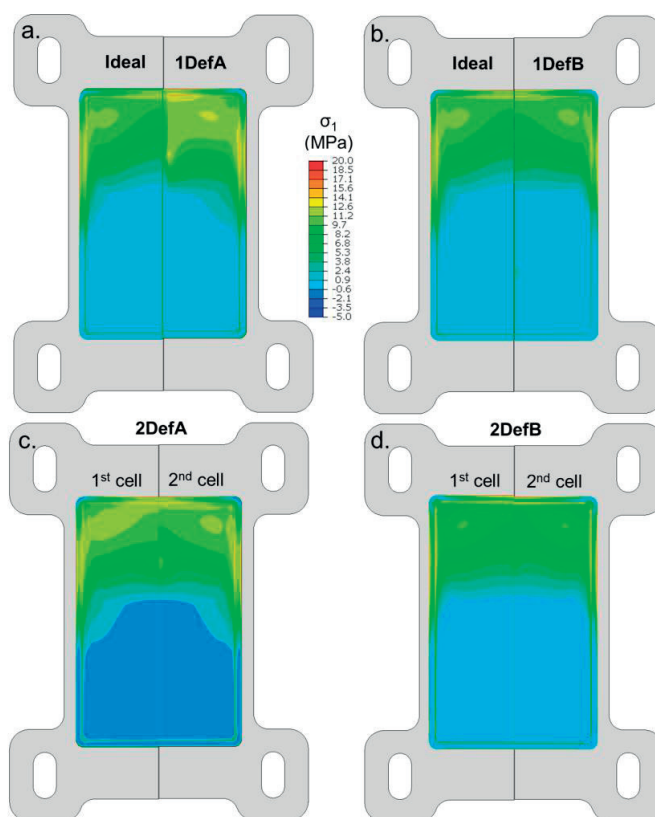


Figure 88: Effect of MIC pre-deformation on the 1st principal stress σ_1 in the anode at the start of operation (HT 0h). (a,b) Simulation with one unit, comparison between the ideal case (left) and pre-deformation profiles (right) 1DefA and 1DefB. (c,d) Comparison of the stress in the first (left) and second cell (right) simulated with the 2 unit models with pre-deformation profiles 2DefA (c) and 2DefB (d). Modified periodic boundary conditions (PBC) and co-flow with a fraction of pre-reformed methane of 0.5.

The investigated MIC pre-deformation cases requiring the meshing of two units highlight similar trends. Similarly to results of one unit model, the effects of using dissimilar pre-deformed MIC shapes are practically negligible. For the MIC pre-deformation profiles 2DefA and 2DefB, the first principal stress in the anode for the upper and lower unit is shown in Figure 88. Overall, the variations in the anode failure probability caused by the MIC pre-deformation cases investigated in the present work are believed practically insignificant. In all 2 SRU cases, the difference between the first and second cell remains limited, with factors between 0.75-1.5 (compared to the ideal case). As suggested by Figure 80, the standard deviation is higher in the case "2DefA". It can however be not excluded that MIC pre-

deformations of higher average magnitude and/or smaller radius of local MIC curvature may affect differently the cell failure probability. For all pre-deformation cases, the magnitude of the stresses in both the electrolyte and compatibility layer are similar to that in Figure 62.

3.4.3 Sealing Failure

The discussions in Chapter 3.3 showed that the uniaxial stress σ_{22} (mode I direction) is mostly governed by the difference in thermal expansion between the GDL and the glass-ceramic materials, and directly affected the contact pressure on the cell active area. In contrast, the shear stress components σ_{12} and σ_{23} at the interfaces between sealant and MIC are governed by the CTE mismatch between Crofer 22 APU (the MIC alloy) and glass-ceramic. This section extends the discussion to the effects of model version, operation conditions using the cumulative distribution of the stress at the interface between the sealant and the MIC. The risk of failure is also discussed in terms of a tentative energy-based calculation performed on the repeating unit models.

Since the stresses during thermal cycling to RT are expected to be dependent upon the temperature variation, in the following Paragraphs 3.4.3.1, 3.4.3.2 and 3.4.3.3 only the manifold sealant at the air outlet side is considered, because it is systematically subjected to higher temperature than the air inlet, regardless of the operation conditions. For reference, reported values of the normal and shear strength of sealants are 79 MPa and 18 MPa, respectively [147]. The shear strength value is referred to the interface between sealant and Crofer 22 APU.

3.4.3.1 Effect of variation in the model assumptions

The differences between “Model v1” and “Model v2” yield to specific evolution of the contact pressure on the cell (see Paragraph 3.4.1 for further details). Consequently, the σ_{22} in the manifold sealants for the two versions is different, as shown in Figure 89. The boundary conditions (i.e. FBC and PBC), which approximate the conditions of the SRU in the stack, do not affect relevantly the stress in the sealants simulated by the “Model v2”. This indicates that upon thermal cycling, the CTE mismatches between the materials rather than the SRU deformation control the stress in the manifold sealants. In the “Model v1”, i) the GDL interfaces are under tensile stresses (about -0.08 MPa, see Paragraph 3.4.1) and ii) there is no contact interface $\partial\Omega_{ct}$. This means that the whole assembly load, in addition to the tensile forces on the GDL interfaces, is completely supported by the manifold sealants, which undergo compression. This compressive force induces the bending of the region of the MIC bonded to the sealant. Hence, the manifold sealants are subjected to compressive and tensile stresses, respectively at the outer and inner regions. The bending of the MIC locally is also the reason of the higher shear stress components in “Model v1” than “Model v2”.

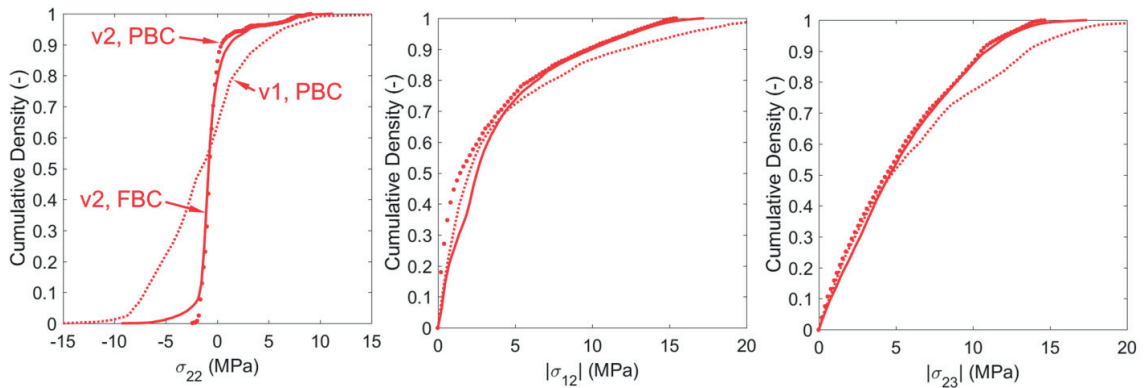


Figure 89: Cumulative probability density function of the opening and shear stress at the sealing interfaces in the air outlet manifold at room temperature, after 10 kh of operation in co-flow with a fraction of pre-reformed methane of 0.5 (CO 0.5) simulated by the “Model v1” and “Model v2” models with modified periodic (PBC) or enforced flatness (FBC) boundary conditions.

3.4.3.2 Effect of operation conditions

The variation of the temperature profiles for the different polarisation cases is expected to affect the stress in the sealants upon thermal cycling. Figure 90 shows the simulated i) uniaxial stress σ_{22} and ii) shear stress components σ_{12} and σ_{23} at the interfaces between the sealant and the MIC. For the second thermal cycling, the uniaxial stress σ_{22} correlates to the variation of contact pressure on the active area between HT 10 kh and RT 10 kh. From Figure 74, the mean contact pressure on the active area decreases by about 73% and 56%, respectively for CR 0.1 and CR 1.0 (extreme cases). However, the mirror of this difference is not observed in the uniaxial stress σ_{22} , because the mean value of the stress is about -0.8 MPa for all four polarisation cases. The reason is that the contact pressure at the interface $\partial\Omega_{ct}$ (see Figure 48) increases for higher temperatures of the manifold sealants.

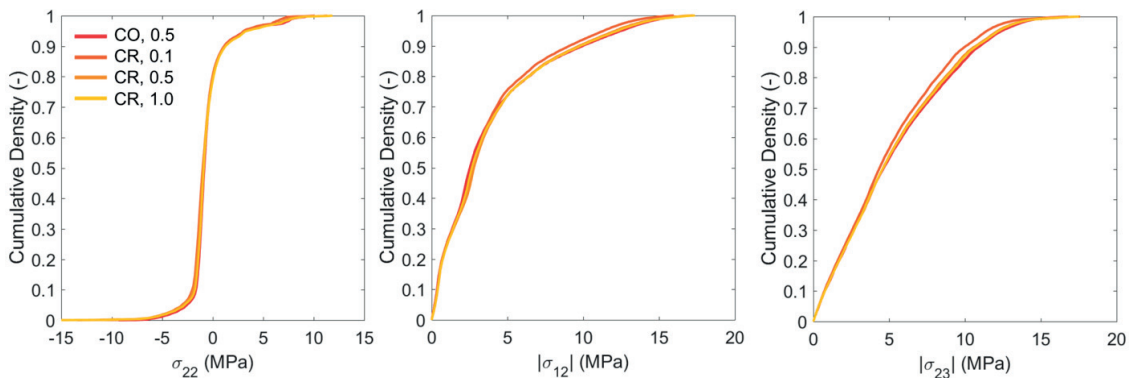


Figure 90: Effect of the operation conditions on the cumulative probability density function of the opening and shear stress at the sealing interfaces in the air outlet manifold at room temperature, after 10 kh of operation. Case of ideal MICs with modified periodic boundary conditions and “Model v2”.

Hence, the fraction of assembly load supported by the contact interface $\partial\Omega_{ct}$ increases for higher temperatures of the manifold sealants. As a result, the uniaxial stress σ_{22} remains close to constant, regardless of the polarisation conditions. Both shear components of the stress tensor at the interface between the outlet manifold sealants and MIC σ_{12} and σ_{23} are proportional to the temperature variation during the second thermal cycling (i.e. between HT 10 kh and RT 10 kh), because such stresses are caused by the CTE mismatch between the glass-ceramic and the Crofer 22 APU MIC material. Under the polarisation in counter-flow with PR=0.1, the mean temperature at the outlet manifold sealant is the lowest with respect to the other cases, i.e. about 1042 K. Consequently, the shear stress components are the lowest (see Figure 90). For the other polarisation cases, the increase of the shear stress for counter-flow PR=0.5, counter-flow PR=1.0 and co-flow PR=0.5, follows that of the mean temperature at the outer manifold sealant, which equal 1060 K, 1070 K and 1075 K, respectively. These differences in shear stress between the polarisation cases are however very low, because i) the cool down to RT dominates and ii) the elastic modulus is lower at high temperatures, hence the effect of the CTE mismatch on the stresses is reduced.

3.4.3.3 Effect of pre-deformed MIC

The effects of the MIC pre-deformation on both the uniaxial stress σ_{22} and the shear stress components σ_{12} and σ_{23} are shown in Figure 91. In the “Model v1” with MIC pre-deformation, the loss of contact pressure on the active area after the second thermal cycle is less pronounced than with ideal MIC (see Paragraph 3.4.1). As a result, the fraction of the assembly load supported by the manifold sealants is lower, and their stresses very similar to those computed by the “Model v2” with MIC pre-deformation. In the “Model v2”, the effects of MIC pre-deformation on the simulated stress in the manifold sealants are very similar.

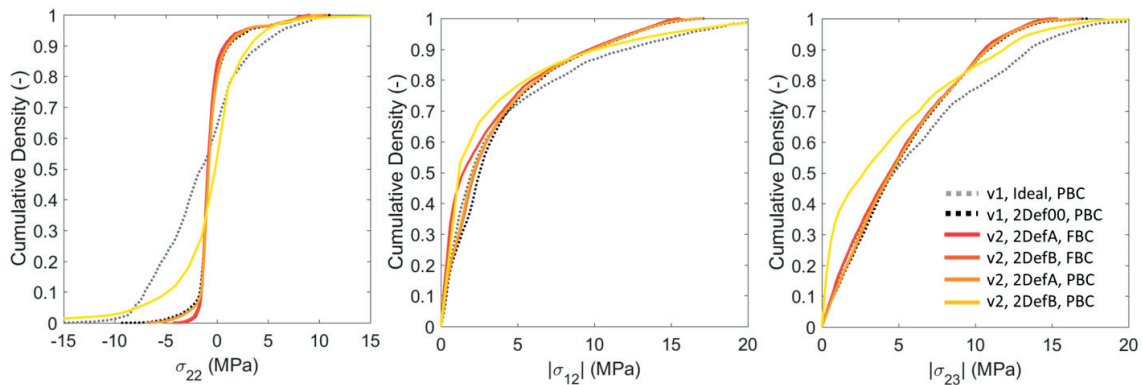


Figure 91: Effect of MIC pre-deformation and boundary conditions on the cumulative probability density function of the opening and shear stress at the sealing interfaces in the air outlet manifold at room temperature, after 10 kh of operation in co-flow with a fraction of pre-reformed methane of 0.5 (CO 0.5).

A larger distribution of both the uniaxial stress σ_{22} and of the shear stresses σ_{12} and σ_{23} is found for the case “2DefB” with PBC, supposedly because the simulated variation in the SRU bending is larger upon thermal cycling (see Paragraph 3.3.2).

3.4.3.4 Energy-based analysis

This section provides the results of the energy-based calculation described in Chapter 3.1. The upper (a1) or lower (a2) interface of the air inlet or outlet sealant are disabled, i.e. four release calculations are performed for each of the first or second thermal cycle. The joined surface pairs are therefore either free of interaction or subjected to frictionless contact. The elastic energy in the model is computed before and after the release to obtain an averaged elastic energy release rate, referred to as ERR hereafter (see Chapter 3.1 for a discussion on the partial validity of this use).

Partial interpenetration of the detached parts occurred for all simulated cases. At a first appraisal, the values computed without frictionless contact are therefore expected to represent overestimations, yet cannot be rigorously considered as an upper bound for the range of total ERR values.

The detachment simulation implies that manifold sealants on both sides of the symmetry axis fail at the same time and at the same interface. Further, in the case of modified periodic boundary conditions, the simulation corresponds to the simultaneous release of all interfaces in the stack. The restrictions to the applicability limits of the computed indicator may seem at a first appraisal problematic. VCCT computations (see Chapter 3.1) were therefore performed on simplified geometries to verify that the order of magnitude of the repeating unit model prediction is the same and estimates how the strain energy release rate varies as a function of the crack extension.

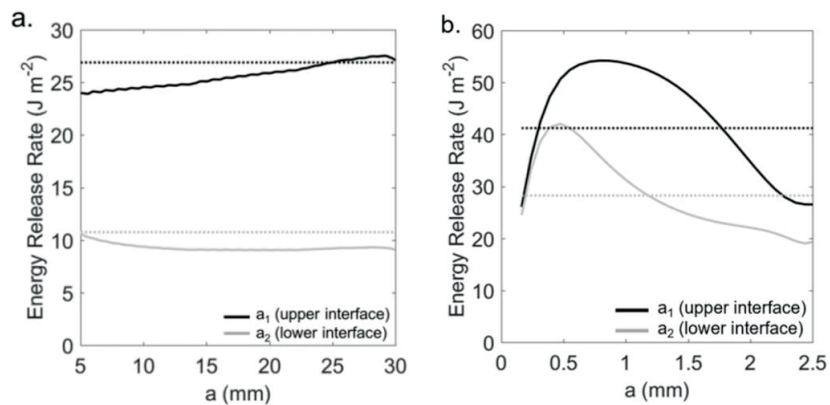


Figure 92: Energy release rate computed for the stripe (a) and axisymmetric (b) simplification of the manifold sealing region shown in Figure 58 a and b, respectively. Dashed lines correspond to computations based on total energy variation, similar to that applied at the stack scale.

Figure 92 shows the VCCT simulation results for the stripe and axisymmetric simplified models presented in Chapter 3.1. In both cases, the upper interface (a_1) appears more critical. As anticipated,

the computed strain energy-release rate remains close to independent of the crack length for the stripe case (Figure 92-a), but not for the axisymmetric case (Figure 92-b). The crack length-dependent VCCT and averaged detachment-based calculations however fall within the same order of magnitude. The release of energy is also higher for the axisymmetric case. Reported fracture toughness of glass-ceramic based sealants ranges between 0.6 and 1.1 MPa(m^{0.5}) [167]. The outcome of the analysis using the repeating unit model is therefore expected to support the improvement of the understanding of the sealant failure, despite the theoretical limitations.

Figure 93 provides the overview of all the ERR estimated by surface detachment in the stack “Model v2”. Analysis based on the implemented procedure for ERR estimation and on stress cumulative distribution function differs. The variations observed among the cases are much more significant than for the stress-based analysis.

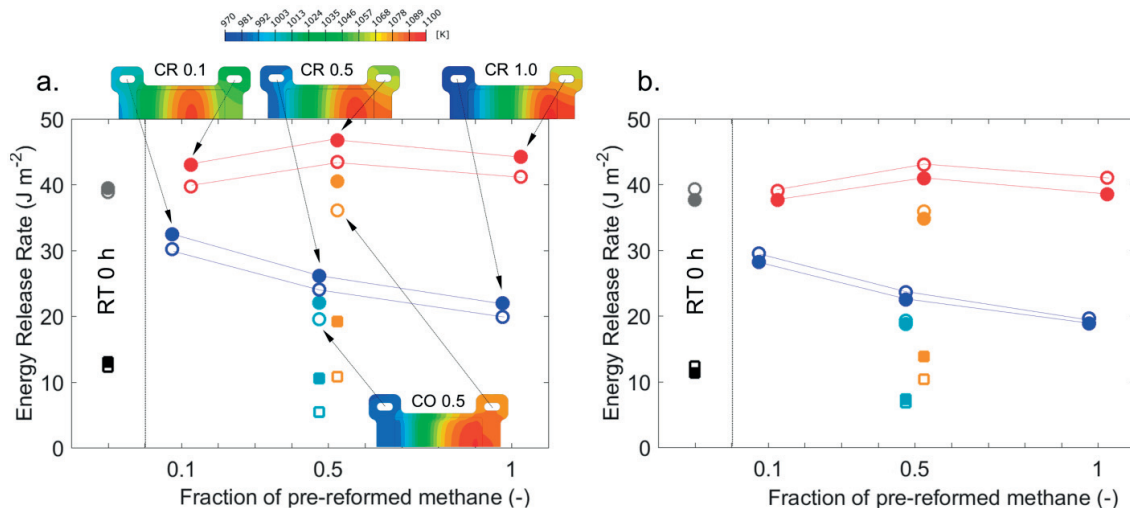


Figure 93: Elastic energy release rate at the manifold sealants computed by releasing the interfaces without (a) or with frictionless contact (b). Detachment simulations were performed after the first (RT 0 h, black and grey) and after the second thermal cycle (blue: air inlet, red: air outlet) after 10 kh of operation in co- (light blue and red) or counter-flow with varying fraction of methane pre-reforming. Square and circles refer to FBC and PBC, respectively. Filled and empty markers refer to the interface a1 (upper) and a2 (lower), respectively. Thickness of the sealing is 0.7 mm.

As a first verification, the calculated ERR is practically the same for the inlet and outlet manifold sealants after the first thermal cycle. The computed discrepancy is lower than 0.5 % in the worst case. The range of ERR values calculated with interface detachment of 0.7 mm thick sealant after the first and second thermal cycle is 10-35 Jm⁻², which falls within the same range as the VCCT values both with stripe and axisymmetric geometries, approximately 10-50 Jm⁻² (see Figure 92). The difference in the geometry likely accounts for a non-negligible share of the difference. The ERR computed for the FBC is in average about three times higher than for the PBC case, which suggests that the risk of sealant failure is dependent upon position in the stack.

The case without frictionless sliding is first discussed (Figure 93-a). The ERR calculated for the interface a1 (upper) is higher than for a2 (lower) by about 6% and 2%, respectively with FBC and PBC, which is qualitatively in line with the VCCT on axisymmetric calculations. For all polarisation cases, the ERR calculated with interface detachment is always higher at the air outlet than at the inlet manifold sealant. Operation in counter flow proves more critical after the second thermal cycle, based on the case PR=0.5. For all counter-flow cases (PR=0.1, 0.5 and 1.0 and PBC), the ERR of the outer manifold sealant is higher than after the first thermal cycle, for both interface a1 and a2, whereas at the inlet it is lower. The most critical case is CR 0.5, with an increase in ERR by about 20% compared to the first thermal cycle. The results suggest a detrimental effect of long-term operation, which is not clearly highlighted by the stress-based analysis. In reality, the properties of the interface are further expected to change and contribute to additional time and history dependence.

In co-flow with PR=0.5 and PBC, the ERR increases (decreases) by about 4% for interface a1 (a2) after the second thermal cycle. For the same operation conditions but in FBC, the ERR increases at interface a1 by about 40% compared to the first thermal cycle. Hence, after the second thermal cycle the interface a1 (upper) is more critical than a2 (lower).

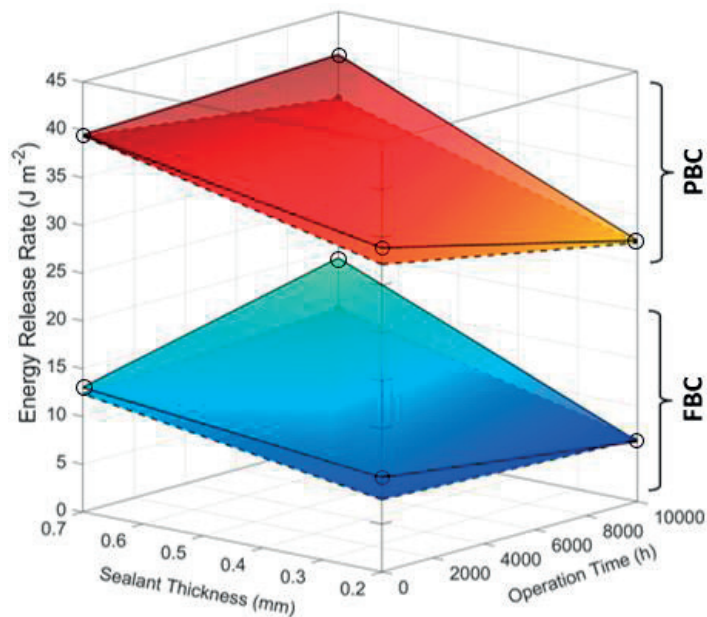


Figure 94: Elastic energy release rate at the manifold sealants computed by releasing the interfaces without (planes with continuous contour) or with frictionless contact (planes with dashed contour). Detachment simulations were performed after the first and second thermal cycle after 10 kh of operation in co-flow and for two sealing thickness (0.2 and 0.7 mm), and varying boundary conditions (EFLT and MPBC). For each condition, only the worst case is shown (corners of the planes, which are provided as a guide).

The ERR is lower by approximately 7% on average with frictionless contact (Figure 93-b), because only sliding at the interface occurs in all cases. The ERR after the first thermal cycle is lower for the interface

a1 (upper) than for a2 (lower) by about 10% and 5%, respectively with FBC and PBC, i.e. opposite to ERR calculated without frictionless contact. Frictionless contact does not change the overall trends after the second thermal cycle: all counter-flow cases are more critical than co-flow with PR=0.5. For all polarisation cases, the ERR calculated with frictionless contact is also always higher at the outlet than at the inlet manifold sealant. For all counter-flow cases (PRF=0.1, 0.5 and 1.0), the ERR calculated with frictionless contact is higher than after the first thermal cycle. Similarly to ERR calculated without frictionless contact, the most critical case is CR 0.5, where the ERR increases by about 10%. After the second thermal cycle with 0.7 mm thick sealant, the interface a2 (lower) is more critical than a1 (upper).

Figure 94 provides an overview of the worst case for each operation point and model assumption, for comparing the ERR computed for sealant thicknesses of 0.2 mm and 0.7 mm. The difference between the boundary conditions FBC and PBC is also large and follows the same trend regardless of the thickness of the sealant. The reduction of the sealant thickness to 0.2 mm is beneficial and yields a decrease of the ERR by about 25 %. This trend is approximately the same for both the first and second thermal cycles.

3.5 Modelling the impact of creep on the probability of failure of a solid oxide fuel cell stack

Post-print version of the article published in the Journal of the European Ceramic Society 34 (2014) 2695–2704, DOI: 10.1016/j.jeurceramsoc.2013.12.055

Authors: Fabio Greco, Henrik Lund Frandsen, Arata Nakajo, Mads Find Madsen, Jan Van herle

Corresponding author: Fabio Greco

Contribution of the corresponding author: model development and simulation, writing of the manuscript, generation of the images/plots.

The results in Paragraph 3.4.2 demonstrate that the evolution of the risk of failure in the cell is not necessarily monotonic during operation under constant conditions: the probability of failure of anode is found to be higher after 10 h than at the start of the operation, which warrants further detailed analysis. This Chapter provides a complementary study, as a start for investigating the evolution of the probability of failure during changes in the operations conditions. The analysis is performed using different thermo-electrochemical and thermo-mechanical models and stack design than the main results provided in this Thesis. The details of the model implementation are provided in the published work from which this chapter is adapted [57]. The model description hereafter is focused on the differences with the significantly more advanced models that are presented in Chapter 3.1, which has superior capabilities and was developed later in this thesis.

3.5.1 Description of the modelling approach

3.5.1.1 Geometry and mechanical properties

A similar uncoupled thermo-mechanical and electrochemical approach as described in Chapter 3.1 is used for the present study.

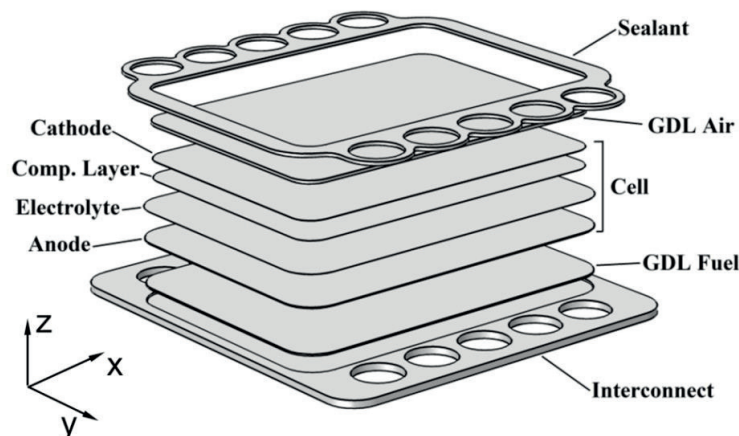


Figure 95: Representation of the three dimensional model of the SRU and denomination of the components.

The modelled geometry is shown in Figure 95. The anode-supported cell with a 320 μm thick substrate is housed into a metallic frame, which works not only as interconnect, but also as structure for the manifolds and the cell. The sealant is in contact both with the interconnect and with the electrolyte. The contact area of the seal with the electrolyte is a narrow contour around the cell 3 mm wide. Therefore, the footprint of the cathode on the cell is active, whereas the part of the cell that adheres to the sealant is electrochemically inactive and referred to as the sealed area similar to the case of Chapter 3.1.

Depending upon the design of the stack and loading system, the mechanical load externally applied to an SOFC stack can vary more or less significantly during operation, because the thickness variation of the SRUs during operation, due to thermal expansion and creep, can reflect on the strain of the tie rods. This possibility is accounted for in the present study, in contrast to that of Chapter 3.1, where the load is user-specified and does not change as the stack deforms. Assuming a stress state below the elastic limit of the steel, the uniaxial stress in the tie rods is:

$$\sigma_{tr} = E m_{tr} \varepsilon_{tr} = E m_{tr} \frac{\Delta z}{t_{SRU}}$$

where E_{tr} is the Young's modulus of the steel (220 GPa, room temperature assuming cooling of the loading system), Δz is the increase of the SRU thickness and t_{SRU} is the total thickness of a SRU. The force on the SRU is then:

$$F_{SRU} = \Delta z \left(\frac{E m_{tr} \pi D_{tr}^2}{t_{SRU}} \right)$$

with D_{tr} the diameter of the tie rods. Standard, instead of modified periodic boundary conditions (Chapter 3.1) are imposed on equivalent nodes on the lower and upper faces of the computational domain.

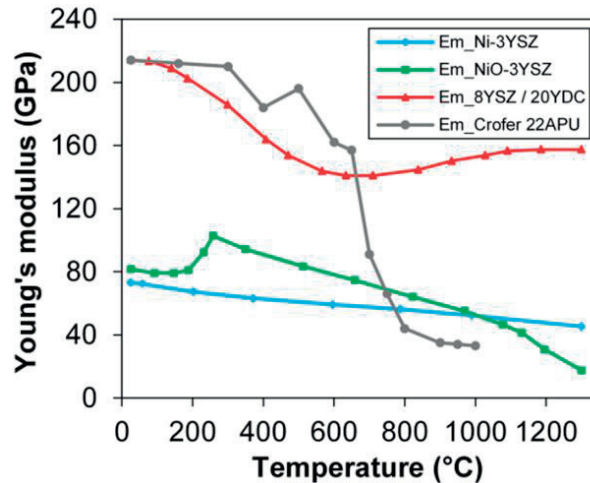


Figure 96: temperature-dependent Young's modulus from data in Ref. [4–6]. The Young's modulus of 20YDC was assumed to be equal to that of 8YSZ.

The approach for the implementation of the material properties is similar to that of Chapter 3.1. Table 29 together with Figure 96 provides the temperature-dependent properties used for the different components, whereas Table 28 lists the Weibull parameters, all from literature data.

The considered anode material is NiO-3YSZ (50-55 wt.% NiO). The reduction strain measured at 850 °C in a gas mixture of 9% H₂ / 91% N₂ by Pihlatie et al. [168] ranges between -0.096% and -0.301% (the minus sign indicating the shrinkage of the material).

Table 28: Weibull parameters and strength of the SOFC materials [15].

Layer/ Material	σ_0 (MPa)	m	V_0 (mm ³)	Samples	T _{meas} (°C)
Anode reduced / Ni-3YSZ	318	9.98	0.846	35	RT
Electrolyte / 8YSZ	282	8	0.273	20	900
Compatibility Layer / 20YDC	497 ^a	3.6 ^a	2.199 ^a	9	RT

a) Values assumed from GDC.

In this analysis, a mean value equal to -0.1985% is used. Creep data for Ni-8YSZ measured by Laurencin et al. [106] for typical SOFC operation temperatures are implemented in the model. In this study the creep of the electrolyte is expected limited for the considered temperature range and not included in the thermo-mechanical simulation. Creep in the YDC and cathode is also not considered for the computation during operation, but the values listed in Table 29 are included in the sintering process described below.

The properties listed in Table 29 for the glass-ceramic correspond to the composition 35BaO-35SiO₂-15CaO-10B₂O₃-5Al₂O₃ mol%. The MIC material is Crofer 22 APU. Material nonlinearity such as creep and plasticity are not implemented into the model, assuming that the creep strain rate of Crofer 22 APU is much higher than that of the cell materials, and therefore less influential when the operating conditions are varied slowly. The considered materials for the fuel and air GDLs are a Ni and Haynes230® foam, respectively, which corresponds to simplified approach compared to that for “Model v1”, using scaling laws and foremost, “Model v2”, which uses computational homogenization.

Table 29: Thermo-mechanical properties and creep parameters of the SRU materials.

Component / Material	Composition	Thickness (mm)	Thermo-Elastic Parameters				Creep Parameters			
			E (GPa)	ν	CTE $\times 10^{-6}$ ($^{\circ}\text{C}^{-1}$)	B ($\text{MPa}\cdot\text{h}^{-1}$)	Q (kJ mol^{-1})	n		
Anode oxidised / NiO-3YSZ	56 wt.% NiO-3 mol.% Y_2O_3	0.320	See Fig. 96	0.391	12.37	$1.040\text{e}+20^{\text{a}}$	640 ^a	2.5 ^a		
Anode reduced / Ni-3YSZ	56 wt.% NiO + 3 mol.% Y_2O_3	0.320	See Fig. 96	0.387	12.41	$3.714\text{e}-02^{\text{c}}$	115 ^c	1.7 ^c		
Electrolyte / 8YSZ	8 mol.% Y_2O_3 fully stab. ZrO_2	0.010	See Fig. 96	0.31	10.90	$4.373\text{e}+07^{\text{a}}$	370 ^a	1.0 ^a		
Compatibility layer / 20YDC	$\text{Ce}_{0.8}\text{Y}_{0.1}\text{Sr}_{0.1}\text{O}_{2.5}$	0.007	See Fig. 96	0.31	12.10	$6.768\text{e}+04^{\text{a}}$	264 ^a	1.0 ^a		
Cathode / LSCF	$\text{La}_{0.5}\text{Sr}_{0.5}\text{Fe}_{0.5}\text{Co}_{0.5}\text{O}_{3.5}$	0.040	10 ^b	0.33 ^b	15.34 ^b	$5.551\text{e}+10^{\text{a}}$	392 ^a	1.7 ^a		
Glass-ceramic sealing / G18	mol% 35BaO-35SiO ₂ -15CaO-10B ₂ O ₃ -5Al ₂ O ₃	1.047	67.4 (at 25 °C) 11.0 (at 850 °C)	0.28	11.10	$1.627\text{e}+10$	283	1.59		
Interconnect / Crofer® 22 APU	-	1.5	See Fig. 96	0.30	12.8	-	-	-		
GDL Air / Haynes 230	-	1.0	0.09 (at 25 °C) 0.07 (at 800 °C)	0.30	11.80	-	-	-		
GDL Fuel / Ni foam	-	0.5	0.09 (at 25 °C) 0.06 (at 800 °C)	0.30	16.20	-	-	-		

a) Values implemented only for the sintering simulation.

b) Assumed values.

c) Values for Ni-8YSZ.

3.5.1.2 Thermo-mechanical model

The assumptions and sequence for the modelling of the sintering process of the cell differs from that presented in Chapter 3.1. The FEM software COMSOL was used instead of Abaqus. The simulation starts with the co-firing of the anode and electrolyte, at a uniform temperature of 1400 °C. A sintering shrinkage of NiO-3YSZ of 5.5% and 5% for the electrolyte are implemented, whereas an increase of the Young's modulus of 50% is assumed for both materials. The build-up caused by the different shrinkage of the materials is highly relaxed by creep. The simulation proceeds with the cooling down to room temperature, initially at a reduced rate of 50 °C/h. Below 1000 °C, creep has a negligible effect on the stress relaxation and therefore the cooling down rate is increased to 180 °C/h. The sintering of the compatibility layer is carried out by heating the deposited cell at a rate of 100 °C/h, and then maintaining the half cell at 1300 °C.

The sintering shrinkage of 20YDC is assumed equal to that of 8YSZ during anode and electrolyte co-firing. The Young's modulus of the 20YDC is supposed to increase by 100% during the sintering, from 78.5 GPa (green state) to 157 GPa (sintered). The simulated cooling rate first equals 20 °C/h, followed by an accelerated cooling down of 100 °C/h below 850 °C. The simplified simulation sequence of the sintering of the LSCF cathode proceeds similarly to that of the compatibility layer. It starts at 1150 °C for 4 hours with a sintering shrinkage of 9%, as reported in previous work [169] carried out on a slightly different LSCF composition ($\text{La}_{0.58}\text{Sr}_{0.4}\text{Fe}_{0.8}\text{Co}_{0.2}\text{O}_{3.6}$). During the sintering process, the Young's modulus is increased from 5 GPa to 10 GPa. The cooldown starts at a rate of 20 °C/h until 750 °C, then was increased to 50 °C/h until 450 °C, then 100 °C/h to room temperature.

After the simplified simulation of the sintering of the cell, mechanical interactions between the components show in Figure 95 is implemented by the simulations of a sequence comprising the assembly and heat-up, sealing, Ni reduction and operation, which resemble that described in full details in Chapter 3.1. The sealant is not strongly joined either to the cell or the interconnect before the sealing procedure. During the sealing procedure, the sealant becomes joined to both the cell and the interconnect. Between the cell contour and the sealant and between the cell contour and interconnect, a backlash is expected. This means that the cell contour does not interfere either with the contour housing of the interconnect or with the sealant, otherwise high stresses might arise. This condition is implemented in the model using compliant springs. Mechanical interfaces are here simulated differently than in "Model v1" and "Model v2". For this study, the computational requirements are minimized by replacing contact with compliant springs for the detachment, and via stiff springs for the opposite direction, which approximate a mechanical contact without penetration. This type of mechanical interface is set between the GDLs and the cell, and between the GDLs and interconnect.

The simulation starts with the application of a pressure of 0.7 MPa on the SRU, as reported in Chapter 3.1. The SRU is then heated up from room temperature to the sealing temperature (850 °C) a rate of 100 °C/h, during which creep is not considered. The sealing procedure is then simulated using dashpots

with increasing damping value. Before the sealing procedure the glass sealant is not joined to either the interconnect or the cell and therefore a relative slipping between either glass sealant and cell or glass sealant and interconnect is possible. This condition is simulated by compliant dashpots at the interfaces with a damping factor of $1 \text{ MPa mm}^{-1}\text{h}$. During the sealing procedure, the glass sealant becomes progressively joined to the interconnect and the cell, simulated by a continuous increase of the damping factor of the dashpot at the sealant-cell and sealant-interconnect interfaces from the initial value of $1 \text{ MPa mm}^{-1}\text{h}$ to $10\text{e}+06 \text{ MPa mm}^{-1}\text{h}$. The latter value would represent a stiff dashpot, i.e. the sealant is thoroughly joined to interconnect and cell. During the sealing procedure, only the creep of the glass sealant is considered.

The reduction of the anode is approximated by a change of material properties from the initial values of NiO-3YSZ to the final values of Ni-3YSZ. The temperature is kept constant at $850 \text{ }^\circ\text{C}$ during the entire stage. Creep of both glass sealant and anode has been included in the model. The homogeneous temperature profile of $850 \text{ }^\circ\text{C}$ is then switched to that corresponding to 20 A , before application of the sequence shown in Figure 97. Creep of the reduced anode and sealing material is considered during the simulation of the load profile. The probability of failure computation is identical to that presented in Paragraph 3.1.7.

3.5.1.3 Temperature and electrical load profiles

The sequence considered for the thermo-electrochemical simulations consists in variations in the current at levels of 10 A , 12 A , 15 A and 20 A .

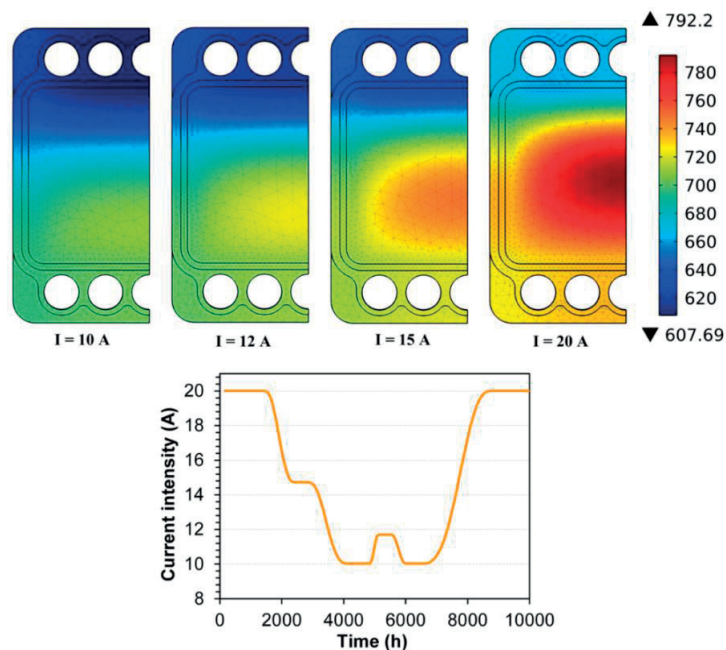


Figure 97: On top: spatial-dependent temperature fields (in $^\circ\text{C}$) on the SRU for different current intensities. At the bottom: thermal load profile over the SOFC stack lifetime implemented into the SRU model

The temperature field in the sealing areas is not calculated, but obtained using a constant extrapolation. For simplicity, the thermal gradient along the z-direction is homogeneous along the z-axis of the stack. The thermal load profile characteristic of the stack lifetime has been determined considering an energy demand over a year for a generic residential SOFC cogeneration system [170], shown in Figure 97. This thermal load profile can represent a smoothed real power demand profile, in which the average of the load changes is taken into account, without the details of daily fluctuations.

3.5.2 Simulation results

After the sintering, the residual stresses in the anode at room temperature change as expected from a compressive stress of -15 MPa on the face away from the interface with the electrolyte, to a tensile stress of +22 MPa on the electrolyte side. The electrolyte and compatibility layers are under beneficial compressive stress state (-450 MPa and -25 MPa, respectively), whereas the stress in the cathode is tensile (50 MPa).

The evolution of the probabilities of failure of the cell layers computed by Weibull analysis is shown in Figure 98, together with the corresponding electrical load profile. During the first polarisation at 20 A for 1400 h, the probability of failure of the anode is reduced by around six orders of magnitude, because of stress relaxation due to creep. The probability of failure of the electrolyte does not vary conspicuously during this functioning mode, whereas that of the compatibility layer increases largely. During the current decrease from 20 A to 15 A, which results in a decrease of the average SOFC stack temperature of about 50 °C in 1000 h, the probability of failure remains low for the anode and constant for the electrolyte and compatibility layers. For the duration of the working load at the current of 15 A, the decrease from 15 A to 10 A and the plateau at 10 A until 4900 h, the failure probability of the anode is not subjected to important changes, whereas that of electrolyte and compatibility layer increases roughly continuously, though it remains below critical values.

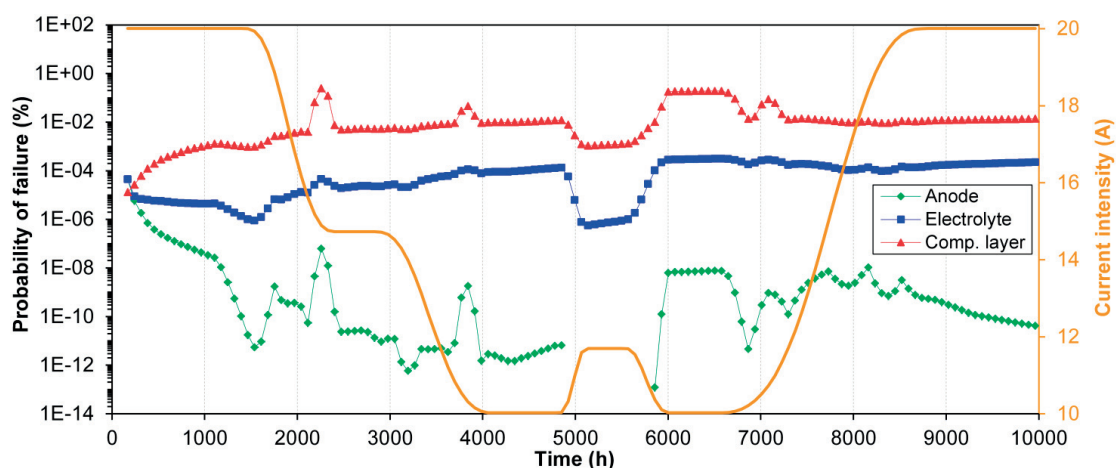


Figure 98: Probability of failure of the anode, electrolyte and compatibility layer for the case of the cell B. The thermal load profile over the SOFC stack lifetime is plotted for reference.

This increase might be ascribable to a stress accumulation in the electrolyte and the compatibility layer. The load switching to 12 A lowers the stress state in the cell, and therefore the failure probability of the anode becomes vanishingly small and that of electrolyte and compatibility layer decrease respectively by around two and one orders of magnitude. During the whole SOFC stack operation, this results to be the most conservative operating condition. On the contrary, the next current decrease to 10 A entails the greatest failure probabilities for both compatibility and electrolyte layer, respectively around 0.2% and 0.0003%. The final current switching from the lowest value, 10 A, to the highest, 20 A, does not generate high failure probabilities. Even though the average temperature on the cell increases by around 100 °C, this change is performed over a time of 2000 h. Therefore, creep can act on the stress relaxation. During the final steady state condition of maximum current (20 A), the anode is subjected to a large stress relaxation and therefore it decreases the failure probability. The failure probability of electrolyte and compatibility layer remains constant during this stage. It is worthwhile noting that the largest increase and decrease of the failure probability occur at lower temperatures, when creep strains are lower. On the other hand, at high temperatures stresses may be relaxed by higher creep strains.

4 Summary and conclusions

4.1 Mechanical properties of SOFC materials

Two setups dedicated to the mechanical testing of high temperature solid oxide fuel cell (SOFC) ceramic-based materials were designed, fabricated and successfully validated, which is a new capability for GEM-EPFL. They measure the elastic and creep behaviour, under reduction or oxidising atmosphere, at room or high temperatures. The four-point bending test configuration was chosen, because of the advantages for testing ceramic materials and because of the need to test large batches of samples up to failure. With the developed setup designs, significant time reduction of the overall tests campaign is achieved, compared to equivalent commercial devices.

A workflow for numerical model-based parameter estimation was complementarily developed for the detailed analysis of the experimental measurements, because of the limitations of the analytical solutions applied in standard post-processing, in terms of accuracy and flexibility of the constitutive laws that can be investigated. It consists in metamodel-based optimisation using a finite element method (FEM) model that simulates with selected level of detail the four-point bending experiments. To our knowledge, the data available on the primary creep of the Ni-YSZ is very scarce. The present measurements show that primary creep is not negligible. They are expected to lead to significant advances for the understanding of the material deformation mechanisms and the thermo-mechanical simulation of SOFC stacks. The model-based parameter estimation allowed to quantify the measurement errors induced by post-processing with analytical solutions. For the elastic properties, analytical solutions provide fast and in most cases sufficiently accurate estimations, but they cannot for instance detect changes in the mechanical properties of Ni-YSZ induced by aging. They show relevant limitations for the determination of the creep parameters.

Weibull testing on relatively large batches of anode samples was carried out with the developed setup. Testing was performed on NiO-YSZ, Ni-YSZ and on (Ni)-YSZ skeleton (Ni removed) samples to help understanding the factors that control the strength of the material. The measured Weibull moduli were low for a technological material, but the main function of the material in SOFC stacks is not structural. In both NiO-YSZ and Ni-YSZ, the residual stresses caused by the mismatch in the coefficient of thermal expansion (CTE) between the two phases with respect to the stress-free condition governed the dependence of the strength and Weibull modulus upon temperature. The results suggest that plasticity of the Ni phase contributed largely to the strength of Ni-YSZ. This entails that in developing Ni-YSZ anode microstructures, adjustments of the Ni content and spatial distribution can be effective to find a better trade-off between maximised electrochemical performance and improved strength. Some trends in the dataset however warrant further investigations. The strength of (Ni)-YSZ samples decreased with the temperature increase, which does not follow the behaviour reported in the literature for dense samples.

Computational homogenisation was performed as a complementary approach to estimate the thermo-elastic properties of the Ni-YSZ cermet. The rationale of the work was however not limited to a

validation, but performed in the view of investigating other cell layers or aged samples that cannot be measured by mechanical testing, and the relationships between the mechanical properties and the microstructural parameters. A preliminary grid and volume independence analysis provided the necessary RVE volume and spatial resolutions for the accurate estimations of the thermo-elastic properties and minimised computational requirements. The thermo-elastic properties obtained from computational homogenisation were similar to those obtained by the estimation methods (elastic modulus) and from dilatometry tests (CTE). The changes in thermo-elastic properties upon ageing were found relatively mild; the lowest change was on the CTE. Upon ageing, estimation of the thermo-elastic properties would be challenging by direct mechanical testing, because the errors on the measurements may be larger than the properties variation.

An extension of the computational homogenisation for visco-elastic behaviour was applied to estimate the anisotropic elastic and creep properties of the gas-diffusion layers in SOFC stacks (GDL), which were then implemented in the stack thermo-mechanical model of this work. The anisotropy of both elastic and creep properties was significant. Thus, implementation in thermo-mechanical models of averaged mechanical properties obtained by scaling laws may not allow capturing adequately the mechanical behaviour of the electrically conducting material in a stack. Further, computational homogenisation enables the use of continuum domains instead of detailed geometries, which in complex contact stack thermo-mechanical models helps to reduce the computational requirements and the simulation runtime.

4.2 Thermo-mechanical modelling of SOFC stacks

4.2.1 Overview of the thermo-mechanical results

The geometry of a commercial stack (SOLIDpower) was considered for the stack thermo-mechanical modelling study. The stress state in the cell layers followed the expected trends. The GDC compatibility layer that mitigates the formation of insulating phases at the interface between electrolyte and LSCF cathode is under beneficial compressive stresses upon stack production and after thermal cycling. However, the latter decreased rapidly upon simulation of the long-term polarisation and over a large cell area. The electrolyte is under compressive stresses over the whole simulated stack lifetime. Imperfections of this layer, e.g. variations of the thickness because of the imperfect deposition, are not considered in the study, but may in reality affect the accuracy of the simulation results. The long-term polarisation contributed to a large decrease of the compressive stresses. However, no potential risk of cracking was predicted. The reduction of shielding compressive stress in the two layers however suggests that vulnerability to a deleterious event such as Ni re-oxidation not considered in the present study increases upon operation. The simulation results indicate that whenever a change in temperature

profile and the prediction of the occurrence of the event is possible, the interaction with the metallic frame may be used to increase the compressive stress.

The SRU deformed by a large amount upon thermal cycling, because of the CTE mismatch between the materials. However, the model implementation prevented tangential sliding at the interfaces after the first stack heat-up. Potential interface detachment, not considered in this study, may alleviate the large SRU deformations.

Rate-independent plasticity did not generate irreversible deformation, which only arises because of creep. The correlation between the CTE mismatch of the materials and evolution of the contact pressure on the active area was demonstrated. Modelling assumptions affected the results, though by a marginal contribution, within the range of studied conditions. The dependence of the contact pressure distribution on the temperature profile shape was shown. The most deleterious event for the maintenance of the contact pressure is the long-term polarisation followed by thermal cycling, which suggest that degradation may occur in the long term.

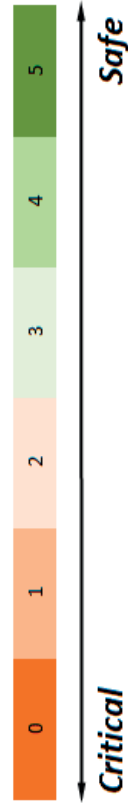
4.2.2 Analysis of the effects of pre-deformation, operation conditions and model formulation

The table below provides a qualitative summary of effects (rows) and potential type of thermo-mechanical issue (column), in a color-coded manner from red (detrimental/critical) to green (beneficial/safe) for comparative purposes. (BC: boundary conditions, PBC: modified periodic boundary conditions, FBC: flat boundary conditions, MIC: interconnect, CO: co-flow, CR: counter-flow. "2Def00", "1DefA/B", "2DefA/B" correspond to MIC pre-deformation profiles).

Loss of contact pressure at the cell interfaces

In this study, the contact pressure simulated by "Model v1" (with Ideal MICs) was largely lost, compared to the "Model v2". Paradoxically, the assembly force in the "Model v1" simulations was about 33% higher than in "Model v2". Here, the contribution of both the mechanical properties of the GDLs and SRU deformation on the maintenance of the contact pressure was found highly relevant, because in "Model v1" the GDL mechanical properties were estimated by simple scaling laws, whereas computational homogenisation of anisotropic elastic and creep properties was used for those of "Model v2". This significant difference indicates that the design of the GDLs can be optimised not only for fluid-dynamic and costs needs, but also for improved mechanical behaviour. In this context, thermo-mechanical simulations at the stack level may help in providing guidelines for such optimisations. For "Model v1", the worst condition was the thermal cycling. Instead, stack qualification and polarisation were found beneficial.

Model	BC	MIC	Operation	Sealant thickness (mm)	Contact Pressure			Cell failure			Sealants failure		
					Qualification	Operation	Thermal cycling	Qualification	short-term	long-term	Thermal cycling	1st Thermal cycle	2nd Thermal cycle
v1		Ideal	CO 0.5	0.7	4	2	0	NA	NA	NA	1	1	
		2Def00			1	1	1				2	2	
v2	PBC	Ideal	CO 0.5	0.2	5	3	3	2	3	4	3	4	
					4	2	2				0	5	2
					4	5	0				2	4	1
					4	4	1				2	4	0
					3	3	2				3	4	1
					4	2	2				3	4	2
					3	2	2				2	4	2
5	3	3	NA	NA	4	5							
FBC		Ideal	CO 0.5	0.7	4	2	2	1	3	4	3	4	
		2DefA/B			2	1	1				3	3	



Counter-flow configuration and high internal reforming is the best case for increased contact pressure. However, it turns out to be the worst case after subsequent thermal cycling, because the contact pressure is close to zero on a large area of the cell, which showcases a history-dependent behaviour, because of creep deformation. In general, the location of the regions where the contact pressure is decreased during thermal cycling corresponds to the location of highest temperature. The relationship between contact pressure and electrical conductivity, including the effect of non-uniform deformation during the assembly, is at present not known. The simulation results indicate that in the case of contact degradation, the detrimental effect does not affect to the same extent co- or counter-flow operation. The assembly of dissimilar pre-deformed MIC profiles affect differently the uniformity of the contact pressure, depending upon the boundary conditions on the simulated domain. In practice, the worst case was found for those SRUs near the end plates, whereas the best case was with ideal MIC shape. This means that in short stacks and/or for the first and final SRUs of the stacks (i.e. near the end plates), the manufacturing tolerances on the MIC geometry must be lower. On the contrary, the effects of pre-deformed MICs on the contact pressure uniformity were less severe for the SRUs far from the end plates. Assembly of similar pre-deformed MICs profiles did not affect the contact pressure uniformity, because of the bending compliance of both GDLs and cell. With the objective of production costs minimisation, the manufacturing tolerances on the MICs can be maintained relatively large, if the pre-deformed profile is the same for all the MICs of the stack. Because the effects of pre-deformation were overall lower than anticipated, the identification of thresholds for reliability warrant future investigations in the view of cost reductions.

Failure of the cell

The simulation of polarization showed that the cell probability failure does not decrease monotonically at the beginning of operation. A slight increase was found in the short-term polarisation, before decreasing in the long-term. The practical relevance of this phenomenon can be investigated in the light of proof-testing, and operation strategies that mitigate this first mild increase in stress should be studied.

The cell reliability is highly affected by the operation conditions. The failure probability increases dramatically if the fraction of internal reforming is above 0.5 (with counter-flow configuration). In terms of cell reliability, counter-flow configuration with 90% of internal reforming is the worst condition among those analysed in this study, because it leads to failure probabilities higher than 0.1 in the short-term polarisation, which is not suitable for real applications. However, after long-term polarisation this became the best condition. The sensitivity of the anode failure probability to the polarisation conditions is predominant for high fractions of internal reforming: by increasing the PR (in counter-flow) from 0.1 to 0.5, the cell failure probability is reduced in the short-term polarisation by almost four orders of

magnitude. The results suggests that the effects of transients during load following or variations in thermal conditions because of position in the stack are likely significant.

Thermal cycling after long-term polarisation increases the risk of cell failure. However, the probability remains relatively low. Here, as expected, a reduction of the CTE mismatch between the glass-ceramic and Ni-YSZ by tailoring of the material compositions would increase the tolerance of the cell to thermal cycling.

With the deformation profiles considered in this work, the effects of MIC pre-deformations on the risks of cell failure are negligible. The reason was that the compliance of both the cell and GDLs was sufficient to accommodate the deformed components. Considering this aspect, thinner cells are favoured, because they can tolerate larger component imperfections before failure.

Risk of sealant failure

The analysis of the risk of failure of the sealants was performed by i) cumulative distribution of the stresses and ii) a tentative energy-based calculation. A variation of the energy based calculation including frictionless contact after interface detachment was implemented, because otherwise unrealistic interpenetration of the sealant in the MIC occurred during the simulation of artificial detachment, though still valid for qualitative assessments. From the results, the risk of sealants failure:

- is reduced for thinner sealants. The thinner sealants were found beneficial also for the contact pressure. However, modelling artefacts also contributed to this last improvement, which requires further verifications.
- is reduced by simulating flat boundary conditions at the two MICs of the modelled repeating unit, which approximates the conditions of those units near the end plates. In terms of design, this means that large stacks made by sub-assemblies with intermediate separation are favoured.
- is the lowest for operation in co-flow
- decreases after long-term polarisation in co-flow combined with thermal cycling, whereas it increases if the polarisation is in counter-flow. The worst condition is counter-flow with PR of 0.5.

4.2.3 Modelling the impact of creep on the probability of failure of a solid oxide fuel cell stack

A three-dimensional finite elements model of an SRU with an anode supported SOFC has been developed. Creep in the glass sealant and in the anode has been considered. During steady state operation, the probability of failure of the anode was found to decrease, whereas that of the electrolyte and compatibility layer was noticed to increase slightly. This behaviour can be ascribed to

stress redistributions in the layers of the cell. Due to the lower creep strains at lower temperatures, particular care should be taken during changes from high to lower temperatures because the effect of the spatial thermal gradient on the failure probability appears as relevant.

4.3 Recommendations for further work

Recommendations for future developments based on the results obtained during the thesis and specific points of practical relevance are listed hereafter:

- The available data of the mechanical properties of the SRU materials remains limited, in particular of the evolution of such mechanical properties because of ageing. This may pose important limitations on the prediction of the failure modes by numerical models.
- The next step in the investigation of the anisotropic elastic and creep properties of the GDLs obtained from computational homogenisation is a confirmation by direct mechanical testing.
- On purpose experiment for the validation of numerical simulations is a challenge, but may be worth the far-reaching effort, which likely requires the prototyping of model systems.
- The strong dependence between evolution of the SRU deformation and stress relaxation because of creep in the materials warrants the implementation of the primary creep regime in the material constitutive laws of stack numerical models. The highest priority should be given to the materials of those components governing the overall stiffness of the SRU, i.e. for the stack design analysed in this work, the MICs and the GDLs.
- To reduce production costs while maintaining the required mechanical reliability, the fabrication tolerances of the stack components can be maximised by implementing optimisation problems accounting for SRU models with pre-deformed MICs. An analysis for first estimate of the critical tolerances threshold should be however performed before the optimisation task.
- The bending stiffness of the movable part in the SEP setup may be increased to improve the measurement accuracy, for example by installing additional guides on the sample dispenser. Furthermore, developments for a ROR (ring-on-ring) equivalent instead of the four-point bending configuration may be attempted if the testing of higher volume of material is needed.

Bibliography

- [1] The World Bank, Electricity production from oil, gas and coal sources (% of total), <https://Data.Worldbank.Org/Indicator/EG.ELC.FOSL.ZS>. (n.d.).
- [2] E. Panos, R. Kannan, The role of domestic biomass in electricity, heat and grid balancing markets in Switzerland, *Energy*. 112 (2016) 1120–1138. doi:10.1016/j.energy.2016.06.107.
- [3] J.T.S. Irvine, P. Connor, eds., *Solid Oxide Fuels Cells: Facts and Figures*, Springer London, London, 2013. <http://link.springer.com/10.1007/978-1-4471-4456-4> (accessed April 3, 2016).
- [4] 2018 March, <http://www.novocell.ind.br/en/home>, (n.d.).
- [5] Technical Plan - Fuel Cells / Multi-Year Research, Development and Demonstration Plan, United States Department of Energy, 2012.
- [6] A. Nakajo, J. van Herle, D. Favrat, Current state of models for the prediction of mechanical failures in solid oxide fuel cells, 2013. <http://www.scopus.com/inward/record.url?eid=2-s2.0-84883199516&partnerID=40&md5=ab7761f0abfa528b4b02ff3a78b634fa>.
- [7] T. Kawada, S. Watanabe, S. Hashimoto, T. Sakamoto, A. Unemoto, M. Kurumatani, K. Sato, F. Iguchi, K. Yashiro, K. Amezawa, K. Terada, M. Kubo, H. Yugami, T. Hashida, J. Mizusaki, Classification of Mechanical Failure in SOFC and Strategy for Evaluation of Operational Margin, in: ECS, 2009: pp. 467–472. doi:10.1149/1.3205556.
- [8] R.J. Kee, H. Zhu, D.G. Goodwin, Solid-oxide fuel cells with hydrocarbon fuels, *Proc. Combust. Inst.* 30 (2005) 2379–2404. doi:10.1016/j.proci.2004.08.277.
- [9] R.J. Kee, H. Zhu, A.M. Sureshini, G.S. Jackson, Solid Oxide Fuel Cells: Operating Principles, Current Challenges, and the Role of Syngas, *Combust. Sci. Technol.* 180 (2008) 1207–1244. doi:10.1080/00102200801963458.
- [10] J. Larminie, A. Dicks, *Fuel cell systems explained*, J. Wiley, Chichester, West Sussex, 2003.
- [11] J. Meusinger, E. Riensche, U. Stimming, Reforming of natural gas in solid oxide fuel cell systems, *J. Power Sources*. 71 (1998) 315–320.
- [12] A. Nakajo, F. Mueller, J. Brouwer, J. Van herle, D. Favrat, Progressive activation of degradation processes in solid oxide fuel cells stacks: Part I: Lifetime extension by optimisation of the operating conditions, *J. Power Sources*. 216 (2012) 449–463. doi:10.1016/j.jpowsour.2012.05.078.
- [13] K. Kendall, *High-temperature solid oxide fuel cells: fundamentals, design and applications*, Elsevier Advanced Technology, Oxford, 2003. <http://site.ebrary.com/lib/alltitles/docDetail.action?docID=10206725> (accessed June 18, 2013).
- [14] D.J.L. Brett, A. Atkinson, N.P. Brandon, S.J. Skinner, Intermediate temperature solid oxide fuel cells, *Chem. Soc. Rev.* 37 (2008) 1568. doi:10.1039/b612060c.

- [15] A. Nakajo, J. Kuebler, A. Faes, U.F. Vogt, H.J. Schindler, L.-K. Chiang, S. Modena, J. Van herle, T. Hocker, Compilation of mechanical properties for the structural analysis of solid oxide fuel cell stacks. Constitutive materials of anode-supported cells, *Ceram. Int.* 38 (2012) 3907–3927. doi:10.1016/j.ceramint.2012.01.043.
- [16] N.H. Menzler, F. Tietz, S. Uhlenbruck, H.P. Buchkremer, D. Stöver, Materials and manufacturing technologies for solid oxide fuel cells, *J. Mater. Sci.* 45 (2010) 3109–3135. doi:10.1007/s10853-010-4279-9.
- [17] T. Dey, D. Singdeo, M. Bose, R.N. Basu, P.C. Ghosh, Study of contact resistance at the electrode–interconnect interfaces in planar type Solid Oxide Fuel Cells, *J. Power Sources.* 233 (2013) 290–298. doi:10.1016/j.jpowsour.2013.01.111.
- [18] M.C. Tucker, L. Cheng, L.C. DeJonghe, Selection of cathode contact materials for solid oxide fuel cells, *J. Power Sources.* 196 (2011) 8313–8322. doi:10.1016/j.jpowsour.2011.06.044.
- [19] A. Nakajo, F. Mueller, J. Brouwer, J. Van herle, D. Favrat, Mechanical reliability and durability of SOFC stacks. Part I : Modelling of the effect of operating conditions and design alternatives on the reliability, *Int. J. Hydrog. Energy.* 37 (2012) 9249–9268. doi:10.1016/j.ijhydene.2012.03.043.
- [20] B.P. McCarthy, L.R. Pederson, Y.S. Chou, X.-D. Zhou, W.A. Surdoval, L.C. Wilson, Low-temperature sintering of lanthanum strontium manganite-based contact pastes for SOFCs, *J. Power Sources.* 180 (2008) 294–300. doi:10.1016/j.jpowsour.2008.01.097.
- [21] M. Tucker, L. Cheng, L. DeJonghe, Cathode Contact Materials for Solid Oxide Fuel Cells, in: 2011: pp. 2625–2630. doi:10.1149/1.3570262.
- [22] A. Mat, B. Timurkutluk, C. Timurkutluk, Y. Kaplan, Effects of ceramic based pastes on electrochemical performance of solid oxide fuel cells, *Ceram. Int.* 40 (2014) 8575–8583. doi:10.1016/j.ceramint.2014.01.073.
- [23] A. Morán-Ruiz, K. Vidal, M.Á. Laguna-Bercero, A. Larrañaga, M.I. Arriortua, Effects of using $(\text{La}_{0.8}\text{Sr}_{0.2})_{0.95}\text{Fe}_{0.6}\text{Mn}_{0.3}\text{Co}_{0.1}\text{O}_3$ (LSFMC), $\text{LaNi}_{0.6}\text{Fe}_{0.4}\text{O}_{3-\delta}$ (LNF) and $\text{LaNi}_{0.6}\text{Co}_{0.4}\text{O}_{3-\delta}$ (LNC) as contact materials on solid oxide fuel cells, *J. Power Sources.* 248 (2014) 1067–1076. doi:10.1016/j.jpowsour.2013.10.031.
- [24] R. Steinberger-Wilckens, L. Blum, H.-P. Buchkremer, S. Gross, L.B. De Haart, K. Hilpert, H. Nabielek, W.J. Quadackers, U. Reisgen, R.W. Steinbrech, Overview of the development of solid oxide fuel cells at Forschungszentrum Juelich, *Int. J. Appl. Ceram. Technol.* 3 (2006) 470–476.
- [25] M. Lang, C. Auer, P. Jentsch, T. Weckesser, SOFC Stacks for Mobile Applications, *Mater. Sci. Forum.* 638–642 (2010) 1170–1175. doi:10.4028/www.scientific.net/MSF.638-642.1170.
- [26] B. Kuhn, E. Wessel, J. Malzbender, R.W. Steinbrech, L. Singheiser, Effect of isothermal aging on the mechanical performance of brazed ceramic/metal joints for planar SOFC-stacks, *Int. J. Hydrog. Energy.* 35 (2010) 9158–9165. doi:10.1016/j.ijhydene.2010.06.063.

- [27] L. Blum, S.M. Groß, J. Malzbender, U. Pabst, M. Peksen, R. Peters, I.C. Vinke, Investigation of solid oxide fuel cell sealing behavior under stack relevant conditions at Forschungszentrum Jülich, *J. Power Sources*. 196 (2011) 7175–7181. doi:10.1016/j.jpowsour.2010.09.041.
- [28] M. Peksen, A coupled 3D thermofluid–thermomechanical analysis of a planar type production scale SOFC stack, *Int. J. Hydrog. Energy*. 36 (2011) 11914–11928. doi:10.1016/j.ijhydene.2011.06.045.
- [29] S.-S. Wei, T.-H. Wang, J.-S. Wu, Numerical modeling of interconnect flow channel design and thermal stress analysis of a planar anode-supported solid oxide fuel cell stack, *Energy*. 69 (2014) 553–561. doi:10.1016/j.energy.2014.03.052.
- [30] S.M. Kelly, D.M. England, S. Mukerjee, J. Weber, Fuel cell stack having a featured interconnect element, 2012. <http://www.google.com/patents/US8197981>.
- [31] T.T. Molla, K. Kwok, H.L. Frandsen, Efficient modeling of metallic interconnects for thermo-mechanical simulation of SOFC stacks: Homogenized behaviors and effect of contact, *Int. J. Hydrog. Energy*. (2016). doi:10.1016/j.ijhydene.2016.03.002.
- [32] J.W. Fergus, Sealants for solid oxide fuel cells, *J. Power Sources*. 147 (2005) 46–57. doi:10.1016/j.jpowsour.2005.05.002.
- [33] Y.-S. Chou, J.W. Stevenson, P. Singh, Thermal cycle stability of a novel glass–mica composite seal for solid oxide fuel cells: Effect of glass volume fraction and stresses, *J. Power Sources*. 152 (2005) 168–174. doi:10.1016/j.jpowsour.2005.03.213.
- [34] K.S. Weil, J.S. Hardy, B.J. Koepfel, New Sealing Concept for Planar Solid Oxide Fuel Cells, *J. Mater. Eng. Perform.* 15 (2006) 427–432. doi:10.1361/105994906X117233.
- [35] H. Yakabe, T. Ogiwara, M. Hishinuma, I. Yasuda, 3-D model calculation for planar SOFC, *J. Power Sources*. 102 (2001) 144–154.
- [36] P. Fan, G. Li, Y. Zeng, X. Zhang, Numerical study on thermal stresses of a planar solid oxide fuel cell, *Int. J. Therm. Sci.* 77 (2014) 1–10. doi:10.1016/j.ijthermalsci.2013.10.008.
- [37] M. Xu, T.S. Li, M. Yang, M. Andersson, I. Fransson, T. Larsson, B. Sundén, Modeling of an anode supported solid oxide fuel cell focusing on thermal stresses, *Int. J. Hydrog. Energy*. 41 (2016) 14927–14940. doi:10.1016/j.ijhydene.2016.06.171.
- [38] M. Xu, T. Li, M. Yang, M. Andersson, Solid oxide fuel cell interconnect design optimization considering the thermal stresses, *Sci. Bull.* 61 (2016) 1333–1344. doi:10.1007/s11434-016-1146-3.
- [39] C.S. Montross, H. Yokokawa, M. Dokiya, Thermal stresses in planar solid oxide fuel cells due to thermal expansion differences, *Br. Ceram. Trans.* 101 (2002) 85–93. doi:10.1179/096797802225003956.
- [40] T. Zhang, Q. Zhu, W.L. Huang, Z. Xie, X. Xin, Stress field and failure probability analysis for the single cell of planar solid oxide fuel cells, *J. Power Sources*. 182 (2008) 540–545. doi:10.1016/j.jpowsour.2008.04.027.

- [41] A. Nakajo, J. Van herle, D. Favrat, Sensitivity of Stresses and Failure Mechanisms in SOFCs to the Mechanical Properties and Geometry of the Constitutive Layers, *Fuel Cells*. 11 (2011) 537–552. doi:10.1002/face.201000108.
- [42] R. Clague, A.J. Marquis, N.P. Brandon, Finite element and analytical stress analysis of a solid oxide fuel cell, *J. Power Sources*. 210 (2012) 224–232. doi:10.1016/j.jpowsour.2012.03.027.
- [43] C.H. Hsueh, Thermal stresses in elastic multilayer systems, *Thin Solid Films*. 418 (2002) 182–188.
- [44] J. Malzbender, Mechanical and thermal stresses in multilayered materials, *J. Appl. Phys.* 95 (2004) 1780. doi:10.1063/1.1642289.
- [45] K.S. Weil, B.J. Koeppel, Comparative finite element analysis of the stress–strain states in three different bonded solid oxide fuel cell seal designs, *J. Power Sources*. 180 (2008) 343–353. doi:10.1016/j.jpowsour.2008.01.093.
- [46] K. Weil, B. Koeppel, Thermal stress analysis of the planar SOFC bonded compliant seal design, *Int. J. Hydrog. Energy*. 33 (2008) 3976–3990. doi:10.1016/j.ijhydene.2007.11.008.
- [47] T.L. Jiang, M.-H. Chen, Thermal-stress analyses of an operating planar solid oxide fuel cell with the bonded compliant seal design, *Int. J. Hydrog. Energy*. 34 (2009) 8223–8234. doi:10.1016/j.ijhydene.2009.07.089.
- [48] W. Jiang, S.T. Tu, G.C. Li, J.M. Gong, Residual stress and plastic strain analysis in the brazed joint of bonded compliant seal design in planar solid oxide fuel cell, *J. Power Sources*. 195 (2010) 3513–3522. doi:10.1016/j.jpowsour.2009.12.066.
- [49] W. Jiang, Y. Zhang, W. Woo, S.T. Tu, Three-dimensional simulation to study the influence of foil thickness on residual stress in the bonded compliant seal design of planar solid oxide fuel cell, *J. Power Sources*. 209 (2012) 65–71. doi:10.1016/j.jpowsour.2012.02.060.
- [50] Y.-C. Zhang, W. Jiang, S.-T. Tu, J.-F. Wen, Simulation of creep and damage in the bonded compliant seal of planar solid oxide fuel cell, *Int. J. Hydrog. Energy*. 39 (2014) 17941–17951. doi:10.1016/j.ijhydene.2014.08.130.
- [51] W. Jiang, Y.-C. Zhang, W.Y. Zhang, Y. Luo, W. Woo, S.T. Tu, Growth and residual stresses in the bonded compliant seal of planar solid oxide fuel cell: Thickness design of window frame, *Mater. Des.* 93 (2016) 53–62. doi:10.1016/j.matdes.2015.12.145.
- [52] H. Yakabe, I. Yasuda, Model Analysis of the Expansion Behavior of LaCrO₃ Interconnector under Solid Oxide Fuel Cell Operation, *J. Electrochem. Soc.* 150 (2003) A35. doi:10.1149/1.1522384.
- [53] A. Selimovic, M. Kemm, T. Torisson, M. Assadi, Steady state and transient thermal stress analysis in planar solid oxide fuel cells, *J. Power Sources*. 145 (2005) 463–469. doi:10.1016/j.jpowsour.2004.11.073.
- [54] A. Nakajo, Z. Wuillemin, J. Van herle, D. Favrat, Simulation of thermal stresses in anode-supported solid oxide fuel cell stacks. Part I: Probability of failure of the cells, *J. Power Sources*. 193 (2009) 203–215. doi:10.1016/j.jpowsour.2008.12.050.

- [55] A. Nakajo, Z. Wullemin, J. Van herle, D. Favrat, Simulation of thermal stresses in anode-supported solid oxide fuel cell stacks. Part II: Loss of gas-tightness, electrical contact and thermal buckling, *J. Power Sources*. 193 (2009) 216–226. doi:10.1016/j.jpowsour.2008.12.039.
- [56] A. Nakajo, F. Mueller, J. Brouwer, J. Van herle, D. Favrat, Mechanical reliability and durability of SOFC stacks. Part II: Modelling of mechanical failures during ageing and cycling, *Int. J. Hydrog. Energy*. 37 (2012) 9269–9286. doi:10.1016/j.ijhydene.2012.03.023.
- [57] F. Greco, H.L. Frandsen, A. Nakajo, M.F. Madsen, J. Van herle, Modelling the impact of creep on the probability of failure of a solid oxide fuel cell stack, *J. Eur. Ceram. Soc.* 34 (2014) 2695–2704. doi:10.1016/j.jeurceramsoc.2013.12.055.
- [58] F. Greco, A. Nakajo, Z. Wullemin, J. Van herle, Thermo-Mechanical Reliability of SOFC Stacks during Combined Long-Term Operation and Thermal Cycling, *ECS Trans.* 68 (2015) 1921–1931. doi:10.1149/06801.1921ecst.
- [59] F. Greco, A. Nakajo, Z. Wullemin, J. Van herle, The Effects of Component Tolerances on the Thermo-Mechanical Reliability of SOFC Stacks, *ECS Trans.* 78 (2017) 2271–2283. doi:10.1149/07801.2271ecst.
- [60] ABAQUS 6.14 Documentation, Dassault Systèmes Simulia Corp., Providence, RI, USA, 2014.
- [61] J. Laurencin, B. Morel, Y. Bultel, F. Lefebvre-Joud, Thermo-Mechanical Model of Solid Oxide Fuel Cell Fed with Methane, *Fuel Cells*. 6 (2006) 64–70. doi:10.1002/fuce.200500096.
- [62] J. Laurencin, G. Delette, M. Dupeux, An estimation of ceramic fracture at singularities by a statistical approach, *J. Eur. Ceram. Soc.* 28 (2008) 1–13. doi:10.1016/j.jeurceramsoc.2007.06.003.
- [63] J. Laurencin, G. Delette, F. Lefebvre-Joud, M. Dupeux, A numerical tool to estimate SOFC mechanical degradation: Case of the planar cell configuration, *J. Eur. Ceram. Soc.* 28 (2008) 1857–1869. doi:10.1016/j.jeurceramsoc.2007.12.025.
- [64] G. Delette, J. Laurencin, S. Murer, D. Leguillon, Effect of residual stresses on the propagation of interface cracks between dissimilar brittle materials: Contribution of two and three-dimensional analyses, *Eur. J. Mech. - ASolids*. 35 (2012) 97–110. doi:10.1016/j.euromechsol.2012.02.001.
- [65] R. Clague, A.J. Marquis, N.P. Brandon, Time independent and time dependent probability of failure of solid oxide fuel cells by stress analysis and the Weibull method, *J. Power Sources*. 221 (2013) 290–299. doi:10.1016/j.jpowsour.2012.07.116.
- [66] J.R. Sack, J. Urrutia, *Handbook of Computational Geometry*, Elsevier, 1999.
- [67] C.-K. Lin, T.-T. Chen, A.-S. Chen, Y.-P. Chyou, L.-K. Chiang, Finite Element Analysis of Thermal Stress Distribution in Planar SOFC, in: *ECS, 2007*: pp. 1977–1986. doi:10.1149/1.2729310.
- [68] C.-K. Lin, T.-T. Chen, Y.-P. Chyou, L.-K. Chiang, Thermal stress analysis of a planar SOFC stack, *J. Power Sources*. 164 (2007) 238–251. doi:10.1016/j.jpowsour.2006.10.089.

- [69] C.-K. Lin, L.-H. Huang, L.-K. Chiang, Y.-P. Chyou, Effects of Clamping Load on the Thermal Stress Distribution in a Planar SOFC with Compressive Sealing, in: ECS, 2009: pp. 349–358. doi:10.1149/1.3205543.
- [70] C.-K. Lin, L.-H. Huang, L.-K. Chiang, Y.-P. Chyou, Thermal stress analysis of planar solid oxide fuel cell stacks: Effects of sealing design, *J. Power Sources*. 192 (2009) 515–524. doi:10.1016/j.jpowsour.2009.03.010.
- [71] C.-K. Lin, K. Anam, S.-H. Wu, R.-Y. Lee, Simulation of Cracking of Electrode Assembly in Planar Solid Oxide Fuel Cell, *ECS Trans*. 57 (2013) 2597–2606. doi:10.1149/05701.2597ecst.
- [72] C.-K. Lin, W.-H. Shiu, S.-H. Wu, R.-Y. Lee, Simulation of Interfacial Cracking of the Joint between Glass-Ceramic Sealant and Metallic Interconnect in a Planar Solid Oxide Fuel Cell Stack, *ECS Trans*. 68 (2015) 2981–2990. doi:10.1149/06801.2981ecst.
- [73] W. Jiang, Y. Luo, W. Zhang, W. Woo, S.T. Tu, Effect of temperature fluctuation on creep and failure probability for planar solid oxide fuel cell, *J. Fuel Cell Sci. Technol*. 12 (2015) 051004.
- [74] M. Peksen, R. Peters, L. Blum, D. Stolten, 3D coupled CFD/FEM modelling and experimental validation of a planar type air pre-heater used in SOFC technology, *Int. J. Hydrog. Energy*. 36 (2011) 6851–6861. doi:10.1016/j.ijhydene.2011.02.068.
- [75] B.X. Huang, R.W. Steinbrech, J. Malzbender, Direct observation of ferroelastic domain effects in LSCF perovskites, *Solid State Ion*. 228 (2012) 32–36. doi:10.1016/j.ssi.2012.08.025.
- [76] Y. Luo, W. Jiang, Q. Zhang, W.Y. Zhang, M. Hao, Effects of anode porosity on thermal stress and failure probability of planar solid oxide fuel cell with bonded compliant seal, *Int. J. Hydrog. Energy*. 41 (2016) 7464–7474. doi:10.1016/j.ijhydene.2016.03.117.
- [77] Y. Wang, W. Jiang, Y. Luo, Y. Zhang, S.-T. Tu, Evolution of thermal stress and failure probability during reduction and re-oxidation of solid oxide fuel cell, *J. Power Sources*. 371 (2017) 65–76. doi:10.1016/j.jpowsour.2017.10.034.
- [78] W. Jiang, Y. Zhang, Y. Luo, J.M. Gong, S.T. Tu, Creep analysis of solid oxide fuel cell with bonded compliant seal design, *J. Power Sources*. 243 (2013) 913–918. doi:10.1016/j.jpowsour.2013.06.096.
- [79] W. Jiang, Y. Zhang, W. Woo, S.T. Tu, Effect of Al₂O₃ film on thermal stress in the bonded compliant seal design of planar solid oxide fuel cell, *J. Power Sources*. 196 (2011) 10616–10624. doi:10.1016/j.jpowsour.2011.08.074.
- [80] J. Rösler, H. Harders, M. Bäker, Mechanical behaviour of engineering materials. Metals, ceramics, polymers, and composites, Springer, Berlin; New York, 2007. <http://site.ebrary.com/id/10230547> (accessed May 5, 2014).
- [81] F.H. Norton, The Creep of Steel at High Temperatures, McGraw-Hill Book Company, Incorporated, 1929. <http://books.google.ch/books?id=vswxAAAAMAAJ>.

- [82] M. Peksen, 3D CFD/FEM analysis of thermomechanical long-term behaviour in SOFCs: Furnace operation with different fuel gases, *Int. J. Hydrog. Energy*. 40 (2015) 12362–12369. doi:10.1016/j.ijhydene.2015.07.018.
- [83] W.N. Liu, X. Sun, M.A. Khaleel, Effect of Creep of Ferritic Interconnect on Long-Term Performance of Solid Oxide Fuel Cell Stacks, *Fuel Cells*. 10 (2010) 703–717. doi:10.1002/face.200900075.
- [84] K.P. Recknagle, B. Koeppel, X. Sun, M. Khaleel, S. Yokuda, P. Singh, Analysis of Percent On-Cell Reformation of Methane in SOFC Stacks and the Effects on Thermal, Electrical, and Mechanical Performance, in: *ECS, 2007*: pp. 473–478. doi:10.1149/1.2729027.
- [85] Y.J. Kim, M.C. Lee, Numerical investigation of flow/heat transfer and structural stress in a planar solid oxide fuel cell, *Int. J. Hydrog. Energy*. 42 (2017) 18504–18513. doi:10.1016/j.ijhydene.2017.04.140.
- [86] L.-K. Chiang, H.-C. Liu, Y.-H. Shiu, C.-H. Lee, R.-Y. Lee, Thermo-electrochemical and thermal stress analysis for an anode-supported SOFC cell, *Renew. Energy*. 33 (2008) 2580–2588. doi:10.1016/j.renene.2008.02.023.
- [87] H. Yakabe, Y. Baba, T. Sakurai, M. Satoh, I. Hirosawa, Y. Yoda, Evaluation of residual stresses in a SOFC stack, *J. Power Sources*. 131 (2004) 278–284. doi:10.1016/j.jpowsour.2003.12.057.
- [88] H. Yakabe, Y. Baba, T. Sakurai, Y. Yoshitaka, Evaluation of the residual stress for anode-supported SOFCs, *J. Power Sources*. 135 (2004) 9–16. doi:10.1016/j.jpowsour.2003.11.049.
- [89] W. Fischer, J. Malzbender, G. Blass, R.W. Steinbrech, Residual stresses in planar solid oxide fuel cells, *J. Power Sources*. 150 (2005) 73–77. doi:10.1016/j.jpowsour.2005.02.014.
- [90] M. Peksen, 3D thermomechanical behaviour of solid oxide fuel cells operating in different environments, *Int. J. Hydrog. Energy*. 38 (2013) 13408–13418. doi:10.1016/j.ijhydene.2013.07.112.
- [91] M. Peksen, A. Al-Masri, L. Blum, D. Stolten, 3D transient thermomechanical behaviour of a full scale SOFC short stack, *Int. J. Hydrog. Energy*. 38 (2013) 4099–4107. doi:10.1016/j.ijhydene.2013.01.072.
- [92] M. Peksen, 3D transient multiphysics modelling of a complete high temperature fuel cell system using coupled CFD and FEM, *Int. J. Hydrog. Energy*. 39 (2014) 5137–5147. doi:10.1016/j.ijhydene.2014.01.063.
- [93] X. Sun, A.M. Tartakovsky, M.A. Khaleel, Probabilistic-Based Design Methodology for Solid Oxide Fuel Cell Stacks, *J. Fuel Cell Sci. Technol.* 6 (2009) 021004. doi:10.1115/1.2971054.
- [94] C.O. Colpan, F. Hamdullahpur, I. Dincer, Heat-up and start-up modeling of direct internal reforming solid oxide fuel cells, *J. Power Sources*. 195 (2010) 3579–3589. doi:10.1016/j.jpowsour.2009.12.021.
- [95] T. Choudhary, Sanjay, Computational analysis of IR-SOFC: Transient, thermal stress, carbon deposition and flow dependency, *Int. J. Hydrog. Energy*. 41 (2016) 10212–10227. doi:10.1016/j.ijhydene.2016.04.016.

- [96] J. Lamon, Statistical approaches to failure for ceramic reliability assessment, *J. Am. Ceram. Soc.* 71 (1988) 106–112.
- [97] T. Klemensø, E. Lund, B.F. Sørensen, Optimal Shape of Thin Tensile Test Specimen, *J. Am. Ceram. Soc.* 90 (2007) 1827–1835. doi:10.1111/j.1551-2916.2007.01538.x.
- [98] H.L. Frandsen, T. Ramos, A. Faes, M. Pihlatie, K. Brodersen, Optimization of the strength of SOFC anode supports, *J. Eur. Ceram. Soc.* 32 (2012) 1041–1052. doi:10.1016/j.jeurceramsoc.2011.11.015.
- [99] J. Wei, G. Pećanac, J. Malzbender, Review of mechanical characterization methods for ceramics used in energy technologies, *Ceram. Int.* 40 (2014) 15371–15380. doi:10.1016/j.ceramint.2014.07.089.
- [100] H.L. Frandsen, D.J. Curran, S. Rasmussen, P.V. Hendriksen, High throughput measurement of high temperature strength of ceramics in controlled atmosphere and its use on solid oxide fuel cell anode supports, *J. Power Sources.* 258 (2014) 195–203. doi:10.1016/j.jpowsour.2014.02.036.
- [101] R. Danzer, A general strength distribution function for brittle materials, *J. Eur. Ceram. Soc.* 10 (1992) 461–472.
- [102] F.I. Baratta, Requirements for flexure testing of brittle materials, *Methods Assess. Struct. Reliab. Brittle Mater.* (1984) 194–222.
- [103] Y.-T. Chiu, C.-K. Lin, J.-C. Wu, High-temperature tensile and creep properties of a ferritic stainless steel for interconnect in solid oxide fuel cell, *J. Power Sources.* 196 (2011) 2005–2012. doi:10.1016/j.jpowsour.2010.09.083.
- [104] T. Murata, Y. Imai, The Temperature and Stress Dependences of the Steady-State Creep Rate of Ferritic Iron-Chromium Alloys, *Sci. Rep. Res. Inst. Tohoku Univ. Ser Phys. Chem. Metall.* 25 (1974) 103–111.
- [105] G.W. Hollenberg, G.R. Terwilliger, R.S. Gordon, Calculation of Stresses and Strains in Four-Point Bending Creep Tests, *J. Am. Ceram. Soc.* 54 (1971) 196–199.
- [106] J. Laurencin, G. Delette, F. Usseglio-Viretta, S. Di Iorio, Creep behaviour of porous SOFC electrodes: Measurement and application to Ni-8YSZ cermets, *J. Eur. Ceram. Soc.* 31 (2011) 1741–1752. doi:10.1016/j.jeurceramsoc.2011.02.036.
- [107] T. Most, J. Will, Sensitivity analysis using the Metamodel of Optimal Prognosis, *Proc Weimar. Optim.- Stochastiktage.* 8 (2011) 24–25.
- [108] T. Most, J. Will, Metamodel of Optimal Prognosis-an automatic approach for variable reduction and optimal metamodel selection, *Proc Weimar. Optim.- Stochastiktage.* 5 (2008) 20–21.
- [109] Dynardo GmbH, Weimar, ed., *Methods for multi-disciplinary optimization and robustness analysis*, (2016).
- [110] M. Pihlatie, A. Kaiser, M. Mogensen, Mechanical properties of NiO/Ni-YSZ composites depending on temperature, porosity and redox cycling, *J. Eur. Ceram. Soc.* 29 (2009) 1657–1664. doi:10.1016/j.jeurceramsoc.2008.10.017.

- [111] A.G. Evans, D. Rajdev, D.L. Douglass, The mechanical properties of nickel oxide and their relationship to the morphology of thick oxide scales formed on nickel, *Oxid. Met.* 4 (1972) 151–170.
- [112] A. Morales-Rodríguez, A. Bravo-León, A. Domínguez-Rodríguez, S. López-Esteban, J.S. Moya, M. Jiménez-Melendo, High-temperature mechanical properties of zirconia/nickel composites, *Ceram. Met. Interfaces.* 23 (2003) 2849–2856. doi:10.1016/S0955-2219(03)00309-1.
- [113] A. Morales-Rodríguez, A. Bravo-León, A. Domínguez-Rodríguez, M. Jiménez-Melendo, High-Temperature Plastic Behavior of TZP–Ni Cermets, *J. Am. Ceram. Soc.* 91 (2008) 500–507. doi:10.1111/j.1551-2916.2007.02121.x.
- [114] J. Bai, R. Raj, Influence of grain size variability on the strain rate dependence of the stress exponent in mixed-mode power law and diffusional creep, *Metall. Mater. Trans. A.* 36 (2005) 2913–2919.
- [115] D. Zhu, R.A. Miller, Determination of creep behavior of thermal barrier coatings under laser imposed high thermal and stress gradient conditions, *J. Mater. Res.* 14 (1999) 146–161. doi:10.1557/JMR.1999.0023.
- [116] D. Zhu, R.A. Miller, Determination of creep behavior of thermal barrier coatings under laser imposed high thermal and stress gradient conditions, *J. Mater. Res.* 14 (1999) 146–161. doi:10.1557/JMR.1999.0023.
- [117] R. Soltani, T.W. Coyle, J. Mostaghimi, Creep Behavior of Plasma-Sprayed Zirconia Thermal Barrier Coatings, *J. Am. Ceram. Soc.* 90 (2007) 2873–2878. doi:10.1111/j.1551-2916.2007.01822.x.
- [118] E. Withey, C. Petorak, R. Trice, G. Dickinson, T. Taylor, Design of 7wt.% Y₂O₃–ZrO₂/mullite plasma-sprayed composite coatings for increased creep resistance, *J. Eur. Ceram. Soc.* 27 (2007) 4675–4683. doi:10.1016/j.jeurceramsoc.2007.02.214.
- [119] G. Thurn, G.A. Schneider, F. Aldinger, High-temperature deformation of plasma-sprayed ZrO₂ thermal barrier coatings, *Mater. Sci. Eng. A.* 233 (1997) 176–182.
- [120] A.H. Chokshi, Diffusion, diffusion creep and grain growth characteristics of nanocrystalline and fine-grained monoclinic, tetragonal and cubic zirconia, *Scr. Mater.* 48 (2003) 791–796.
- [121] A. Lakki, R. Herzog, M. Weller, H. Schubert, C. Reetz, O. Görke, M. Kilo, G. Borchardt, Mechanical loss, creep, diffusion and ionic conductivity of ZrO₂-8 mol% Y₂O₃ polycrystals, *J. Eur. Ceram. Soc.* 20 (2000) 285–296.
- [122] C.B. Carter, M.G. Norton, *Ceramic Materials*, Springer Science+Business Media, LLC, [New York], 2007.
- [123] S.B. Batdorf, J.G. Crose, AEROSPACE CORP EL SEGUNDO CALIF., A Statistical Theory for the Fracture of Brittle Structures Subjected to Nonuniform Polyaxial Stresses, Defense Technical Information Center, 1973. <https://books.google.ch/books?id=1dRIOAAACAAJ>.

- [124] M. Radovic, E. Lara-Curzio, Mechanical properties of tape cast nickel-based anode materials for solid oxide fuel cells before and after reduction in hydrogen, *Acta Mater.* 52 (2004) 5747–5756. doi:10.1016/j.actamat.2004.08.023.
- [125] A. Selçuk, A. Atkinson, Strength and toughness of tape-cast yttria-stabilized zirconia, *J. Am. Ceram. Soc.* 83 (2000) 2029–2035.
- [126] K. Kwok, D. Boccaccini, Å.H. Persson, H.L. Frandsen, Homogenization of steady-state creep of porous metals using three-dimensional microstructural reconstructions, *Int. J. Solids Struct.* 78–79 (2016) 38–46. doi:10.1016/j.ijsolstr.2015.09.020.
- [127] T. Kanit, S. Forest, I. Galliet, V. Mounoury, D. Jeulin, Determination of the size of the representative volume element for random composites: statistical and numerical approach, *Int. J. Solids Struct.* 40 (2003) 3647–3679. doi:10.1016/S0020-7683(03)00143-4.
- [128] J. Johnson, J. Qu, Effective modulus and coefficient of thermal expansion of Ni–YSZ porous cermets, *J. Power Sources.* 181 (2008) 85–92. doi:10.1016/j.jpowsour.2008.03.035.
- [129] G. Delette, J. Laurencin, F. Usseglio-Viretta, J. Villanova, P. Bleuet, E. Lay-Grindler, T. Le Bihan, Thermo-elastic properties of SOFC/SOEC electrode materials determined from three-dimensional microstructural reconstructions, *Int. J. Hydrog. Energy.* 38 (2013) 12379–12391. doi:10.1016/j.ijhydene.2013.07.027.
- [130] R. Hill, Elastic properties of reinforced solids: some theoretical principles, *J. Mech. Phys. Solids.* 11 (1963) 357–372.
- [131] Fiji, v1.50, Rashband, W., Bethesda, 2016., n.d.
- [132] Avizo, v8, FEI Visualization Sciences Group, Hillsboro, 2016., n.d.
- [133] K.N. Grew, A.A. Peracchio, A.S. Joshi, J.R. Izzo Jr., W.K.S. Chiu, Characterization and analysis methods for the examination of the heterogeneous solid oxide fuel cell electrode microstructure. Part 1: Volumetric measurements of the heterogeneous structure, *J. Power Sources.* 195 (2010) 7930–7942. doi:10.1016/j.jpowsour.2010.07.005.
- [134] B. Münch, L. Holzer, Contradicting Geometrical Concepts in Pore Size Analysis Attained with Electron Microscopy and Mercury Intrusion, *J. Am. Ceram. Soc.* 91 (2008) 4059–4067. doi:10.1111/j.1551-2916.2008.02736.x.
- [135] M.B. DeGostin, A. Nakajo, B.N. Cassenti, A.A. Peracchio, G.J. Nelson, W.K.S. Chiu, Geometric sensitivity of electrochemical fin shape on three dimensional microstructure network conductivity analysis, *J. Power Sources.* 291 (2015) 181–194. doi:10.1016/j.jpowsour.2015.04.153.
- [136] L. Holzer, B. Iwanschitz, T. Hocker, B. Münch, M. Prestat, D. Wiedenmann, U. Vogt, P. Holtappels, J. Sfeir, A. Mai, T. Graule, Microstructure degradation of cermet anodes for solid oxide fuel cells: Quantification of nickel grain growth in dry and in humid atmospheres, *J. Power Sources.* 196 (2011) 1279–1294. doi:10.1016/j.jpowsour.2010.08.017.

- [137] G.J. Nelson, K.N. Grew, J.R. Izzo, J.J. Lombardo, W.M. Harris, A. Faes, A. Hessler-Wyser, J. Van herle, S. Wang, Y.S. Chu, A.V. Virkar, W.K.S. Chiu, Three-dimensional microstructural changes in the Ni-YSZ solid oxide fuel cell anode during operation, *Acta Mater.* 60 (2012) 3491–3500. doi:10.1016/j.actamat.2012.02.041.
- [138] M. Tsuda, E. Takemura, T. Asada, N. Ohno, T. Igari, Homogenized elastic–viscoplastic behavior of plate-fin structures at high temperatures: Numerical analysis and macroscopic constitutive modeling, *Int. J. Mech. Sci.* 52 (2010) 648–656. doi:10.1016/j.ijmecsci.2009.06.007.
- [139] S.W. Tsai, E.M. Wu, A general theory of strength for anisotropic materials, *J. Compos. Mater.* 5 (1971) 58–80.
- [140] Z. Xue, J.W. Hutchinson, Constitutive model for quasi-static deformation of metallic sandwich cores, *Int. J. Numer. Methods Eng.* 61 (2004) 2205–2238. doi:10.1002/nme.1142.
- [141] X. Badiche, S. Forest, T. Guibert, Y. Bienvenu, J.-D. Bartout, P. Ienny, M. Croset, H. Bernet, Mechanical properties and non-homogeneous deformation of open-cell nickel foams: application of the mechanics of cellular solids and of porous materials, *Mater. Sci. Eng. A.* 289 (2000) 276–288.
- [142] M. Tsuda, N. Ohno, Duplex model for homogenized elastic–viscoplastic behavior of plate–fin structures at high temperatures, *Int. J. Plast.* 27 (2011) 1560–1576. doi:10.1016/j.ijplas.2010.10.011.
- [143] A. Nakajo, Z. Willemin, P. Metzger, S. Diethelm, G. Schiller, J. Van herle, D. Favrat, Electrochemical Model of Solid Oxide Fuel Cell for Simulation at the Stack Scale I. Calibration Procedure on Experimental Data, *J. Electrochem. Soc.* 158 (2011) B1083. doi:10.1149/1.3596433.
- [144] A. Nakajo, P. Tanasini, S. Diethelm, J. Van herle, D. Favrat, Electrochemical Model of Solid Oxide Fuel Cell for Simulation at the Stack Scale II: Implementation of Degradation Processes, *J. Electrochem. Soc.* 158 (2011) B1102. doi:10.1149/1.3596435.
- [145] A. Nakajo, F. Mueller, J. Brouwer, J. Van herle, D. Favrat, Progressive activation of degradation processes in solid oxide fuel cell stacks: Part II: Spatial distribution of the degradation, *J. Power Sources.* 216 (2012) 434–448. doi:10.1016/j.jpowsour.2012.05.077.
- [146] ThyssenKrupp. Material data sheet no. 4046., (n.d.).
- [147] E.V. Stephens, J.S. Vetrano, B.J. Koeppel, Y. Chou, X. Sun, M.A. Khaleel, Experimental characterization of glass–ceramic seal properties and their constitutive implementation in solid oxide fuel cell stack models, *J. Power Sources.* 193 (2009) 625–631. doi:10.1016/j.jpowsour.2009.02.080.
- [148] F.L. Lowrie, R.D. Rawlings, Room and high temperature failure mechanisms in solid oxide fuel cell electrolytes, *J. Eur. Ceram. Soc.* 20 (2000) 751–760.
- [149] A. Atkinson, A. Selcuk, Mechanical behaviour of ceramic oxygen ion-conducting membranes, *Solid State Ion.* 134 (2000) 59–66.

- [150] F. Iguchi, Y. Endo, T. Ishida, T. Yokobori, H. Yugami, T. Otake, T. Kawada, J. Mizusaki, Oxygen partial pressure dependence of creep on yttria-doped ceria ceramics, *Solid State Ion.* 176 (2005) 641–644. doi:10.1016/j.ssi.2004.09.005.
- [151] X. Guan, H. Zhou, Y. Wang, J. Zhang, Preparation and properties of Gd³⁺ and Y³⁺ co-doped ceria-based electrolytes for intermediate temperature solid oxide fuel cells, *J. Alloys Compd.* 464 (2008) 310–316. doi:10.1016/j.jallcom.2007.09.116.
- [152] H. Lein, K. Wiik, T. Grande, Thermal and chemical expansion of mixed conducting La_{0.5}Sr_{0.5}Fe_{1-x}Co_xO_{3-δ} materials, *Solid State Ion.* 177 (2006) 1795–1798. doi:10.1016/j.ssi.2006.02.033.
- [153] H.L. Lein, Ø.S. Andersen, P.E. Vullum, E. Lara-Curzio, R. Holmestad, M.-A. Einarsrud, T. Grande, Mechanical properties of mixed conducting La_{0.5}Sr_{0.5}Fe_{1-x}Co_xO_{3-δ} (0 ≤ x ≤ 1) materials, *J. Solid State Electrochem.* 10 (2006) 635–642. doi:10.1007/s10008-006-0140-0.
- [154] H.L. Lein, K. Wiik, M. Einarsrud, T. Grande, E. Lara-curzio, High-Temperature Creep Behavior of Mixed Conducting La_{0.5}Sr_{0.5}Fe_{1-x}Co_xO_{3-δ} (0.5 ≤ x ≤ 1) Materials, *J. Am. Ceram. Soc.* 89 (2006) 2895–2898. doi:10.1111/j.1551-2916.2006.01176.x.
- [155] M. Pihlatie, A. Kaiser, P.H. Larsen, M. Mogensen, Dimensional Behavior of Ni–YSZ Composites during Redox Cycling, *J. Electrochem. Soc.* 156 (2009) B322. doi:10.1149/1.3046121.
- [156] L.J. Gibson, M.F. Ashby, *Cellular Solids: Structure and Properties*, Cambridge University Press, 1999. <http://books.google.ch/books?id=lySUR5sn4N8C>.
- [157] H. Choe, D.C. Dunand, Mechanical properties of oxidation-resistant Ni–Cr foams, *Mater. Sci. Eng. A.* 384 (2004) 184–193. doi:10.1016/j.msea.2004.06.045.
- [158] ThyssenKrupp. Material data sheet no. 1001., (n.d.).
- [159] S. Biswas, T. Nithyanantham, N.T. Saraswathi, S. Bandopadhyay, Evaluation of elastic properties of reduced NiO-8YSZ anode-supported bi-layer SOFC structures at elevated temperatures in ambient air and reducing environments, *J. Mater. Sci.* 44 (2008) 778–785. doi:10.1007/s10853-008-3141-9.
- [160] M. Hauth, V. Lawlor, P. Cartellieri, C. Zechmeister, S. Wolff, C. Bucher, J. Malzbender, J. Wei, A. Weber, G. Tsotridis, H.L. Frandsen, K. Kwok, T.T. Molla, Z. Wullemin, J. Van herle, F. Greco, T. Cornu, A. Nakajo, A. Atkinson, L. Vandeperre, X. Wang, Production and Reliability Oriented SOFC Cell and Stack Design, *ECS Trans.* 78 (2017) 2231–2249. doi:10.1149/07801.2231ecst.
- [161] A. Müller, S. Goswami, W. Becker, D. Stolten, L.G.J. (Bert) de Haart, R.W. Steinbrech, Assessment of the Sealing Joints within SOFC Stacks by Numerical Simulation, *Fuel Cells.* 6 (2006) 107–112. doi:10.1002/fuce.200500115.
- [162] D. Gross, T. Seelig, *Fracture Mechanics*, Springer Berlin Heidelberg, Berlin, Heidelberg, 2011. <http://link.springer.com/10.1007/978-3-642-19240-1> (accessed July 3, 2014).

- [163] B.F. Sørensen, S. Sarraute, O. Jørgensen, A. Horsewell, Thermally induced delamination of multilayers, *Acta Mater.* 46 (1998) 2603–2615. doi:10.1016/S1359-6454(97)00472-2.
- [164] E.F. Rybicki, M.F. Kanninen, A finite element calculation of stress intensity factors by a modified crack closure integral, *Eng. Fract. Mech.* 9 (1977) 931–938. doi:10.1016/0013-7944(77)90013-3.
- [165] A. Agrawal, A.M. Karlsson, Obtaining mode mixity for a bimaterial interface crack using the virtual crack closure technique, *Int. J. Fract.* 141 (2006) 75–98. doi:10.1007/s10704-006-0069-4.
- [166] R. Krueger, Virtual crack closure technique: History, approach, and applications, *Appl. Mech. Rev.* 57 (2004) 109. doi:10.1115/1.1595677.
- [167] Y. Zhao, J. Malzbender, S.M. Gross, The effect of room temperature and high temperature exposure on the elastic modulus, hardness and fracture toughness of glass ceramic sealants for solid oxide fuel cells, *J. Eur. Ceram. Soc.* 31 (2011) 541–548. doi:10.1016/j.jeurceramsoc.2010.10.032.
- [168] M. Pihlatie, T. Ramos, A. Kaiser, Testing and improving the redox stability of Ni-based solid oxide fuel cells, *J. Power Sources.* 193 (2009) 322–330. doi:10.1016/j.jpowsour.2008.11.140.
- [169] S. Lee, H.S. Song, S.H. Hyun, J. Kim, J. Moon, Interlayer-free nanostructured La_{0.58}Sr_{0.4}Co_{0.2}Fe_{0.8}O_{3-δ} cathode on scandium stabilized zirconia electrolyte for intermediate-temperature solid oxide fuel cells, *J. Power Sources.* 187 (2009) 74–79. doi:10.1016/j.jpowsour.2008.10.101.
- [170] T. Wakui, R. Yokoyama, Optimal sizing of residential SOFC cogeneration system for power interchange operation in housing complex from energy-saving viewpoint, *Energy.* 41 (2012) 65–74. doi:10.1016/j.energy.2011.06.056.

Curriculum Vitae

Fabio GRECO

Avenue de Beaulieu 22

CH-1004 Lausanne

Switzerland

+41 789 752 591

 fabio.greco87@gmail.com

 fabiogreco87

 **LinkedIn**



Education

École polytechnique fédérale de Lausanne, Switzerland Doctoral assistant	02.2013 - end: spring 2018
Polytechnic of Turin, C.so Duca degli Abruzzi 24, Torino, Italy Master of Science in Mechanical Engineering , degree mark: 110/110	07.2012
Polytechnic of Turin, C.so Duca degli Abruzzi 24, Torino, Italy Bachelor of Science in Mechanical Engineering	10.2009
Industrial school "A. Meucci", Viale Ferrari, Casarano, Italy Industrial expert mechanical specialization	07.2006

Core experience

École polytechnique fédérale de Lausanne, Switzerland Project title: <i>"Improved reliability of anode-supported solid oxide fuel cells (SOFCs)"</i> .	02.2013 - ongoing
Altran Italia S.p.A, Strada del Drosso 33, Torino, Italy Junior consultant FMEA (failure mode and effects analysis) analyst; main client: Iveco/CNH Industrial	10.2012 - 12.2012
DTU Risø Campus, Department of Energy Conversion and Storage, Roskilde, Denmark Internship and master thesis project Project title: <i>"Assessment of the time dependent mechanical response of SOFCs and impact on stack performance"</i> .	10.2011 - 04.2012
BOSCH Prisma Project German class offered by Robert Bosch S.p.A.	12.2010 - 05.2011

Additional experience

École polytechnique fédérale de Lausanne, Switzerland Teaching in mechanical engineering classes	02.2013 - 06.2016
FATA GROUP S.p.A. , Via dei Prati, 2, Pianezza TO, Italy Bachelor thesis project Project title: <i>"Analytical and numerical models of the cold rolling of thin sheets of aluminium"</i> .	05.2009 - 10.2009

Torsello Domenico Infissi, Via Pavia 8, Casarano, Italy

06.2003 - 05.2006

Worker (part-time job)

Fabrication of metal sheet, welding, painting

Languages



Italian (mother tongue)



French (B2)



English (C2)



German (A1)

Computer Skills

Solidworks® *expert*

Abaqus® (FEA) *expert*

Microsoft® Office *very good*

Internet browsers *very good*

Matlab® *very good*

Comsol Multiphysics® *very good*

OptiSLang® *good*

AutoCAD® *good*

LabVIEW *basic*

FeatureCAM® *basic*

Scientific publications

Modelling the impact of creep on the probability of failure of a solid oxide fuel cell stack, Greco, F., Frandsen, H.L., Nakajo, A., Madsen, M.F., Van herle, J., 2014, Journal of the European Ceramic Society 34(11), pp. 2695-2704.

Thermo-mechanical reliability of SOFC stacks during combined long-term operation and thermal cycling, Greco, F., Nakajo, A., Wuillemin, Z., Van Herle, J., 2015, ECS Transactions 68(1), pp. 1921-1931.

Accelerated creep in solid oxide fuel cell anode supports during reduction, Frandsen, H.L., Makowska, M., Greco, F., Kuhn, L.T., Hendriksen, P.V., 2016, Journal of Power Sources 323, pp. 78-89.

Lifetime Issues for Solid Oxide Fuel Cell Interconnects (Book Chapter), Bianco, M., Linder, M., Larring, Y., Greco, F., Van herle, J., 2017, Solid Oxide Fuel Cell Lifetime and Reliability: Critical Challenges in Fuel Cells, pp. 121-144.

The effects of component tolerances on the thermo-mechanical reliability of SOFC stacks, Greco, F., Nakajo, A., Wuillemin, Z., Van Herle, J., 2017, ECS Transactions 78(1), pp. 2271-2283.

Production and reliability oriented SOFC cell and stack design, Hauth, M., Lawlor, V., Cartellieri, P., Zechmeister, C., Wolff, S., Bucher, C., Malzbender, J., Wei, J., Weber, A., Tsotridis, G., Frandsen, H.L., Kwok, K., Molla, T.T., Wuillemin, Z., Van Herle, J., Greco, F., Cornu, T., Nakajo, A., Atkinson, A., Vandeperre, L., Wang, X., 2017, ECS Transactions 78(1), pp. 2231-2249.

Attended conferences

CERMODEL 2013, F. Greco, H.L. Frandsen, M.F. Madsen, J. Van herle. *Modelling the impact of creep on the failure probability of a solid oxide fuel cell stack (oral presentation)*. July 10-12, Trento, Italy.

COMSOL Conference 2013, F. Greco, A. Nakajo, J. Van herle. *Residual stresses and failure probability of solid oxide fuel cells due to the sintering process (poster presentation)*. October 23-25, 2013, Rotterdam, The Netherlands.

ModVal11, F. Greco, A. Nakajo, J. Van herle. *Modelling the impact of creep on the failure probability of a solid oxide fuel cell stack (poster presentation)*. March 17-19, 2014, Winterthur, Switzerland.

11th European SOFC & SOE Forum, F. Greco, A. Nakajo, J. Van herle. *Mechanical properties of interconnects, sealants and gas diffusion layers for planar solid oxide fuel cell stacks. Part I: interconnects and gas diffusion layers (poster presentation)*. July 1-4, 2014, Lucerne, Switzerland.

SOFC-XIV, ECS Conference on Electrochemical Energy Conversion & Storage, F. Greco, A. Nakajo, Z. Wuillemin, J. Van herle. *Thermo-mechanical reliability of SOFC stacks during combined long-term operation and thermal cycling (poster presentation)*. July 26-31, 2015, Glasgow, The United Kingdom.

ModVal13, F. Greco, A. Nakajo, J. Van herle. *Four-point bending testing: estimation of the accuracy and identification of the mechanical properties (poster presentation)*. March 22-23, 2016, Lausanne, Switzerland.

12th European SOFC & SOE Forum, F. Greco, A. Nakajo, D. Montinaro, J. Van herle. *Four-point bending testing: estimation of the accuracy and identification of the mechanical properties of SOFC materials, (poster presentation)*. July 5-8, 2016, Lucerne, Switzerland.

ModVal14, F. Greco, A. Nakajo, J. Van herle. *Parameter estimation of the elastic and creep properties of Ni-YSZ anode based on four-point bending measurements (oral presentation)*. March 2-3, 2017, Karlsruhe, Germany.

SOFC-XIV, ECS Conference on Electrochemical Energy Conversion & Storage, F. Greco, A. Nakajo, Z. Wuillemin, J. Van herle. *The effect of component tolerances on the thermo-mechanical reliability of SOFC stacks (oral presentation)*. July 23-28, 2017, Hollywood FL, The United States of America.

13th European SOFC & SOE Forum, F. Greco, A. Nakajo, Z. Wuillemin, J. Van herle. *Thermo-mechanical reliability of SOFC stacks: impact of component tolerances and operating conditions, (oral presentation)*. July 3-6, 2018 (planned), Lucerne, Switzerland.

Doctoral courses

Mechanics of Thin Films, EPFL, Spring semester 2013.

Nonlinear Finite Element Analysis, Luxembourg Summer School in Computational Engineering Sciences, 1-7 July, 2013.

Multiphysics Finite Element Methods, EPFL, Winter semester 2014.

Non-destructive Evaluation Methods, EPFL, Spring semester 2016.

Extracurricular activities

Body-building
Car hill-climbing
Cooking
Travelling

Personal details

30 years old
Swiss C EU/EFTA residence permit (lucrative activity)
Driving licence (category: B)
Italian nationality
Unmarried

